



**UNIVERSIDADE ESTADUAL DE CAMPINAS**  
Faculdade de Engenharia Mecânica

**SHOHREH IRAJI**

**Experimental, Numerical, and Porosity-Permeability Prediction Investigations for  
Multiscale Fluid Flow in Heterogeneous Carbonate Rocks**

**Investigações Experimentais, Numéricas e de Predição de Porosidade-Permeabilidade para  
Fluxo de Fluido Multiscale em Rochas Carbonáticas Heterogêneas**

**Campinas**

**2023**

**SHOHREH IRAJI**

**Experimental, Numerical, and Porosity-Permeability Prediction Investigations for  
Multiscale Fluid Flow in Heterogeneous Carbonate Rocks**

**Investigações Experimentais, Numéricas e de Predição de Porosidade-Permeabilidade para  
Fluxo de Fluido Multiscale em Rochas Carbonáticas Heterogêneas**

Thesis presented to the School of Mechanical Engineering and Institute of Geosciences of the University of Campinas in partial fulfillment of the requirements for the degree of Doctor in Science and Petroleum Engineering, in the area of Reservoirs and Management.

Tese apresentada à Faculdade de Engenharia Mecânica e Instituto de Geociências da Universidade Estadual de Campinas como requisito parcial para obtenção do título de Doutor em Ciências e Engenharia de Petróleo, na área de Reservatórios e Gestão.

Supervisor/Orientador:

PROF. DR. ANTONIO CARLOS BANNWART

ESTE TRABALHO CORRESPONDE À VERSÃO  
FINAL DA TESE DEFENDIDA PELO ALUNO  
SHOHREH IRAJI, E ORIENTADA PELO PROF.  
DR. ANTONIO CARLOS BANNWART

CAMPINAS

2023

Ficha catalográfica  
Universidade Estadual de Campinas  
Biblioteca da Área de Engenharia e Arquitetura  
Rose Meire da Silva - CRB 8/5974

Ir12e Iraj, Shohreh, 1990-  
Experimental, numerical, and porosity-permeability prediction investigations for multiscale fluid flow in heterogeneous carbonate rocks / Shohreh Iraj. – Campinas, SP : [s.n.], 2023.

Orientador: Antonio Carlos Bannwart.  
Coorientador: Alexandre Campana Vidal.  
Tese (doutorado) – Universidade Estadual de Campinas, Faculdade de Engenharia Mecânica.

1. Reservatórios de petróleo. 2. Meios porosos. 3. Rochas carbonáticas. 4. Modelagem multiescala. 5. Aprendizado profundo. 6. Reservatórios (Simulação). 7. Análise de imagem. I. Bannwart, Antonio Carlos, 1955-. II. Vidal, Alexandre Campana, 1969-. III. Universidade Estadual de Campinas. Faculdade de Engenharia Mecânica. IV. Título.

### Informações Complementares

**Título em outro idioma:** Investigações experimentais, numéricas e de predição de porosidade-permeabilidade para fluxo de fluido multiescala em rochas carbonáticas heterogêneas

**Palavras-chave em inglês:**

Petroleum reservoirs  
Porous media  
Carbonate rocks  
Multiscale modeling  
Deep learning  
Reservoirs (Simulation)  
Image analysis

**Área de concentração:** Reservatórios e Gestão

**Titulação:** Doutora em Ciências e Engenharia de Petróleo

**Banca examinadora:**

Antonio Carlos Bannwart [Orientador]  
Alessandra Winter Spagnol  
Iara Frangiotti Mantovani  
William Godoy de Azevedo Lopes da Silva  
Guilherme Daniel Avansi

**Data de defesa:** 13-06-2023

**Programa de Pós-Graduação:** Ciências e Engenharia de Petróleo

**Identificação e informações acadêmicas do(a) aluno(a)**

- ORCID do autor: <https://orcid.org/0000-0001-6285-6785>

- Currículo Lattes do autor: <http://lattes.cnpq.br/0272548486322414>

**UNIVERSIDADE ESTADUAL DE CAMPINAS**  
**FACULDADE DE ENGENHARIA MECÂNICA**  
**TESE DE DOUTORADO ACADÊMICO**

**Experimental, Numerical, and Porosity-Permeability  
Prediction Investigations for Multiscale Fluid Flow in  
Heterogeneous Carbonate Rocks**

**Investigações Experimentais, Numéricas e de Predição  
de Porosidade-Permeabilidade para Fluxo de Fluido  
Multiscale em Rochas Carbonáticas Heterogêneas**

Autor: Shohreh Irají

Orientador: Dr. Antonio Carlos Bannwart

A Banca Examinadora composta pelos membros abaixo aprovou esta Tese:

**Dr. Antonio Carlos Bannwart – Presidente**  
**Faculdade de Engenharia Mecânica/Universidade Estadual de Campinas**

**Dr. Iara Frangiotti Mantovani**  
**Universidade Federal de Santa Catarina**

**Dr. William Godoy de Azevedo Lopes da Silva**  
**Equinor Brasil Energia Ltda**

**Dr. Guilherme Daniel Avansi**  
**Centro de Estudos de Energia e Petróleo/Universidade Estadual de Campinas**

**Dr. Alessandra Winter Spagnol**  
**Centro de Estudos de Energia e Petróleo/Universidade Estadual de Campinas**

A Ata de Defesa com as respectivas assinaturas dos membros encontra-se disponível no SIGA – Sistema de fluxo de Tese e na Secretaria de Pós-graduação da Faculdade de Engenharia Mecânica.

Campinas, 13 de Junho de 2023.

## ACKNOWLEDGMENTS

I would like to express my deepest appreciation and gratitude to my first supervisor, Prof. Dr. Alexandre Campana Vidal, for his excellent technical guidance, constructive criticism, and unwavering support throughout my thesis work. Without his valuable feedback and patience, this thesis would not have been possible.

I would also like to express my sincere appreciation to my second supervisor, Prof. Dr. Antonio Carlos Bannwart, for his encouragement and outstanding technical support and comments.

I am grateful for the financial support of Equinor Brazil, who provided me with a full scholarship during my studies. I would also like to extend my sincere thanks to the Center of Energy and Petroleum Studies (CEPETRO) for providing laboratory instruments and to the School of Mechanical Engineering (FEM) for their support.

I am deeply grateful to Dr. Eddy Ruidiaz Munoz, Dr. Mateus Basso, Dr. Guilherme Furlan Chinelatto, Mr. Ramin Soltanmohammadi, and Mr. Tales Rodrigues De Almeida for their time and valuable comments, which greatly contributed to the success of this work.

I would like to extend my gratitude to the examiners of this thesis, Dr. Alessandra Winter Spagnol Dr. Guilherme Daniel Avansi, Dr. William Godoy de Azevedo Lopes da Silva, and Dr. Iara Frangiotti Mantovani, for their valuable time and insights.

Finally, I would like to express my special thanks and appreciation to all members of my family for their unwavering encouragement and support throughout my academic journey.

DEDICATION

*I wish to dedicate my thesis:*

*To my mother*

*For all her support, encouragement, and especially for her unconditional  
love, sacrifice, and unreserved affection.*

## **RESUMO**

Os reservatórios de pré-sal no Brasil foram recentemente identificados como uma fonte altamente promissora de produção de hidrocarbonetos devido ao seu alto potencial. No entanto, esses reservatórios são caracterizados por sistemas porosos extremamente complexos, ricos em vugs e fraturas, que geralmente apresentam grande variação no tamanho e geometria dos poros. Essas características contribuem para a complexidade da simulação do fluxo de fluidos nos reservatórios, aumentando assim a incerteza e a dificuldade na gestão dos mesmos. Para mitigar riscos e incertezas associados à produção de reservatórios do pré-sal, é imprescindível obter uma compreensão abrangente e uma avaliação apropriada do fluxo de fluidos e das propriedades petrofísicas. Isso requer o desenvolvimento de técnicas avançadas de simulação e modelagem capazes de capturar efetivamente as características complexas do reservatório e permitir previsões precisas do comportamento do reservatório.

Esta tese apresenta uma investigação abrangente sobre o fluxo de fluidos em meios porosos heterogêneos e a caracterização petrofísica de rochas de reservatório usando uma variedade de técnicas experimentais, de simulação e de análise de dados. Especificamente, a pesquisa se concentra nos reservatórios do Pré-Sal Brasileiro e tem como objetivo desenvolver uma compreensão mais abrangente dos processos complexos associados ao fluxo de fluidos nesses reservatórios, o que tem implicações significativas para a produção de hidrocarbonetos e armazenamento de carbono e hidrogênio.

Parte da pesquisa envolveu a realização de experimentos e simulações em amostras de afloramento da Lagoa Salgada, no Rio de Janeiro, Brasil, para investigar o impacto da geometria dos poros no fator de recuperação de fluidos, perfil de saturação e estimativas de permeabilidade relativa. Dados de tomografia computadorizada foram empregados para gerar modelos representativos de amostras de rochas dos reservatórios de pré-sal. Um algoritmo foi aplicado para manipular e processar as imagens adquiridas, e as imagens resultantes foram empilhadas para criar um grid 3D de alta resolução do meio poroso dentro dos reservatórios. Isso envolveu a remoção das regiões relacionadas às partes externas, a aplicação de regras para definição de segmentação e facies, e a estimativa da porosidade e permeabilidade de cada bloco do grid. Para reduzir o tempo computacional, foram aplicadas técnicas de upscaling e, em seguida, uma técnica de history matching foi empregada para coincidir os resultados experimentais e de simulação e estimar a

permeabilidade relativa de duas principais facies definidas dentro dos reservatórios. Esse processo permitiu a criação de um modelo de reservatório atualizado capaz de avaliar o desempenho passado e presente, bem como prever o comportamento futuro do fluxo de fluidos. Este trabalho fornece informações valiosas sobre o fluxo de fluidos em sistemas porosos heterogêneos e serve como base para escolhas operacionais.

Outra parte da pesquisa examinou os efeitos das características da rede de poros e da heterogeneidade no fluxo de fluidos através de meios porosos complexos e heterogêneos. Técnicas de imagem de CT de alta resolução foram utilizadas para examinar amostras de afloramento, e um Modelo de Rede de Poros (PNM) foi empregado para quantificar a relação entre as principais características do sistema poroso. Além disso, imagens de alta resolução das amostras foram usadas para criar dois cortes transversais para modelagem em escala de poros. A análise mostrou que os poros sem saída e as cavidades presentes na amostra causaram uma quantidade significativa de fluido a permanecer estagnado, levando a um comportamento de canalização do fluido injetado, a uma quebra prematura e a uma baixa eficiência. O estudo também realizou uma série de experimentos de fluxo em plugues de rocha, acoplados a digitalização médica por CT para avaliar a propagação do fluxo e os perfis de saturação. Os resultados destacaram o impacto da heterogeneidade e da presença de poros desconectados ou sem saída nos padrões de fluxo e saturação, revelando um deslocamento preferencial e heterogêneo de fluido em algumas regiões os plugues.

A última parte da pesquisa envolveu um estudo abrangente da Formação Barra Velha na Bacia de Santos, empregando uma combinação de dados convencionais de perfuração, análises de microCT ( $\mu$ CT) de dados de plugue, e descrição de laminais petrográficas para caracterizar e avaliar com precisão as sequências do reservatório. O estudo focou em alcançar uma definição precisa de quatro tipos de rochas de reservatório (RRTs) integrando os valores petrofísicos dos plugues e seus dados de perfuração correspondentes usando o algoritmo de classificação não supervisionada K-means. Os resultados da classificação foram então integrados com diversas técnicas convencionais para avaliar a qualidade e as características geológicas da sequência estudada. Além disso, a modelagem de rede de poros a partir da análise de  $\mu$ CT de plugues foi utilizada especificamente para a caracterização dos poros e gargantas das amostras de núcleos de cada RRT. O estudo utilizou algoritmos de aprendizado profundo e aprendizado de máquina para desenvolver modelos

preditivos para a porosidade da perfuração e o tipo de rocha com base em dados de registro de poços. Os modelos ResNet e 1D CNN foram treinados e avaliados para prever a porosidade da perfuração, enquanto o algoritmo XGBoost foi aplicado para prever o tipo de rocha.

Em resumo, esta tese fornece um estudo abrangente e integrado do fluxo de fluidos e caracterização petrofísica de rochas de reservatório, oferecendo valiosos insights nos processos complexos associados ao fluxo de fluidos em meios porosos heterogêneos. As descobertas da pesquisa têm implicações significativas para a produção de hidrocarbonetos e armazenamento de carbono e hidrogênio, podendo facilitar a previsão de tipo de rocha precisa, caracterização petrofísica e o desenvolvimento de modelos preditivos confiáveis.

**Palavras-chave:** Geometria de poros, meios porosos vulgares, modelagem de rede de poros, modelagem em escala de poros, propagação de fluidos, linhas de fluxo de fluido, poros sem saída, upscaling, correspondência de histórico, caracterização petrofísica, tipos de rochas reservatórios, classificação não supervisionada, aprendizado profundo

## **ABSTRACT**

The pre-salt reservoirs in Brazil have recently been identified as a highly promising source of hydrocarbon production due to their substantial potential. However, these reservoirs are characterized by an intricate pore network, vuggy nature, and heterogeneity, which give rise to variations in pore size and geometry. These features contribute to the complexity of simulating fluid flow within the reservoirs, thereby increasing uncertainty and difficulty in reservoir management. To mitigate risks and uncertainties associated with pre-salt reservoir production, it is imperative to obtain a comprehensive understanding and an appropriate assessment of fluid flow transfer and petrophysical properties. This necessitates the development of advanced simulation and modeling techniques that can effectively capture complex reservoir features and enable accurate predictions of reservoir behavior.

This thesis presents a comprehensive investigation into fluid flow in heterogeneous porous media and the petrophysical characterization of reservoir rocks using a range of experimental, simulation, and data analysis techniques. Specifically, the research focuses on the Brazilian Pre-salt reservoirs and aims to develop a more comprehensive understanding of the complex processes underlying fluid flow in these reservoirs, which has significant implications for hydrocarbon production and carbon and hydrogen storage.

Part of the research involved conducting experiments and simulations on outcrop samples from Lagoa Salgada in Rio de Janeiro, Brazil, to investigate the impact of pore geometry on fluid recovery factor, saturation profile, and relative permeability estimations. CT imaging was employed to generate representative models of rock samples. An algorithm was applied to manipulate and process the acquired images, and the resulting images were stacked to create a 3D fine-scale grid of the porous media within the reservoirs. This involved removing the regions related to the exterior parts, applying rules for segmentation and facies definition, and estimating the porosity and permeability of each grid block. To reduce computation time, upscaling techniques were applied and following this, a history-matching technique was employed to match experimental and simulation results and estimate the relative permeability of two main defined facies within the reservoirs. This process enabled the creation of an updated reservoir model capable of assessing past and present performance, as well as forecasting future fluid flow behavior.

This work provides valuable insights into fluid flow in heterogeneous porous systems and serves as a foundation for sensible operational choices.

Another part of the research examined the effects of pore network characteristics and heterogeneity on fluid flow through complex and heterogeneous porous media. High-resolution CT imaging techniques were used to examine outcrop stromatolite samples, and Pore Network Model (PNM) was employed to quantify the relationship between key features of the porous system. Moreover, high-resolution images of the samples were used to create two cross-sections from horizontal and vertical plates for pore-scale modeling. The analysis showed that dead-end pores and vugs present in the sample caused a significant amount of fluid to remain stagnant, leading to a channeling-like behavior of the injected fluid, early breakthrough, and low areal-swept efficiency. The study also conducted a series of core flooding experiments coupled with medical CT scanning to assess flow propagation and saturation profiles. The results highlighted the impact of heterogeneity and the presence of disconnected or dead-end pores on flow patterns and saturation, revealing preferential and heterogeneous displacement of fluid in some regions of the plugs and bypassing it in others.

The final part of the research involved a comprehensive study of the Barra Velha Formation in the Santos Basin, employing a combination of conventional well log data, microCT ( $\mu$ CT) analyses of plug data, and thin section description to accurately characterize and evaluate the reservoir sequences. The study focused on achieving a precise definition of four reservoir rock types (RRTs) by integrating the petrophysical values of the plugs and their corresponding well log data using the K-means unsupervised classification algorithm. The classification results were then integrated with several conventional techniques to evaluate the quality and geological characteristics of the studied sequence. Additionally, pore network modeling from  $\mu$ CT analysis of plugs was used specifically for the characterization of pores and throats of plug samples from each RRT. The study utilized deep learning and machine learning algorithms to develop predictive models for plug porosity and rock type based on well log data. The ResNet and 1D CNN models were trained and evaluated for plug porosity prediction. The XGBoost algorithm was also applied to predict rock type.

Overall, this thesis provides a comprehensive and integrated study of fluid flow and petrophysical characterization of reservoir rocks, offering valuable insights into the complex processes underlying fluid flow in heterogeneous porous media. The research findings have significant implications for hydrocarbon production and carbon and hydrogen storage and can facilitate

accurate rock type prediction, petrophysical characterization, and the development of reliable predictive models.

**Keywords:** Pore geometry, vuggy porous media, pore network modeling, pore-scale modeling, fluid propagation, flow streamlines, dead-end pores, upscaling, history matching, petrophysical characterization, reservoir rock types, unsupervised classification, deep learning

## LIST OF FIGURES

Figure 1-1. Applied workflow for Chapter 2. FW represents the formation water, $S_{oi}$ and $S_{or}$ denote the initial and residual oil saturations, respectively, ROI presents the region of interest. .....	28
Figure 1-2. Implemented workflow for Chapter 3. SW and DW represent the sea and distilled water, respectively.....	29
Figure 1-3. Applied workflow for Chapter 4.....	30
Figure 2-1. a) Fine-grained (Facies 1) and vugular (Facies 2) facies of microbial carbonates rock block from Lagoa Sagada outcrop, Brazil, b) Selected plug samples for the different facies. ....	39
Figure 2-2. Applied workflow for experimental, image processing, and simulation steps.....	40
Figure 2-3. Schematic of the core flooding apparatus embedded in a CT-scanner.....	41
Figure 2-4. a) Heterogeneous and fragile plug sample, b) plug sample covered with thermal plastic, c) process of encapsulating with resin, and d) plug sample encapsulated with thermal plastic and resin. ....	44
Figure 2-5. a) First test: applying resin directly over the vugular plug sample, b) Second test: applying epoxy resin directly over the fine-grained plug sample. ....	45
Figure 2-6. a) Third test: applying resin and thermal plastic over the fine-grained plug sample, b) Forth test: applying resin and thermal plastic over the vugular plug sample.....	45
Figure 2-7. Relative permeability for a) fine-grained facies (Rock Type 1), b) vugular facies (Rock Type 2).....	48
Figure 2-8. Position and completions of the injector (a), producer (b), and physical diffuser (c) for F1-1 vugular sample. ....	48
Figure 2-9. History-matching process. ....	51
Figure 2-10. Porosity profile for three plug samples.....	53
Figure 2-11. First cross-section image of F1-1 vugular plug sample for: (a) $N_2$ -saturated (Dry CT), (b) FW-saturated (Wet CT). ....	53
Figure 2-12. Oil recovery results for the three plug samples. ....	55
Figure 2-13. Saturation profile during injection of oil and FW injection for a) F1-1 vugular sample, b) F2-5 fine-grained sample. ....	56
Figure 2-14. First cross-section image of F1-1 vugular plug sample for: a) 0 PV oil injection, b) 0.2 PV oil injection, and c) 2.0 PV oil injection.....	56

Figure 2-15. a) Examples of 2D CT images of noncircular plug samples b) 2D CT images after processing and excluding the exterior region (ROI) c) CT values of line 256 for the first image (Figure 2-15-a) d) histogram of CT value of the first image after processing (Figure 2-15-b).....	58
Figure 2-16. 3D representation of the simulation model for a) F1-1 vugular sample (with the process of stacking cross-section images) b) F2-5 fine-grained sample c) F-6 fine-grained sample. .....	60
Figure 2-17. First (a) and second (b) approach the definition of initial oil saturation for the F1-1 vugular sample.....	61
Figure 2-18. Porosity models visualization for the F1-1 vugular sample for upscaling factors of 1, 3, 5, 6 and 12 a) 3D view b) 2D view in the middle J plane. ....	62
Figure 2-19. Water cut results for models with upscaling factors of 3, 5, 6 simulation model for a) F1-1 vugular sample and b) F2-5 fine-grained sample.....	62
Figure 2-20. Base model and field history or experimental data for F2-6 plug sample for a) Cumulative oil production b) Cumulative water production.....	63
Figure 2-21. Experiments progress for F2-6 plug sample.....	64
Figure 2-22. Time Series Results for F2-6 plug sample for a) Cumulative oil production b) Cumulative water production. ....	64
Figure 2-23. Oil and water relative permeability for a) F1-1 vugular sample b) F2-5 fine-grained sample c) F-6 fine-grained sample. ....	65
Figure 3-1. a) Coastal zone in Rio de Janeiro State with the marked location of the study area (Lagoa Salgada), b) two main facies of rock sample, and c) plug samples from the two facies...	77
Figure 3-2. Implemented workflow of the study.....	79
Figure 3-3. 3D high-resolution full model of columnar sample. ....	80
Figure 3-4. A diagram of the experimental setup: core flooding equipment and the medical CT imaging system.....	80
Figure 3-5. Image processing procedure for a) 2D microCT scan, b) 2D medical CT scan images .....	84
Figure 3-6. 3D representation of sample obtained from microCT scan images for a) grain (gray), b) grain (gray) and total pores (blue), c) total pores (blue), d) connected pores (blue) and isolated pores (gray), e) separated pore space, f) pore network model.....	85

Figure 3-7. 3D representation of sample obtained from medical CT scan images for a) grain (gray), b) grain (gray) and total pores (blue), c) total pores(blue), d) connected pores (blue) and isolated pores (gray), e) connected pores filled with oil, f) oil flow pattern.....	86
Figure 3-8. 3D visualization of $F1 - 1$ columnar sample obtained from microCT scan images for a) grain (gray) and total pores (blue), b) connected pores (blue), c) pore network model. ....	89
Figure 3-9. 3D visualization of $F2 - 6$ fine-grained sample obtained from microCT scan images for a) grain (gray) and total pores (blue), b) connected pores (blue), c) pore network model. ....	89
Figure 3-10. Probability distribution graphs of PNM properties for columnar (blue) and fine-grained (red) samples for a) coordination number in Log scale for the entire data set, b) coordination number in linear scale for the most frequent data set, c) shape factor, d) throat length, e) pore radius, f) throat radius. ....	90
Figure 3-11. The correlation between the pore area and pore volume columnar (blue) and fine-grained (red) samples.....	92
Figure 3-12. The relationship between: a and b) coordination number and pore radius, c and d) throat length and throat radius: in columnar (blue) and fine-grained (red) samples. ....	93
Figure 3-13. Porosity distribution for the samples. ....	94
Figure 3-14. Porous system for a) $F1 - 1$ columnar plug, b) $F - 5$ fine-grained plug, c) $F2 - 6$ fine-grained plug.....	95
Figure 3-15. Flow lines of DW (yellow lines) during flooding of DW and displacement of FW for a) $F1 - 1$ columnar plug, b) $F - 5$ fine-grained plug, c) $F2 - 6$ fine-grained plug. ....	96
Figure 3-16. Flow lines of FW (red lines) during injection of FW and displacement of DW for a) $F1 - 1$ columnar plug, b) $F - 5$ fine-grained plug, c) $F2 - 6$ fine-grained plug. ....	96
Figure 3-17. Analyzing flow regimes for a) $F1 - 1$ columnar plug, b) $F2 - 6$ fine-grained plug. ....	97
Figure 3-18. Analyzing flow regimes graph.....	97
Figure 3-19. Flow lines of oil (yellow lines) during flooding of oil and displacement of FW for a) $F1 - 1$ columnar plug, b) $F - 5$ fine-grained plug (white elliptic displays the area with an increase in the number of oil flow lines), c) $F2 - 6$ fine-grained plug.....	98
Figure 3-20. Saturation curves for oil drainage stage for a) $F1 - 1$ columnar plug, b) $F2 - 5$ fine-grained plug. ....	100

Figure 3-21. Flow lines of oil (yellow lines) during injection of FW and displacement of oil for a) <i>F1</i> – 1 columnar plug, b) <i>F</i> – 5 fine-grained plug, c) <i>F2</i> – 6 fine-grained plug. ....	101
Figure 3-22. Saturation curves for FW imbibition stage for a) <i>F1</i> – 1 columnar plug, b) <i>F2</i> – 5 fine-grained plug.....	102
Figure 3-23. The results of oil recovery factor for FW and SW flooding.....	104
Figure 4-1. Location of the Santos Basin, South Atlantic, offshore Brazil, showing the polygon (green) that delimitates the pre-salt occurrences and the location of the wells (A and B).....	116
Figure 4-2. Comparison of radius of investigation and vertical resolution for well logs, core, plugs, and thin sections. ....	118
Figure 4-3. Applied workflow image for rock typing classification and reservoir quality evaluation. ....	118
Figure 4-4. a) The architecture of the Residual neural network (ResNet) model, b) one layer of each residual block.....	124
Figure 4-5. The architecture of the 1D Convolutional neural network model. ....	125
Figure 4-6. a, b) Porosity histogram for plug samples of well A and well B, c, d) permeability histogram for plug samples of well A and well B. ....	127
Figure 4-7. Aspects of the Crystal shrub-dominated facies: a, b) photomicrography showing crystal shrubs among dolomitic cement and pore space (blue), yellow arrow highlighting the growth framework porosity, c, d) photomicrograph showing crystal shrub surrounded by dolomite cement and partially preserved growth framework pores (yellow arrow), e, f) photomicrograph of the spherulitic shrubstone with dominated intercrystalline porosity (blue arrow) and interparticle porosity (red arrow) growth framework pore obliterated by dolomite. shr - crystal shrub; sphl - spherulite; dol - dolomite cement. ....	129
Figure 4-8. Aspects of the reworked facies: a, b) photomicrography showing an spherulitic rudstone with preserved interparticle porosity (blue area), red arrow highlighting the interparticle porosity and orange arrow showing the intraparticle porosity, c, d) photomicrograph showing an intraclastic grainstone cemented by dolomite (blue arrow highlights the intercrystalline porosity), e, f) thin section scan image of bioclastic rudstone (coq - coquinas fragments) with interparticle porosity (red arrow) and moldic porosity (green arrow), g, h) thin section scan image of volcanic rudstone with interparticle porosity (red arrow). sphl - spherulite; coq - coquinas fragments; vol - volcanic intraclast. ....	131

Figure 4-9. Aspects of the spherulitestone facies: a, b) photomicrography showing an spherulitestone cemented by dolomite, c, d) photomicrograph showing a spherical spherulite surrounded by dolomite cement and presence of vugular porosity (purple arrow), e, f) thin section scan image of spherulitestone with dominated intercrystalline porosity (blue arrow). sphl - spherulite; dol - dolomite cement. ....	132
Figure 4-10. Porosity-permeability plot of the 774 data from wells A and B: a) permeability in linear scale, b) permeability in log scale. ....	133
Figure 4-11. Elbow Diagram to determine the appropriate cluster number. ....	133
Figure 4-12. Porosity-permeability plot of the studied reservoir sequence discriminated into four RRTs according to K-means unsupervised classification algorithm: a) permeability in linear scale, b) permeability in log scale. ....	134
Figure 4-13. The resulted RRTs of the studied reservoir interval for the: a) Porosity-permeability graph merged with the $R_{35}$ technique of Winland (Winland, 1972), b) RQI- $\phi z$ plot and the segmented FZI values merged with the FZI-RQI technique of Amaefule (Amaefule et al., 1993), c) Porosity-permeability graph merged with the GHE technique of Corbett (Corbett and Potter, 2004). ....	137
Figure 4-14. Porosity-permeability plot of the studied reservoir sequence and mathematical models of permeability estimation. ....	138
Figure 4-15. The resulted RRTs of the studied reservoir for the: a) RQI- permeability plot, b) RQI-porosity plot. ....	138
Figure 4-16. The resulted RRTs for the RQI-FZI plot of the studied reservoir. ....	139
Figure 4-17. Aspects of plugs from reservoir rock type 2 showing average values of $R_{35}$ , FZI, mean pore radius ( $p$ ) and mean throat radius ( $t$ ). a, b) CT-scan of crystal shrub-dominated facies with growth framework porosity and its distribution of pores and throats with tortuosity of 1.9, c, d) CT-scan of reworked facies with interparticle porosity and its distribution of pores and throats with tortuosity of 2.6. ....	140
Figure 4-18. Aspects of crystal shrub-dominated facies plugs from reservoir rock type 3 showing average values of $R_{35}$ , FZI, mean pore radius ( $p$ ) and mean throat radius ( $t$ ). a, b) CT-scan with vug porosity and silica and dolomite cementation and its distribution of pores and throats with tortuosity of 3, c, d) CT-scan with intercrystalline porosity and its distribution of pores and throats	

with tortuosity of 1.9. The distribution of pores and throats was affected by the cementation process. ....	141
Figure 4-19. Aspects of plugs from reservoir rock type 4 showing average values of R35, FZI, mean pore radius (p) and mean throat radius (t). a, b) CT-scan of intraclastic grainstone moderated cemented with dominated interparticle porosity and its distribution of pores and throats with tortuosity of 2.4, c, d) CT-scan of spherulitic grainstone with intercrystalline porosity and its distribution of pores and throats with tortuosity of 2.2. ....	142
Figure 4-20. Stratigraphic modified Lorenz (SML) plot: a) well A, b) well B. ....	143
Figure 4-21. The loss function curves for porosity prediction for: a) ResNet model, b) 1D CNN model. ....	144
Figure 4-22. The plug porosity and predicted porosity using ResNet and 1D CNN models for: a) Well A, b) Well B. ....	145
Figure 4-23 Cross plot of plug porosity versus predicted porosity for ResNet and 1D CNN models. ....	146
Figure 4-24. The actual and predicted rock type using XGBoost model for: a) Well A, b) Well B, with red arrows indicating the depths at which the two rock types differ. ....	147
Figure 4-25. Cross plot of predicted versus actual rock types, with the percentage of data points labeled for each combination of rock types. ....	147
Figure 4-26. The plug permeability and predicted permeability using mathematical formulas for each reservoir rock type and correlation with predicted porosity values from ResNet and 1D CNN models for: a) Well A, b) Well B. ....	149
Figure 4-27. Cross plot of plug permeability versus predicted permeability using mathematical formulas for each reservoir rock type and correlation with predicted porosity values from ResNet and 1D CNN models. ....	149
Figure 7-1. Rio de Janeiro State, highlighting the coastal zone and the location of the study area. The latitude and longitude of the core sample discussed in this paper were 041° 07' 58'' W and 21° 54' 10'' S. ....	166
Figure 7-2. a): comparison of microbialite outcrops of Lagoa Salgada (with highlighted columnar facies) and Pre-salt rock, b) columnar plug sample, c) encapsulated plug sample. ....	167
Figure 7-3. Schematic diagram of the core flooding apparatus, illustrating the experimental setup used in this study. ....	170

Figure 7-4. Using horizontal and vertical plates, perpendicular plates, two cross-sections are obtained and used as geometry in COMSOL Multiphysics (simulator). .....	171
Figure 7-5. Using a 3D model, 2D microCT images were acquired and employed in numerical simulator. ....	172
Figure 7-6. Visualization of the porosity distribution along the length of the core sample using medical-CT scanning. ....	175
Figure 7-7. The 3D model of the core and pores with flow streamlines during single-phase FW injection. The figures on the top and bottom show the core from the lateral and top views, respectively.....	176
Figure 7-8. Flow streamlines in 2D cross-sections that derived from medical-CT scanning during single phase flow. The figure on the left shows DW displacing FW (flow rate = 0.1 $cm^3/min$ ), whereas the one on the right shows FW displacing DW (flow rate = 0.5 $cm^3/min$ ). ....	177
Figure 7-9. a): the flow of oil streamlines (yellow lines), during the process of oil drainage, pushing FW by oil; b): the water flow lines (yellow lines) during the displacement of oil and injection of FW.....	179
Figure 7-10. a): oil saturation profile after 0.2 and 2.0 PV of oil injection; b): oil saturation during FW injection, obtained from CT images examination.....	180
Figure 7-11. Oil recovery factor determined by measuring produced liquid during FW and SW injection experiments. ....	180
Figure 7-12. The Reynolds number alongside the core length.....	181
Figure 7-13. a): velocity profile inside horizontal cross-section, we zoomed inside a dead-end vug and a dead-end pore as well to evaluate velocity in dead-end regions; b): velocity profile in vertical cross-section that obtained from microCT data. The color bars beside each figure represent the velocity value, dark-red represents high and dark-blue low water velocity. ...	183
Figure 7-14. a): streamlines inside the horizontal cross-section; b): streamlines inside the vertical cross-section. The color of streamlines and the arrows designate velocity and flow direction, respectively.....	184
Figure 7-15. Variation in relative pressure within the horizontal cross-section. The relative pressure also appears in magnified dead-end zones. The color bar represents the pressure value. ....	185

Figure 7-16. Saturation profile during water flooding (horizontal cross-section). The color bar depicts the water saturation profile, where blue represents higher water saturation and red represents greater oil saturation.....	186
Figure 7-17. Saturation profile of vertical cross-section in each 0.2 PVI, during water flooding with constant flow rate of 0.1 <i>cm</i> <sup>3</sup> / <i>min</i> .....	186
Figure 7-18. a): average water saturation during water flooding in each cross-section; b): water saturation in produced liquid (water saturation in outlet).....	187

## LIST OF TABLES

Table 2-1. Petrophysical characterization of the three plug samples. ....	39
Table 2-2. Composition of FW aqueous phase. ....	40
Table 2-3. Core flooding results for the three plug samples. ....	54
Table 3-1. Petrophysical characteristics of the plugs. ....	78
Table 3-2. Average composition of SW and FW. ....	78
Table 3-3. Oil properties.....	79
Table 3-4. The average CT attenuation data of the fluids at experiment condition. ....	87
Table 3-5. Summary of the median of pore network characteristics of both facies sample.....	91
Table 3-6. Coefficient of variation for pore radius, throat radius, and throat length for both facies sample.....	94
Table 3-7. The outcomes of core flooding experiments conducted on three plugs.....	99
Table 4-1. Applications of available well logs. ....	117
Table 4-2. Summary statistics for plug samples of wells A and B.....	128
Table 4-3. Summary statistics for plug samples data, reservoir quality parameters and well log data. ....	135
Table 4-4. Summary of the mean value of pore network characteristics of different reservoir rock types.....	142
Table 7-1. Composition of SW and FW. ....	168
Table 7-2. Relative permeability and simulation parameters.....	174

## TABLE OF CONTENTS

1	Introduction .....	25
2	Core scale investigation of fluid flow in the heterogeneous porous medium based on X-ray computed tomography images: upscaling and history matching approaches.....	34
2.1	Introduction.....	36
2.2	Material and Method.....	39
2.2.1	Materials .....	39
2.2.2	Experimental Procedure .....	41
2.2.3	Simulation Procedure .....	45
2.3	Results and Discussion .....	53
2.3.1	Experiments .....	53
2.3.2	Simulation.....	58
2.4	Conclusion .....	66
2.5	Acknowledgments .....	67
2.6	References.....	68
3	The impact of heterogeneity and pore network characteristics on single and multi-phase fluid propagation in complex porous media: An X-ray computed tomography study .....	72
3.1	Introduction.....	74
3.2	Material and Methodology.....	77
3.2.1	Materials .....	77
3.2.2	Methodology.....	79
3.3	Results and Discussion .....	89
3.3.1	Porosity and Pore Network Modeling .....	89
3.3.2	Single-phase Studies.....	95
3.3.3	Two-phase Studies.....	97
3.4	Conclusion .....	105

3.5	Acknowledgements.....	106
3.6	References.....	107
4	Application of unsupervised learning and deep learning for rock type classification and petrophysical characterization using multi-scale data.....	110
4.1	Introduction.....	113
4.1.1	Geological setting.....	115
4.2	Materials and methods.....	117
4.2.1	Dataset and workflow.....	117
4.2.2	Reservoir rock types (RRTs) and hydraulic flow units (HFUs).....	118
4.2.3	Thin section description and $\mu$ CT analysis.....	122
4.2.4	Porosity, permeability, and rock type prediction by machine learning algorithms.....	122
4.3	Results.....	127
4.3.1	Basic petrophysics.....	127
4.3.2	Facies descriptions.....	128
4.3.3	Reservoir rock types (RRTs).....	132
4.3.4	Hydraulic flow units (HFUs).....	142
4.3.5	Porosity, permeability, and rock type prediction by machine learning algorithms.....	144
4.4	Conclusions.....	150
4.5	Acknowledgments.....	151
4.6	References.....	152
5	Conclusions.....	156
6	References.....	160
7	Appendix I: Investigation of Pore Geometry Influence on Fluid Flow in Heterogeneous Porous Media: A Pore-Scale Study.....	162
7.1	Introduction.....	164
7.1.1	Geological Setting.....	166
7.2	Materials and Methodology.....	167
7.2.1	Materials.....	167

7.2.2	Experiment Procedure .....	168
7.2.3	Underlying Physics.....	170
7.3	Results and Discussion .....	175
7.3.1	Experimental Results.....	175
7.3.2	Numerical Modeling.....	181
7.4	Conclusions.....	189
7.5	Acknowledgments .....	190
7.6	References.....	191
8	Appendix II: Laboratory and numerical examination of oil recovery in Brazilian Pre-salt analogues based on CT images.....	194
9	Appendix III: Experimental investigation of single-phase flow pattern in highly heterogeneous carbonates rocks .....	201
10	Appendix IV: Insights into multi-phase flow pattern characteristics and petrophysical properties in heterogeneous porous media .....	211
11	Appendix V: Upscaling challenges of heterogeneous carbonate rocks: a case study of Brazilian pre-salt analogous .....	217
12	Appendix VI: Experimental investigation of waterflooding performance by increasing copper ions in brazilian pre-salt rock .....	224

# 1 INTRODUCTION

The Pre-salt reservoirs are a complex geological system with unique challenges for hydrocarbon exploration and production. The deposition of the Pre-salt sediments occurred during the early stages of the opening of the South Atlantic Ocean, resulting in a complex interplay of tectonic, sedimentary, and diagenetic processes that affected the reservoir properties (Bruhn et al., 2017). The sediments were deposited in a shallow marine environment, consisting mainly of carbonates, siliciclastic, and evaporites, which were subsequently covered by thick layers of salt during the Cretaceous period (Mohriak et al., 2008). The salt layers have played a crucial role in preserving the reservoirs, but they also pose challenges for drilling and completion operations due to their high density and mechanical strength (Jackson and Hudec, 2017).

The discovery of the Pre-salt reservoirs has attracted significant attention from the oil and gas industry due to their large size and high productivity potential. The initial discovery well, was drilled in 2006, and since then, several other fields have been discovered, including the giant fields of Tupi (former Lula field), Buzios, and Sapinhoa (Petrobras, 2021). The Pre-salt reservoirs are estimated to contain up to 100 billion barrels of recoverable oil and gas, making them one of the largest hydrocarbon accumulations discovered in recent years (ANP, 2021). Despite the significant potential of the Pre-salt reservoirs, their complex geological setting and heterogeneity present significant challenges for hydrocarbon exploration and production. The reservoir properties, such as porosity, permeability, and rock type, can vary significantly both laterally and vertically, leading to significant uncertainties in hydrocarbon reservoir modeling and prediction (Mohriak et al., 2008).

In heterogeneous reservoirs, the distribution of various properties can significantly impact petrophysical characteristics, including mineralogy, pore size, sedimentology, and physical properties of solids and fluids. As a result, the properties of such reservoirs may vary significantly from one point to another, making them more challenging to quantify than homogeneous reservoirs (Fitch et al., 2015; Abutaha et al., 2022). This multiscale heterogeneity can affect single and multiphase fluid flow in permeable geologic media, leading to complex fluid flow behavior (Kang et al., 2017; Reynolds et al., 2018; Zahasky et al., 2020). Heterogeneous carbonate rocks, in

particular, are more difficult to characterize and find recovery mechanisms than sandstone rocks due to their intricate pore structure (Jensen et al., 2000; Hendry et al., 2021; Sen et al., 2021).

Developing predictive models for fluid flow in heterogeneous reservoirs is particularly challenging due to the high variability in carbonate reservoirs, leading to a high level of uncertainty in the estimate of hydrocarbon production (Zahasky et al., 2020). The heterogeneous reservoir properties are below the resolution of traditional reservoir model grid blocks, making it difficult to predict and match the history of fluid flow and storage in the subsurface. To assess heterogeneity, both numerical and experimental measures can be employed. However, laboratory research on heterogeneous reservoirs is challenging due to the delicate and fragile structure of these porous media, making them more susceptible to damage during experiments. Fluid flow modeling is also challenging due to the heterogeneity and complex pore geometry of carbonate reservoirs, which can impact fluid flow behavior (Vik et al., 2013). Therefore, designing and implementing enhanced recovery techniques is a difficult task, often requiring expensive laboratory core flooding experiments to support the decision-making process.

To better understand the relationship between petrophysical properties and fluid flow in heterogeneous reservoirs, a range of numerical and experimental measures can be employed. Numerical simulations, such as Pore Network Models (PNM) and pore-scale simulation, can provide valuable insights into the fluid flow behavior in porous media by simulating the complex pore geometry and fluid-rock interactions. These models can be used to investigate the impact of heterogeneity on fluid flow behavior and predict the macroscopic behavior of reservoir rocks. Experimental measures, such as core flooding experiments and thin section descriptions, can provide direct measurements of petrophysical properties and validate the numerical simulations.

Non-invasive X-ray computed tomography (CT) imaging has emerged as a powerful tool for the petrophysical characterization of reservoir rocks. CT images can provide high-resolution 3D images of the rock pore structure, which can be used to estimate porosity, permeability, and pore connectivity. The utilization of this method is central to the detection of internal porous media, 3-D pore and grain characterization, mineralogy analysis, and monitoring single and multiphase fluid flow in rock, etc. Furthermore, CT images can be used to generate digital rock models that can be used for numerical simulations (Lin et al., 2018; Jackson et al., 2020; Zahasky et al., 2020).

This thesis presents a comprehensive analysis and contributes to the understanding of fluid flow in heterogeneous porous media, the impact of heterogeneity and pore network characteristics on fluid propagation, and the petrophysical characterization of reservoir rocks. The research employs a range of techniques to address fundamental questions in the field of reservoir characterization and fluid flow in porous media. These techniques include CT imaging, image analysis, Pore Network Models, numerical and pore-scale simulation, core flooding experiments, thin section description, unsupervised classification algorithms, and deep learning models. By combining these tools, the research aims to investigate and analyze the research questions and to develop a more comprehensive understanding of the complex processes underlying fluid flow in heterogeneous porous media, which has significant implications for hydrocarbon production and carbon and hydrogen storage in subsurface reservoirs of the Brazilian Pre-salt reservoirs.

In this thesis, three main chapters are presented, each addressing a unique aspect of the research topic. The chapters provide valuable insights into the fluid flow and petrophysical characterization of reservoir rocks, contributing to the development of reliable predictive models and sensible operational choices.

In chapter 2 of this thesis, a paper published in the *Geoenergy Science and Engineering Journal* titled “Core Scale Investigation of Fluid Flow in the Heterogeneous Porous Medium Based on X-Ray Computed Tomography Images: Upscaling and History Matching Approaches” is presented. The paper describes experiments and simulations conducted on outcrop samples from Lagoa Salgada in Rio de Janeiro, Brazil, as a possible flow analog to one of the most typical Brazilian Pre-salt carbonate reservoirs rocks. The aim of the study was to investigate the impact of pore geometry on recovery factor, saturation profile, and relative permeability estimations using both experimental and simulation approaches.

To provide direct visualization of the geometry and description of pore structure, CT imaging was integrated with experimental measurements of petrography and core flooding. The resulting data was used to create a 3D fine-scale grid to simulate the porous media and the fluid flow. Upscaling techniques were then applied to reduce computation time, and the simulated produced fluid cuts for different upscaled models were compared with the experimental results from core flooding. A history-matching technique was then applied to match experimental and simulation results, calculating the relative permeability of two main defined facies and creating an updated model

capable of assessing past and present performance and future forecasting. This chapter provides valuable insight into fluid flow in heterogeneous porous systems and serves as a foundation for sensible operational choices, accurate assessments of oil recovery efficiency, and the development of reliable predictive models (Iraji et al., 2023). The workflow of Chapter 2 is presented in Figure 1-1, which is fully described in the chapter.

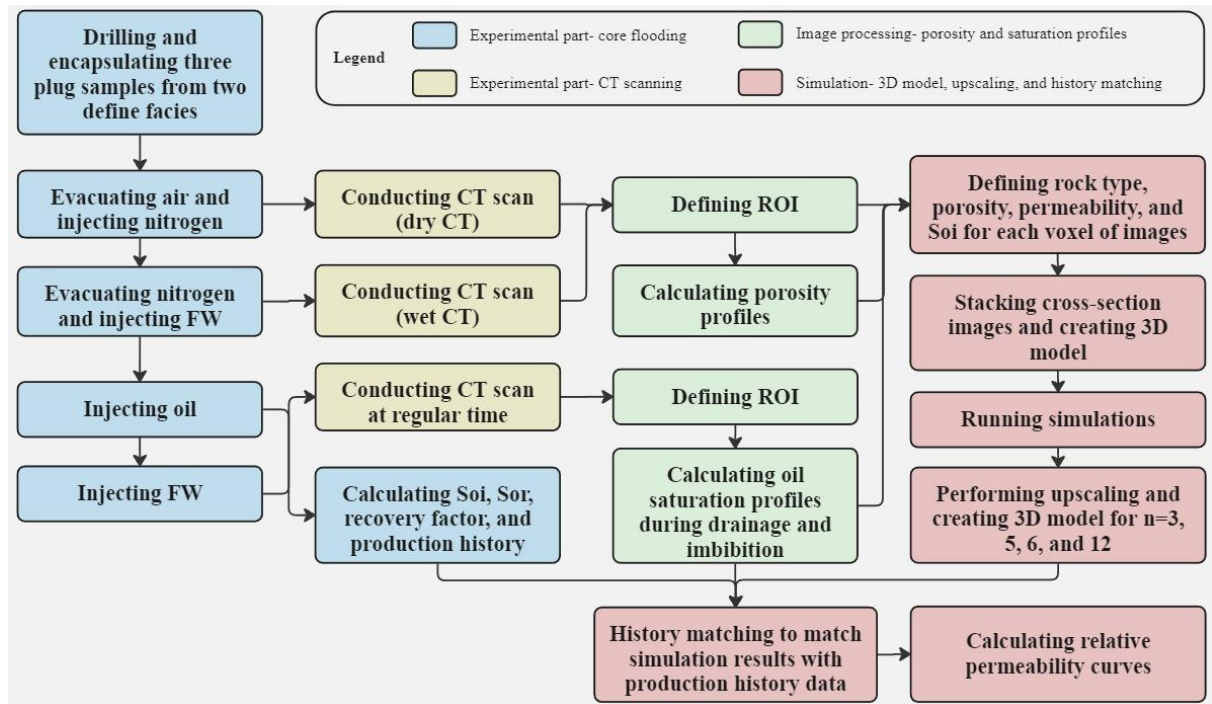


Figure 1-1. Applied workflow for Chapter 2. FW represents the formation water,  $S_{oi}$  and  $S_{or}$  denote the initial and residual oil saturations, respectively, ROI presents the region of interest.

Chapter 3 of this study titled “The Impact of Heterogeneity and Pore Network Characteristics on Single and Multi-Phase Fluid Propagation in Complex Porous Media: An X-Ray Computed Tomography Study” was conducted and submitted to the *Journal of Petroleum Science* as a part of this thesis. This research investigated the effects of pore network characteristics and heterogeneity on fluid flow through complex and heterogeneous porous media, specifically using high-resolution CT imaging techniques to examine outcrop stromatolite samples of the Lagoa Salgada. The study employed Pore Network Model (PNM) to quantify the relationship between key features of the porous system, including pore and throat radius, throat length, coordination number, shape factor, and pore volume.

The study also conducted a series of core flooding experiments coupled with medical CT scanning to assess flow propagation and saturation profiles. The results highlighted the impact of

heterogeneity and the presence of disconnected or dead-end pores on flow patterns and saturation, revealing preferential and heterogeneous displacement of fluid in some regions of the plugs and bypassed it in others. The study's findings have important implications for various applications, including oil and gas recovery, carbon capture and storage, and groundwater management. The workflow of the procedure is presented in Figure 1-2 for a quick overview. However, for a comprehensive understanding of the method, the chapter provides a detailed description of each step involved in the process.

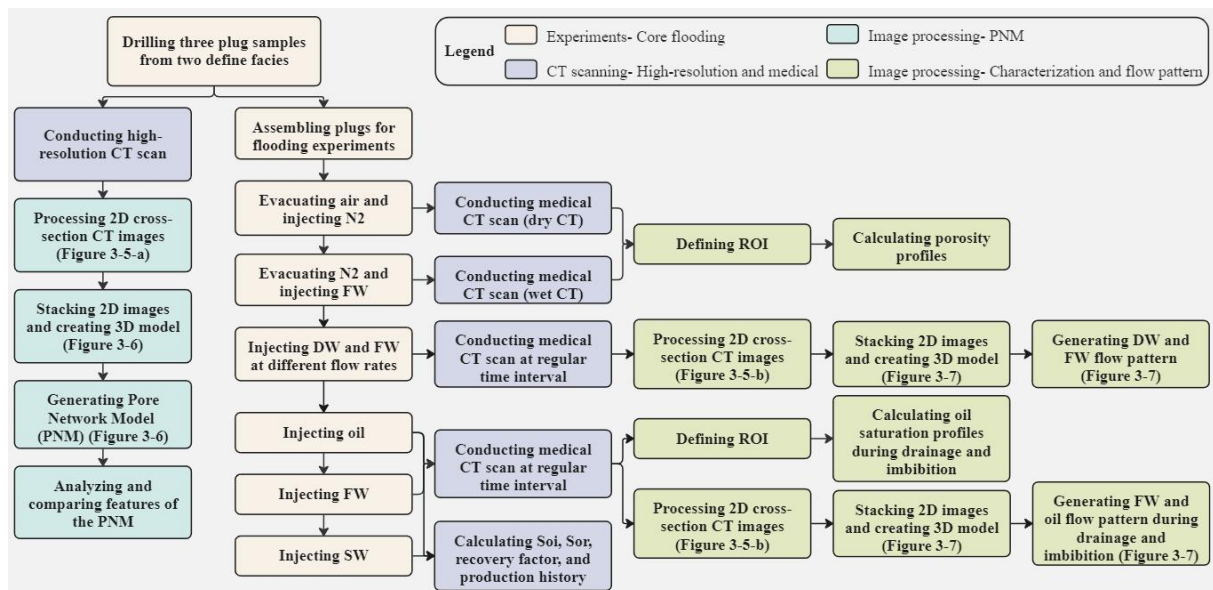


Figure 1-2. Implemented workflow for Chapter 3. SW and DW represent the sea and distilled water, respectively.

Chapter 4 of this thesis is a paper which has been submitted to the *Geoenergy Science and Engineering Journal*. Titled “Application of Unsupervised Learning and Deep Learning for Rock Type Prediction and Petrophysical Characterization using Multi-Scale Data”, it presents a comprehensive study of the Barra Velha Formation in the Santos Basin. The chapter employs a combination of conventional well log data, microCT ( $\mu$ CT) analyses of plug data, and thin section description to accurately characterize and evaluate the reservoir sequences. The study was conducted to achieve a precise definition of four reservoir rock types (RRTs) by integrating the petrophysical values of the plugs and their corresponding well-log data using the K-means unsupervised classification algorithm.

The classification results were then integrated with several conventional techniques to evaluate the quality and geological characteristics of the studied sequence. The chapter also includes the

identification of facies and classification of porosity types through thin section description. Additionally, pore network modeling from  $\mu$ CT analysis of plugs was used specifically for the characterization of pores and throats of plug samples from each RRT. Another objective of this chapter was to create predictive models for determining both plug porosity and rock type using deep learning and machine learning algorithms, and well log data. Two deep learning models, ResNet and 1D CNN, were employed to predict plug porosity and the XGBoost algorithm was applied to predict rock type. To assess the models' performance, the predicted outcomes were compared with actual data. Overall, this chapter presents a comprehensive and integrated study of the Barra Velha Formation, which provides a detailed understanding of the reservoir quality and facilitates accurate rock type prediction and petrophysical characterization. Additionally, Figure 1-3 illustrates the workflow that was applied in Chapter 4, which will be described in detail in the subsequent sections.

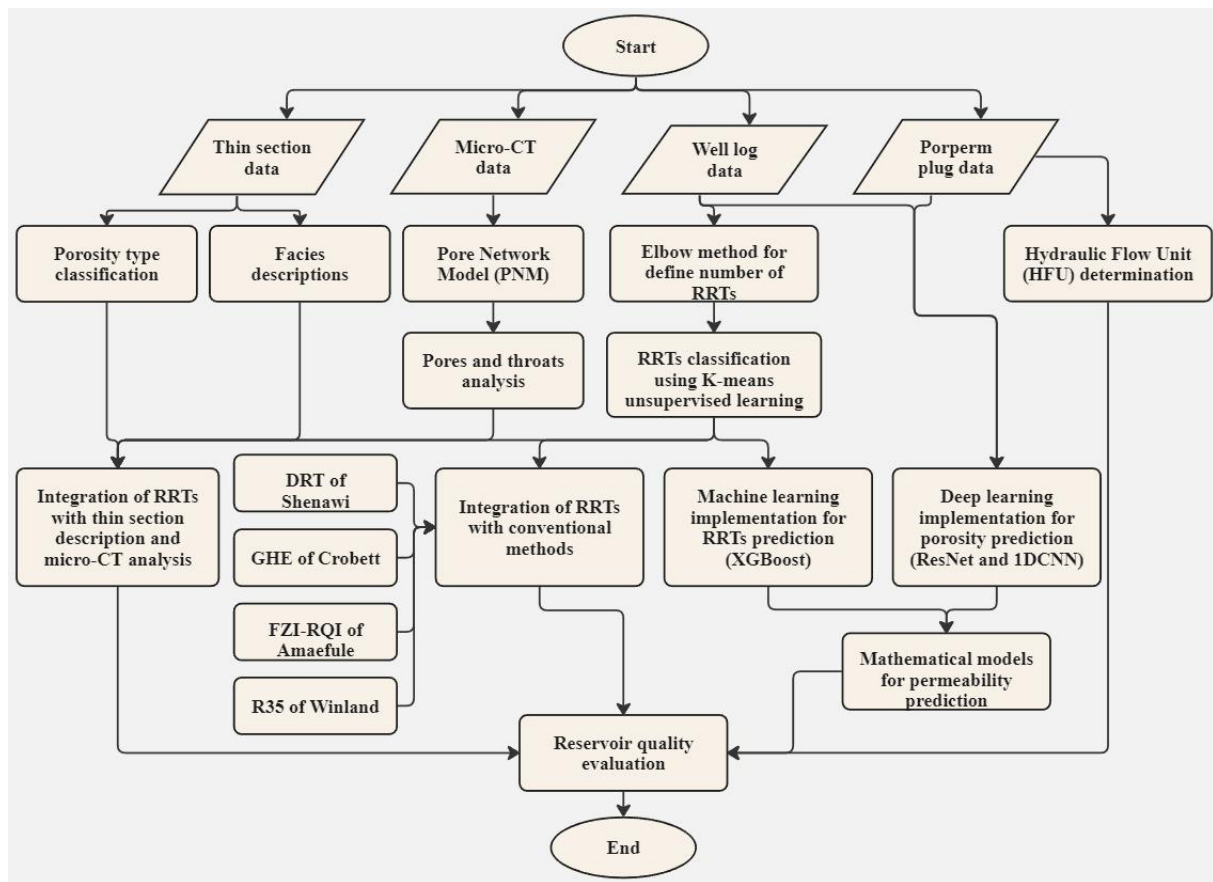


Figure 1-3. Applied workflow for Chapter 4.

Appendix I of this thesis includes a paper published in the *Energy Geoscience Journal*, titled “Investigation of pore geometry influence on fluid flow in heterogeneous porous media: a pre-

scale study”. The paper combines single-phase and multi-phase core flooding with medical-CT scanning to generate flow streamlines and assess water flooding efficiency. The study also involves microCT scanning of the core sample, from which two cross-sections from horizontal and vertical plates were constructed and used as geometry in a numerical simulator (COMSOL Multiphysics) to examine the impact of pore geometry on fluid flow and obtain flow streamlines, saturation, and velocity profiles in the sample. The paper concludes that the presence of dead-end pores and vugs in the sample causes a significant proportion of fluid to remain stagnant, resulting in the channeling-like behavior of the injected fluid, fast breakthrough, and low areal-swept efficiency. The study also highlights the importance of pore scale modeling to improve the prediction of fluid flow in reservoirs.

Appendix II contains a paper titled “Laboratory and Numerical Examination of Oil Recovery in Brazilian Pre-Salt Analogues Based on CT Images”, which was presented at the *Third EAGE Conference on Pre-Salt Reservoir*. This paper discusses a study on the manipulation of 2-D tomography images to create a 3-D fine-scale grid for simulating the porous media and fluid flow. Additionally, upscaling techniques were applied to create the coarse simulation grids and the oil recovery factor and water cut results were calculated for different upscaled models. These results were compared with the experimental results obtained from core flooding. The study provides valuable insights into the petrophysical properties of the rock samples and can help in improving our understanding and modeling of pre-salt reservoirs (Iraji et al., 2022a).

Appendix III contains a paper titled “Experimental Investigation of Single-Phase Flow Pattern in Highly Heterogeneous Carbonates Rocks”, which was presented at the *Rio Oil & Gas Conference*. This paper focuses on the challenges of drainage strategies in heterogeneous microbialite carbonate rocks and the impact of pore size distribution on the flow rate through these rocks. The paper also describes the core flooding integrated with medical CT scan experiments performed to obtain the flow patterns in single-phase flow and the impact of flow rate on these streamlines, in both columnar and fine-grained carbonate composite samples. The findings of this paper provide valuable insights into the behavior of miscible displacement in this type of rock and the factors that influence single-phase flow patterns (Iraji et al., 2022c).

In Appendix IV of this thesis, a paper titled “Insights into Multi-Phase Flow Pattern Characteristics and Petrophysical Properties in Heterogeneous Porous Media” is included, which was presented at

the *Second EAGE Conference on Pre-Salt Reservoir*. This paper presents research on the petrophysical characteristics and fluid flow patterns in pre-salt reservoir rocks, using stromatolite composite samples from different facies. The paper examines porosity and absolute permeability in samples and investigates multi-phase flow patterns during core flooding experiments integrated with medical CT scan experiments (Soltanmohammadi et al., 2021).

Appendix V of this thesis includes a paper titled “Upscaling Challenges of Heterogeneous Carbonate Rocks: A Case Study of Brazilian Pre-Salt Analogous”, which was presented at the *Third EAGE Conference on Pre-Salt Reservoir*. This paper discusses the complexities of producing petroleum through carbonate pre-salt reservoirs in Brazil, particularly in relation to the heterogeneity of porous distribution. The study uses high and low-resolution CT images from stromatolite samples for 2D and 3D fluid flow simulation, providing a more trustworthy understanding of fluid movement and identifying the optimum upscaling factor number to reduce computational time during the numerical simulation (Soltanmohammadi et al., 2022).

In Appendix VI of this thesis, a paper titled “Experimental investigation of waterflooding performance by increasing copper ions in Brazilian Pre-Salt rock” is included. This paper was presented at the *83rd EAGE Annual Conference & Exhibition* and investigates the effectiveness of low-salinity water injection with a laboratory experimental approach. The study includes three different core samples from different wells of the Brazilian Pre-Salt carbonate reservoirs to examine the variation in oil recovery factor during seawater injection followed by seawater with the addition of copper ions. The findings demonstrate the application potential of the low salinity water injection process and the effectiveness of the mechanism of desorption of the acidic oil from the rock surface by forming acid-copper complexes (Iraji et al., 2022b).

It is important to highlight the transition from pore scale and plug scale investigation in the initial chapters (2 and 3) and appendices to a reservoir scale study in the fourth chapter. The objective of this transition was to demonstrate the applicability of the insights gained from the smaller-scale investigations and their potential to enhance our understanding and decision-making processes at larger scales.

The first two chapters, along with the accompanying appendixes, focused on analyzing fluid flow and petrophysical characterization at the pore scale and plug scale, providing valuable insights into

the complex processes underlying fluid flow in heterogeneous porous media. Building upon the knowledge obtained from the pore scale and plug scale investigations, the fourth chapter shifted its focus to the reservoir scale study, aiming to extend the understanding gained from the smaller scales to a larger scale.

Additionally, this integrated approach can prove invaluable in situations where data availability for certain intervals of the reservoir is limited. By leveraging the insights gained from the pore scale and plug scale investigations, it becomes possible to extrapolate and infer information about these data-scarce intervals. This utilization of knowledge from smaller scales enables the enhancement of our understanding and provides valuable insights even in the absence of extensive data coverage. In reservoir characterization, where obtaining comprehensive data throughout the entire reservoir can be challenging and costly, this approach offers a practical and efficient means to fill in the gaps.

This integrated methodology opens up opportunities for optimizing hydrocarbon recovery and developing effective reservoir management plans. By employing a multi-scale approach and integrating data from various sources, including advanced imaging techniques, simulations, and machine learning algorithms, it becomes possible to bridge the knowledge gap and obtain a more comprehensive understanding of the reservoir as a whole. Ultimately, this thesis demonstrates how the integration of insights from smaller-scale investigations into larger-scale reservoir studies can significantly enhance our understanding and decision-making capabilities, even in instances where data may be scarce. It provides a pathway for leveraging existing knowledge and maximizing the value of available data, allowing for more informed decisions and improved performance in oil and gas reservoirs.

Overall, this thesis showcases the progressive exploration of fluid flow and petrophysical characterization from smaller scales to larger scales, highlighting the value of this integrated approach in advancing our understanding of reservoir behavior and supporting decision-making processes in the energy industry.

**2 CORE SCALE INVESTIGATION OF FLUID FLOW IN THE  
HETEROGENEOUS POROUS MEDIUM BASED ON X-RAY  
COMPUTED TOMOGRAPHY IMAGES: UPSCALING AND  
HISTORY MATCHING APPROACHES**

**Author: Shohreh Iraj**

**Co-Authors: Ramin Soltanmohammadi, Eddy Ruidiaz Munoz, Mateus Basso, Alexandre  
Campane Vidal**

**CAMPINAS**

**2023**

## ABSTRACT

In this paper, experiments and simulations were performed on outcrop samples from Lagoa Salgada in Rio de Janeiro, Brazil, as a possible flow analog to one of the most typical Brazilian Pre-salt carbonate reservoirs rocks. The rocks were microbial carbonates where plugs comprising two main facies were sampled, simplified as fine-grained and vugular facies. The plugs were utilized to study the impact of pore geometry with both experimental and simulation approaches on recovery factor, saturation profile, and relative permeability estimations. To provide direct visualization of the geometry, description of pore structure, and calculation of concentration profiles, computed tomography (CT) imaging was integrated with experimental measurements of petrography and core flooding. The injection of two pore volumes of formation water (FW) resulted in a recovery factor between 28 and 34 percent for the plug samples. Furthermore, based on porosity generated by dry and wet CT, as well as saturation profiles resulting from CT data collected during drainage and imbibition processes along the length of the plugs, it is revealed that the distribution of these properties was diverse and heterogeneous. An algorithm was used to process the 2D tomography images of the samples to remove the region related to the exterior parts. The images were then stacked to create a 3D fine-scale grid to simulate the porous media and the fluid flow by applying rules to segment of rock types, porosity, and permeability estimations of each grid block. Coarse-scale grids were created by applying upscaling techniques to reduce computation time. Simulated produced fluid cuts for different upscaled models were compared with the experimental results from core flooding. A history-matching technique was then applied to match experimental and simulation results, calculating the relative permeability of two main defined facies and creating an updated model capable of assessing past and present performance and future forecasting. Since relative permeability is essential for accurate simulation, estimating these curves in the heterogeneous pre-salt reservoir considering different facies, greatly influences reasonable future prediction performance and the ability to make informed operational decisions.

**Keywords:** Multiphase Fluid Flow Through Porous Media, Relative Permeability, Heterogeneous Porous System, Numerical Modeling/Method, Transport Properties

## 2.1 INTRODUCTION

The exploration of Brazilian pre-salt Santos and Campos Basins reservoirs has been one of the most important oil field discoveries since the 2000s. These unconventional in-situ and reworked carbonate rocks were deposited in passive-margin basins after the separation of the South American and African plates and the emergence of the South Atlantic Ocean during the Cretaceous, which make up the bulk of these reservoirs (Bruhn et al., 2017). These carbonate rocks typically feature intricate and heterogeneous geometries and a variety of porosity networking patterns, vugs, and fractures (Matula, 1969; Lucia, 1983; Sharma, 2008; Abedi and Kharrat, 2016).

Petrophysical properties are influenced by the distribution of other characteristics, including mineralogy, pore size, sedimentology, and rock and fluids' chemical and physical characteristics. As a result, petrophysical characteristics in a heterogeneous reservoir might vary dramatically from location to location while remaining moderately stable throughout a homogeneous reservoir (Fitch et al., 2015; Abutaha et al., 2022). Compared to sandstone rocks, heterogeneous carbonate rocks often make it harder to estimate petrophysical features and discover recovery mechanisms (Jensen et al., 2000; Irajy et al., 2015; Irajy and Ayatollahi, 2019; Hadavimoghaddam et al., 2021; Hendry et al., 2021; Sen et al., 2021). Single and multiphase fluid flow is influenced by multiscale heterogeneity in permeable geologic media (Kang et al., 2017; Reynolds et al., 2018; Zahasky et al., 2020). Due to the high heterogeneity in carbonate reservoirs, creating predictive models is generally tricky and results in high uncertainty in the estimate for hydrocarbon production. Since the variations of heterogeneous reservoir properties occur in the scale below the standard reservoir model grid size of blocks, anticipating and history-matching storage and fluid movement in the subsurface is extremely difficult (Zahasky et al., 2020). Numerical and experimental measurements can evaluate heterogeneity. Due to the fragile structure of this type of porous media, laboratory investigations are challenging and fluid flow modeling is highly demanding due to the considerable heterogeneity and complex pore geometry of carbonate reservoirs. Designing and implementing enhanced recovery procedures is challenging, especially because such expensive decisions often require supporting laboratory core flooding work (Vik et al., 2013).

The predictive power of existing rock analysis techniques is constrained by the inability to define multiscale variability (Guice et al., 2014). Recent technological advancements in core analysis can reduce uncertainty in identifying reservoir rock characteristics and thus boost profitability. X-ray

computed tomography (CT) can reveal unmatched information about the interior structure of materials without causing any damage. This method is vital for a wide range of scientific and industrial processes; in petroleum engineering and geological sciences, its application is for interior porous media detection, 3D pore and grain characterization, mineralogy analysis, and visualizing fluid flow in rock. Technological advancements have made it possible to develop novel techniques for measuring single and multiphase fluid flow at small sizes using CT images. This technique enables the depiction of how multiple fluids are distributed within porous materials, and it also allows for the identification of fluid patterns of different phases (Gao et al., 2020; Lin et al., 2021; Su et al., 2022). CT imaging is becoming more frequently utilized for centimeter-scale image samples with less than ten micro-meter voxel resolutions due to the increased accessibility of computational and data management systems (Lin et al., 2018; Abedi et al., 2020; Jackson et al., 2020; Zahasky et al., 2020).

Laboratory studies on reservoir plug samples often determine the petrophysical parameters for reservoir modeling. Therefore, accurate and representative experimental laboratory data are required for the petrophysical description of a reservoir. However, the petrophysical properties of rocks sampled that disregard the extent of the heterogeneities are likely to change, raising the issue of suitable sampling (Vik et al., 2013; Drexler et al., 2022). In this study, conventional petrography and core flooding methods were integrated with CT scanning for a precise understanding of a high-resolution pore network characterization, variability of the porosity, concentration profiles, and fluid flow modeling plug samples of outcrops of Lagoa Salgada, Brazil. These outcrops are stromatolites, regarded as layered microbial structures, and potentially flow analogous to the most productive and heterogeneous Brazilian Pre-salt reservoirs (Rezende et al., 2013; Ceia et al., 2022). In this study, two microbiological facies were identified from the comparative pore geometry analysis of the rocks, and plugs were collected while considering these facies and heterogeneities.

The simulations of flow models are required to determine how variability and heterogeneity affect fluid flow. However, simulating fluid flow in heterogeneous porous media can be difficult, mainly when dealing with multiphase flows. Moreover, for flow modeling, an accurate description of the pore space is required (Al-Kharusi and Blunt, 2007). Since the CT imaging technique prepares straight visualization of the geometry compared with the other methods available for the characterization of the porous system (Withers et al., 2021), in this study, three-dimensional

heterogeneous porous media were constructed from CT images of both facies samples and were used in simulations. Moreover, this paper utilized a methodology that defines a region of interest or cropped image containing only the image of the rock and eliminates the region related to the exterior parts in the CT images of heterogeneous plug samples without cylindrical geometry. Furthermore, the application of an empirical correlation between porosity and permeability is discussed, along with its implementation for upscaling.

Implementing experimental and simulation results would be beneficial for analyzing different solutions and industrial approaches and understanding and selecting applied scenarios. In addition, defining the appropriate relative permeability curves is crucial in the execution of numerical simulations to estimate reservoir performance, productivity, injectivity, and recovery factor and inform operational decisions. Moreover, these curves are essential for various technological applications, including hydrocarbon recovery, carbon sequestration, hydrogen storage, hydrology, and microfluidics (Basbug and Karpyn, 2008). Therefore, determining these curves in the heterogeneous reservoirs where multiphase fluid flow behavior in porous media encounters constraints and limitations is more vital. Here to calculate relative oil and water permeability and produce a model representation that align with the current actual reservoir performance and reasonable future prediction, history-matching was carried out to compare and match simulation results with production history data (oil and water production).

Although extensive research has been carried out on Brazilian pre-salt reservoirs (Bruhn et al., 2017; Ceia et al., 2022), there has been no detailed investigation of fluid flow behavior in this heterogeneous and vuggy system considering different facies and pore geometry. Therefore, much uncertainty still exists about the reservoir performance. By accurately describing the pore space for different facies, this study provided an opportunity to advance the understanding of fluid flow behavior, obtain models that display an acceptable match with experimental results and saturation profiles from CT data, and define appropriate relative permeability curves for this system.

## 2.2 MATERIAL AND METHOD

### 2.2.1 MATERIALS

Experiments were conducted on Lagoa Salgada outcrops from Rio de Janeiro state, southeast Brazil. Before drilling plugs, target areas and rock facies were obtained based on the geological description and petrography. Regarding the pore size distribution, two primary facies (fine-grained with comparatively small pores and vugular (columnar) with huge, linked pores and vugs) were chosen for experimental and simulation investigation (Figure 2-1-a). Two fine-grained plug samples and one from vugular facies were selected to examine how the geometry affects oil recovery, saturation profile, and relative permeability estimations (Figure 2-1-b and Table 2-1). Due to plug samples' high heterogeneity and fragility, preserving the flow inside porous media during flooding studies was a crucial difficulty. A detailed explanation of the encapsulation methods and "from block to plug" procedure to address this issue can be found in section 2.2.2.1.

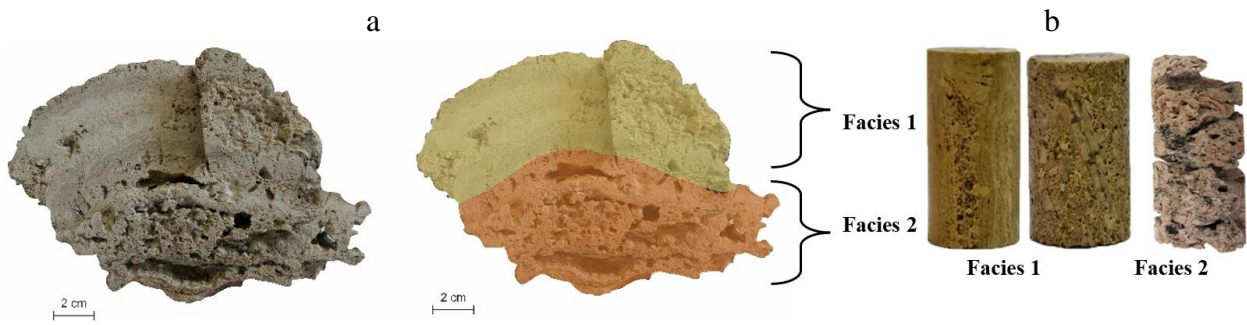


Figure 2-1. a) Fine-grained (Facies 1) and vugular (Facies 2) facies of microbial carbonates rock block from Lagoa Sagada outcrop, Brazil, b) Selected plug samples for the different facies.

Table 2-1. Petrophysical characterization of the three plug samples.

Facies	Fine-grained		Vugular (columnar)
Plug Sample	F2-5	F2-6	F1-1
Length, <i>cm</i>	8.90	9.72	8.90
Diameter, <i>cm</i>	3.78	3.77	3.68
Porosity, %	29.8	24.3	52.4
Gas Permeability, <i>mD</i>	963	1200	-

Due to the massive number of connected vugs and pores in the vugular plug, pressure drop could not be monitored during gas injection, resulting in the inability to determine gas permeability. The average liquid permeability for this plug sample was 5434.83 *mD* using three different flow rates.

Formation water (FW) as an available aqueous phase with composition given in Table 2-2 and crude oil of Brazilian pre-salt reservoir with density, molar mass, and viscosity (at

20°C) of  $0.8751 \text{ g/cm}^3$ ,  $120 \text{ g/mol}$ , and  $5 \text{ cP}$ , water content of 0.01% (ASTM-D1744, 1992), and the Acid number of  $0.0275 \text{ mg KOH/g}$  (ASTM-D664, 2011) were utilized in this study. Moreover, the SARA tests show the weight percentage of saturates, aromatics, resins, and asphaltene components of 93.26, 0.59, 5.82, and 0.33, respectively (ASTM-2007-11, 2012; ASTM-D6560-12, 2012).

Table 2-2. Composition of FW aqueous phase.

Salt	Composition, g/L
<i>NaCl</i>	163.620
<i>Na<sub>2</sub>SO<sub>4</sub></i>	0.088
<i>NaHCO<sub>3</sub></i>	0.487
<i>KCl</i>	6.911
<i>MgCl<sub>2</sub>.6H<sub>2</sub>O</i>	3.068
<i>CaCl<sub>2</sub>.2H<sub>2</sub>O</i>	19.100
<i>SrCl<sub>2</sub>.6H<sub>2</sub>O</i>	0.029
<i>BaCl<sub>2</sub>.2H<sub>2</sub>O</i>	0.033
<i>FeSO<sub>4</sub>.7H<sub>2</sub>O</i>	0.022
TDS, g/L	193.358

Figure 2-2 presents a summary of the applied workflow for both the experimental and simulation parts, and the following sections provide a comprehensive explanation of each step.

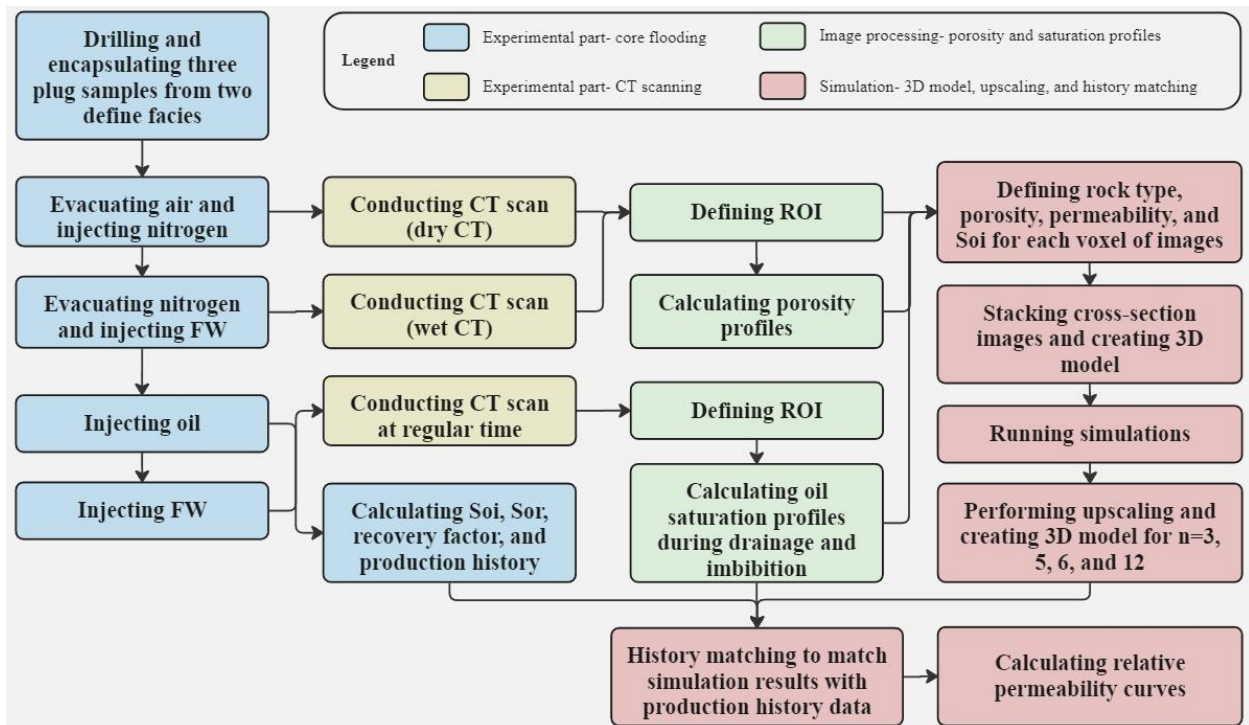


Figure 2-2. Applied workflow for experimental, image processing, and simulation steps.



To display the spatial arrangement of X-ray attenuation coefficients in the sample, the signals or X-ray attenuation numbers are numerically treated and are given in Hounsfield units at each location in the processed images. The images often serve as a digital 3D representation and visualize the variations in X-ray attenuation. The 3D model can be numerically examined and digitally color-coded for better visualization. For instance, in reservoir rocks with consistent mineralogy and saturation, bright colors (high CT values) have low porosity, while dark colors (low CT values) have high porosity (Abutaha et al., 2022).

This study seeks to obtain experimental data to help understand flow transfer properties, like relative permeability, using simulations and history matching. Therefore, the following experimental approach was adopted to acquire the porosity profile and the initial characterization of the plug and understand the drainage and imbibition process to build saturation maps based on the concentration profile; this approach was repeated for all three plug samples:

- a) Encapsulating the clean and dry plug (section 2.2.2.1) and assembling it into the aluminum core holder, increasing and stabilizing temperature and confining pressure to 106°C and 2200 *psi*, respectively.
- b) Evacuating the air inside the porous system and injecting nitrogen into the plug until the pore pressure stabilizes at 735 *psi*. Conducting CT scan for the  $N_2$ -saturated plug (dry CT).
- c) Evacuating the  $N_2$  inside the porous system of the plug and then injecting FW at the same temperature as the experiment into the plug until stabilizing the pressure. Conducting CT scan for the FW-saturated plug (wet CT).

Concurrently, with the measured dry and wet CT data (steps b and c), the mean porosity in each cross-section image was obtained by applying the following equation, and the porosity profiles along the plug samples were generated as,

$$\phi = \frac{CTR_w - CTR_g}{CT_w - CT_g} \quad (2-1)$$

where  $CTR_w$  and  $CTR_g$  are the average CT value of the FW-saturated plug (wet CT) and  $N_2$ -saturated plug (dry CT).  $CT_w$  and  $CT_g$  are the average CT value of the FW and  $N_2$  at test conditions, respectively.

- d) Injecting two pore volumes of oil with a constant rate of 0.1 *ml/min* into the FW-saturated plug coupled with CT scanning during the injection to reach initial water saturation.
- e) Injecting FW at a constant rate of 0.1 *ml/min* coupled with CT scanning until no additional oil production is observed and reaching residual oil saturation. Recording pressure drop, produced water, and oil volumes for the oil recovery factor calculation.

Meanwhile, fluid saturation distribution and propagation were assessed using measured CT data from stages d (drainage) and e (imbibition). During the drainage and imbibition processes, oil saturation profiles along the plug samples were calculated as,

$$S_o = \frac{CTR_w - CTR_{wo}}{\phi(CT_w - CT_o)} \quad (2-2)$$

where,  $CTR_w$  and  $CTR_{wo}$  are the CT value of the FW-saturated plug (wet CT) and plug sample containing oil and FW (drainage or imbibition process).  $CT_w$  and  $CT_o$  are the average CT value of the FW and oil at test conditions, respectively.

#### 2.2.2.1 ENCAPSULATION PROCEDURE

The preliminary plugs underwent a surface cleaning process to remove unconsolidated debris, enabling a more precise analysis of their original textural characteristics and petrophysical parameters. Creating representative core plugs from these rocks posed a significant challenge due to their high heterogeneity and friability. Please refer to Figure 2-4-a for an example of a plug sample.

To encapsulate the plug samples, a thermal plastic material was utilized. This material conforms to surfaces when heated, ensuring that the marginal limits of the plug remained unaltered and preserving its flow characteristics. Numerous attempts were made to determine the optimal heating time and amount of heat applied. Figure 2-4-b depicts a plug sample covered with thermal plastic.

After achieving a more homogeneous core using thermal plastic, encapsulation resin tests were conducted to maintain the integrity of the rock during testing. This resin is a liquid-based material to which a catalyzer is added, enhancing its mechanical resistance by altering its properties. Both liquids are mixed and poured into a container to surround the sample, as shown in Figure 2-4-c. The mixture of liquid resin and catalyzer was left to dry overnight. Following this process, the

sample was removed from the cylinder, revealing a highly homogeneous encapsulation geometry suitable for core flooding activities. Figure 2-4-d showcases a plug encapsulated using liquid resin.

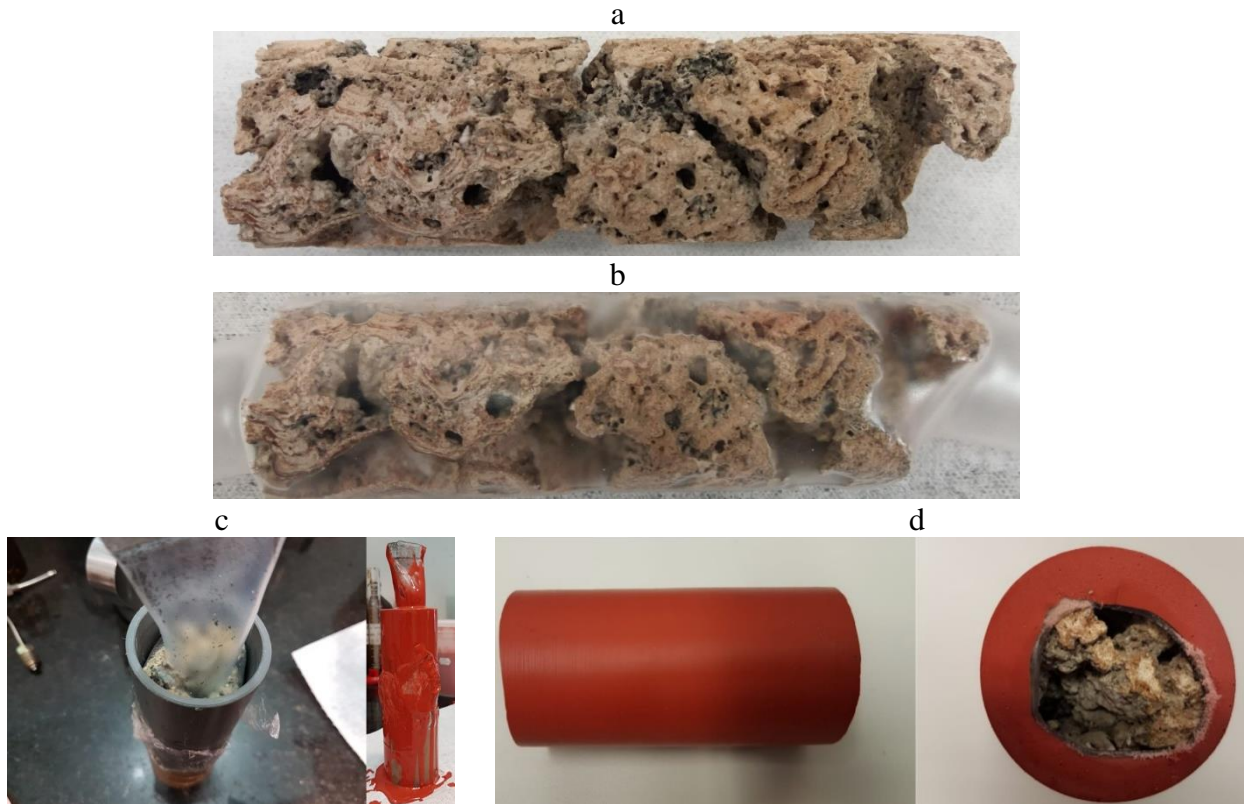


Figure 2-4. a) Heterogeneous and fragile plug sample, b) plug sample covered with thermal plastic, c) process of encapsulating with resin, and d) plug sample encapsulated with thermal plastic and resin.

#### 2.2.2.1.1 LIMITATIONS AND CHALLENGES ENCOUNTERED

The initial attempts to encapsulate the samples proved to be challenging, and unfortunately, they did not yield the desired results. The resin encapsulation initially involved applying the resin directly to the rock surface without the thermoplastic layer. As expected, this led to collapse in the vugular spaces, resulting in an irregular plug sample. Figure 2-5-a displays plug sample covered with resin, highlighting two main observations from this procedure. Firstly, a pre-layer (in our case, the thermo-plastic) is necessary to prevent collapse in the vugular area. Secondly, the thickness of the epoxy resin needs to be increased to provide greater mechanical resistance for the plug.

A second encapsulation trial was performed on a plug with less vugular area, resulting in a more representative core (Figure 2-5-b). However, there was still some collapse in the vugular area. Consequently, it was decided to incorporate thermo-plastic cover to continue the petrophysical characterization and core flooding preparation.



Figure 2-5. a) First test: applying resin directly over the vugular plug sample, b) Second test: applying epoxy resin directly over the fine-grained plug sample.

The next encapsulation test involved a plug with less vugular area, with the application of thermo-plastic. In this case, the resin adhered completely to the rock surface, resulting in a homogeneous core (Figure 2-6-a). After the resin dried, the final diameter of the core sample reached 43 mm.

The final encapsulation test aimed to validate the encapsulation protocol on a highly vugular plug sample. In this case, the thermo-plastic layer was adjusted, followed by covering the plug sample with the conformed thermo-plastic. Finally, the epoxy resin was applied carefully to the core and left to dry overnight. As a result of this methodology, Figure 2-6-b demonstrates a plug sample with highly vugular areas completely encapsulated. The final diameter remained consistent with the previous experiment.



Figure 2-6. a) Third test: applying resin and thermal plastic over the fine-grained plug sample, b) Forth test: applying resin and thermal plastic over the vugular plug sample.

### 2.2.3 SIMULATION PROCEDURE

After the acquisition of the 2D CT-scan images of the plug samples during core flooding experiments (DICOM files representing cross-sections along the plug length, which contain information about the apparatus and the image), a Python routine was operated to process 2D CT images to produce porous system structures. The Pixel size for our case was 0.1035 mm (obtained

in the RefDs.PixelSpacing attribute). Since each cross-section image had 512×512 pixels (512×512 matrix containing CT attenuation coefficient values in Hounsfield units (HU) for each pixel), the size of the images was roughly 53×53 mm. Therefore, each slice (cross-section) had 1 mm thickness, as an example, 88 slices (2D images) were acquired for the F2-5 fine-grained plug sample.

To begin image processing, for each 2D image, a region of interest (ROI) was defined for advanced assessment. This ROI represents an edited and cropped image containing only the rock's image (pores, vugs, and grains), removing the region related to the exterior parts, including air, encapsulation parts (epoxy resin and thermal plastic sleeve), and core holder. Given the presence of vugs and large pores, the plug samples were heterogeneous and noncircular. Therefore, an algorithm that plots different lines from the midpoint of the images (assuming that the midpoint of the image is always in the rock section) to the edges was applied to select the ROI for 2D images. When the threshold CT value of the border was detected, the point in the line was selected as a boundary point. Considering these boundary points, a polygon was generated, and for each image pixel, it was determined whether it was in the interior or exterior of the polygon. The CT values of points inside the polygon were considered nonchanged, and outside points were set to NaN or null (Lamas et al., 2019).

Since all plug samples contained fine-grained facies and vugs and large pores, for all three samples, both facies were considered in the processing, and the separation of these facies was applied based on an adaptive threshold value of CT. With this, points or pixels of images with  $CT > CT_{thres}$  were assigned to Rock Type 1 (fine-grained), and points with  $CT < CT_{thres}$  correlated to Rock Type 2 (vugular). The F1-1 sample contained more regions related to rock type 2, while for F2-5 and F2-6, most plug areas were considered rock type 1.

A linear correlation with the CT value was applied to calculate the porosity for each pixel. For the fine-grained facies (Rock Type 1) porosity calculations, limits of 0.1% and 35% were considered with a linear relationship with the CT values. However, for the vugular facies (Rock Type 2), the porosity range of 85% to 98% was considered, again with a linear correlation with CT value.

For the vugular facies (Rock Type 2), a value of 10 D was considered for the permeability of points. However, permeability for fine-grained facies (Rock Type 1) was calculated using the correlation

with porosity, and normally the permeability presents a skew or log-normal distribution. Several researchers have utilized the relationship between porosity with the logarithm of permeability. Therefore, the linear correlation of  $\log(k)$  with porosity was considered according to (2-3) (Chilingar and Long, 2017; Lima et al., 2020; Lamas et al., 2021). It should be mentioned that the application of this formula is limited to regions of rock where the heterogeneities are not very considerable, which means that it can be applied only in the regions where vugs are not present. Therefore, this equation was only applied for rock type 1 as,

$$\ln(k) = A\phi + B \quad (2-3)$$

It is possible to determine the coefficients (A and B) using dry and wet CT-scan measurements (the calculated porosity for each slice of the plug samples) and the average permeability of the plugs (using the permeameter). By considering the permeability of  $k_i$  for each slice with the porosity of  $\phi_i$ , the average permeability can be calculated according to equation (2-4) (Lamas et al., 2021). Moreover, the average permeability should be quantitatively identical to the average permeability determined by the permeameter.

$$\bar{k} = \frac{\sum_{i=1}^n L_i}{\sum_{i=1}^n \frac{L_i}{k_i}} \quad (2-4)$$

where,  $\bar{k}$  is the average permeability, n is the number of slices or 2D cross-section images for each plug sample, and L is the slice thickness equal to 1 mm.

Therefore, the resulting average permeability (calculated with an initial guess of A and B coefficients and equations (2-3) and (2-4) is compared with the experimental average permeability. Suppose the error is not within the tolerance. In that case, the coefficients are updated, and the calculations are repeated with the updated A and B until there is an acceptable error between the two average permeabilities. At this point, the coefficients are recorded for permeability calculation for each image voxel, according to porosity data.

Figure 2-7 displays the oil and water relative permeabilities for fine-grained and vugular facies; for rock type 2, a linear relationship between saturation and relative permeabilities was considered. The aim was to optimize these relative permeabilities with the production results obtained from the

core flooding experiments. The core flooding experiments obtained data on residual oil saturation and connate water saturation.

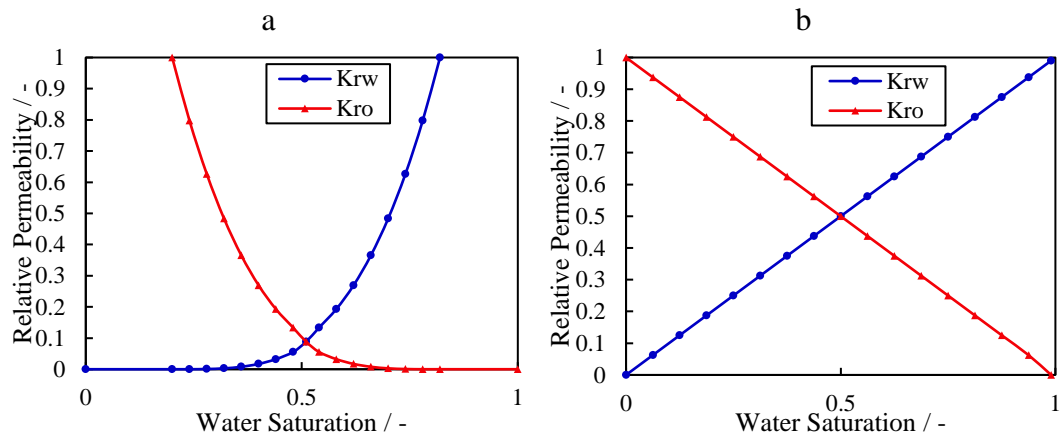


Figure 2-7. Relative permeability for a) fine-grained facies (Rock Type 1), b) vugular facies (Rock Type 2).

Positions and completions of wells were designed to depict the core holder diffuser; one producer in the first slice and an injector in the last slice were considered. Figure 2-8 includes the detail of the wells. The producer was kept with a constant pressure of  $100 \text{ kgf/cm}^2$  ( $1,422 \text{ psi}$ ) and the injector operated with a flow rate of  $0.1 \text{ cm}^3/\text{min}$ .

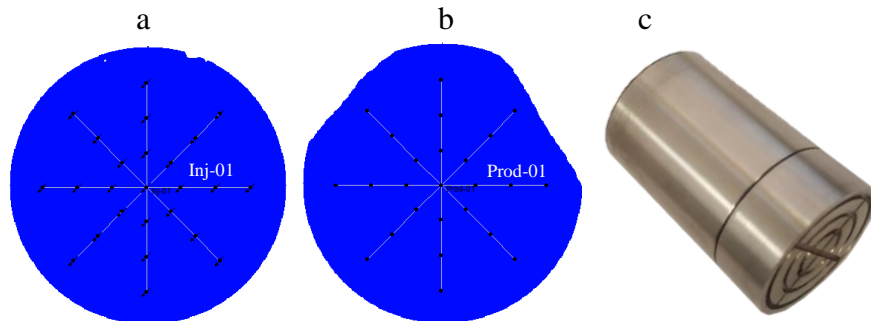


Figure 2-8. Position and completions of the injector (a), producer (b), and physical diffuser (c) for F1-1 vugular sample.

The three-dimensional model (high-fidelity or reference model) was then generated by stacking these cross-section images to identify and quantify of the porous phase and flow transfer. The output files for the simulation, considering a cartesian grid, were created automatically by the Python Code. One simulation block was created from each pixel of the image. For instance, the reference model for the F2-5 fine-grained plug sample was composed of  $512 \times 512 \times 86$  blocks (22,544,384 blocks). The output files included all the necessary files for running the simulator containing the porosity, permeability, rock type, and null blocks. The simulator used in this work was the Computer Modeling Group Ltd. (CMG)-IMEX®, a commercial Black-Oil reservoir simulator.

Simulations of the complete models (reference models) were time-consuming since they contained many grid blocks, and their simulation time was impractical. Hence, it became apparent that an upscaling technique and dealing with coarser grids was required before performing any history-matching procedure. Based on earlier findings, an upscaling Python routine was adapted to create upscaled models where groups of blocks were merged into a coarser simulation grid. Then, Upscaling was used to find values for attributes in the coarse grid that accurately reflect the values in the corresponding fine grid (high-fidelity model) (Lamas et al., 2021).

The reference model was created directly from CT data, and each image pixel was converted into one simulation grid. Preliminary rules were applied to create the upscaling algorithm with any given upscaling factor.

Static features like porosity and fluid saturations can be discovered by applying arithmetic averaging. The routine automatically grouped the blocks and averaged the porosity and saturation for each block. If null blocks from the reference model were present in the region of the upscaled block, in the first step porosity and saturation were set to zero in these blocks, and then the arithmetic average was performed. When all the blocks from reference models were null, blocks were considered null. Regarding rock type, the value considered was that with the most frequent value in the reference blocks. The primary techniques for scaling up permeability can be classified into two categories: (a) averaging-based and (b) flow-based techniques. Although flow-based methods are generally more suggested, average approaches require less computing work and are occasionally a decent choice (Odsæter et al., 2015; Lamas et al., 2021). Finally, equation (2-5) was considered for upscaled permeability calculation, assuming the predicted coefficients do not vary with scale as,

$$k_{upscaled} = \exp \left( \frac{1}{n} \sum_{i=1}^n \ln (k_i) \right) = \exp \left( A \frac{1}{n} \sum_{i=1}^n \phi_i + B \right) \quad (2-5)$$

where  $n$  is the upscaling factor considering each upscaled (coarse) block to be generated from  $n \times n \times 1$  fine blocks, therefore, upscaling did not apply in the K direction or flow injection direction.

According to (2-5), the relation between porosity and permeability is not restricted to the scale. Upscaled permeability can be calculated by both weight averaging of porosity (and using the A

and B coefficients) or  $\ln(k_i)$ . The application of these formulas for calculating upscaled permeability has been recently validated and approved (Lamas et al., 2021).

After making these adjustments to the model and selecting an upscaled model for each plug sample as the base model, history-matching was started. History-matching is an efficient method to compare and match simulation results with production history data. Kruger carried out the first research on history-matching by calculating the areal permeability distribution to produce a reservoir representation that was in line with the performance of the actual reservoirs (Kruger, 1961). A reservoir simulator is used in the history-matching process to adapt relative permeability, capillary pressure, porosity, absolute permeability, etc. Many researchers have widely used the automatic history-matching approach in core flood investigation as computer technology has advanced (Kerig and Watson, 1987; Akin and Demiral, 1997; Akin and Kovscek, 1999; Basbug and Karpyn, 2008). In addition, some researchers investigated the applications of this technique with computerized X-ray tomography (Farokhpoor et al., 2016; Meneses et al., 2019; Vargas et al., 2022).

The generalized history-matching study process started with defining and selecting parameter values from the base study, submitting these parameter values and ranges into the simulations' dataset to study the experiments' definition, and then selecting the results or objective functions to match. The simulations were then run, and the results were analyzed. Experiments were developed and run using the base model and defined parameters in CMG's CMOST. As simulated jobs were completed, CMOST examined the outcomes to assess how closely they corresponded to historical data. Next, the parameter values for new simulation jobs were decided by an optimizer. Finally, the results converged to one or more optimal solutions that offered an acceptable history match when additional simulation jobs were finished. History match error is calculated utilizing the following equations (CMG, 2019) as,

$$TermError_j = \frac{\sqrt{\frac{\sum_{t=1}^{Nt(j)} (Y_{j,t}^s - Y_{j,t}^m)^2}{Nt(j)}}}{\Delta Y_j^m + 4 Merr_j} \quad (2-6)$$

$$Q_j = \frac{\sum_{j=1}^{N(i)} TermError_{i,j} \cdot 100\% \cdot tw_{i,j}}{\sum_{j=1}^{N(i)} tw_{i,j}} \quad (2-7)$$

$$Q_{global} = \frac{\sum_{i=1}^{N_w} [w_i Q_i]}{\sum_{i=1}^{N_w} w_i} \quad (2-8)$$

where  $Y_{j,t}^s$  is the simulated value,  $Y_{j,t}^m$  is the measured value,  $Nt(j)$  is the number of measurements,  $\Delta Y_j^m$  is the maximum difference, and  $Merr_j$  is the measurement error (standard deviation from the mean). Each local objective function ( $Q_j$ ) is made up of a weighted arithmetic average of each of the terms, and the global objective function ( $Q_{global}$ ) is comprises a weighted arithmetic average of the local objective functions (CMG, 2019).

DECE (Design Exploration Controlled Evolution) method was employed as an optimization method for history matching. It can handle continuous, discrete parameters, and hard constraints, complete utilization of distributed computing power, and fast and stable convergence (CMG, 2019). In Design Exploration step, the search space was explored randomly to gather as much information as possible about the solution space. In this stage, experimental design and Tabu search approaches were used to select parameter values and produce simulation datasets. In controlled evolution stage, objective was to perform statistical analyses for simulation results acquired in design exploration stage. DECE algorithm carefully examines each applicant value of parameter and decides if there is a possibility to enhance result quality by rejecting specific candidate values from being selected again (Mirzabozorg et al., 2012; Heidaryan, 2019) (Figure 2-9).

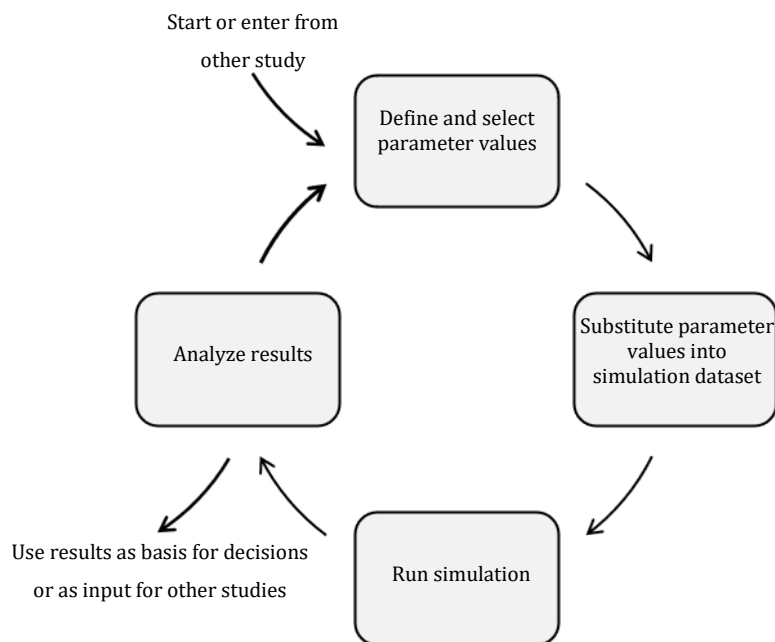


Figure 2-9. History-matching process.

The main parameters used in the history-matching process for fitting simulation with experiments (production history data resulted from core flooding experiments for oil and water production in our three plug samples) were those used to calculate oil-water relative permeability curves. The curves are described using the following power-law relationships or the Brooks-Corey model, respectively:

$$k_{ro} = k_{ro,max} \left( \frac{S_o - S_{or}}{1 - S_{or} - S_{wc}} \right)^{n_o} \quad (2-9)$$

$$k_{rw} = k_{rw,max} \left( \frac{S_w - S_{wc}}{1 - S_{or} - S_{wc}} \right)^{n_w} \quad (2-10)$$

where  $k_{ro,max}$  and  $k_{rw,max}$  are the maximum relative permeabilities for oil and water,  $S_o$  and  $S_w$  are oil and water saturation,  $S_{or}$  and  $S_{wc}$  are residual oil and connate water saturation, and  $n_o$  and  $n_w$  are Corey exponents to oil and water, respectively. All these parameters were considered history-matching parameters, and the formulas were applied for relative permeability determination.

## 2.3 RESULTS AND DISCUSSION

### 2.3.1 EXPERIMENTS

The collected dry and wet CT data were used to determine the mean porosity in each cross-section image (2-1), and the resulting profiles over the longitudinal direction of the plugs are displayed in Figure 2-10.

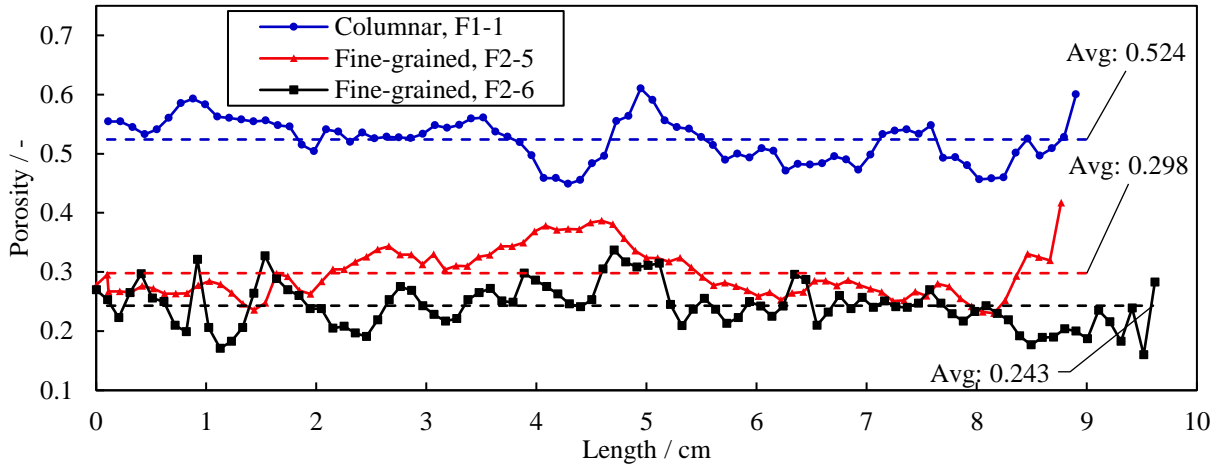


Figure 2-10. Porosity profile for three plug samples.

For instance, to acquire the first data point for the F1-1 sample in Figure 2-10 (Porosity of 0.55), the first CT cross-section images for nitrogen- saturated plug sample (Dry CT) and FW-saturated plug sample (Wet CT) (Figure 2-11) were processed to select the ROI (please refer to Figure 2-15-a and b). Then the average CT value of the chosen area was calculated and porosity was computed according to equation (2-1). The CT values of  $N_2$  and FW were -545.52 and 433.028 HU, respectively. This procedure was repeated for all other cross-section images of the three samples to obtain the porosity profiles along the plugs.

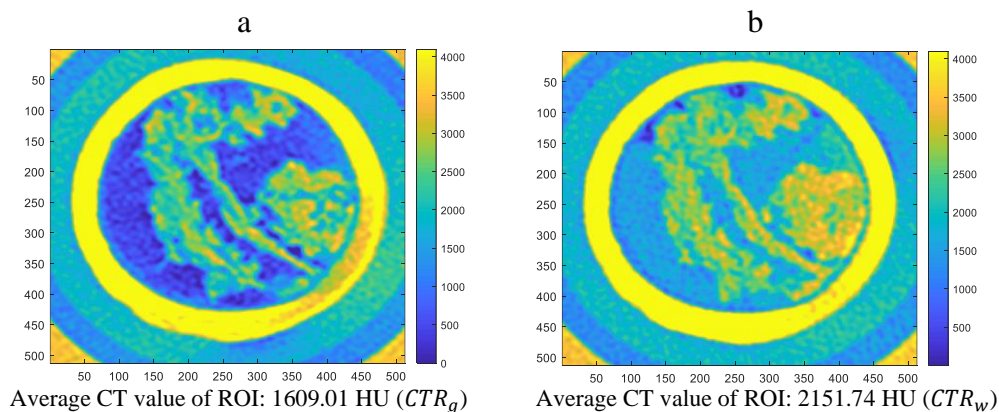


Figure 2-11. First cross-section image of F1-1 vugular plug sample for: (a)  $N_2$ -saturated (Dry CT), (b) FW-saturated (Wet CT).

F1-1 vugular sample with a mean porosity of 0.524 represented a higher profile, which indicates the presence of large pores and vugs in this plug. Heterogeneous behavior with fluctuation over the length is apparent for all three porosity profiles; the range of [0.45 0.61], [0.23 0.42], and [0.16 0.33] were detected for F1-1, F2-5, and F2-6 plug samples, respectively. For the vugular sample, the porosity reached the peak at approximately the middle of the plug while, for each of the fine-grained plug samples, the maximum porosity peak occurs at opposite ends of the samples, with one peak located on the upstream or injection side and the other on the opposite side

After acquiring the initial characteristic and porosity profiles of the plug sample, to begin investigating the saturation map in the immiscible process and two-phase flow, the drainage process started by injecting light oil at the rate of 0.1  $ml/min$  into the FW-saturated samples to reach initial water saturation; this flooding experiment was coupled with CT scanning. In the next step, the imbibition started by injection of FW at a rate of 0.1  $ml/min$  followed by CT scanning to explore the oil recovery process and saturation map.

Data in Table 2-3 were calculated by recording produced water and oil volumes during oil and water flooding experiments. For each plug sample, the volume of produced water during oil injection represents the oil initially in place. For instance, for the F2-6 fine-grained sample, 21  $cm^3$  water was collected during the oil injection process, and according to the pore volume of 26.26  $cm^3$ , an initial oil saturation of 0.80 and initial water saturation of 0.20 were determined. And the volume of oil production during the water injection process was used to calculate residual oil saturation (0.571 for F2-6 plug sample) and the recovery factor. Figure 2-12 displays the oil recovery factor results for FW injection.

Table 2-3. Core flooding results for the three plug samples.

Facies		Fine-grained		Vugular (columnar)
Plug Sample		F2-5	F2-6	F1-1
PV, $cm^3$		29.76	26.26	49.70
<b>Oil</b>	OIIP, $cm^3$	21.00	21.00	32.00
<b>Drainage</b>	$S_{wi}$ , fraction	0.294	0.200	0.356
<b>FW</b>	$S_{oi}$ , fraction	0.706	0.800	0.644
<b>Imbibition</b>	$S_{or}$ , fraction	0.487	0.571	0.422

**Note:** PV is the Pore Volume, OIIP is the Oil Initially in Place,  $S_{wi}$  is the Initial (connate) water saturation,  $S_{oi}$  is the Initial oil saturation, and  $S_{or}$  is the residual oil saturation.

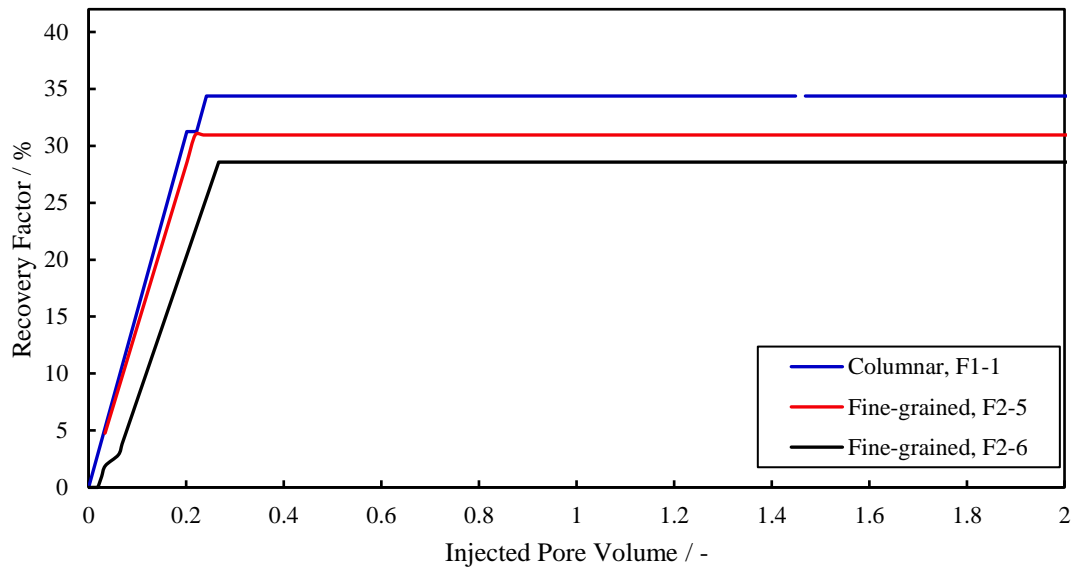


Figure 2-12. Oil recovery results for the three plug samples.

Changes in the oil saturation distribution within all the plug samples were tracked by continuous CT scanning over the longitudinal section of the samples during the oil drainage and FW imbibition flooding tests. These saturation profiles versus the length of the plugs were also produced from analyzing the CT data, like the porosity profiles. Figure 2-13 displays the oil saturation profiles for the vugular sample and one fine-grained sample as an example. The oil saturation profiles in these figures represent three stages of the experiment: the beginning of the oil injection procedure (0.2 pore volume oil injection: red line), the end of the oil injection process or the start of FW injection process (2.0 pore volume oil injection: blue line), and the end of the FW injection process (2 pore volume FW injection: black line).

For instance, to acquire the first data points for the F1-1 sample for 0.2 and 2.0 PV Oil Inj (oil saturation of 0.23 and 0.80), the first cross-section images for the start (PV Oil Inj), end (2.0 PV Oil Inj), and after 0.2 PV of oil injection process (Figure 2-14) were processed to select the ROI (please refer to Figure 2-15-a and b). Then, the average CT value of the chosen area was calculated and oil saturation was computed according to equation (2-2). The CT values of oil and FW were 29.68 and 433.028 HU, respectively. For each cross-section image, the calculated porosity of the corresponding image (from equation (2-1)) was utilized in the formula. This procedure was repeated for all other cross-section images of the samples at different injection times of oil of FW to obtain the saturation profiles along the samples.

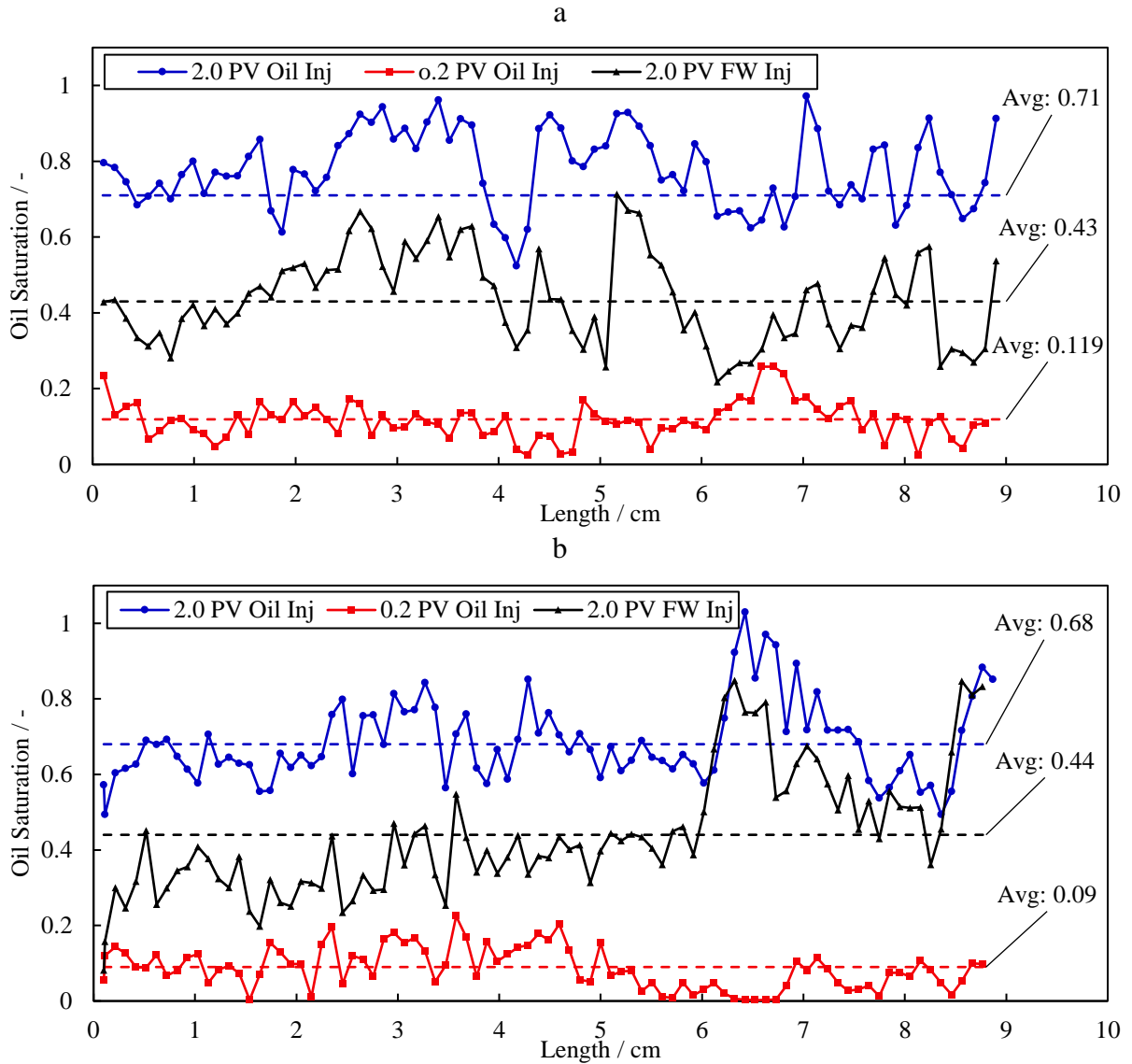
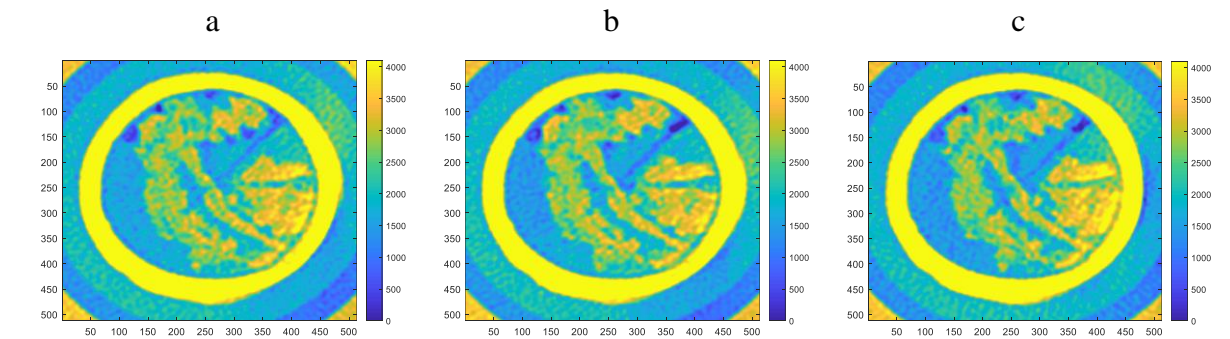


Figure 2-13. Saturation profile during injection of oil and FW injection for a) F1-1 vugular sample, b) F2-5 fine-grained sample.



Average CT value of ROI: 2061.24 HU  
( $CTR_w$ )

Average CT value of ROI: 2051.45 HU  
( $CTR_{wo}$  for 0.2 PV Oil Inj)

Average CT value of ROI: 2010.95 HU  
( $CTR_{wo}$  for 2.0 PV Oil Inj).

Figure 2-14. First cross-section image of F1-1 vugular plug sample for: a) 0 PV oil injection, b) 0.2 PV oil injection, and c) 2.0 PV oil injection.

According to Figure 2-13, during all the flooding steps, heterogeneous oil saturation profiles along the length of the plugs were observed. In the F1-1 vugular plug sample, the range of oil saturation of [0.023 0.257], [0.52 0.97], and [0.21 0.71] were measured for the stages of the start of oil injection, the end of oil injection (start of FW injection), and the end of FW injection, respectively. While for the F2-5 fine-grained plug sample, slightly more fluctuation was detected for oil saturation profiles and the range of [0.002, 0.22], [0.49, 1], and [0.08, 0.84] were measured for the same steps of the injection process. For both plug samples, the heterogeneity and variation in the profiles were more noticeable at the start and end of FW injection or at the higher level of oil saturation.

The area between the two saturation profiles for the start and end of the oil injection process (blue and red) represents the amount of oil accumulated in each plug sample. The area between the two saturation profiles for the start and end of FW injection process (blue and black) indicates the amount of oil that has been produced from the plug. In other words, more oil was produced in the section of the plug sample where the discrepancies between the two lines were raised. Therefore, a significant amount of oil remained unswept in the vugular sample at core lengths of 2, 4.5, 5.5, and 8 *cm*. Also, according to the porosity profile, these spots exhibit lower porosity than other areas of the plug and suggest that the saturation is greatly influenced by the sample's heterogeneity and there is a clear relation between the oil saturation and the porosity profiles. The same results can be obtained for the fine-grained sample at the 3.5 *cm* point and 6 *cm* to the end of the plug length in the outlet. Also, in the parts around 6 *cm* the oil saturation profile for the end of FW injection (black lines) overlapped or was even higher in comparison with the saturation profile at the start of FW injection (blue line), indicating the displaced oil by FW injection from the inlet or upstream and accumulated in this part. Hence, the changes in the oil saturation profile upstream of the plug sample were more noticeable.

At the end of the oil drainage process, 0.71 and 0.68 average oil saturations were observed for vugular and fine-grained plug samples, respectively. These values were reduced to 0.43 and 0.44 oil saturation at the end of the FW imbibition process. These data obtained from CT values revealed an agreement with the saturation data obtained by recording the oil and water production during core flooding experiments ( $S_{oi}$  and  $S_{or}$  in Table 2-3).

### 2.3.2 SIMULATION

Figure 2-15-a displays three examples of 2D CT-scan (cross-section DICOM images) of the F1-1 vugular plug sample acquired during core flooding experiments. Figure 2-15-b indicates the images after processing and characterizing ROI by excluding the region related to the exterior parts by setting null or NaN for those points. This algorithm was used to process all 2D images or all CT image layers of our three plug samples and the images were then used to produce porous system structures for three samples.

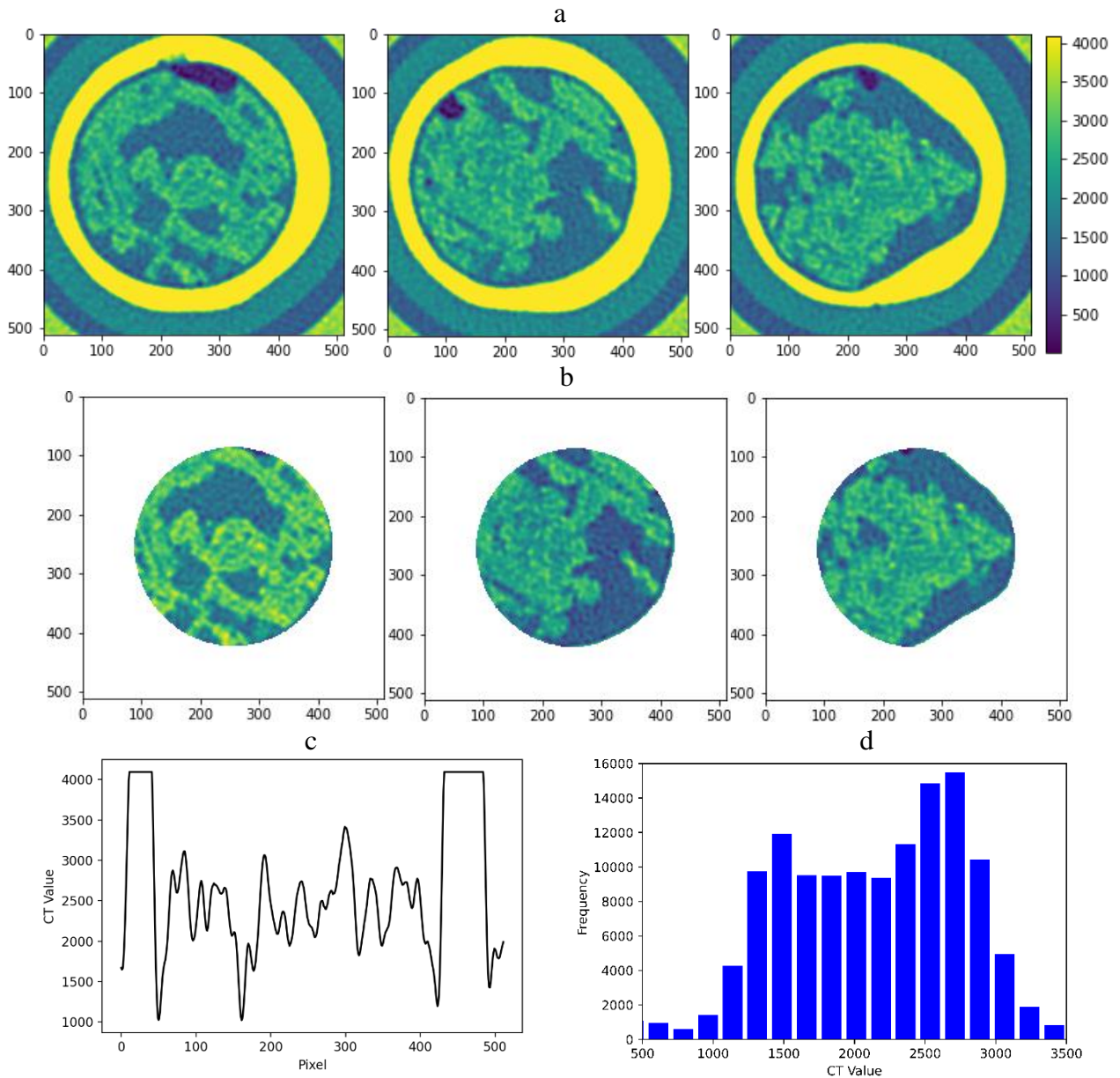


Figure 2-15. a) Examples of 2D CT images of noncircular plug samples b) 2D CT images after processing and excluding the exterior region (ROI) c) CT values of line 256 for the first image (Figure 2-15-a) d) histogram of CT value of the first image after processing (Figure 2-15-b).

Figure 2-15-c plots as an example the CT values of the middle line (line 256) for the first image versus pixel. According to this image, it was possible to detect the threshold CT value for observing the border. Figure 2-15-d shows the histogram of the CT values for the same image after processing (only the rock parts) that shows a bimodal distribution, representing two different fine-grained and vugular rock types. By analyzing the histogram of all acquired images, the value of 1500 HU was selected for the threshold limit and Rock Type 1 (fine-grained) or Rock Type 2 (vugular) were set for each pixel of all images given the fact that the CT value of that point is higher or lower than the threshold CT value.

All the images had 512×512 pixels (with the size of 53×53 mm), and the resulting processed images contained many null blocks (all white parts in Figure 2-15-b) so, for simplification, they were first converted to 343×343 pixels images by cropping the images (area outside this size in all images belong to the null part).

The 3D models of the samples were generated by stacking the processed 2D images and converting each pixel of the images to a simulation grid. As an example, the F2-5 fine-grained sample had 88 slices or 2D images. For more accuracy, the first and last layers were not considered for generating the model. Each slice had 1 mm in length, with a total of 86 mm, or 86 slices for F2-5. The fine grid simulation model (without upscaling) for F2-5 was constituted of  $343 \times 343 \times 86$  (10,117,814 blocks) with 7,807,510 active grid blocks (excluding outer regions of the rock) and 2,310,304 null blocks.

The porosity of the pixels, or grids, was defined with a linear correlation with the CT value for each rock type, considering the limits described in the method section. In the case of permeability definition, for each plug sample, the constant value of 10 D was set for grids with Rock Type 2 facies. However, for Rock Type 1, equation (2-3) was applied. While for each plug sample, parameters A and B were calculated by applying the iteration method (please check the method section) and comparing the average permeability with experimental permeability. For example, for F1-1 vugular plug sample, values of 12.6879 and 3.0178 were calculated for A and B, respectively. 3D representation models of the porous system (fine or high-fidelity model) for all plug samples are indicated in Figure 2-16. For F1-1 vugular plug sample, the process of stacking cross-section images was also displayed (Figure 2-16-a).

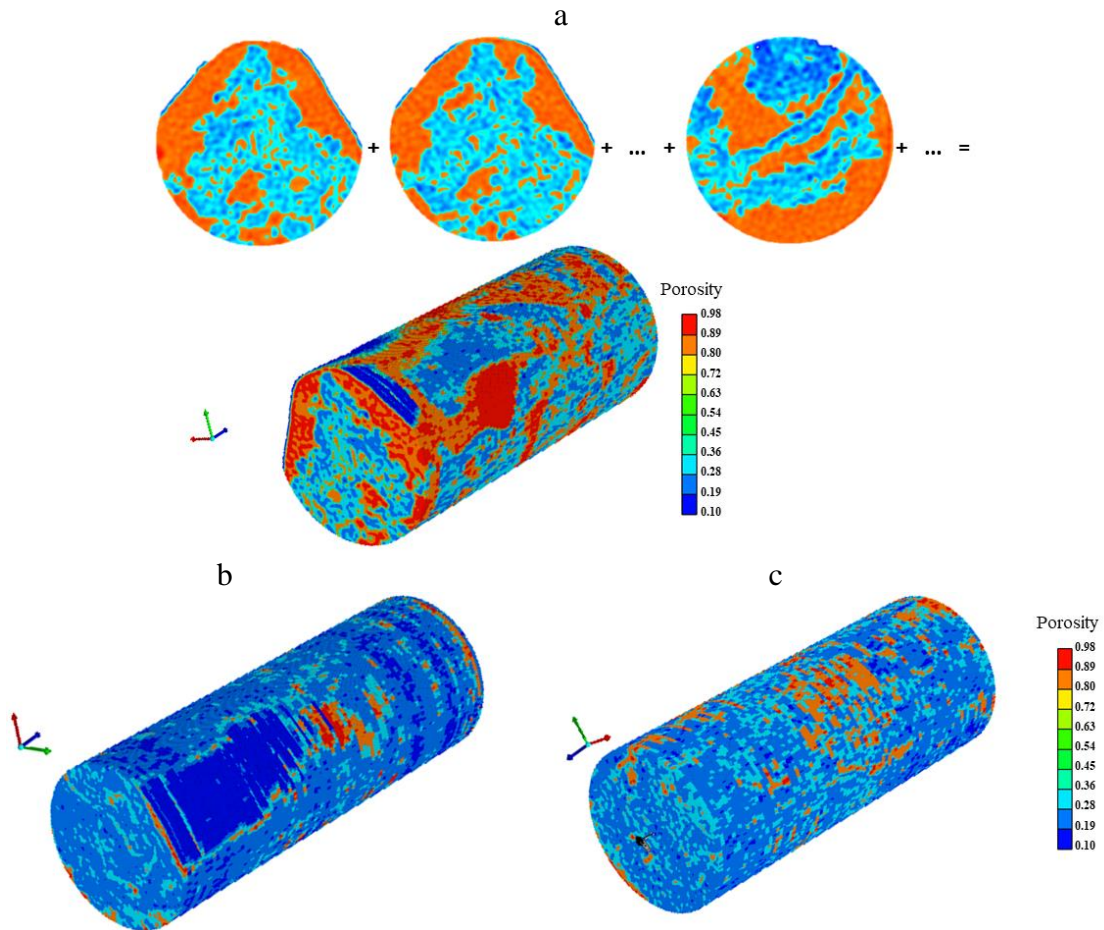


Figure 2-16. 3D representation of the simulation model for a) F1-1 vugular sample (with the process of stacking cross-section images) b) F2-5 fine-grained sample c) F-6 fine-grained sample.

Moreover, for each model, two approaches were applied to define the initial oil saturation according to the experiment results. In the first approach, average oil saturation obtained from CT values after the oil flooding stage and before starting the water injection stage (the average value of plot of 2.0 PV Oil Inj in Figure 2-13) was set for grid blocks with Rock type 1. While, for rock type 2, initial oil saturation of one was considered for the grids. In this approach, it was assumed that during oil injection all the large pores and vugs (Rock type 2) became fully saturated with oil, while fine pores or Rock type 1 attained average initial oil saturation of the experiments (As an example 0.71 for the F1-1 plug sample according to Figure 2-13-a). This approach is displayed in Figure 2-17-a for the F1-1 vugular plug sample. In the second approach, the results from the plot of 2.0 PV Oil Inj in Figure 2-13, showing the oil saturation profile after the oil flooding stage for each layer of the plugs, were considered for the initial oil saturation of grid blocks in each layer of the models (K direction). The visualization of the initial oil saturation distribution of this approach

is indicated in Figure 2-17-b for the F1-1 vugular plug sample. By analyzing the results of the simulation of the models with these two approaches for initial oil saturation and comparing them with experimental results, the second approach proved more realistic and was selected for further investigation.

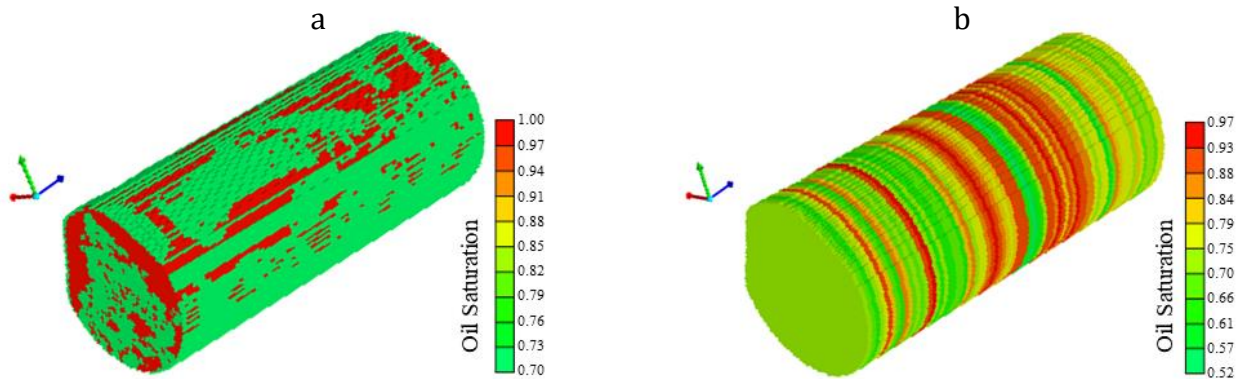


Figure 2-17. First (a) and second (b) approach the definition of initial oil saturation for the F1-1 vugular sample.

Due to the time-consuming process of simulating these fine models (reference models) with many grid blocks, the upscaling technique was applied to build coarser grids using a Python routine described in the method section and before performing any history-matching procedure. For every three models, upscaled models were created with four upscaling factors ( $n = 3, 5, 6,$  and  $12$ ), considering each upscaled block to be generated from  $n \times n \times 1$  refined blocks. For example, Figure 2-18 compares a 3D and 2D (for the J middle plane) porosity visualization for the F1-1 vugular plug sample with different upscaling factors. In this figure,  $n = 1$  refers to the reference model created directly from CT data. In this case, the simulation model comprised 9 294 271, 1 044 775, 376 119, 265 756, and 66 439 grid blocks and 7 142 385, 802 753, 292 153, 204 446, 56 629 active grid blocks for  $n = 1, 3, 5, 6,$  and  $12$ , respectively.

The models were run and the results of oil and water production were analyzed. In the case of the oil recovery factor, the different coarse models showed no considerable difference. However, for the water cut results, bigger differences were observed. Figure 2-19 displays these results for one vugular and one fine-grained sample. According to the results, models with  $n = 3$  and  $5$  showed an acceptable consonance while models with  $n = 6$  and  $12$  indicated slightly different results compared to finer models, especially at the start of production. Therefore, for all the studies, the base model with an upscale factor of 5 (with an acceptable processing time and results) was created and selected for further analysis during the history-matching process.

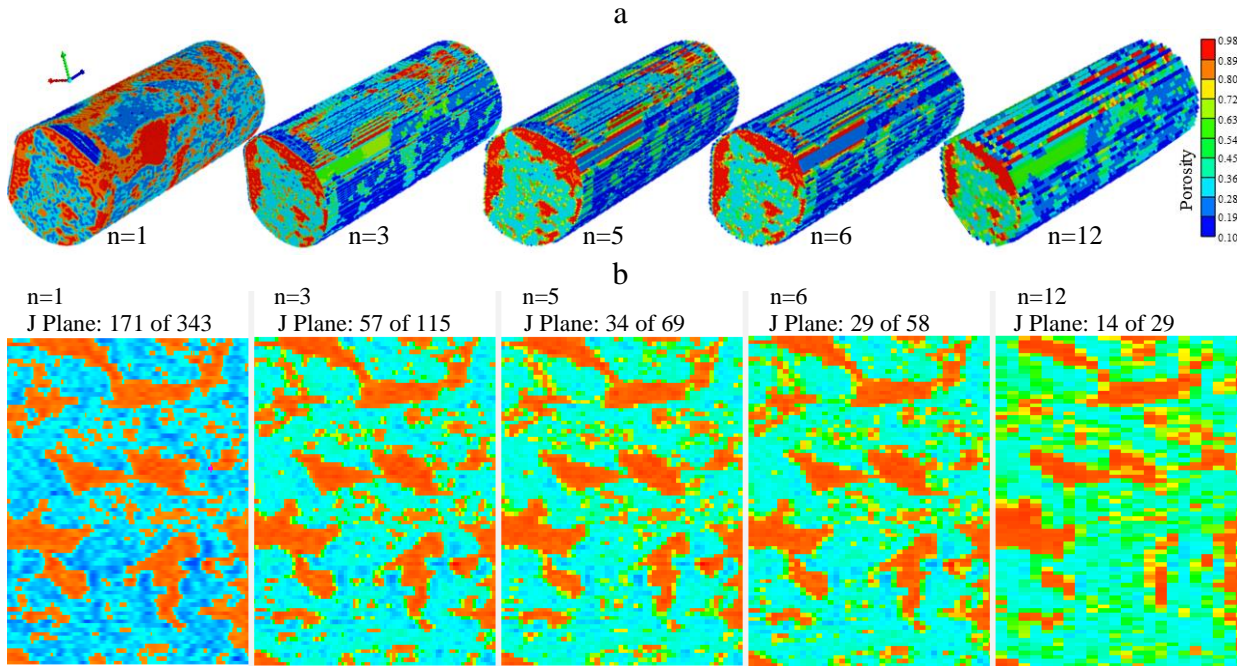


Figure 2-18. Porosity models visualization for the F1-1 vugular sample for upscaling factors of 1, 3, 5, 6 and 12 a) 3D view b) 2D view in the middle J plane.

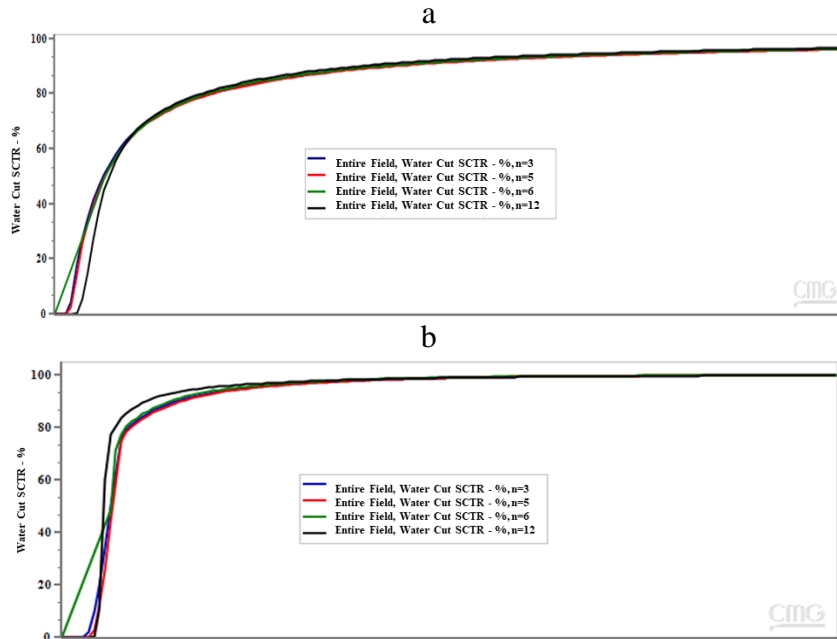


Figure 2-19. Water cut results for models with upscaling factors of 3, 5, 6 simulation model for a) F1-1 vugular sample and b) F2-5 fine-grained sample.

Figure 2-20 compares the production history results created by experimental core flooding production data for oil and water (in blue circles) with the base model simulation results (in black line) for the F2-6 plug sample. In this step, history-matching was conducted for all samples to match simulation results with production history data. The parameters of  $n_o$ ,  $n_w$ ,  $k_{ro,max}$ ,  $k_{rw,max}$ ,

$S_{or}$ , and  $S_{wc}$  in the Brooks-Corey equation, to measure oil and water relative permeability, were defined as the uncertain inputs in the history-matching process. For all the parameters, the ranges and the default values were specified. It should be mentioned that the default values for  $S_{or}$  and  $S_{wc}$  were based on the oil and water produced volume during core flooding experiments of each plug sample (Table 2-3). The lower and upper limits were based on the saturation profile obtained from CT values at the start and end of the water flooding experiments (2.0 PV Oil Inj and 2.0 PV FW Inj graphs in Figure 2-13). In the case of  $n_o$  and  $n_w$ , the default, lower limit, and upper limit values were set to 3, 1, and 6, respectively, while 0.5, 0.01, and 1 were selected for  $k_{ro,max}$  and  $k_{rw,max}$ . In this study, the objective function was defined to minimize the history-matching error between history production data and simulation outcomes by applying the DECE engine, in which parameters are carefully chosen to produce the best and optimal results.

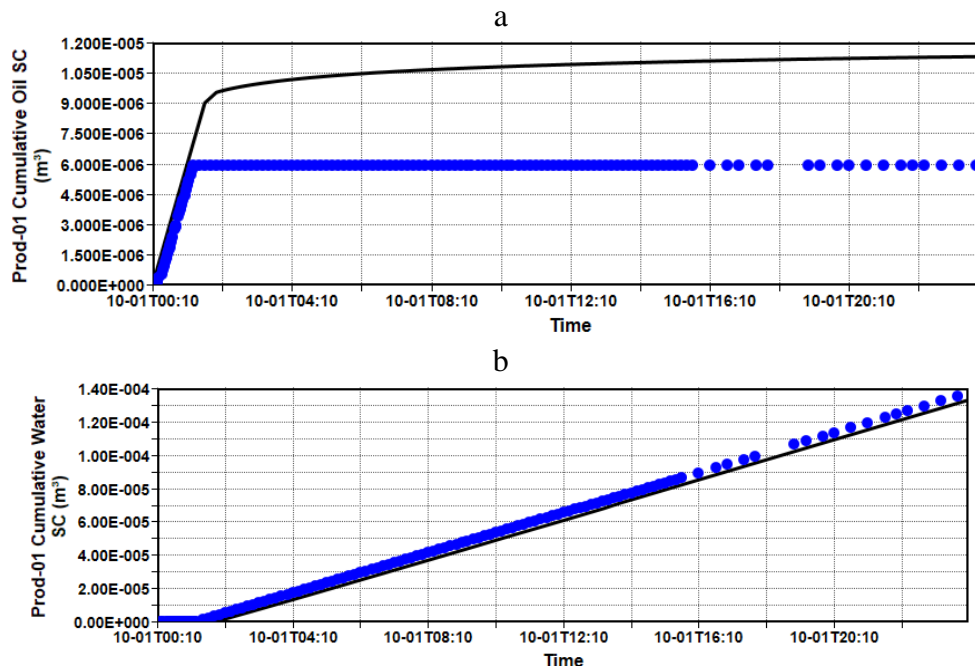


Figure 2-20. Base model and field history or experimental data for F2-6 plug sample for a) Cumulative oil production b) Cumulative water production.

The experiments progress area displays global history-match error versus the experiment number for the base, general, and optimal (red diamond-shaped point) solutions after completing the history-matching process for F2-6 plug sample (Figure 2-21). Each experiment is represented by one blue data point. As the experiments advanced, more blue data points were added until the run was completed. The error for the optimal solution for this plug sample reached 2.15%. Moreover, the error values of 2.67% and 5.68% were measured for F2-5 and F1-1 samples, respectively.

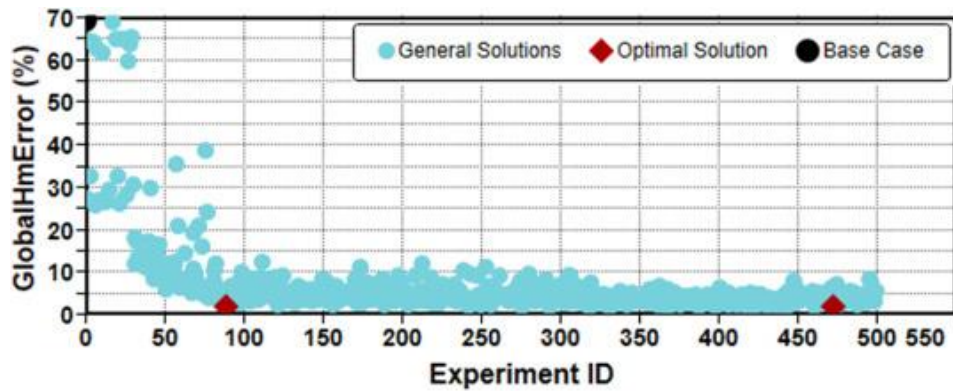


Figure 2-21. Experiments progress for F2-6 plug sample.

Figure 2-22 displays Cumulative oil production and Cumulative water production results for the base (black line), general (light blue lines), optimal (red line), and field history or experimental (dark blue circles) solutions for the F2-6 plug sample.

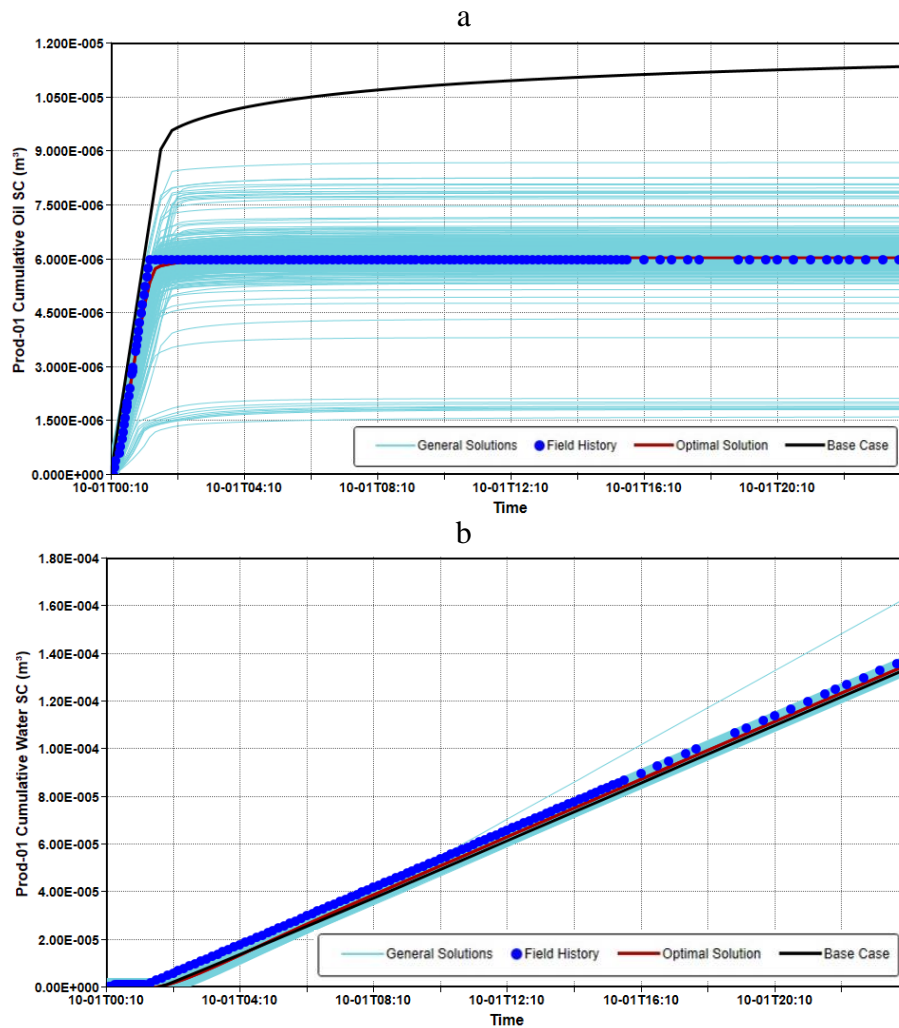


Figure 2-22. Time Series Results for F2-6 plug sample for a) Cumulative oil production b) Cumulative water production.

For all three models, a high percentage of general solutions had an error of less than six percent, so these experiments had acceptable results for further analysis and calculating relative permeability curves. Therefore, instead of using the results to obtain parameters for just the optimal case with a minimum error value, the results of the best 50 cases were selected since they were successfully fit simulation results with experiments. According to the obtained parameter values for all the 50 best experiments, oil and water relative permeabilities were calculated by the Brooks-Corey equation, and the averages of all the best 50 cases' relative permeabilities for the models were measured (Figure 2-23). These findings contribute to our understanding of fluid flow transfer in heterogeneous pre-salt reservoirs and provide a basis for appropriate evaluation of oil recovery efficiency, creating robust predictive models, better characterizing pre-salt reservoirs to lower risks, and for wise operational decisions.

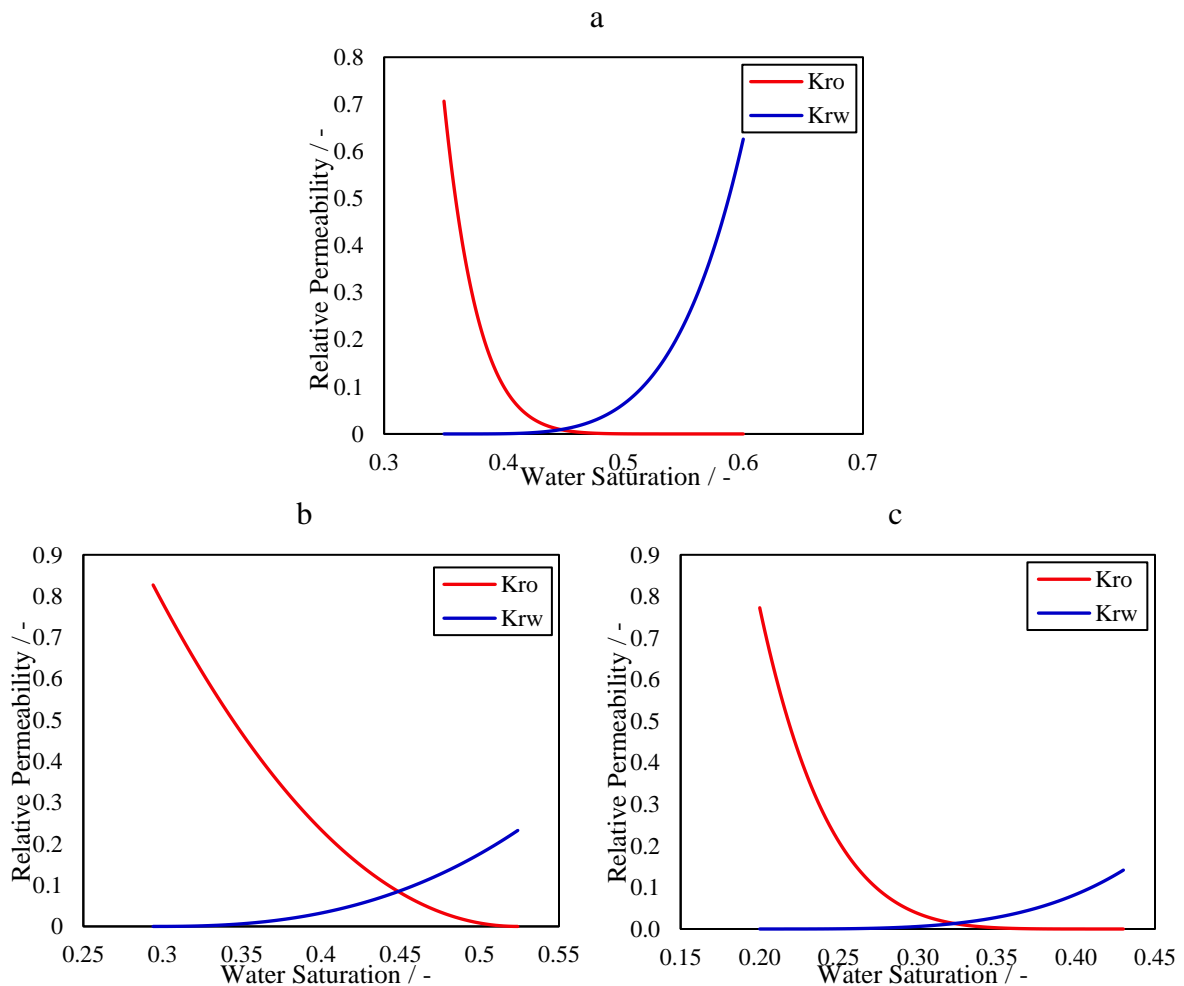


Figure 2-23. Oil and water relative permeability for a) F1-1 vugular sample b) F2-5 fine-grained sample c) F-6 fine-grained sample.

## 2.4 CONCLUSION

In this research, stromatolite carbonate outcrop samples from Lagoa Salgada in Rio de Janeiro State, Brazil, as a possible flow analog to typical Brazilian Pre-salt reservoirs rocks, were evaluated for their petrophysical characteristics and fluid flow through porous media. Due to the high heterogeneity, differentiation, and significant pore size distribution variability, two fine-grained and vugular facies were defined for both experimental and simulation investigation to examine the effect of pore geometry on oil recovery, saturation profile, and relative permeability estimations. During the experimental measurements, conventional methods like petrography and core flooding were integrated with CT scanning to develop recovery factors, concentration profiles, and the visualization of the pore network geometry within plugs. The porosity profiles calculated with acquired CT values revealed a heterogeneous distribution that changed along the plug's length. Core flooding experiment results showed 28% to 34% recovery factor of for three plug samples during water injection based on the original oil in place.

During drainage and imbibition processes, changes in the oil saturation profiles utilizing CT data revealed various distributions over the plugs' length. The average of these oil saturation profiles at the end of the oil and water injection operation, which represent initial and residual oil saturation, agreed with the results from the production data of the core flooding studies. Since different pathways were chosen throughout time, there was a change in the saturation profiles forms for drainage and imbibition flow transfer.

An algorithm was operated to process the 2D CT images of the samples, define a region of interest, and generate a fine-scale or high-fidelity grid model by converting each pixel of the image into one simulation block for the CMG simulator by applying rules for segmentation of rock types, porosity, and permeability estimations considering a Cartesian grid. Due to the high computational time for simulations of the fine-scale model, in sequence, an algorithm was adapted to create upscaled or coarser models where groups of blocks were merged into a coarser grid with any given dimension of an upscaled block. The simulation results for different upscaling factors were compared with experimental results of cumulative oil and water production from core flooding experiments. History-matching was conducted to match these results and calculate relative oil and water permeability using the Brooks-Corey model. The identified curves, therefore, assist in our understanding of fluid flow in these heterogeneous porous systems and serve as a foundation for

sensible operational choices, accurate assessments of oil recovery efficiency, the development of reliable predictive models, and a better understanding of pre-salt reservoirs to reduce risks.

## **2.5 ACKNOWLEDGMENTS**

We gratefully acknowledge the support of EPIC – Energy Production Innovation Center, hosted by the University of Campinas (UNICAMP) and sponsored by FAPESP – São Paulo Research Foundation (2017/15736-3 process). We acknowledge the support and funding from Equinor Brazil and the support of ANP (Brazil's National Oil, Natural Gas and Biofuels Agency) through the R&D levy regulation. Acknowledgments are extended to the Center of Energy and Petroleum Studies (CEPETRO) and the School of Mechanical Engineering (FEM). We also thank the Computer Modelling Group Ltd. (CMG) for software licenses and technical support.

## 2.6 REFERENCES

- Abedi, B., Castaño, E.P.M., Heidaryan, E., Shadloo, M.S., 2020. Pore-Scale Visualization on Polymer Flooding: Application of Singular Value Decomposition-Based Image Analysis Method. *Journal of Porous Media* 23.
- Abedi, B., Kharrat, R., 2016. Study the effect of fracture inclination, spacing and intensity on polymer flooding efficiency. *Journal of Natural Gas Science and Engineering* 34, 645-649.
- Abutaha, S.M., Geiger, J., Gulyás, S., Fedor, F., 2022. Calculating the representative elementary volume of porosity using X-ray computed tomography: Boda Claystone Formation core sample/Hungary.
- Akin, S., Demiral, M., 1997. Effect of flow rate on imbibition three-phase relative permeabilities and capillary pressures, SPE Annual Technical Conference and Exhibition. OnePetro.
- Akin, S., Kovscek, A., 1999. Imbibition studies of low-permeability porous media, SPE western regional meeting. OnePetro.
- Al-Kharusi, A.S., Blunt, M.J., 2007. Network extraction from sandstone and carbonate pore space images. *Journal of petroleum science and engineering* 56, 219-231.
- ANP, A.N.d.P., 2021. Boletim Mensal da Produção de Petróleo e Gás Natural.
- ASTM-2007-11, S., 2012. Standard Test Method for Determination of Asphaltenes (Heptane Insolubles) in Crude Petroleum and Petroleum Products.
- ASTM-D664, 2011. Standard test method for acid number of petroleum products by potentiometric titration-ASTM D 664-11A. ASTM International, West Conshohocken, PA.
- ASTM-D1744, 1992. Standard Test Method for Determination of Water in Liquid Petroleum Products by Karl Fischer Reagent. Annual Book of Standards.
- ASTM-D6560-12, S., 2012. Standard Test Method for Determination of Asphaltenes (Heptane Insolubles) in Crude Petroleum and Petroleum Products.
- Basbug, B., Karpyn, Z.T., 2008. Determination of relative permeability and capillary pressure curves using an automated history-matching approach, SPE Eastern Regional/AAPG Eastern Section Joint Meeting. OnePetro.
- Bruhn, C.H., Pinto, A.C., Johann, P.R., Branco, C., Salomão, M.C., Freire, E.B., 2017. Campos and Santos basins: 40 Years of reservoir characterization and management of shallow-to ultra-deep water, post-and pre-salt reservoirs-Historical overview and future challenges, OTC Brasil. OnePetro.
- Ceia, M., Missagia, R., Archilha, N., Baggieri, R., Santos, V., Fidelis, S., Oliveira, L., Neto, I.L., 2022. Petrophysical characterization of Lagoa Salgada'stramatolites—A Brazilian pre-salt analog. *Journal of Petroleum Science and Engineering* 218, 111012.
- Chilingar, G., Long, W., 2017. Correlation between porosity and permeability of carbonate rock reservoirs. *Energy Sources, Part A: Recovery, Utilization, and Environmental Effects* 39, 1116-1117.
- CMG, 2019. CMOST for Conventional & Tight Reservoirs, CMOST v2019.10, Tutorial. Computer Modelling Group Ltd., Houston.
- Drexler, S., Bastos Alves, R., Silos, V., Ferreira De Siqueira, M., Toelke, J., 2022. New Method to Simulate Digital Petrophysical Properties in Heterogeneous Carbonates Using Multiscale Micro Computed Tomography Imaging and Customized Laboratory Experiments, International Petroleum Technology Conference. OnePetro.

- Farokhpoor, R., Westphal, E., Idowu, N., Oren, P., Fletcher, B., 2016. Gas-water steady-state relative permeability determination with two approaches; experimental and digital rock analysis, strengths and weaknesses. SCA2016-12.
- Fitch, P.J., Lovell, M.A., Davies, S.J., Pritchard, T., Harvey, P.K., 2015. An integrated and quantitative approach to petrophysical heterogeneity. *Marine and Petroleum Geology* 63, 82-96.
- Gao, Y., Raeini, A.Q., Selem, A.M., Bondino, I., Blunt, M.J., Bijeljic, B., 2020. Pore-scale imaging with measurement of relative permeability and capillary pressure on the same reservoir sandstone sample under water-wet and mixed-wet conditions. *Advances in Water Resources* 146, 103786.
- Guice, K., Lun, L., Gao, B., Gupta, R., Gupta, G., Kralik, J.G., Glotzbach, R., Kinney, E., Leitzel, G., Rainey, J., 2014. An evaluation of digital rock physics technology for the prediction of relative permeability and capillary pressure for a middle eastern carbonate reservoir, International Petroleum Technology Conference. OnePetro.
- Hadavimoghaddam, F., Ostadhassan, M., Heidaryan, E., Sadri, M.A., Chapanova, I., Popov, E., Cheremisin, A., Rafieepour, S., 2021. Prediction of dead oil viscosity: Machine learning vs. classical correlations. *Energies* 14, 930.
- Heidaryan, E., 2019. A note on model selection based on the percentage of accuracy-precision. *Journal of Energy Resources Technology* 141.
- Hendry, J., Burgess, P., Hunt, D., Janson, X., Zampetti, V., 2021. Seismic characterization of carbonate platforms and reservoirs: an introduction and review. Geological Society, London, Special Publications 509, 1-28.
- Hounsfield, G.N., 1973. Computerized transverse axial scanning (tomography): Part 1. Description of system. *The British journal of radiology* 46, 1016-1022.
- Iraji, B., Shadizadeh, S.R., Riazi, M., 2015. Experimental investigation of CO<sub>2</sub> huff and puff in a matrix-fracture system. *Fuel* 158, 105-112.
- Iraji, S., Ayatollahi, S., 2019. Experimental investigation on asphaltene biodegradability using microorganism: cell surface properties' approach. *Journal of Petroleum Exploration and Production Technology* 9, 1413-1422.
- Iraji, S., Soltanmohammadi, R., De Almeida, T.R., Munoz, E.R., Basso, M., Vidal, A.C., 2022a. Laboratory and numerical examination of oil recovery in Brazilian Pre-salt analogues based on CT images, Third EAGE Conference on Pre Salt Reservoirs.
- Iraji, S., Soltanmohammadi, R., Munoz, E.R., Basso, M., Vidal, A.C., 2023. Core scale investigation of fluid flow in the heterogeneous porous media based on X-ray computed tomography images: Upscaling and history matching approaches. *Geoenergy Science and Engineering*, 211716.
- Iraji, S., Soltanmohammadi, R., Munoz, E.R., Winter, A., de Almeida, R.V., Vidal, A.C., 2022b. Experimental Investigation of Waterflooding Performance by Increasing Copper Ions in Brazilian Pre-Salt Rock, 83rd EAGE Annual Conference & Exhibition. European Association of Geoscientists & Engineers, pp. 1-5.
- Iraji, S., Soltanmohammadi, R., De Almeida, T Rodrigues, Munoz, E.R., Vidal, A.C., 2022c. Experimental investigation of single-phase flow pattern in highly heterogeneous carbonates rocks, Rio Oil & Gas 2022. IBP, Rio de Janeiro | Brasil.
- Jackson, M.P., Hudec, M.R., 2017. Salt tectonics: Principles and practice. Cambridge University Press.
- Jackson, S.J., Lin, Q., Krevor, S., 2020. Representative elementary volumes, hysteresis, and heterogeneity in multiphase flow from the pore to continuum scale. *Water Resources Research* 56, e2019WR026396.

- Jensen, J., Lake, L.W., Corbett, P.W., Goggin, D., 2000. Statistics for petroleum engineers and geoscientists. Gulf Professional Publishing.
- Kang, P.K., Lee, J., Fu, X., Lee, S., Kitanidis, P.K., Juanes, R., 2017. Improved characterization of heterogeneous permeability in saline aquifers from transient pressure data during freshwater injection. *Water Resources Research* 53, 4444-4458.
- Kerig, P., Watson, A., 1987. A new algorithm for estimating relative permeabilities from displacement experiments. *SPE Reservoir Engineering* 2, 103-112.
- Kruger, W., 1961. Determining areal permeability distribution by calculations. *Journal of Petroleum Technology* 13, 691-696.
- Lamas, L., Ruidiaz, E., Vidal, A., 2019. AUTOMATED METHODOLOGY FOR DETECTING BORDER IN CT-SCAN IMAGES OF NON-CIRCULAR ROCK SAMPLES. *Brazilian Journal of Petroleum and Gas* 13.
- Lamas, L., Ruidiaz, E., Vidal, A., 2021. Study of empirical correlation between permeability and porosity with application for permeability upscaling. *Journal of the Brazilian Society of Mechanical Sciences and Engineering* 43, 1-12.
- Lima, M., Pontedeiro, E., Ramirez, M., Boyd, A., Van Genuchten, M.T., Borghi, L., Couto, P., Raouf, A., 2020. Petrophysical correlations for the permeability of coquinas (carbonate rocks). *Transport in Porous Media* 135, 287-308.
- Lin, Q., Bijeljic, B., Foroughi, S., Berg, S., Blunt, M.J., 2021. Pore-scale imaging of displacement patterns in an altered-wettability carbonate. *Chemical Engineering Science* 235, 116464.
- Lin, Q., Bijeljic, B., Pini, R., Blunt, M.J., Krevor, S., 2018. Imaging and measurement of pore-scale interfacial curvature to determine capillary pressure simultaneously with relative permeability. *Water Resources Research* 54, 7046-7060.
- Lucia, F., 1983. Petrophysical parameters estimated from visual descriptions of carbonate rocks: a field classification of carbonate pore space. *Journal of petroleum technology* 35, 629-637.
- Matula, M., 1969. Engineering Geologic Investigations Of Rock Heterogeneity, The 11th US Symposium on Rock Mechanics (USRMS). American Rock Mechanics Association.
- Meneses, A.F.O., Carrillo M, L.F., Otero, E.H.H., Santos, N.S., 2019. Experimental estimation of relative permeabilities through computed tomography, SPWLA 60th Annual Logging Symposium. OnePetro.
- Mirzabozorg, A., Nghiem, L., Chen, Z., Yang, C., Hajizadeh, Y., 2012. History matching saturation and temperature fronts with adjustments of petro-physical properties; SAGD case study, SPE Kuwait International Petroleum Conference and Exhibition. OnePetro.
- Mohriak, W., Nemčok, M., Enciso, G., 2008. South Atlantic divergent margin evolution: rift-border uplift and salt tectonics in the basins of SE Brazil. Geological Society, London, Special Publications 294, 365-398.
- Odsäter, L.H., Berg, C.F., Rustad, A.B., 2015. Rate dependency in steady-state upscaling. *Transport in Porous Media* 110, 565-589.
- Petrobras, B., 2021. Fact Sheet.
- Reynolds, C.A., Blunt, M.J., Krevor, S., 2018. Multiphase flow characteristics of heterogeneous rocks from CO<sub>2</sub> storage reservoirs in the United Kingdom. *Water Resources Research* 54, 729-745.
- Rezende, M.F., Tonietto, S.N., Pope, M.C., 2013. Three-dimensional pore connectivity evaluation in a Holocene and Jurassic microbialite buildup. *AAPG bulletin* 97, 2085-2101.
- Sen, S., Abioui, M., Ganguli, S.S., Elsheikh, A., Debnath, A., Benssaou, M., Abdelhady, A.A., 2021. Petrophysical heterogeneity of the early Cretaceous Alamein dolomite reservoir from North

- Razzak oil field, Egypt integrating well logs, core measurements, and machine learning approach. *Fuel* 306, 121698.
- Sharma, M., 2008. Stromatolites studies in India: An overview. *Journal of Palaeosciences* 57, 63-67.
- Soltanmohammadi, R., Iraj, S., De Almeida, T.R., Munoz, E.R., Fioravanti, A.R., Vidal, A.C., 2021. Insights into Multi-Phase Flow Pattern Characteristics and Petrophysical Properties in Heterogeneous Porous Media, Second EAGE Conference on Pre-Salt Reservoir. European Association of Geoscientists & Engineers, pp. 1-5.
- Soltanmohammadi, R., Iraj, S., De Almeida, T.R., Munoz, E.R., Vidal, A.C., 2022. Upscaling Challenges of Heterogeneous Carbonate Rocks: A Case Study of Brazilian Pre-Salt Analogous, Third EAGE Conference on Pre Salt Reservoirs.
- Su, H., Zhou, F., Zheng, A., Wang, L., Wang, C., Yu, F., Kang, L., Li, J., 2022. Heavy oil recovery by alkaline-cosolvent-polymer flood: a multiscale research using micromodels and computed tomography imaging. *SPE Journal* 27, 1480-1492.
- Vargas, J.V., Borges, T., Caicedo, A., de Almeida, R.V., Koroishi, E., 2022. Relative Permeability of Supercritical CO<sub>2</sub> and Carbonated Water in Carbonate Rock Using Experimental and Simulation Methods, 83rd EAGE Annual Conference & Exhibition. European Association of Geoscientists & Engineers, pp. 1-5.
- Vik, B., Bastesen, E., Skauge, A., 2013. Evaluation of representative elementary volume for a vuggy carbonate rock—Part: Porosity, permeability, and dispersivity. *Journal of Petroleum Science and engineering* 112, 36-47.
- Withers, P.J., Bouman, C., Carmignato, S., Cnudde, V., Grimaldi, D., Hagen, C.K., Maire, E., Manley, M., Du Plessis, A., Stock, S.R., 2021. X-ray computed tomography. *Nature Reviews Methods Primers* 1, 1-21.
- Zahasky, C., Jackson, S.J., Lin, Q., Krevor, S., 2020. Pore network model predictions of Darcy-scale multiphase flow heterogeneity validated by experiments. *Water Resources Research* 56, e2019WR026708.

**3 THE IMPACT OF HETEROGENEITY AND PORE NETWORK CHARACTERISTICS ON SINGLE AND MULTI-PHASE FLUID PROPAGATION IN COMPLEX POROUS MEDIA: AN X-RAY COMPUTED TOMOGRAPHY STUDY**

**Author: Shohreh Iraj**

**Co-Author: Tales Rodrigues De Almeida, Ramin Soltanmohammadi, Eddy Ruidiaz Munoz, Mateus Basso, Alexandre Campana Vidal**

**Campinas - SP**

**2023**

## **ABSTRACT**

This study investigates the impact of pore network characteristics on fluid flow through complex and heterogeneous porous media, providing insights into the factors affecting fluid propagation in such systems. Specifically, high-resolution or micro x-ray computed tomography (CT) imaging techniques were utilized to examine outcrop stromatolite samples of the Lagoa Salgada, considered flow analogous to the Brazilian Pre-salt carbonate reservoirs. The petrophysical results comprised two distinct stromatolite depositional facies, the columnar and the fine-grained facies. By generating Pore Network Model (PNM), the study quantified the relationship between key features of the porous system, including pore and throat radius, throat length, coordination number, shape factor, and pore volume. The study found that the less dense pore network of the columnar sample is typically characterized by larger pores and wider and longer throats, but with a weaker connection of throats to pores. Both facies exhibited less variability in the radius of the pores and throats in comparison to throat length. Additionally, a series of core flooding experiments coupled with medical CT scanning was designed and conducted in the plug samples to assess flow propagation and saturation fields. The study revealed that the heterogeneity and presence of disconnected or dead-end pores significantly impacted the flow patterns and saturation. Two-phase flow patterns and oil saturation distribution reveal a preferential and heterogeneous displacement that mainly swept displaced fluid in some regions of plugs and bypassed it in others. The relation between saturation profiles, porosity profiles, and the number of fluid flow patterns for the samples was evident. Only for the columnar plug sample, the enhancement in recovery factor after shifting to lower salinity water injection (SW) was observed.

**Keywords:** Pore Network Model, heterogeneous porous media, flow patterns, dead-end pores

### 3.1 INTRODUCTION

Comprehending the fluid flow through porous media is crucial for various industrial uses, including the recovery of hydrocarbons, underground water and particle movement, CO<sub>2</sub> and hydrogen storage in subsurface reservoirs, flow through porous electrodes in fuel cells, and interstitial flow in biological tissues (Raeini et al., 2014; Anbari et al., 2018).

The total, connected pores, and pore geometry of rocks exert considerable control over the fluid flow within porous systems. Numerous studies, using numerical simulations and two and three-dimensional image analysis, show that the degree of connectivity and throat width are key factors in determining the characteristics and effective transport of porous rocks. The coordination number, which is the total count of throats linked to a specific pore, is used to measure the level of connectivity within the pore network (von Bargen and Waff, 1986; Doyen, 1988; Wimert and Hier-Majumder, 2012; Thomson et al., 2018; Abedi et al., 2020). These geometric characteristics of the pore network can vary depending on a number of variables, however, statistical studies of the structure, shape, size, and arrangement of porous systems enable determining these characteristics that are essential for the measurement of petrophysical properties (Thomson et al., 2018; Rahmat et al., 2020).

To explain the variability of pore network structure and textural alterations, conventional approaches to fundamental rock characteristic description fall short either in directly incorporating measurable geometric characteristics or in measuring the spatial distribution of the pores and grains in the three-dimension network. X-ray computed tomography (CT) facilitates to assess these fundamental qualities and provide a more accurate direct visualization and characterization of the porous structure and geometry. This improves our comprehension of the pore volume and pore-network connectivity and microstructural constraints in various systems (Rezende et al., 2013; Thomson et al., 2018; Thomson et al., 2020; Withers et al., 2021).

A proper description of the pore space is necessary for pore-scale modeling, especially when dealing with multi-phase flows (Al-Kharusi and Blunt, 2007). Pore-scale modeling of complex carbonate reservoirs is one of the scientific frontiers associated with the Brazilian Pre-salt play. The discovery of these reservoirs has been regarded as a significant breakthrough of the past decade and the cornerstone of South America's offshore petroleum industry. The main reservoir of the pre-salt play comprises unusual in-situ carbonate rocks formed by shrub-like and spherulitic calcite

fabrics that were accumulated in extensional basins (Bruhn et al., 2017). These formations have complex geometries and diverse pore network structures. The growth framework, diagenetic modification, and depositional textures influence petrophysical properties based on rock features and control the pore volume and pores-throats connectivity (Matula, 1969; Lucia, 1983; Sharma, 2008). Different carbonate formations have been proposed as analogue rocks for the pre-salt reservoirs, including travertines (Claes et al., 2017) and microbialites such as stromatolites and thrombolites (Rezende et al., 2013).

In contrast to sandstone reservoirs, carbonate formations pose significant challenges in accurately determining petrophysical properties and characterizing reservoirs due to their high heterogeneity. Heterogeneity in reservoir description refers to the dispersion of parameters that impacts fluid flow (Jensen et al., 2000; Hendry et al., 2021; Sen et al., 2021). The heterogeneous nature and non-uniform distribution of petrophysical properties within carbonate formations give rise to significant ambiguity in constructing models and forecasting production performance with reasonable accuracy. The use of flow experiments allows for a precise evaluation of the influence of heterogeneity on fluid flow (Vik et al., 2013; Irajil et al., 2015; Irajil and Ayatollahi, 2019). Understanding the dynamics of fluid flow within the media and the behavior of various phases as they pass through the porous system is essential for enhancing reservoir recovery, predicting oil displacement efficiency and water injection performance, and overcoming the barriers that hinder oil retrieval through conventional recovery methods (Gunde et al., 2010).

The CT technique is a useful tool for observing and quantifying fluid flow and variations in the liquid saturation field in porous media in 3D porous structures. This technique can display the spread and distribution of various fluids in porous materials and can also uncover the flow patterns of fluids using statistical computations (Su et al., 2022).

Heterogeneous stromatolite rock blocks collected from outcrops of Lagoa Salgada as the potential flow analogous of the Brazilian Pre-salt reservoir rock models (Wright and Tosca, 2016) were utilized in this study. Analysis of the geological features and pore geometry of these rock samples facilitated the identification of two distinct facies: fine-grained with smaller pores and less-connected pore networks and columnar (vugular) with a better-connected pore network and large vugs. Therefore, plugs were sampled considering these heterogeneities and facies. The first part of this study concentrated on providing a thorough account of the processing of the high-resolution

or microCT images of the plug samples. The analysis employed digital rock physics (DRP) to evaluate and compare the pore network properties and geometry of the fine-grained and columnar facies samples.

The second part of this article encompasses an extensive examination that merges traditional techniques such as core flooding with medical CT imaging to provide a characterization of porous systems, analyze single-phase and two-phase flow patterns during both drainage and imbibition processes, and explore the impact of varying salinity levels of injected water on oil flow. Moreover, using acquired CT images during flooding experiments, variations in the concentration profiles and saturation field were investigated during different flooding stages of water invasion and oil movement within the heterogeneous plug samples. The study aims to improve the understanding of the complex geometries and diverse networking patterns of the carbonate rocks, which have significant implications for hydrocarbon production and carbon and hydrogen storage in subsurface reservoirs of the Brazilian Pre-salt reservoirs.

## 3.2 MATERIAL AND METHODOLOGY

### 3.2.1 MATERIALS

Outcrops of Lagoa Salgada in Rio de Janeiro State, Brazil, were used to perform experiments and evaluate the pore geometry and flow pattern. Figure 2-1-a displays Rio de Janeiro State, highlighting the coastal zone and location map of the area of study.

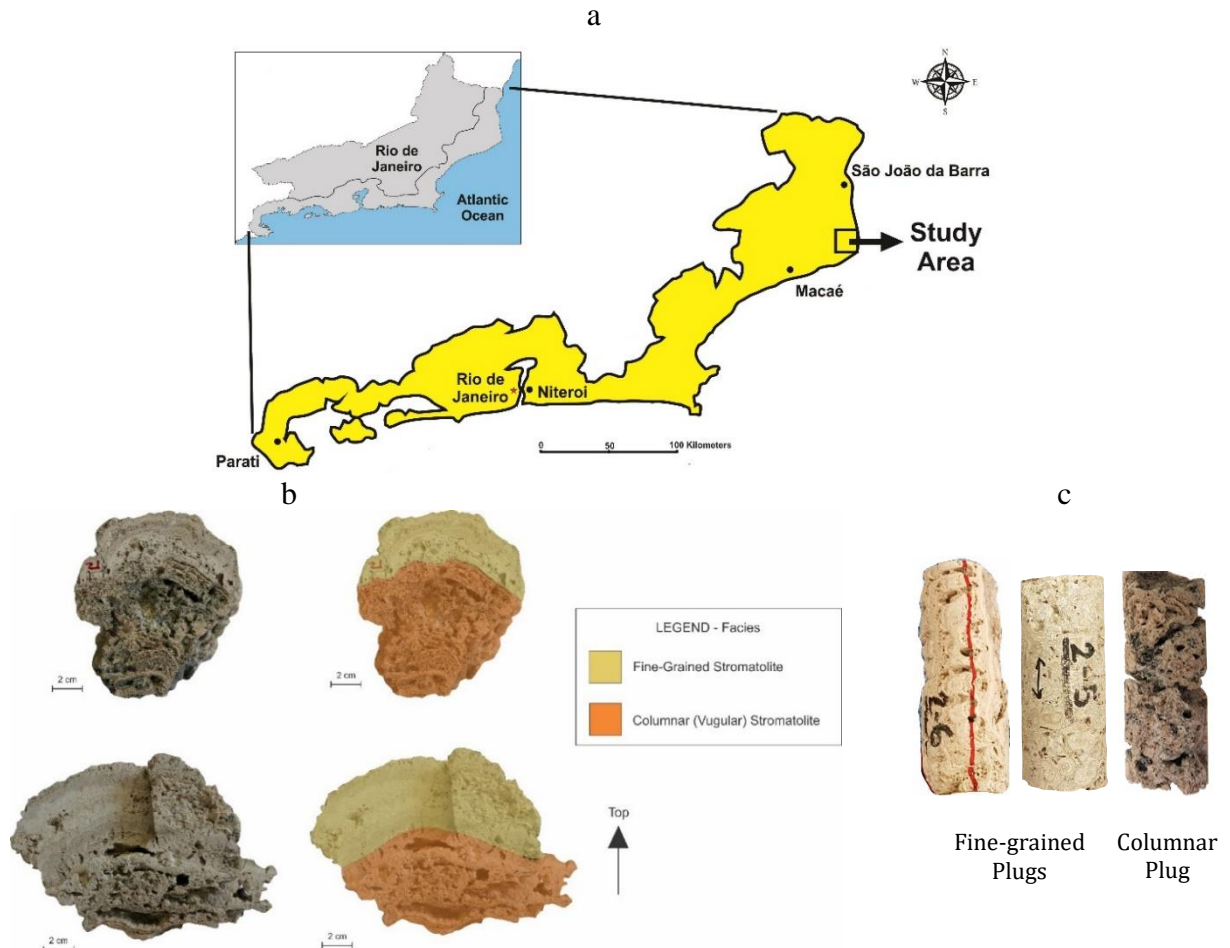


Figure 3-1. a) Coastal zone in Rio de Janeiro State with the marked location of the study area (Lagoa Salgada), b) two main facies of rock sample, and c) plug samples from the two facies.

The geological characterization of the block rock sample was performed based on petrology and petrography to identify regions of interest and obtain representative rock facies prior to plugging samples. Two facies were specified, namely fine-grained and columnar/vugular (Figure 2-1-b). The first facies was with relatively small pores while the other had large pores and vugs. In this work, one plug sample from columnar facies and two from fine-grained were drilled (Figure 2-1-c) to investigate and compare the effect of pore geometry on network characteristic, single-phase and two-phase flow patterns, saturation profile, and oil recovery. Since the plug samples were highly

heterogeneous and frangible, the challenge was the preparation of a representative plug with constant marginal limits and maintained flow characteristics during fluid injection. A full description of the encapsulation techniques to overcome this challenge has been published previously published (Soltanmohammadi et al., 2021; Irajil et al., 2022c; Irajil et al., 2022a; Irajil et al., 2022b; Soltanmohammadi et al., 2022).

Porosity, gas permeability considering Klinkenberg correction, and physical properties of these plugs are listed in Table 3-1. For plug from the columnar facies, given the existence of a large number of linked pores and vugs, we were unable to calculate pressure drop during injection of gas and as a result, we could not measure gas permeability. So liquid permeability calculation was conducted with three flow rates of 0.5, 1, and 5 mL/min using core flooding apparatus. The average liquid permeability of 5434.83 was determined using Darcy's law for the fluid flow in porous media for columnar plug.

Table 3-1. Petrophysical characteristics of the plugs.

Facies	Plug	Length, cm	Diameter, cm	Porosity, %	Gas Permeability, mD
Fine-grained	F2 – 5	8.90	3.78	29.8	963
	F2 – 6	9.72	3.77	24.3	1200
Columnar	F1 – 1	8.90	3.68	52.4	–

The study used three different available aqueous solutions, namely distilled water (DW), sea water (SW) and formation water (FW). The compositions of FW and SW are displayed in Table 2-2.

The oil phase utilized in this investigation was obtained from the pre-salt reservoir. The oil was centrifuged and passed through a 5  $\mu\text{m}$  Millipore filter prior to use. The oil properties including density, viscosity, molar mass, water content, acid number, and the result of SARA tests showing the weight percentage of saturates, aromatics, resins, and asphaltene components are presented in Table 3-3.

Table 3-2. Average composition of SW and FW.

Salt	Formation Water (FW) Composition, g/L	Sea Water (SW) Composition, g/L
<i>NaCl</i>	163.620	23.470
<i>Na<sub>2</sub>SO<sub>4</sub></i>	0.088	0.100
<i>NaHCO<sub>3</sub></i>	0.487	0.192
<i>KCl</i>	6.911	0.724
<i>MgCl<sub>2</sub>.6H<sub>2</sub>O</i>	3.068	10.550
<i>CaCl<sub>2</sub>.2H<sub>2</sub>O</i>	19.100	1.466
<i>SrCl<sub>2</sub>.6H<sub>2</sub>O</i>	0.029	0.039
<i>BaCl<sub>2</sub>.2H<sub>2</sub>O</i>	0.033	–
<i>FeSO<sub>4</sub>.7H<sub>2</sub>O</i>	0.022	–
TDS, g/L	193.358	36.541

Table 3-3. Oil properties.

Properties	Value	Method
Density	0.8751 g/cm <sup>3</sup>	(ASTM-D1298-12b, 2017)
Viscosity	5 cP	(ASTM-D7042, 2014)
Molar mass	120g/mol	(ASTM-D2503-92, 1992)
Water content	0.01%	(ASTM-D1744, 1992)
Acid number	0.0275 mg KOH/g	(ASTM-D664, 2011)
SARA Test		
Components	Weight Percent, %	Method
Saturates	93.26	
Aromatics	0.59	(ASTM-D6560-12, 2012)
Resins	5.82	
Asphaltene	0.33	

### 3.2.2 METHODOLOGY

Figure 3-2 displays an overview of the implemented workflow and this section offers a thorough clarification of each individual stage.

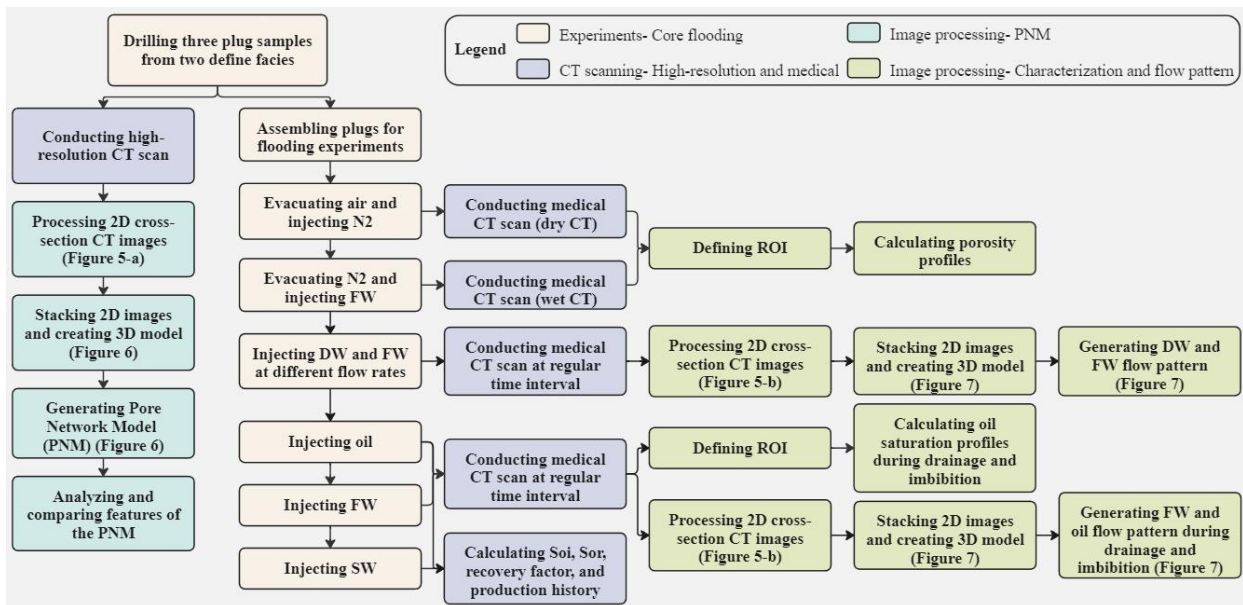


Figure 3-2. Implemented workflow of the study.

In the first step of the study, microCT image acquisition for both columnar and fine-grained plug samples was performed in the ZEISS Xradia Versa X-ray Microscopes, model XRM-500 (Voxel size of 44.69  $\mu\text{m}$ ) at the Laboratory of Porous Media and Thermophysical Properties of the Federal University of Santa Catarina (LMPT/UFSC). Each two-dimensional cross-sectional slice's image resolution (pixels) was 1029x999 with a slice thickness of 40  $\mu\text{m}$ . These 2D microCT images were processed and stacked together to create the 3D representation of the plugs (Figure 3-3). For determination and quantification of the porous phase of the plug samples, pore network modeling

(PNM) was designed to gather information about the pore distribution, size and geometry of the pores and throats, and coordination number.

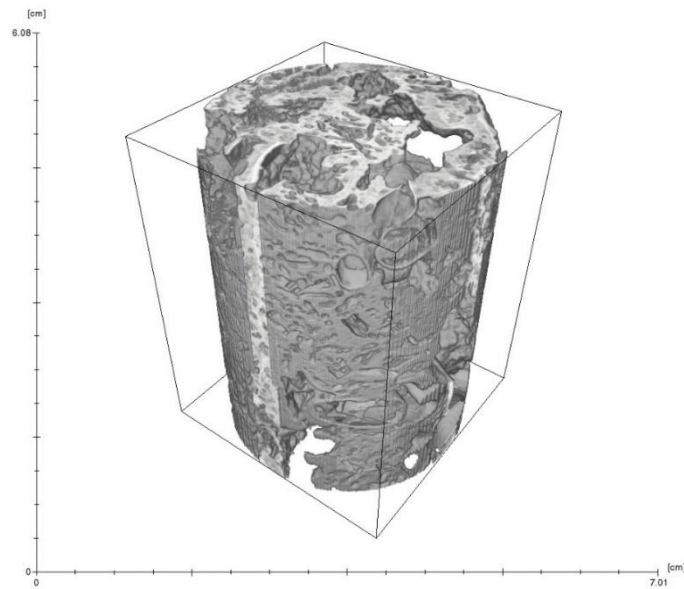


Figure 3-3. 3D high-resolution full model of columnar sample.

In the next step, a series of core flooding experiments were designed and performed in the three plug samples to understand single-phase and two-phase flow propagation and saturation profiles in the plug samples with different pore geometry. The schematic of the core flooding experimental setup equipped with a medical CT scanner is shown in Figure 2-3.

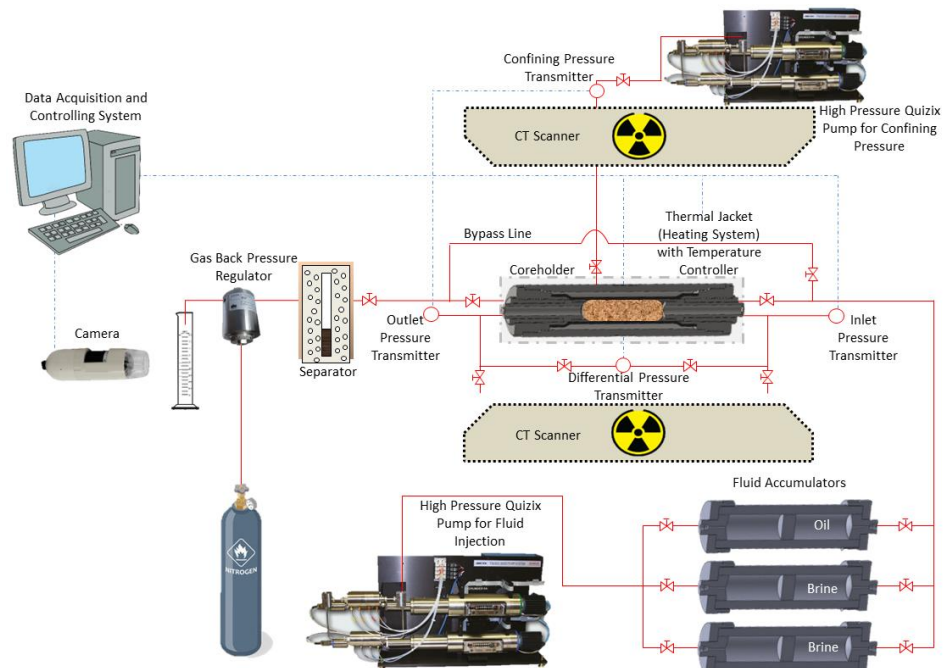


Figure 3-4. A diagram of the experimental setup: core flooding equipment and the medical CT imaging system.

The equipment consists of a horizontally held core holder, two high-pressure Quizix pumps for injection and confining pressure, liquid accumulators to transfer oil and brine, pressure and differential pressure transmitters, a back pressure regulator, a biphasic separator, the heating system, and a high precision data acquisition system connected to processing and controlling software. The Medical Imaging Systems from SIEMENS, specifically the SOMATOM Spirit scanner (Voxel size of  $100 \mu\text{m}$ ) at the Center for Energy and Petroleum Studies of the State University of Campinas (CEPETRO/UNICAMP), was utilized as a Single Source Computed Tomography device to acquire CT data of plug samples during the injection. The image resolution (pixels) was  $512 \times 512$  with a slice thickness of  $0.1 \text{ cm}$ .

This step-by-step procedure was followed for the flooding experiments (this process was applied to each of the three plugs):

- I. Assemble the dry plug sample into the core holder with respect to encapsulation techniques under the experiment conditions ( $106^\circ\text{C}$  temperature and  $150 \text{ bar}$  confining pressure).
  - II. Vacuum the plug to remove air from the void space.
  - III. Inject  $N_2$  into the sample and increase the  $N_2$  injection pressure step by step to the point that the pressure reaches  $50 \text{ bar}$  and then properly stabilizes.
  - IV. Perform CT scanning on the plug that has been saturated with  $N_2$  (dry CT).
  - V. Vacuum the plug to remove  $N_2$  from the void space.
  - VI. Inject FW into the plug and continue the process until the pressure stabilizes (All the fluids were injected at experiment temperature).
  - VII. Perform CT scanning on the plug that has been saturated with FW (wet CT).
- Note: Steps (III) to (VII) were performed to map out the porosity distribution and to obtain the initial description of the porous system.
- VIII. Inject 2.0 pore volume ( $PV$ ) of DW as the tracer with a consistent flow of  $0.1 \text{ ml/min}$  into the sample that has been saturated with FW and perform CT imaging while the process is ongoing.
  - IX. Inject 2.0  $PV$  of FW with a consistent flow  $0.5 \text{ ml/min}$  combined with CT scanning during flooding.
  - X. Decrease flow rate to  $0.1 \text{ ml/min}$  and continue FW injection (several  $PV$ ) until the total removal of the DW tracer.

Note: Steps (VIII) to (X) were performed to study single-phase and miscible process flow patterns.

- XI. Inject 2.0 PV of oil with flow of 0.1 *ml/min* into the sample that has been saturated with FW and acquire CT data during flooding.
- XII. Inject 2.0 PV of FW at a flow rate of 0.1 *ml/min* combined with CT scanning during the injection. Record the production data including pressure drop and produced volumes of oil and water to calculate the recovery factor.

Note: Steps (XI) to (XII) were performed to study two-phase and immiscible process (drainage and imbibition) flow patterns and production of the saturation map during injection process.

- XIII. Inject SW at a constant rate of 0.1 *ml/min*. Continue SW Injection until no further production of oil is observed. Keep track of the production data to measure the recovery factor and residual oil saturation.

Note: Step (XIII) was performed to find the efficiency of the ion change and lower salinity water injection on oil production.

It should be noted that, before starting oil injection (step XI) and after preparation of plug samples saturated with FW, some experiments were conducted by injection of FW at different flow rates (0.1, 0.5, and 1 cc/min for all three samples, for *F1* – 1 vugular sample the higher rate of 5 cc/min were also applied to analyze flow regime and validate the application of the Darcy equation for these heterogeneous porous media with large pores and vugs. If the Darcy regime is dominant in our porous system, by plotting differential pressure over length versus velocity, we will have a straight line. Non-Darcy flow is indicated by a deviation from the straight line. This deviation demonstrates that, in non-Darcy flow, the pressure drop is greater than in viscous flow (Fetter, 2018).

### 3.2.2.1 IMAGE PROCESSING

The X-ray is directed to the sample via a variety of directions during CT imaging process. The material is imaged in several 2D slices using the penetrating power of the X-rays (Lamas et al., 2019; Withers et al., 2021). Every X-ray beam with a single energy level attenuates differently as it passes the sample before being collected by a receiver. After measuring the attenuation from different angles, a 3D matrix is constructed. The attenuation numbers are reported in Hounsfield units (HU) at all points of the images (each array of the matrix) to show the variation of this

parameter in the sample. The spatial distribution of the attenuation coefficient in rock samples is affected by differences in the level of empty space, types of minerals present, and degree of saturation (Hounsfield, 1973; Withers et al., 2021).

The current section describes the procedure of image processing. The dataset contains two sets of images for the plug samples, one with a high resolution ( $44.69 \mu m$ ) and the other with a low resolution ( $100 \mu m$ ). Medical CT scanning for acquiring low-resolution images was repeated during all steps of injection experiments for all samples.

Once the *2D* CT data or sectional images has been obtained using the microCT scanner, the *3D* model was generated by layering these images on top of each other in the Digital Rock Analysis software (PerGeos software version 2020.2), where the images were first binarized and segmented for the recognition and characterization of the porous system. To begin this process:

- I. By cropping the images, a sub-area of the data was extracted. This selected region of interest was chosen to make image processing more computationally efficient (Figure 3-5-a-Cropping).
- II. By applying a non-local means filter, the 8-bit grayscale CT images were treated to remove noise (Figure 3-5-a-Denoising).

Streaks, brightness nonuniformity, and phase shift edges at the rock grain borders are examples of these undesired artifacts and noises (Thomson et al., 2018).

- III. Sharpening filters were implemented to the edges of the images to highlight the delimitation of the pore and rock edges (Figure 3-5-a-Sharpener) (Iassonov et al., 2009; Markussen et al., 2019).
- IV. To partition the different compositional phases of the images (pores/grains separation), segmentation was enforced and a grayscale image was turned into a binary image according to the X-ray attenuation values of each voxel (Knackstedt et al., 2013). The interactive overlay threshold was applied to segment and binarize the images (Figure 3-5-a-Binarization).
- V. A *3D* model was created by arranging the segmented *2D* images on top of one another. Figure 3-6-a to d displays *3D* visualizations of the sample considering grains, total, isolated, and connected pore spaces.

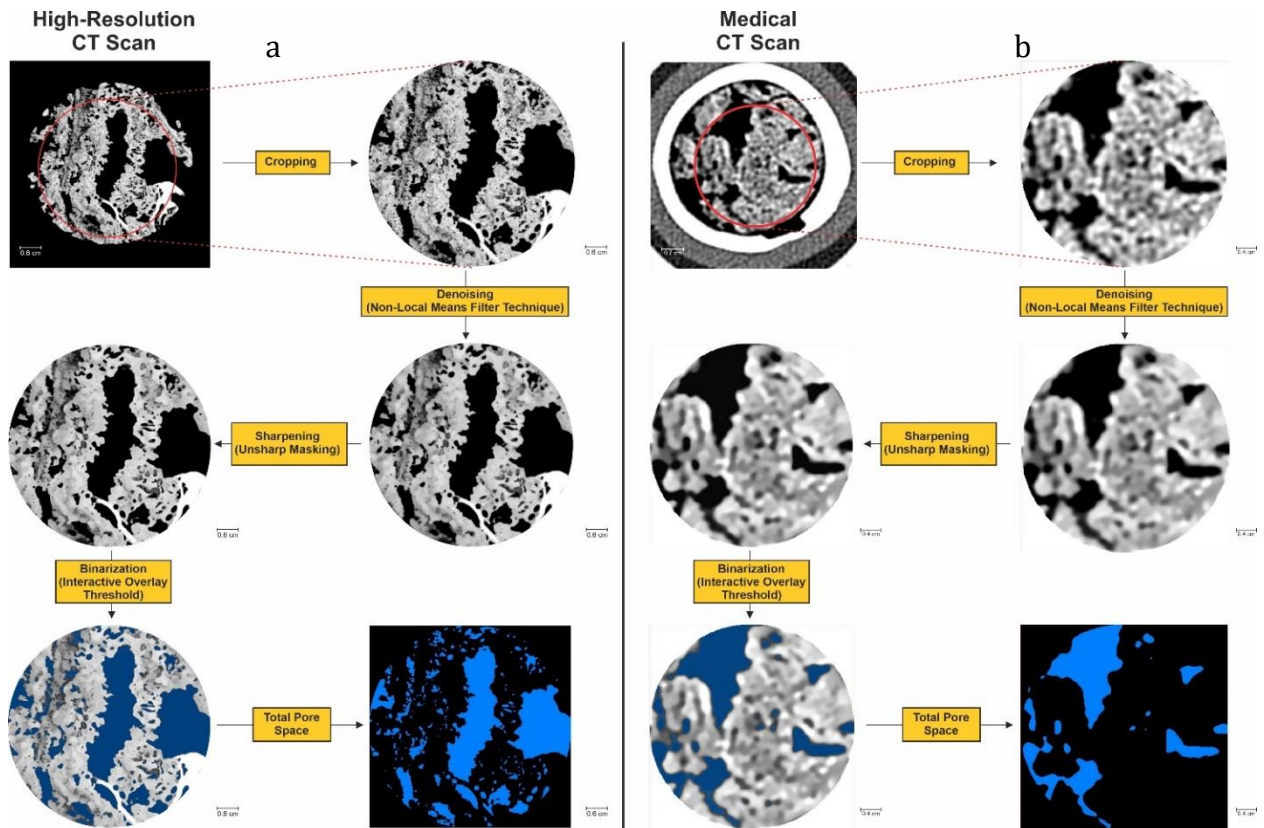


Figure 3-5. Image processing procedure for a) 2D microCT scan, b) 2D medical CT scan images

VI. The Pore Network Model (PNM) (Figure 3-6-f) was generated using PNM module in PerGeos for further processing the 3D models and to evaluate the connection between the characteristics of porous structure, such as the radius of pore and throat, coordination number (the number of connecting throats attached to a specific pore), shape factor, and the volume of pores.

Pores and throats are the two main parts of the pore network, where grain corner pores serve as junctions between distributed linear throats along grains. PNM module utilizes the hybrid algorithm to make a framework of the total pore system. This is achieved by determining the minimum spatial separation of voxels in the foreground (empty region) and background, thus eroding the pore-grain interface, and calculating the line length and connectivity. Lines with an outermost radius larger than their length are classified as pores, while those with a smaller radius are designated as throats. In the next step, the resulting image is resized to fill the border of every pore and throat, and the radius and length of each throat are calculated (Thomson et al., 2018; Thomson et al., 2020). Figure 3-6-e displays the marked image which is the outcome of this

procedure, with distinct pores and throats dyed in different hues, and Figure 3-6-f displays the resulted PNM.

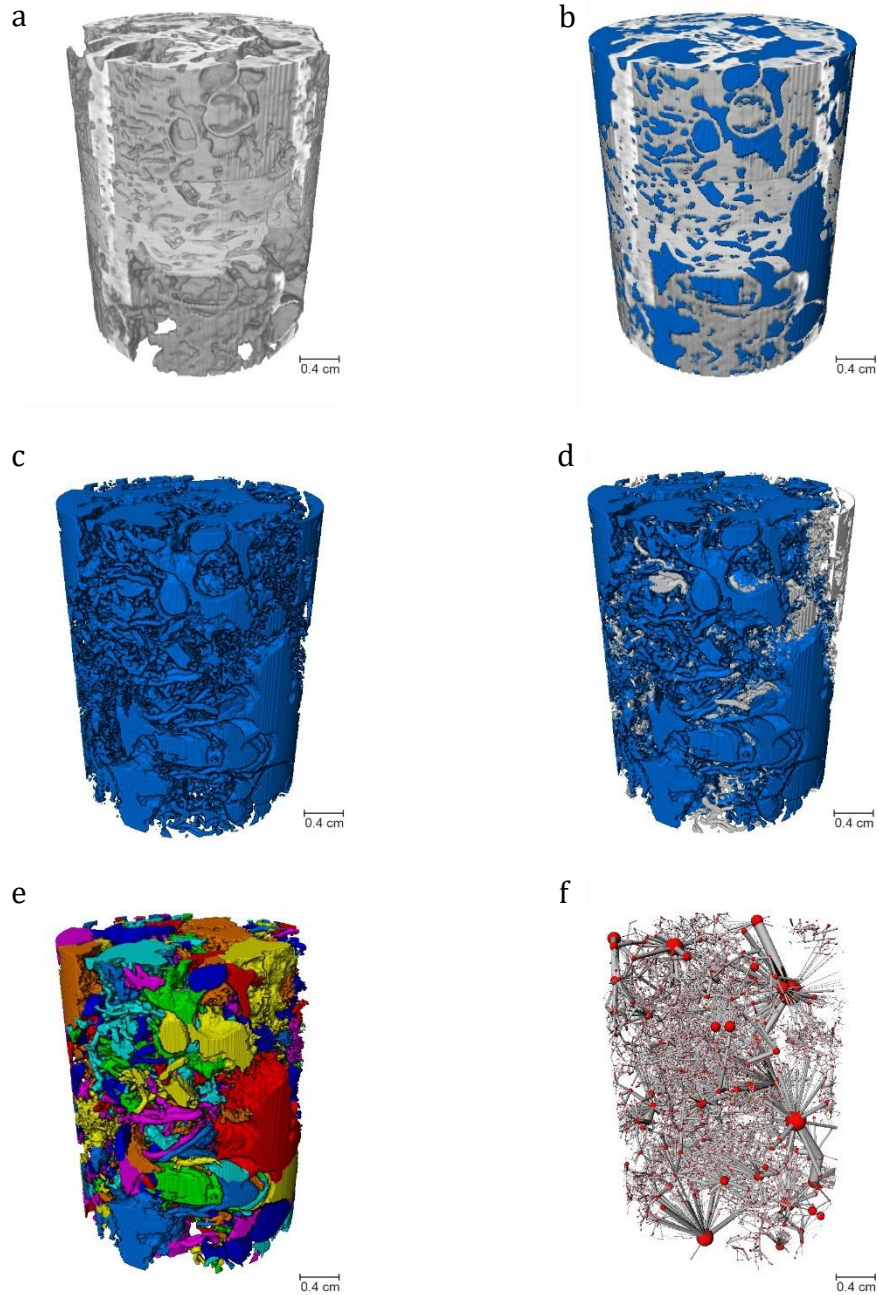


Figure 3-6. 3D representation of sample obtained from microCT scan images for a) grain (gray), b) grain (gray) and total pores (blue), c) total pores (blue), d) connected pores (blue) and isolated pores (gray), e) separated pore space, f) pore network model.

Subsequently, the 2D images acquired from medical CT scanning during flooding experiments were processed. Steps (I) to (V) for binarization, segmentation, and generating 3D models were

repeated and performed for all low-resolution images of plug samples (Figure 3-5-b). 3D representation of the sample for grains, total, isolated, and connected pore spaces for medical CT images are displayed in Figure 3-7-a to d.

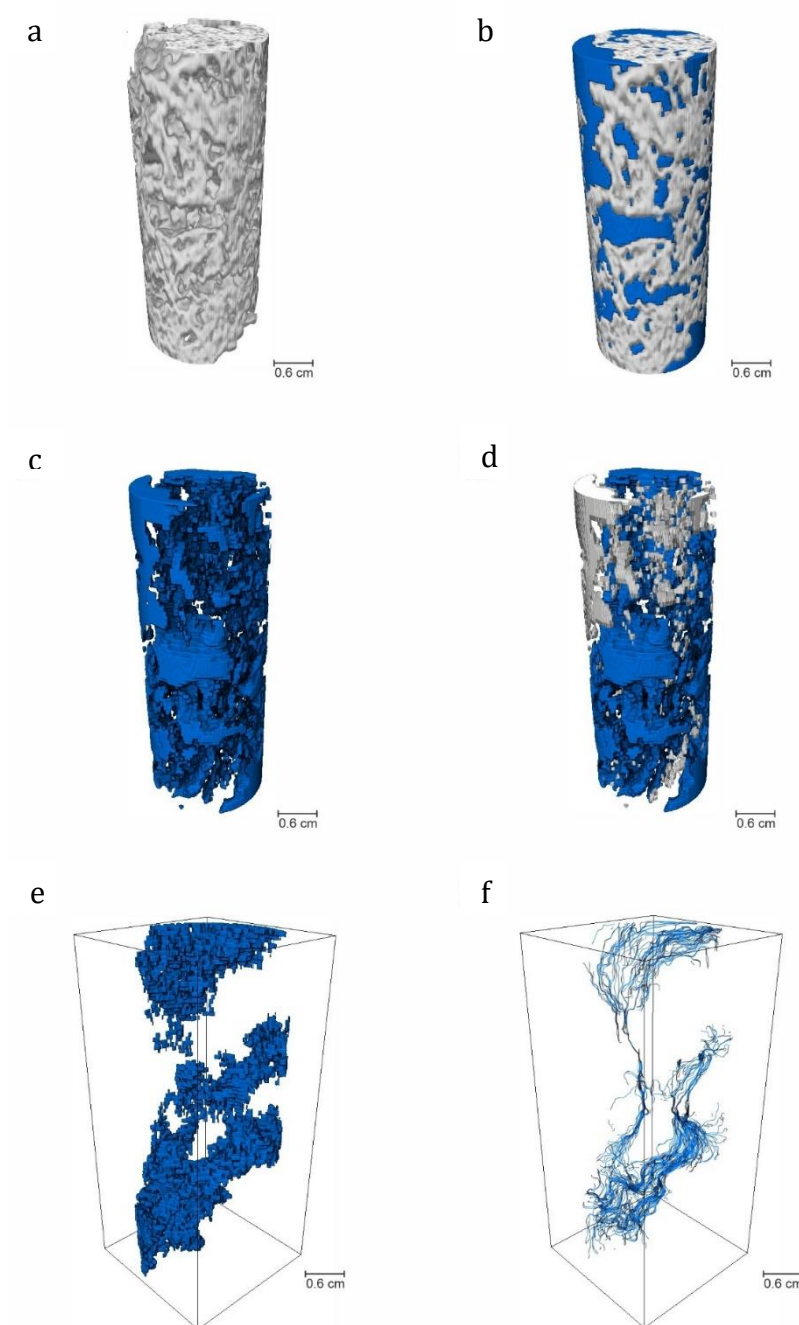


Figure 3-7. 3D representation of sample obtained from medical CT scan images for a) grain (gray), b) grain (gray) and total pores (blue), c) total pores (blue), d) connected pores (blue) and isolated pores (gray), e) connected pores filled with oil, f) oil flow pattern.

Finally, to generate flow patterns, the binary image file of the porous system was used as a mask in the separation of fluids. The injected fluids (brine or oil) were segmented according to the

watershed algorithm and according to the X-ray attenuation values of each fluid (Table 3-4). After this segmentation, the connectivity of the pores was investigated through the Axis Connectivity tool, by analyzing the binary 3D image of all paths of each fluid in the porous system (PerGeos, 2019). If there is no connectivity between the fluid inside the pores, it may be necessary to perform a new segmentation process until connectivity is achieved. This means that the segmentation algorithm should be modified or refined to accurately identify and delineate the connected regions of the fluid within the pores. The goal is to ensure that the segmented regions represent physically connected areas of the fluid, allowing for meaningful analysis and interpretation of the porous media. Figure 3-7-e displays the results of the axis connectivity tool using oil attenuation value and reveals part of the connected pore space in which the oil flows. Moreover, Figure 3-7-f shows resulting oil flow pattern during one flooding experiment.

Table 3-4. The average CT attenuation data of the fluids at experiment condition.

Fluid	CT value (HU)
$N_2$	-545.52
FW	433.03
DW	389.17
Oil	29.68

Meanwhile, using the medical CT images obtained during flooding experiments, the average porosity was determined for each slice, which allowed for the creation of a porosity profile along the plug (according to dry and wet CT). And as previously stated, medical CT imaging of the plugs were performed at each stage of the flooding experiment (every 0.2 PV fluid injection) to evaluate the arrangement of saturation level and indicate the fluid's movement. The following equations were used to obtain porosity and oil saturation profiles during the drainage and imbibition.

$$\phi = \frac{CTR_w - CTR_g}{CT_w - CT_g} \quad (3-1)$$

$$S_o = \frac{CTR_w - CTR_{wo}}{\phi(CT_w - CT_o)} \quad (3-2)$$

where,  $CTR_w$ ,  $CTR_g$ , and  $CTR_{wo}$  represent the CT attenuation coefficient of the plug saturated with FW, saturated with  $N_2$ , and saturated with both oil and FW.  $CT_w$ ,  $CT_g$ , and  $CT_o$  represent the mean CT attenuation coefficient of the FW,  $N_2$  and oil under experimental pressure and temperature, respectively.

In more detail, for calculating porosity and saturation curves during experiments, a script written in the Python programming language was created specifically for the purpose of analyzing and manipulating 2D medical CT images. The first step of this process involves defining a region of interest (ROI) by including both grain and pore spaces of plugs and excluding the components located on the outer side (encapsulation materials, sleeve, core holder, and air). See (Iraji et al., 2023) for additional information about this algorithm for non-cylindrical and vugular samples. In the next step, average CT values of the ROI for acquired images during different stage of experiments were utilized to calculate saturation and porosity profiles during the process (Equations (3-1) and (3-2)).

### 3.3 RESULTS AND DISCUSSION

#### 3.3.1 POROSITY AND PORE NETWORK MODELING

Applying the PNM, the entire porous system was categorized as a system of pores and throats. Figure 3-8 and Figure 3-9 demonstrate the 3D visualization of the porous space structure and pore network model for the columnar and one fine-grained facies sample, respectively. The PNM illustrations (Figure 3-8 and Figure 3-9-c) use gray cylinders to depict the throats and spheres representing pores. The columnar sample features fewer, broader throats connecting the pores and a less dense pore network, while a compact network of narrow throats makes up the model of the fine-grained sample.

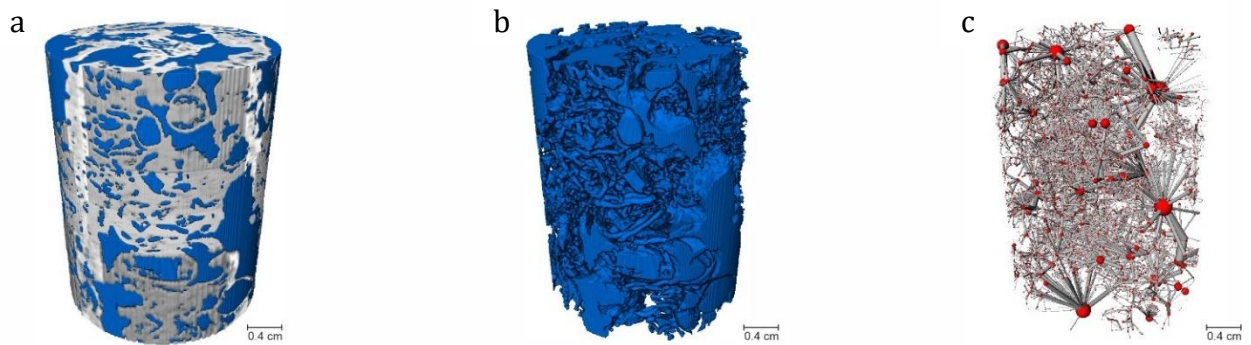


Figure 3-8. 3D visualization of *F1 – 1* columnar sample obtained from microCT scan images for a) grain (gray) and total pores (blue), b) connected pores (blue), c) pore network model.

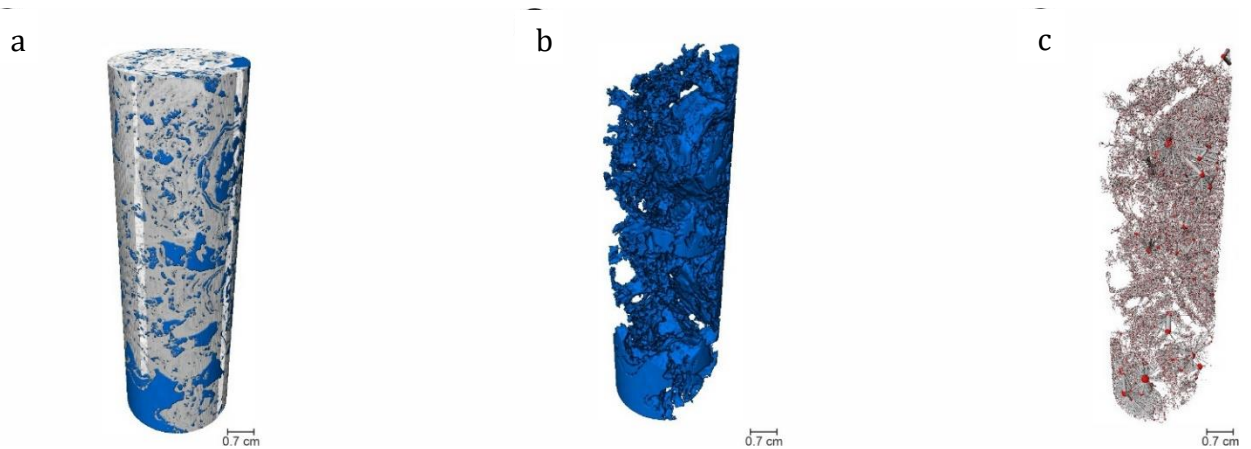


Figure 3-9. 3D visualization of *F2 – 6* fine-grained sample obtained from microCT scan images for a) grain (gray) and total pores (blue), b) connected pores (blue), c) pore network model.

Figure 3-10 compares the probability distribution plots of the pore geometry properties for both facies. The plots demonstrate the distribution of coordination number (Figure 3-10-a and b), shape factor (Figure 3-10-c), throat length (Figure 3-10-d), pore (Figure 3-10-e), and throat radius (Figure

3-10-f). Since most data for coordination number fell between one and 25, two plots were considered, one focusing on all the data in the log scale and the other on most of the data in the linear scale.

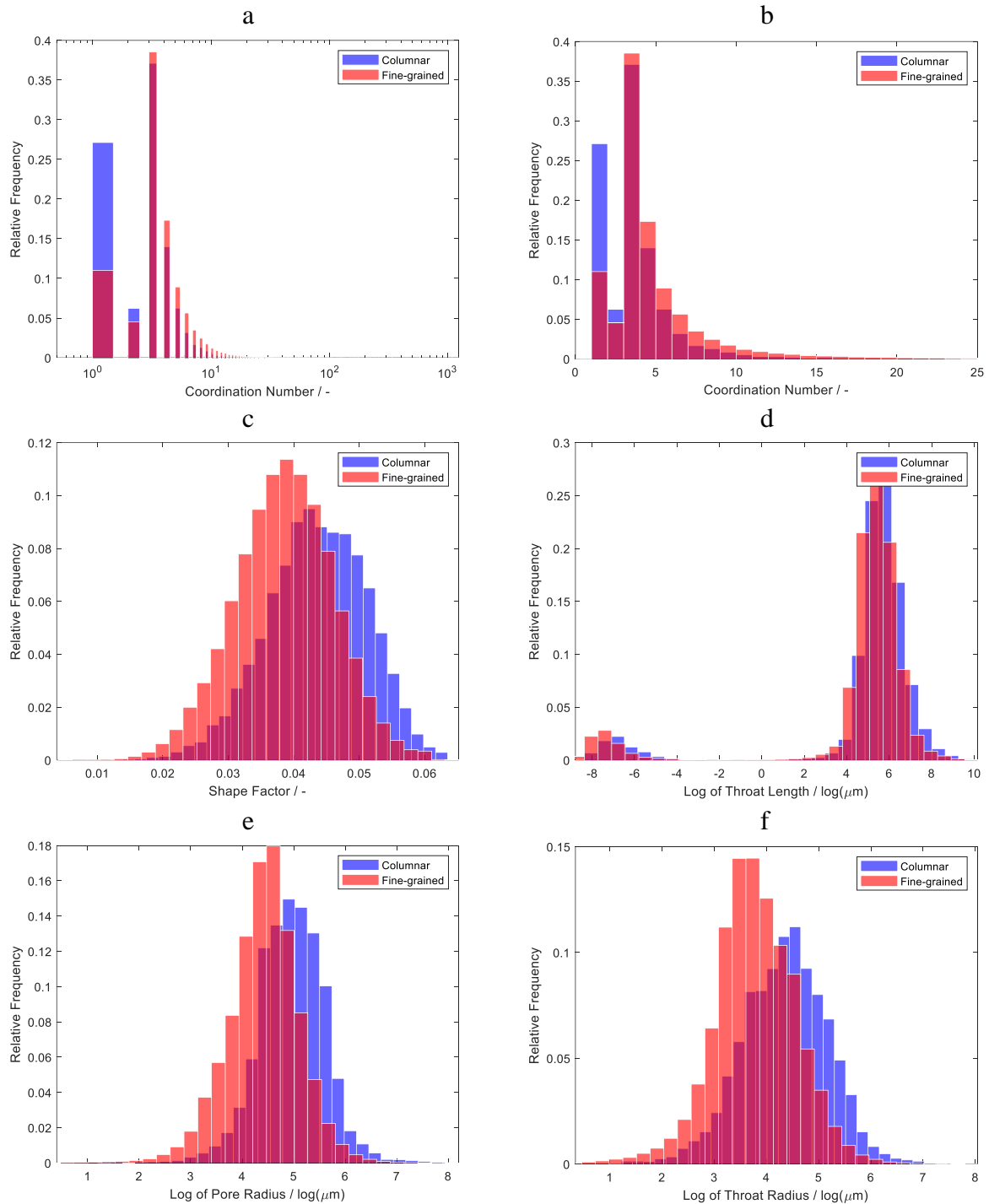


Figure 3-10. Probability distribution graphs of PNM properties for columnar (blue) and fine-grained (red) samples for a) coordination number in Log scale for the entire data set, b) coordination number in linear scale for the most frequent data set, c) shape factor, d) throat length, e) pore radius, f) throat radius.

The medians of all the PNM properties are listed in Table 3-5. Samples from both facies displayed the same median coordination number of 3. However, compared to the fine-grained sample, the columnar sample exhibits substantially higher relative frequency for the coordination number of less than 3, but for higher coordination numbers, the fine-grained sample displayed more frequency (Figure 3-10-a and b), indicating improved pore connectivity. Additionally, the pore network in the fine-grained sample was composed of pores typically 86  $\mu\text{m}$  in radius and throats 43 and 207  $\mu\text{m}$  in radius and length, respectively. While median values of 142, 80, and 272  $\mu\text{m}$  for pore radius, throat radius, and throat length, were measured for the network of the columnar sample. For columnar sample, the pore network was generally comprised of larger pores, wider and longer throats, but with the weaker connection and fewer junctions of throats to pores.

Table 3-5. Summary of the median of pore network characteristics of both facies sample.

Facies Plug	Fine-grained <i>F2 – 6</i>	Columnar <i>F1 – 1</i>
Coordination Number, -	3	3
Shape factor, -	0.0387	0.0437
Pore Radius, $\mu\text{m}$	86.029	141.985
Throat Radius, $\mu\text{m}$	43.090	80.132
Throat Length, $\mu\text{m}$	207.446	271.683
Pore Cross Section Area, $\mu\text{m}^2$	39,790	114,839
Pore Volume, $\mu\text{m}^3$	9,996,530	40,610,900
Number of Pores	90,790	12,128
Number of Throats	207,354	20,090

The shape factor refers to a unitless parameter used to quantify the degree of irregularity of a given geometric shape and represents a shape that matches the pore cross-section. It is defined as,

$$G = \frac{A}{S^2} \quad (3-3)$$

where,  $A$  and  $S$  are the area and perimeter of the pore cross-section, respectively. If  $G \leq \sqrt{3}/36$  then a triangle with the same  $G$  number is the idealized shape; if  $\sqrt{3}/36 < G \leq 1/16$  then it is a square, and if  $1/16 < G$  then it is a circle describing the pore cross-section (Helland et al., 2008). Typically, the triangle represented the pores' cross-section from both facies. However square pores were also available in both samples.

Figure 3-11 displays the correlation between the cross-sectional area and volume of pores for both samples and compares them with sphere and tetrahedron pores. In both fine-grained and columnar

samples, for a given cross-section area, the volume of the most pores are in the same range, and greater in size than sphere and tetrahedron pores.

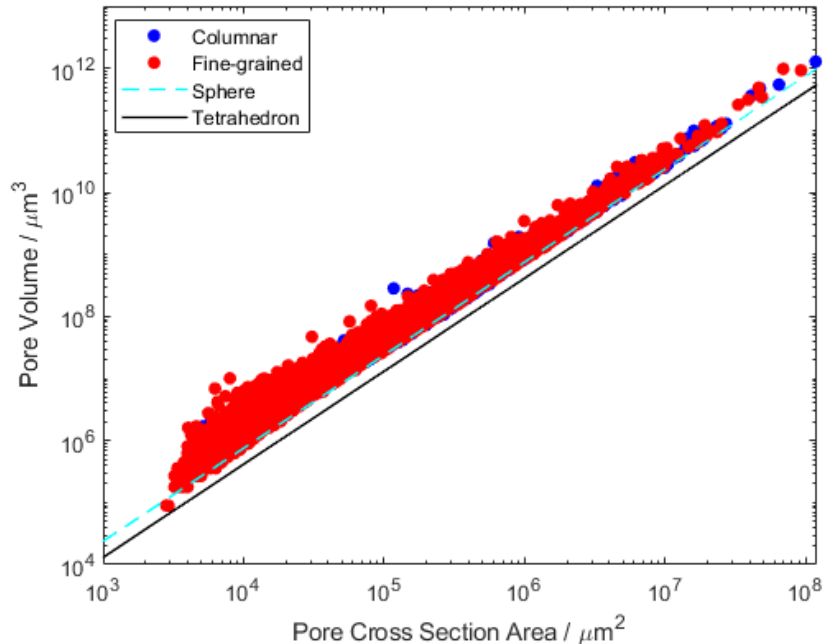


Figure 3-11. The correlation between the pore area and pore volume columnar (blue) and fine-grained (red) samples.

Gaining a deeper understanding of the nature of pore space connectivity requires quantifying the correlation between the key pore geometry characteristics determined by pore network modeling. The relationships between important factors related to pores and throats are shown in Figure 3-12-a and b: coordination number versus pore radius and c and d: throat length versus throat radius. To plot graphs b and d, the pore and throat radius data from each sample were separated into  $500 \mu\text{m}$  intervals. The intermediate amounts of the intervals were shown, and the standard deviation of each range was plotted as the error bar. According to Figure 3-12-a and b, the pore radius and coordination number have an almost positive relation for fine-grained sample, meaning that larger pores often connect to more throats, however, for columnar sample, this relation was weaker. Which means that different slopes can be observed for the two facies, in the fine-grained sample as pore radius rise, the rise in coordination number is more considerable, while in the columnar sample, larger pores are less connected. Figure 3-12-c and d reveal a more evident correlation between throat length and radius in both facies and depicts a significantly smaller variability in throat radius compared with variation in throat length. In comparison to the columnar sample, there are few throats in the fine-grained sample that are longer and wider.

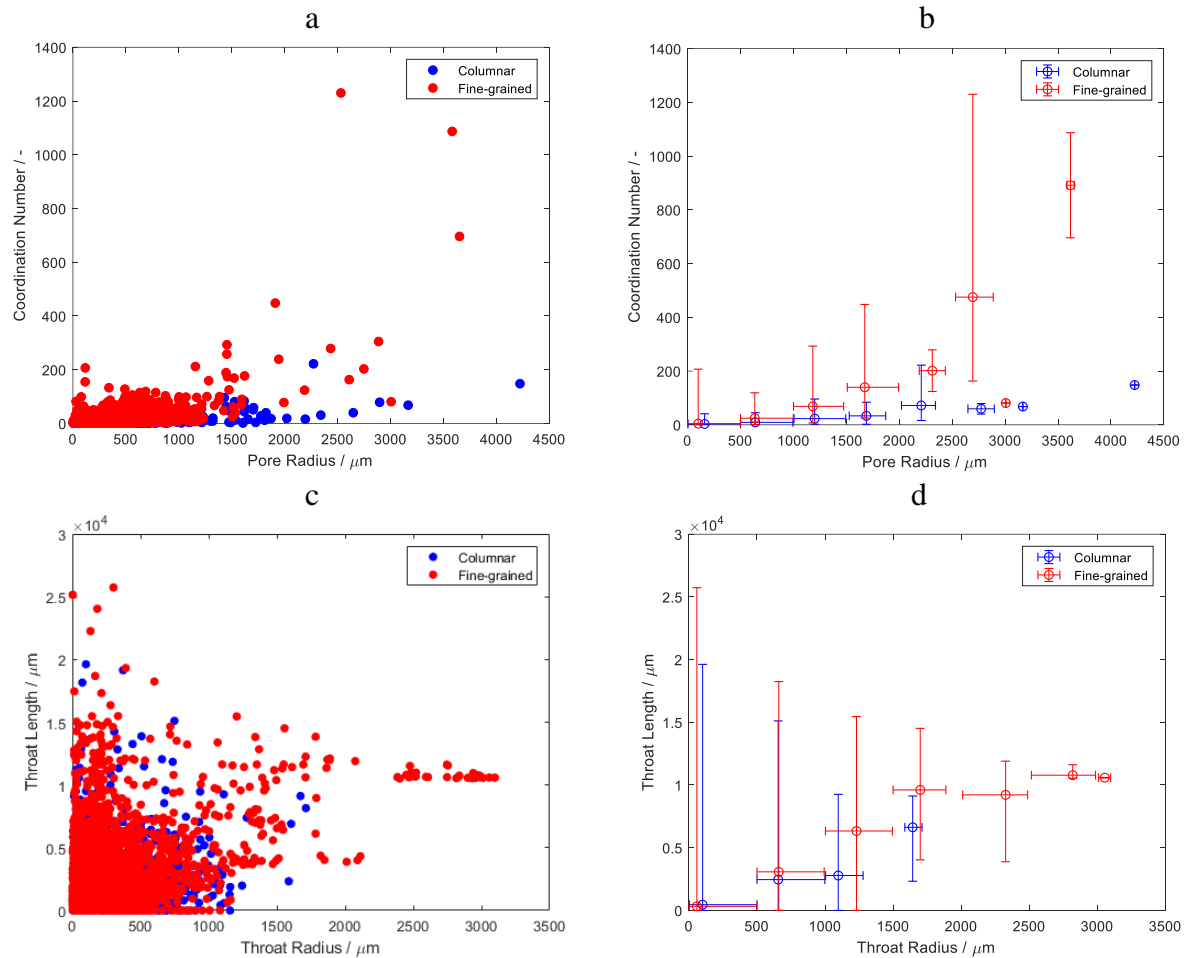


Figure 3-12. The relationship between: a and b) coordination number and pore radius, c and d) throat length and throat radius: in columnar (blue) and fine-grained (red) samples.

The variabilities of pore radius, throat radius, and throat length expressed through their respective coefficients of variation are additional pore geometry features that can be used to describe the PNM. The coefficient of variation is a unitless parameter that can be used as an all-encompassing description of pore geometry despite changes in porosity and mineral composition (Bernabé et al., 2010; Thomson et al., 2018). These results are listed in Table 3-6. The coefficient of variation greater than 1, indicates an unusually high standard deviation of the parameters, which is in good agreement with the high heterogeneity of our sample.

The porosity value for each 2D slice was calculated using the obtained medical CT images from dry and wet flooding experiments and porosity curves were generated over the length of the samples. The curves are shown in Figure 2-10 with the means of 0.524, 0.298, and 0.243 for  $F1 - 1$ ,  $F2 - 5$ , and  $F2 - 6$  plugs, with a higher profile for the columnar sample that reveals the

existence of large-scale void spaces in this sample. Each of three profiles exhibits diverse porosities that differ in magnitude throughout the lengths, with the porosity varies between 0.45 and 0.61, from 0.23 and 0.42, and from 0.16 and 0.33 for  $F1 - 1$ ,  $F2 - 5$ , and  $F2 - 6$  plugs. In the case of the columnar sample, the porosity attained its highest point around the center of the sample. However, for fine-grained plugs, the highest porosity peaks are located at the ends of the plugs.

Table 3-6. Coefficient of variation for pore radius, throat radius, and throat length for both facies sample.

Facies Plug	Fine-grained $F2 - 6$	Columnar $F1 - 1$
$\sigma_r / \langle r \rangle$ Pore	0.8369	0.8555
$\sigma_r / \langle r \rangle$ Throat	1.1897	0.9491
$\sigma_l / \langle l \rangle$ Throat	1.8045	1.7470

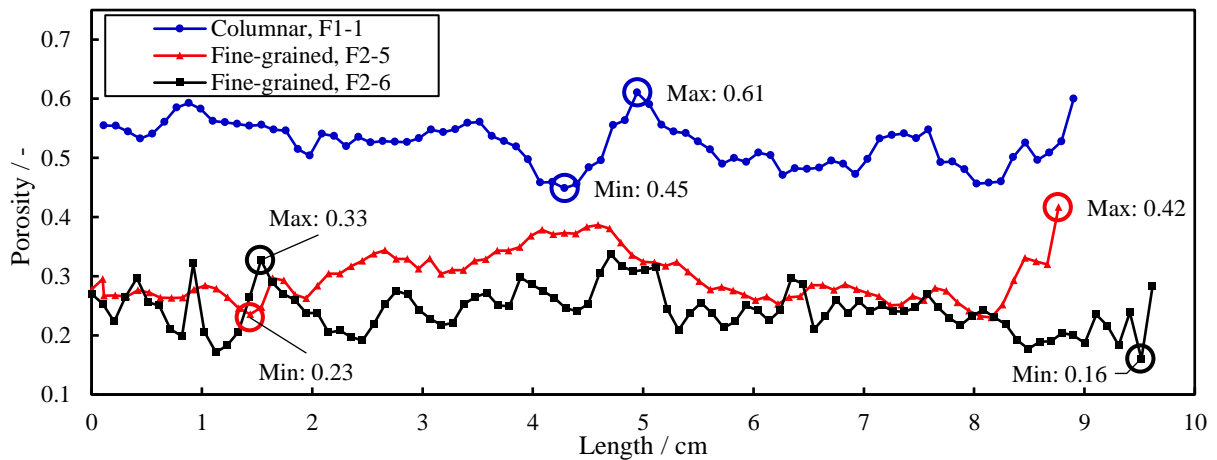


Figure 3-13. Porosity distribution for the samples.

Figure 3-14 displayed the 3D visualization model of the porous system for three samples. Blue segmentations show connected pores and gray segmentations show disconnected pores. In these models white (background color) segmentations indicate grains. The disconnected pores (gray segmentation) are more dominant in the columnar sample. There is a high number of disconnected pores and dead-end pores in too many areas of the samples that would probably block the flow in that direction and cause non-continuity in flow patterns. Since fluid flow patterns in these 3D models were not easy to observe (red lines), the upcoming 3D flow patterns (next figures) were displayed in a 2D plane of the porous system for better visualization and analysis, which means that flow patterns were generated and displayed for all the pores in the 3D model, while the connected pore system (only blue segmentations) of one longitudinal cross-section of the plugs was displayed as a background.

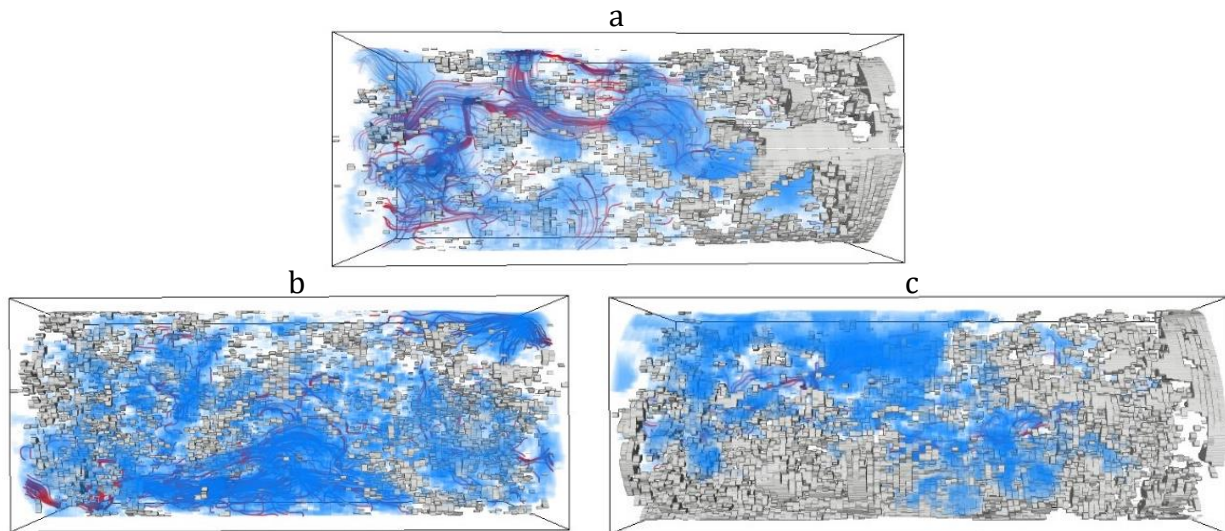


Figure 3-14. Porous system for a)  $F1$  – 1 columnar plug, b)  $F$  – 5 fine-grained plug, c)  $F2$  – 6 fine-grained plug.

### 3.3.2 SINGLE-PHASE STUDIES

The first step of the single-phase studies was the injection of the DW at  $0.1 \text{ ml/min}$  injection rate as a tracer into the plug saturated with FW in conjunction with CT scanning. The process was followed by the injection of FW at a constant injection rate of  $0.5 \text{ ml/min}$  and the conduction of CT scanning during the flooding. To generate flow patterns, the CT image files were processed, and the signals were split into two parts to separate fluids and show the flowlines of displaced and displacing fluid during injection processes.

The flow lines of DW (yellow lines) during displacement of FW by DW in the porous medium for the three samples are indicated in Figure 3-15. As mentioned before, the blue parts in these images indicate connected pores of one longitudinal cross-section of the plugs.

In the case of the columnar sample, flow lines are distributed in only some parts of the sample (Figure 3-15-a) and the upper left side of the plug is practically lacks flow patterns. It implies that the heterogeneity and disconnected/dead-end pores significantly affect the flow patterns. However, there is a more homogenous distribution of flow lines and better dispersion of the fluid along the samples for fine-grained plugs (Figure 3-15-b and c) during this miscible process, indicating higher sweep efficiency.

To obtain further in-depth information on the single-phase studies, after injection of DW the process was followed by the injection of FW with rate of  $0.5 \text{ ml/min}$  coupled with CT scanning to

see the effect of the high rate on the flow patterns. The flow lines of FW (red lines) during this miscible displacement for the three samples are shown in Figure 3-16.

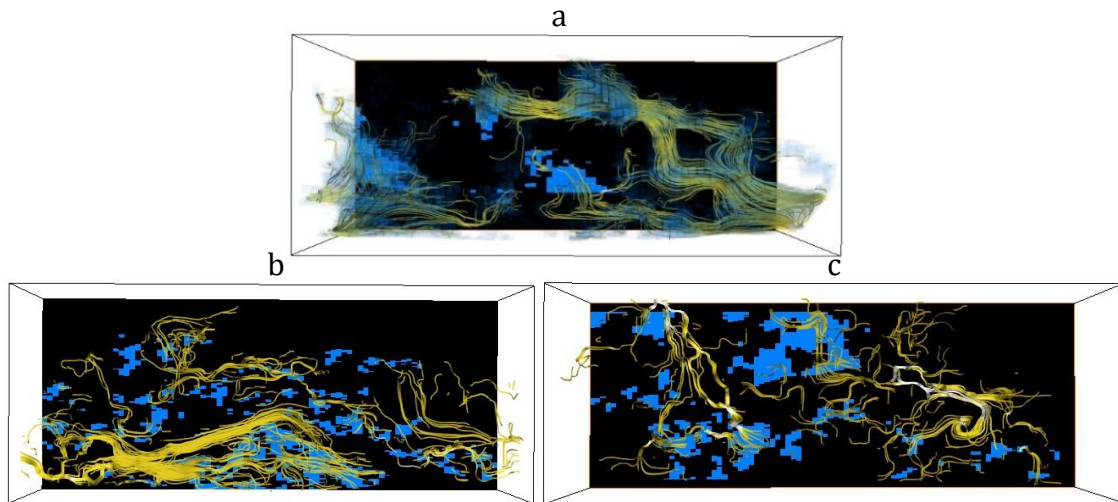


Figure 3-15. Flow lines of DW (yellow lines) during flooding of DW and displacement of FW for a)  $F1 - 1$  columnar plug, b)  $F - 5$  fine-grained plug, c)  $F2 - 6$  fine-grained plug.

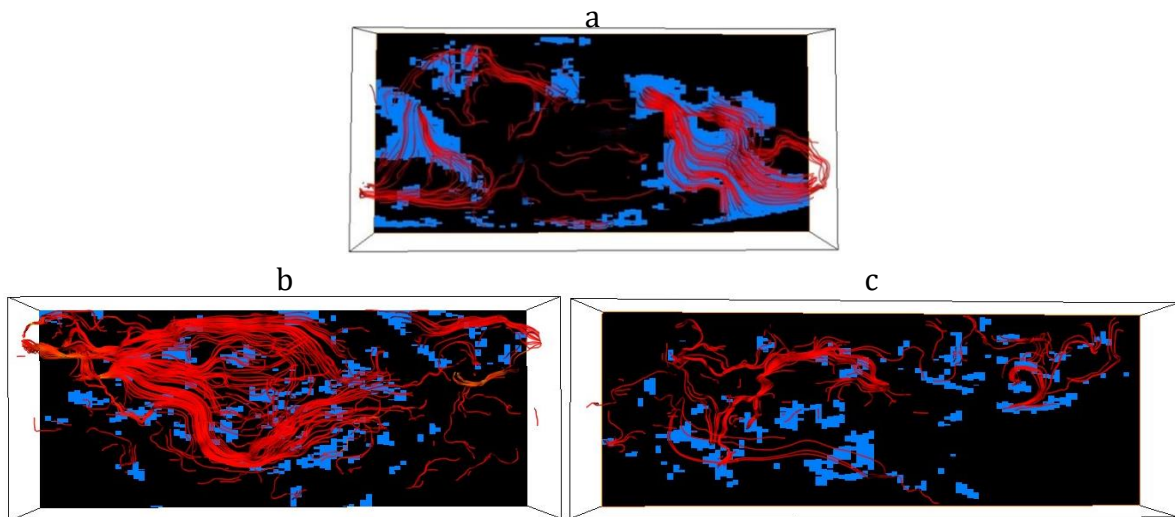


Figure 3-16. Flow lines of FW (red lines) during injection of FW and displacement of DW for a)  $F1 - 1$  columnar plug, b)  $F - 5$  fine-grained plug, c)  $F2 - 6$  fine-grained plug.

By analyzing the flow lines of FW in Figure 3-16-a again we can see the poor distribution of flow lines in the columnar sample, indicating unswept areas. During this high-rate miscible fluid transportation,  $F2 - 5$  revealed significantly better fluid dispersion in comparison with  $F2 - 6$  (Figure 3-16-b and c), which has a good agreement with the high amount of connected pore and their homogenous distribution in this sample (blue parts in Figure 3-14-b).

To conclude the single-phase step and prepare the sample for two-phase studies (preparation of fully FW-saturated plug), the injection rate for FW decreased to  $0.1 \text{ ml/min}$  until the total removal of the DW and then FW was injected at different flow rates to validate the application of the Darcy law. Figure 3-17 displays the example of the result of experiments for analyzing flow regimes in a vugular and a fine-grained plug. For all three samples, the dominant flow regime was Darcy and no deviation from the straight line was observed in the plot of differential pressure over length versus velocity (Figure 3-18).

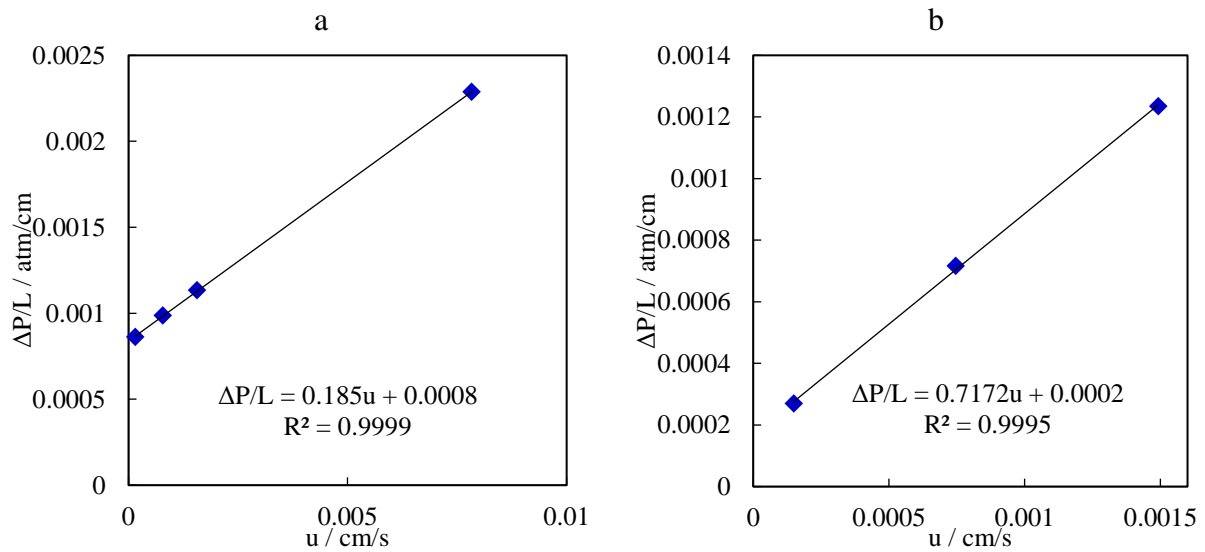


Figure 3-17. Analyzing flow regimes for a) F1 – 1 columnar plug, b) F2 – 6 fine-grained plug.

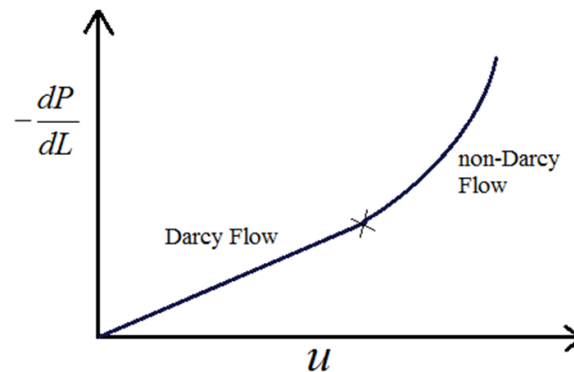


Figure 3-18. Analyzing flow regimes graph.

### 3.3.3 TWO-PHASE STUDIES

#### 3.3.3.1 OIL INJECTION (OIL DRAINAGE)

In this step, the oil was injected (to achieve initial water saturation) at the rate of  $0.1 \text{ ml/min}$  into the samples in order to gain a clearer comprehension of the immiscible process and two-phase flow.

Again, flow lines for this injection process were generated by processing the CT image data. Like the previous section the flow paths and the behavior of fluid during transportation were analyzed. The flow lines of oil (displacing fluid: yellow lines) during displacement of FW in the porous system for the three samples are displayed in Figure 3-19.

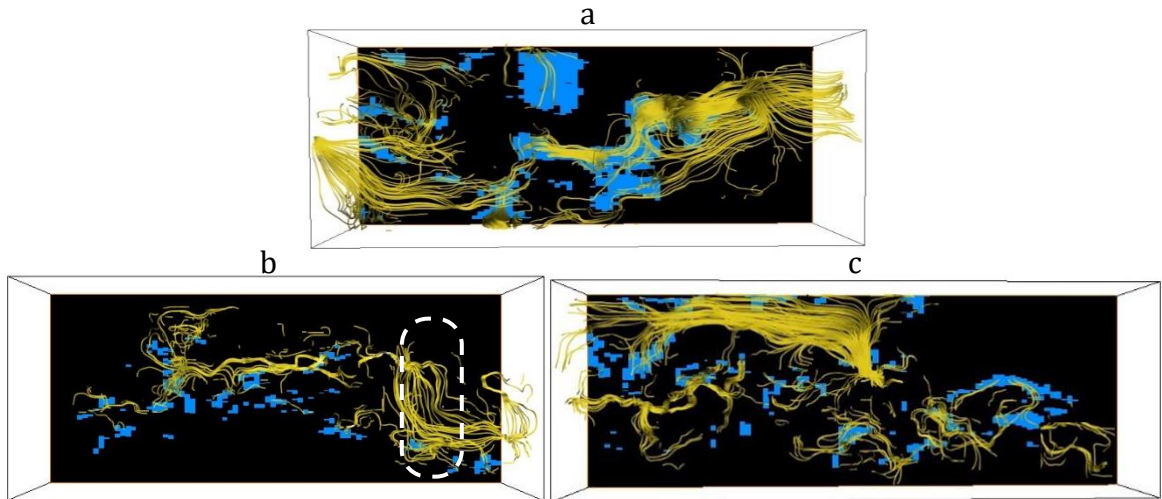


Figure 3-19. Flow lines of oil (yellow lines) during flooding of oil and displacement of FW for a) *F1* – 1 columnar plug, b) *F* – 5 fine-grained plug (white elliptic displays the area with an increase in the number of oil flow lines), c) *F2* – 6 fine-grained plug.

The oil flow pattern for all samples revealed a preferential displacement and mainly swept FW in some regions of plugs and bypassed it in other parts. The oil flooding yielded a relatively heterogeneous reduction of FW saturation, which can be seen from the number of flow lines in different regions of plugs. There are some spaces without any flow lines, indicating that oil was not imbibed into those FW-saturated parts of the porous network, however, in other parts, we can see many oil flow lines that cover most of the pore system.

By analyzing the production data including the amounts of produced oil and water volumes during tests, the same results representing bypassing of FW in the plug were observed. For the columnar sample, the total amount of produced water during oil flooding was approximately  $32 \text{ cm}^3$  (the pore volume was  $49.70 \text{ cm}^3$ ) representing the connate water saturation of 0.356. Table 3-7 (oil drainage columns) provides the results for the three samples.

Although the number of flow lines is more considerable in the columnar sample compared to the fine-grained samples, it resulted in lower level of initial oil saturation at the final step of the oil flooding process (Table 3-7). This could be due to the large pore volume (around  $50 \text{ cm}^3$ ) of this

sample given the existence of large pores, which cause more streamlines of fluid in this process, but still, there are areas that remained untouched during this flooding process.

Table 3-7. The outcomes of core flooding experiments conducted on three plugs.

Facies	Plug	$PV, cm^3$	Oil Drainage			FW	SW
			$OOIP, cm^3$	$S_{wc}$ , fraction	$S_{oi}$ , fraction	Imbibition	Imbibition
						$S_{or}$ , fraction	$S_{or}$ , fraction
Fine-grained	$F2 - 5$	29.76	21.0	0.294	0.706	0.487	0.487
	$F2 - 6$	26.26	21.0	0.200	0.800	0.571	0.571
Columnar	$F1 - 1$	49.70	32.0	0.356	0.644	0.422	0.392

**Description:**  $PV$  refers the Pore Volume,  $OOIP$  stands for Oil Original in Place,  $S_{wc}$  represents the connate water saturation,  $S_{oi}$  represents the Initial oil saturation, and  $S_{or}$  refers to the residual oil saturation.

Throughout both oil and FW injection experiments (next section), the alterations in the level of oil saturation in the plugs were regularly monitored and analyzed over time by utilizing medical CT imaging throughout the tests (Equation (3-2)). The correlations between amount of oil injection and oil saturation values versus length for the columnar and one fine-grained plug are shown in Figure 3-20. The two oil saturation curves in the graphs correspond to the initial and the final steps of oil flooding experiments. According to Figure 3-20, the following observations can be made:

- All curves clearly show variability in oil saturation value over the length. In case of the columnar sample, the saturation varies between 0.02 and 0.25 at initial step of oil flooding, and between 0.52 and 0.97 at the final step of flooding. In case of the fine-grained sample, the values ranged from 0.002 to 0.22, and from 0.49 to 1 at two stages of flooding.
- As the oil saturation level increased, the spatial differences in the oil saturation values became increasingly noticeable.
- Oil breakthrough was observed shortly after the beginning of injection and the level of oil saturation in both samples reached around 0.1 in the final layer (end of plugs) after 0.2  $PV$  oil injection.
- Featuring the lowest point at around midpoint of the core length, the oil saturation curves (for the two steps of the experiments) of the columnar sample displayed a strong correlation with the average porosity curve (Figure 3-13). This can also be observed by the reduced number of flow lines in the middle of the sample (Figure 3-19-a).
- For the fine-grained sample, at the end of the injection, a peak with oil saturation of one was observed at around one-third of the end of the plug; at the same area we can see an increase in the number of oil flow lines (marked white area in Figure 3-19-b).

- For both samples, compared to the initial oil saturation profile (0.2 PV oil-injected), a shift in the shape of the profiles (believed to be caused by the selection of different preferential paths during the flow transfer) was noted at the end of the drainage experiment (2 PV oil-injected). However, this change is more considerable for the fine-grained sample.
- Mean oil saturation at the final step of oil flooding, 0.71 for the *F1* – 1 columnar sample and 0.68 for the *F2* – 5 fine-grained plug, represents initial oil saturation (equivalent to 0.29 and 0.32 connate water saturation). By analyzing the data of core flooding tests, the same results were calculated ( $S_{wc}$  and  $S_{oi}$  in Table 3-7) and show acceptable concurrence with the saturation information acquired from CT measurements.

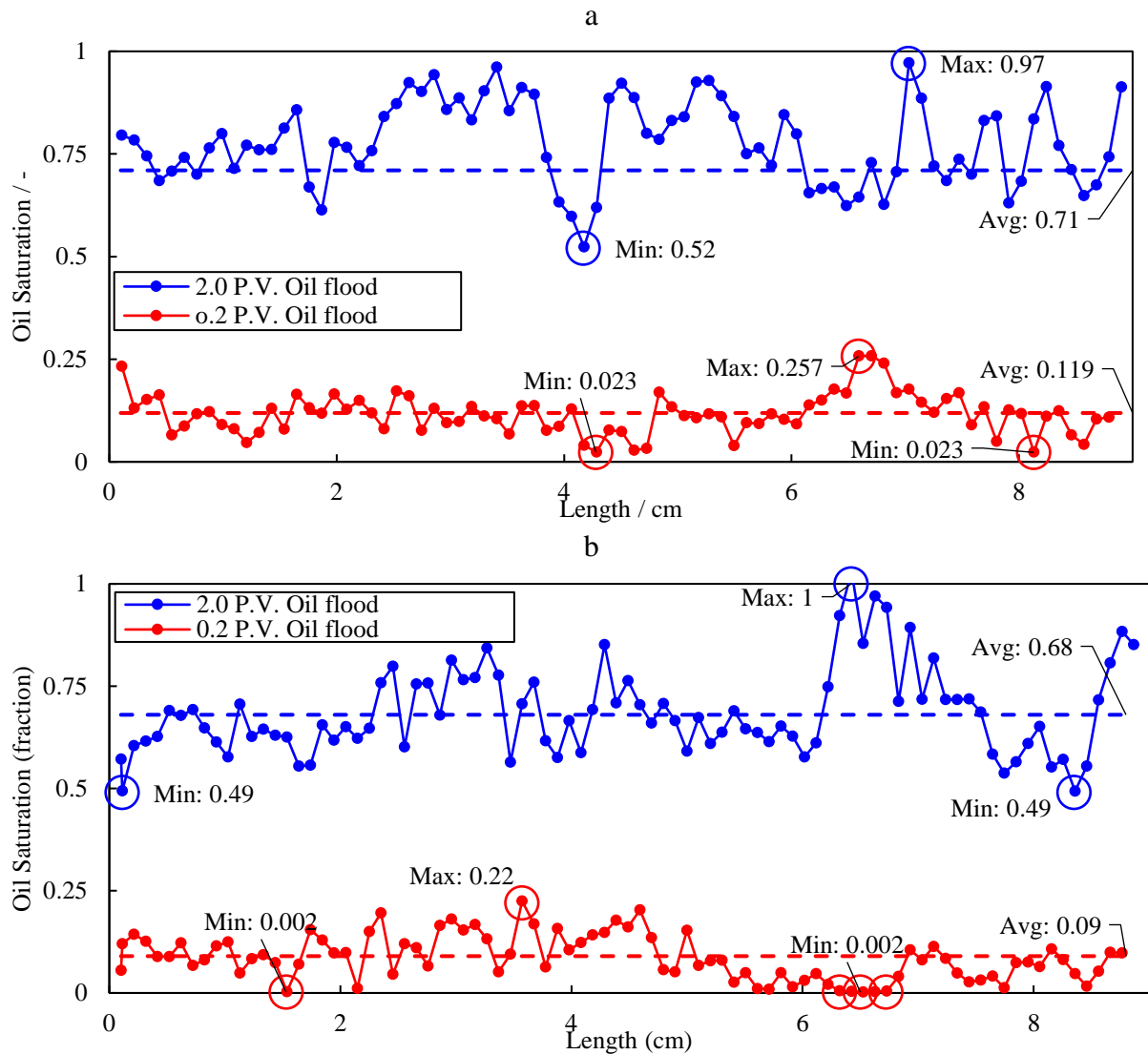


Figure 3-20. Saturation curves for oil drainage stage for a) *F1* – 1 columnar plug, b) *F2* – 5 fine-grained plug.

### 3.3.3.2 FW INJECTION (WATER IMBIBITION)

After the oil injection and reaching initial water saturation, FW was injected at flow rate of 0.1 *ml/min* in conjunction with CT imaging to investigate the process of oil production and to derive flow lines and saturation map for this two-phase immiscible process. Like the previous sections the flow paths and the behavior of fluid during transportation were analyzed. The flow lines of oil (displaced fluid: yellow lines) during displacement of oil (FW imbibition) in the porous system for the three samples are displayed in Figure 3-21.

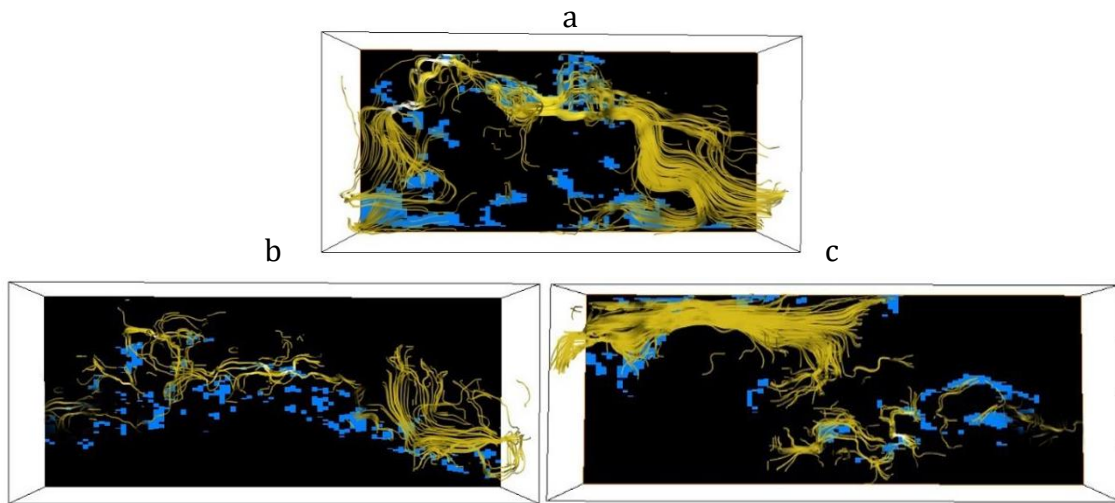


Figure 3-21. Flow lines of oil (yellow lines) during injection of FW and displacement of oil for a) *F1* – 1 columnar plug, b) *F* – 5 fine-grained plug, c) *F2* – 6 fine-grained plug.

For the three samples, the oil flow patterns showed preferential displacement, particularly sweeping oil in some parts and bypassing it in others. The number of flow lines in various plug locations indicates that the FW flooding resulted in a rather diverse drop in oil saturation. While there are many spaces without any particular flow lines, we can see a significant number of oil flow lines that cover nearly the whole region of the pore system in other parts, indicating that FW was imbibed better into those parts of the porous network. This indicates that we were unable to produce a significant portion of the oil due to the heterogeneity in the plugs. Core flooding results for this step showed 0.42, 0.49, and 0.571 residual oil saturation after FW injection for the *F1* – 1, *F2* – 5, and *F2* – 6 plugs (Table 3-7).

The samples were CT-scanned periodically throughout the FW injection test to track the oil saturation level within the plugs and the resulted saturation curves are displayed in Figure 3-22 for

the columnar and a fine-grained sample. The two oil saturation curves in these plots correspond to the initial and the final steps of FW flooding experiments.

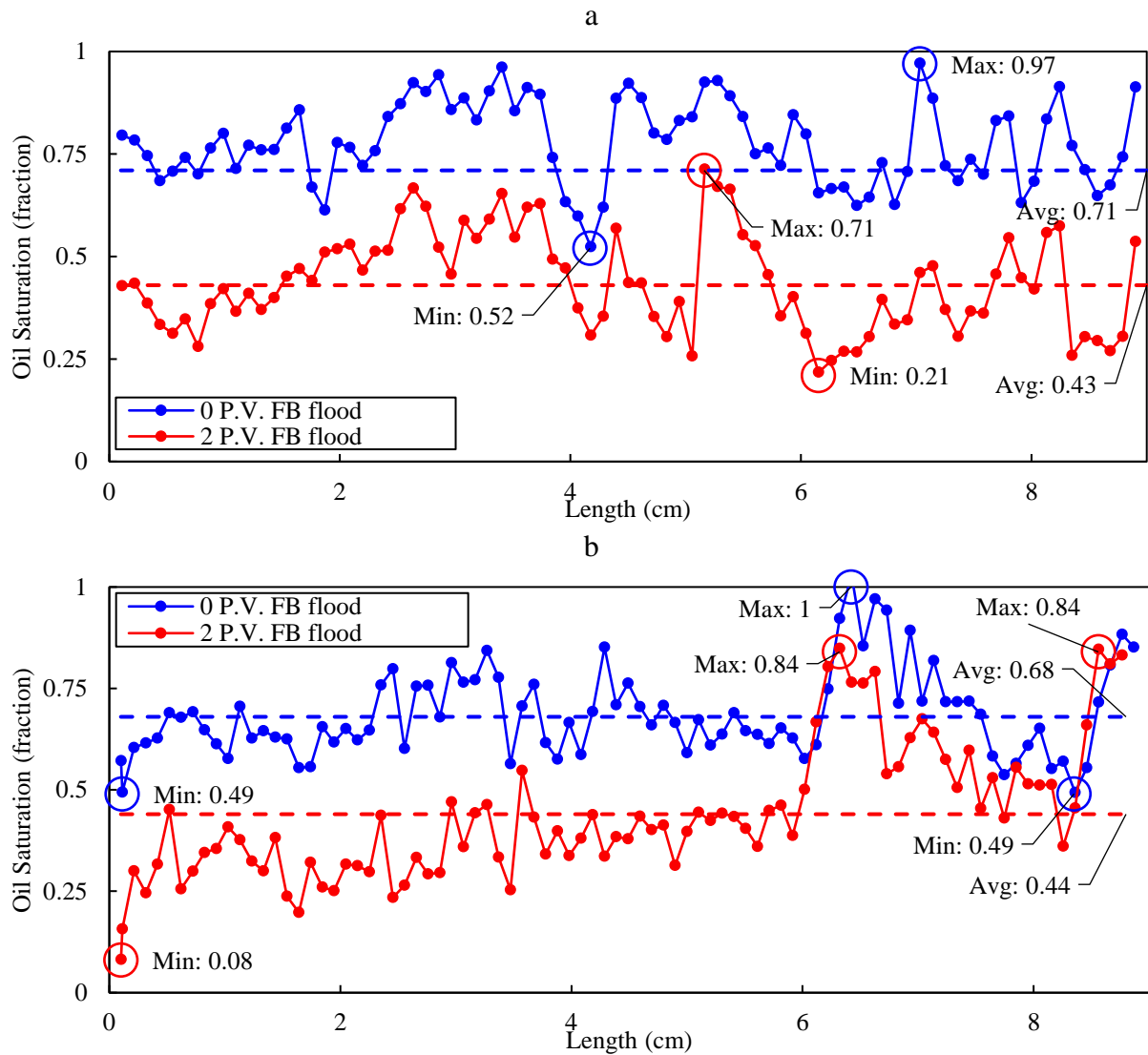


Figure 3-22. Saturation curves for FW imbibition stage for a) *F1* – 1 columnar plug, b) *F2* – 5 fine-grained plug.

The following findings can be drawn from Figure 3-22:

- The change in oil saturation level over the length is seen for both samples. During the final stage of the FW flooding, the oil saturation levels for the columnar sample were between 0.21 to 0.71. On the other hand, the curve for the fine-grained sample revealed more heterogeneity, which varied between 0.08 and 0.84.
- The variations between the two curves exhibit the quantity of oil production. It indicates that oil production was more noticeable from the portion of the plug that the differences between

the two lines increased (for example, at the beginning and end of the plug length for the columnar sample).

- Based on the differences between the two curves in the columnar sample, a high quantity of oil was left behind at around 2, 4.5, 5.5, and 8 *cm* of length; these points also have lower level of porosity.
- As it was observed in the oil injection saturation results, the correlation among the saturation and the porosity curves was again evident.
- In case of fine-grained sample, the oil saturation was decreased further on the upstream side than on the downstream side, and less variation was observed during FW flooding compared to oil flooding.
- In the last third of the fine-grained sample, it was observed that at some points the oil saturation at the final step of the process (2 *PV* FW Inj) was more than at the initial step (0 *PV* FW Inj), it appears that oil has been pushed out from upstream areas and stacked here. The same results can be assessed in Figure 3-21-b where the increasing number of flow lines in downstream of the plug can reveal oil accumulation.
- Compared to the initial oil saturation values (0 *PV* FW Inj), a shift in the shape of the oil saturation profile (2 *PV* FW Inj) was more noticeable for the fine-grained sample.
- In case of the columnar sample, the oil flow lines during oil drainage (Figure 3-19) and FW imbibition (Figure 3-21) are distinct from one another and oil had selected various routes throughout these processes.
- Mean oil saturation at the end of FW injection (0.43 and 0.44 for the columnar and fine-grained sample, respectively), representing residual oil saturation of this process, have a respectable concurrence with the saturation data obtained from core flooding results (FW imbibition  $S_{or}$  in Table 3-7).

To conclude the two-phase step, SW was injected at a rate of 0.1 *ml/min* into plug samples, Figure 3-23 indicates recovery factor for FW flooding and after switching to SW injection. For fine-grained plugs, the recovery remained practically unchanged with further SW injection. For the columnar sample, the enhancement in oil recovery (extra 4.7 %) during this lower salinity water injection (SW) is believed to be caused by the osmosis mechanism, osmotic water transportation to large dead-end pores and mobilization of oil.

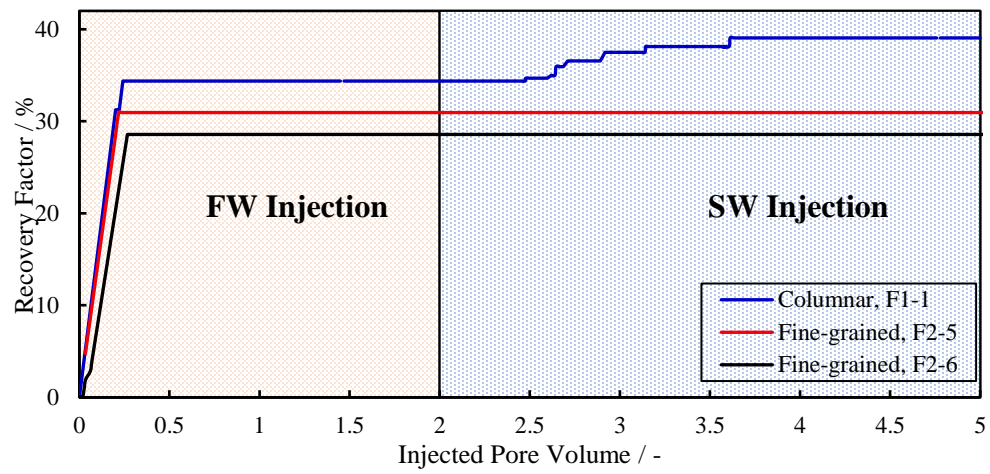


Figure 3-23. The results of oil recovery factor for FW and SW flooding.

### 3.4 CONCLUSION

The primary objective of this investigation was to evaluate the impact of pore geometry, network characteristics, and heterogeneity on fluid flow through complex porous media. To achieve this goal, three plugs were extracted from two distinct facies, namely fine-grained and vugular, which were identified based on the geological examination of the Lagoa Salgada outcrop samples.

For the determination of the structure and geometry of the porous system, PNM was employed for the microCT images of samples from both facies to measure the connection between the features of the porous system, such as the radius of pore and throat, throat length, coordination number, shape factor, and the volume of pores. The median coordination number in samples from both facies was 3. Compared to the fine-grained sample, the less dense pore network of the columnar sample was typically comprised of larger pores, wider and longer throats, but with a weaker connection of throats to pores (fine-grained: pores radius  $\sim 86 \mu m$  and throats radius  $\sim 43 \mu m$ , and columnar: pores radius  $\sim 142 \mu m$  and throats radius  $\sim 80 \mu m$ ). For the fine-grained sample, the pore radius and coordination number showed an almost positive relation, meaning that pores with a greater size often linked to more channels, while in the columnar sample, larger pores were less connected. Both facies depicted significantly less variation in throat radius compared with throat length.

Medical CT imaging was employed in conjunction with core flooding experiments to provide a comprehensive characterization of the porous system, single-phase and two-phase flow patterns, and concentration profiles. Single-phase flow patterns suggested that the heterogeneity and disconnected/dead-end pores greatly affect the flow patterns and there was a more homogenous distribution of flow lines and better fluid dispersion along the samples with better pore network connectivity (fine-grained sample).

Two-phase flow patterns (both drainage and imbibition) for all samples revealed a preferential and heterogeneous displacement that mainly swept displaced fluid in some regions of plugs and bypassed it in other parts. There were some pore spaces without any specific flow lines, while in other areas, there was a sizable number of flow lines that completely covered the pore system, which indicates that displacing fluid was more effectively imbibed into those parts of the porous network. The CT data enabled the identification of oil saturation levels throughout the flooding stages, exhibiting diverse and non-homogenous values. The mean connate water and residual oil

saturations ascertained from CT data at the final step of the oil and water flooding process, exhibited a satisfactory concurrence with the saturation values derived from the amount of produced oil and brine. The heterogeneity of the sample significantly affects the flow patterns and saturation, and the correlation among the saturation and porosity distributions, and the number of fluid flow patterns for the samples was evident. An alteration in the shape of the saturation curves was observed during the oil and water flooding, resulting from the selection of diverse pathways over time. This change was more prominent in the fine-grained sample.

Only for the columnar plug sample, the enhancement in oil recovery after shifting to lower salinity water injection (SW) was observed according to the osmosis mechanism, while for the fine-grained samples, the recovery remained practically unchanged with further SW injection.

Overall, the results of this study emphasize the importance of understanding the heterogeneity and pore size distribution of porous media for predicting fluid propagation and fluid saturation in subsurface systems. These findings have implications for a wide range of applications, including oil and gas recovery, carbon capture and storage, and groundwater management.

### **3.5 ACKNOWLEDGEMENTS**

We gratefully acknowledge the support of EPIC – Energy Production Innovation Center, hosted by the University of Campinas (UNICAMP) and sponsored by FAPESP – São Paulo Research Foundation (2017/15736-3 process). We acknowledge the support and funding from Equinor Brazil and the support of ANP (Brazil's National Oil, Natural Gas and Biofuels Agency) through the R&D levy regulation. Acknowledgments are extended to the Center of Energy and Petroleum Studies (CEPETRO) and the School of Mechanical Engineering (FEM). We also thank PerGeos Software for licenses and technical support.

### 3.6 REFERENCES

- Abedi, B., Castaño, E.P.M., Heidaryan, E., Shadloo, M.S., 2020. Pore-Scale Visualization on Polymer Flooding: Application of Singular Value Decomposition-Based Image Analysis Method. *Journal of Porous Media* 23.
- Al-Kharusi, A.S., Blunt, M.J., 2007. Network extraction from sandstone and carbonate pore space images. *Journal of petroleum science and engineering* 56, 219-231.
- Anbari, A., Chien, H.T., Datta, S.S., Deng, W., Weitz, D.A., Fan, J., 2018. Microfluidic model porous media: Fabrication and applications. *Small* 14, 1703575.
- ASTM-D664, 2011. Standard test method for acid number of petroleum products by potentiometric titration-ASTM D 664-11A. ASTM International, West Conshohocken, PA.
- ASTM-D1298-12b, 2017. Standard test method for density, relative density, or API gravity of crude petroleum and liquid petroleum products by hydrometer method. ASTM International West Conshohocken, PA, USA.
- ASTM-D1744, 1992. Standard Test Method for Determination of Water in Liquid Petroleum Products by Karl Fischer Reagent. *Annual Book of Standards*.
- ASTM-D2503-92, 1992. Standard Test Method for Relative Molecular Mass (Molecular Weight) of Hydrocarbons by Thermoelectric Measurement of Vapor Pressure. *Annual Book of Standards*.
- ASTM-D6560-12, S., 2012. Standard Test Method for Determination of Asphaltenes (Heptane Insolubles) in Crude Petroleum and Petroleum Products.
- ASTM-D7042, 2014. Standard test method for dynamic viscosity and density of liquids by stabinger viscometer (and the calculation of kinematic viscosity). ASTM International.
- Bernabé, Y., Li, M., Mainault, A., 2010. Permeability and pore connectivity: a new model based on network simulations. *Journal of Geophysical Research: Solid Earth* 115.
- Bruhn, C.H., Pinto, A.C., Johann, P.R., Branco, C., Salomão, M.C., Freire, E.B., 2017. Campos and Santos basins: 40 Years of reservoir characterization and management of shallow-to ultra-deep water, post-and pre-salt reservoirs-Historical overview and future challenges, OTC Brasil. OnePetro.
- Claes, H., Erthal, M.M., Soete, J., Özkul, M., Swennen, R., 2017. Shrub and pore type classification: Petrography of travertine shrubs from the Ballık-Belevi area (Denizli, SW Turkey). *Quaternary International* 437, 147-163.
- Doyen, P.M., 1988. Permeability, conductivity, and pore geometry of sandstone. *Journal of Geophysical Research: Solid Earth* 93, 7729-7740.
- Fetter, C.W., 2018. Applied hydrogeology. Waveland Press.
- Gunde, A.C., Bera, B., Mitra, S.K., 2010. Investigation of water and CO<sub>2</sub> (carbon dioxide) flooding using micro-CT (micro-computed tomography) images of Berea sandstone core using finite element simulations. *Energy* 35, 5209-5216.
- Helland, J., Ryazanov, A., Van Dijke, M.I.J., 2008. Characterization of pore shapes for pore network models, *Proceedings of the 11th European Conference on the Mathematics of Oil Recovery (ECMOR XI)*, Bergen, Norway, pp. 8-11.
- Hendry, J., Burgess, P., Hunt, D., Janson, X., Zampetti, V., 2021. Seismic characterization of carbonate platforms and reservoirs: an introduction and review. Geological Society, London, *Special Publications* 509, 1-28.
- Hounsfield, G.N., 1973. Computerized transverse axial scanning (tomography): Part 1. Description of system. *The British journal of radiology* 46, 1016-1022.

- Iassonov, P., Gebrenegus, T., Tuller, M., 2009. Segmentation of X-ray computed tomography images of porous materials: A crucial step for characterization and quantitative analysis of pore structures. *Water resources research* 45.
- Iraji, B., Shadizadeh, S.R., Riazi, M., 2015. Experimental investigation of CO<sub>2</sub> huff and puff in a matrix-fracture system. *Fuel* 158, 105-112.
- Iraji, S., Ayatollahi, S., 2019. Experimental investigation on asphaltene biodegradability using microorganism: cell surface properties' approach. *Journal of Petroleum Exploration and Production Technology* 9, 1413-1422.
- Iraji, S., Soltanmohammadi, R., De Almeida, T.R., Munoz, E.R., Basso, M., Vidal, A.C., 2022a. Laboratory and numerical examination of oil recovery in Brazilian Pre-salt analogues based on CT images, Third EAGE Conference on Pre Salt Reservoirs.
- Iraji, S., Soltanmohammadi, R., Munoz, E.R., Basso, M., Vidal, A.C., 2023. Core scale investigation of fluid flow in the heterogeneous porous media based on X-ray computed tomography images: Upscaling and history matching approaches. *Geoenergy Science and Engineering*, 211716.
- Iraji, S., Soltanmohammadi, R., Munoz, E.R., Winter, A., de Almeida, R.V., Vidal, A.C., 2022b. Experimental Investigation of Waterflooding Performance by Increasing Copper Ions in Brazilian Pre-Salt Rock, 83rd EAGE Annual Conference & Exhibition. European Association of Geoscientists & Engineers, pp. 1-5.
- Iraji, S., Soltanmohammadi, R., De Almeida, T Rodrigues, Munoz, E.R., Vidal, A.C., 2022c. Experimental investigation of single-phase flow pattern in highly heterogeneous carbonates rocks, Rio Oil & Gas 2022. IBP, Rio de Janeiro | Brasil.
- Jensen, J., Lake, L.W., Corbett, P.W., Goggin, D., 2000. *Statistics for petroleum engineers and geoscientists*. Gulf Professional Publishing.
- Knackstedt, M., Carnerup, A., Golab, A., Sok, R., Young, B., Riepe, L., 2013. Petrophysical characterization of unconventional reservoir core at multiple scales. *Petrophysics* 54, 216–223.
- Lamas, L., Ruidiaz, E., Vidal, A., 2019. AUTOMATED METHODOLOGY FOR DETECTING BORDER IN CT-SCAN IMAGES OF NON-CIRCULAR ROCK SAMPLES. *Brazilian Journal of Petroleum and Gas* 13.
- Lucia, F., 1983. Petrophysical parameters estimated from visual descriptions of carbonate rocks: a field classification of carbonate pore space. *Journal of petroleum technology* 35, 629-637.
- Markussen, Ø., Dypvik, H., Hammer, E., Long, H., Hammer, Ø., 2019. 3D characterization of porosity and authigenic cementation in Triassic conglomerates/arenites in the Edvard Grieg field using 3D micro-CT imaging. *Marine and Petroleum Geology* 99, 265-281.
- Matula, M., 1969. *Engineering Geologic Investigations Of Rock Heterogeneity*, The 11th US Symposium on Rock Mechanics (USRMS). American Rock Mechanics Association.
- PerGeos, S., 2019. *Tutorials*. ThermoFisher Scientific.
- Raeni, A.Q., Blunt, M.J., Bijeljic, B., 2014. Direct simulations of two-phase flow on micro-CT images of porous media and upscaling of pore-scale forces. *Advances in water resources* 74, 116-126.
- Rahmat, A., Nasiri, H., Goodarzi, M., Heidaryan, E., 2020. Numerical investigation of anguilliform locomotion by the SPH method. *International Journal of Numerical Methods for Heat & Fluid Flow* 30, 328-346.
- Rezende, M.F., Tonietto, S.N., Pope, M.C., 2013. Three-dimensional pore connectivity evaluation in a Holocene and Jurassic microbialite buildup. *AAPG bulletin* 97, 2085-2101.

- Sen, S., Abioui, M., Ganguli, S.S., Elsheikh, A., Debnath, A., Benssaou, M., Abdelhady, A.A., 2021. Petrophysical heterogeneity of the early Cretaceous Alamein dolomite reservoir from North Razzak oil field, Egypt integrating well logs, core measurements, and machine learning approach. *Fuel* 306, 121698.
- Sharma, M., 2008. Stromatolites studies in India: An overview. *Journal of Palaeosciences* 57, 63-67.
- Soltanmohammadi, R., Iraj, S., De Almeida, T.R., Munoz, E.R., Fioravanti, A.R., Vidal, A.C., 2021. Insights into Multi-Phase Flow Pattern Characteristics and Petrophysical Properties in Heterogeneous Porous Media, Second EAGE Conference on Pre-Salt Reservoir. European Association of Geoscientists & Engineers, pp. 1-5.
- Soltanmohammadi, R., Iraj, S., De Almeida, T.R., Munoz, E.R., Vidal, A.C., 2022. Upscaling Challenges of Heterogeneous Carbonate Rocks: A Case Study of Brazilian Pre-Salt Analogous, Third EAGE Conference on Pre Salt Reservoirs.
- Su, H., Zhou, F., Zheng, A., Wang, L., Wang, C., Yu, F., Kang, L., Li, J., 2022. Heavy oil recovery by alkaline-cosolvent-polymer flood: a multiscale research using micromodels and computed tomography imaging. *SPE Journal* 27, 1480-1492.
- Thomson, P.-R., Aituar-Zhakupova, A., Hier-Majumder, S., 2018. Image segmentation and analysis of pore network geometry in two natural sandstones. *Frontiers in Earth Science* 6, 58.
- Thomson, P.-R., Jefferd, M., Clark, B.L., Chiarella, D., Mitchell, T.M., Hier-Majumder, S., 2020. Pore network analysis of brae formation sandstone, North Sea. *Marine and Petroleum Geology* 122, 104614.
- Vik, B., Bastesen, E., Skauge, A., 2013. Evaluation of representative elementary volume for a vuggy carbonate rock—Part: Porosity, permeability, and dispersivity. *Journal of Petroleum Science and Engineering* 112, 36-47.
- von Barga, N., Waff, H.S., 1986. Permeabilities, interfacial areas and curvatures of partially molten systems: results of numerical computations of equilibrium microstructures. *Journal of Geophysical Research: Solid Earth* 91, 9261-9276.
- Wimert, J., Hier-Majumder, S., 2012. A three-dimensional microgeodynamic model of melt geometry in the Earth's deep interior. *Journal of Geophysical Research: Solid Earth* 117.
- Withers, P.J., Bouman, C., Carmignato, S., Cnudde, V., Grimaldi, D., Hagen, C.K., Maire, E., Manley, M., Du Plessis, A., Stock, S.R., 2021. X-ray computed tomography. *Nature Reviews Methods Primers* 1, 1-21.
- Wright, P., Tosca, N., 2016. A geochemical model for the formation of the pre-salt reservoirs, Santos Basin, Brazil: implications for understanding reservoir distribution. *AAPG Search and Discovery*, article 51304.

**4 APPLICATION OF UNSUPERVISED LEARNING AND DEEP LEARNING FOR ROCK TYPE CLASSIFICATION AND PETROPHYSICAL CHARACTERIZATION USING MULTI-SCALE DATA**

**Author: Shohreh Iraj**

**Co-Author: Gabriela Fernandes Matheus, Mateus Basso, Alexandre Campana Vidal**

**Campinas - SP**

**2023**

## ABSTRACT

Well log data, routine core analyses, microcomputed X-ray tomography ( $\mu CT$ ) images, and sedimentary petrography were integrated to accurately characterize and evaluate the carbonate reservoirs of the Barra Velha formation (Aptian) of the Santos Basin in Brazilian pre-salt. In these carbonate reservoirs, the porous system is extremely diverse and variable, making it challenging to establish rock typing with comparable petrophysical properties. Based on this integrated study, the reservoir sequences were characterized and a precise definition of four reservoir rock types (RRTs) was performed by integrating the petrophysical values of the plugs and their corresponding well log data of two cored wells using K-means unsupervised classification algorithm. The classification results were integrated with several conventional techniques to evaluate the quality and geological characteristics of the studied sequence by assessing different parameters such as flow and storage capacity, reservoir quality index, flow zone indicator, pore spaces interpretation, and average pore and throat radius. The study involved a detailed analysis of thin sections to identify various facies such as shubstones, reworked, and spherulitestone, and to classify different types of porosity such as interparticle, intraparticle, intercrystalline, vug, moldic, fracture, and growth framework porosity. Pore Network Modeling from  $\mu CT$  analysis of plugs was used specifically for the characterization of pores and throats of plug samples from each RRT. These data sets were utilized as supporting evidence to provide a more precise and comprehensive knowledge of reservoir quality. The study aimed to develop predictive models by implementing deep learning and machine learning algorithms trained on well log data to estimate plug porosity and rock type. Two deep learning models, ResNet and 1D CNN, were trained and evaluated for plug porosity prediction, with the 1D CNN model showing superior performance. Additionally, the XGBoost algorithm was applied to predict rock type, achieving high accuracy on both the training and validation datasets. The predicted results were compared with actual data to assess the effectiveness of the models and were then used to estimate plug permeability values. The results demonstrate the potential of deep learning and machine learning approaches in reservoir characterization and management, enabling the evaluation of subsurface reservoir properties even with incomplete datasets, which could lead to an improved understanding of the reservoir properties and better management of the reservoir. This integrated study provides deeper insight into the complex reservoir properties and can aid in improving decision-making processes and optimizing management and production strategies in the challenging pre-salt carbonate reservoirs or similar complex reservoirs.

Keywords: micro-computed tomography ( $\mu$ CT) images, K-means unsupervised classification algorithm, reservoir rock types (RRTs), Pore Network Modeling, deep learning algorithms, ResNet, 1D CNN, XGBoost algorithm

## 4.1 INTRODUCTION

The Exploration of the massive Pre-salt carbonate reservoirs located in the southeastern part of Brazil is known to be the cornerstone of South America's offshore petroleum industry. This discovery has firmly established Brazil among the leading offshore hydrocarbon producers (Bruhn et al., 2017; Soltanmohammadi et al., 2021; Irajil et al., 2022b).

Determining the spatial dispersion pattern of petrophysical characteristics in the carbonates of the sub-salt interval is challenging, since they are very varied and heterogeneous regarding grain arrangement, pore structure, and geological changes over time (Rezende and Pope, 2015; Wright and Barnett, 2015; Irajil et al., 2022c; Soltanmohammadi et al., 2022). The quality-reducing (e.g., cementation, silicification, compaction, neomorphism, authigenic minerals) and quality-enhancing (e.g., fracturing and dissolution) diagenetic processes fundamentally influence and control the petrophysical properties (Shehata et al., 2021). Rock type and flow unit determination could be used as diagnostic tools to discriminate and assess reservoir quality. Rock types can be accomplished by implementing different conventional methods of the effective pore radius  $R_{35}$  of Winland (Winland, 1972; Kolodzie, 1980), reservoir quality index ( $RQI$ ) and flow zone indicator ( $FZI$ ) plot (Amaefule et al., 1993; Bize Forest et al., 2019), discrete rock types ( $DRT$ ) technique (Shenawi et al., 2007; El Sawy et al., 2020), the global hydraulic elements ( $GHE$ ) system (Corbett and Potter, 2004; Hosa et al., 2020), and flow unit from SML plot (stratigraphic modified Lorenz) (Maglio-Johnson, 2001; Omeje et al., 2022). A recent study conducted in the Santos Basin of the Brazilian pre-salt reservoir examined the Barra Velha Formation using data from different wells. The study tested multiple rock-typing methods, including  $FZI$  and Winland  $R_{35}$ , for identifying flow units and successfully subdivided the formation into four distinct flow units (Rebelo et al., 2022).

Micro-computed tomography (microCT/ $\mu$ CT) and petrographic analysis could be used as supporting techniques to assess reservoir quality. The evaluation of the microCT images is important since they bring a direct internal structural visualization of the rock samples, which enables the characterization of distinct categories of pore structures, pore connectivity and also the calculation of void spaces (do Nascimento et al., 2015; Lima et al., 2020; Irajil et al., 2023). On the other hand, the petrographic analysis contributes to the characterization of pore types and

mineralogy, and assessment of depositional environments and diagenetic processes during basin formation (Iraji and Ayatollahi, 2019; Rubo et al., 2019; Belila et al., 2020).

The diverse characteristics of the Pre-salt carbonate reservoirs poses challenges in creating clear clustering of the samples based on conventional methods, resulting in uncertainties in defining rock types and reservoir descriptions. Therefore, a precise understanding of the appropriate cluster number and classification of rock types with distinct lithotypes, based on their characteristics is necessary. In this regard, the K-mean unsupervised learning technique was applied to categorize different rock types based on their petrophysical characteristics (well logs and plug data), with the number of clusters considered as a hyperparameter. The results were then used to integrate with the mentioned conventional techniques to assess reservoir quality.

Supervised learning and unsupervised learning are the two primary categories of machine learning. Supervised learning is a machine learning approach that uses labeled datasets (training sets) to instruct models and generate the intended response. A set of input data and their corresponding correct outputs are included in this training dataset, allowing the model to assess its accuracy through the loss function, learn over time, and adjust until reducing the error to an acceptable level. Unsupervised learning methods, on the other hand, such as the mentioned K-mean technique, do not employ labeled data to determine the pattern between inputs. There are two main categories of problems in supervised learning with two main tasks: classification and regression. In classification problems, machine learning algorithms are utilized to effectively categorize test data into discrete categories/classes (e.g., lithology, facies, rock types). While in regression problems, an algorithm is used to analyze and comprehend the connection between features for predicting accurate predictions (for instance, porosity, saturation, permeability) (Xu et al., 2019; IBM, 2020).

In the past few years, machine learning has been frequently applied in the analysis of well logs, lithofacies and depositional environments, and seismic data inversion (Qi and Carr, 2006; Maiti et al., 2007; Motie et al., 2018; Ahmadi et al., 2020; Hadavimoghaddam et al., 2021; Zhao et al., 2021; Gholami et al., 2022). Several attempts were made to use artificial neural architectures to forecast petrophysical characteristics in uncored wells or intervals to improve reservoir characterization using multiple well log data (Wong et al., 1995; Bhatt and Helle, 2002; Lim and Kim, 2004; Verma et al., 2012; Okon et al., 2021).

Although several studies have been carried out on Barra Velha formation, limited studies have used a precise technique like deep learning to characterize the reservoir properties of the Barra Velha formation in the Santos Basin, SE Brazil. This study set out to describe the reservoir's characteristics of this formation, using the integration of well log data, borehole imaging, both conventional and microCT analyses of plug data, and thin section description. Deep Learning was employed in our research to predict porosity, permeability, and rock types.

#### **4.1.1 GEOLOGICAL SETTING**

The creation of the passive margin Santos Basin started in the Upper Jurassic/Early Cretaceous period owing to the breakup of Western Gondwana and the opening of the South Atlantic Ocean (Heilbron et al., 2000; Mohriak et al., 2008; Beasley et al., 2010; Belila et al., 2020; Irají et al., 2022c). This basin is in the southwest segment of the Brazilian continental margin, between Cabo Frio High and the Florianópolis High (Moreira et al., 2007) (Figure 4-1).

The geological evolution of the Santos basin is connected to the presence of an extensional tectonic regime. The sub-salt interval in the Santos Basin correlated with the Guaratiba Group, which spans the Neovalanginian to Neoaptian and ends with the Ariri Formation's evaporite deposition (Moreira et al., 2007). The Camboriú Formation encompasses the basalts that are linked to the rift phase during the Gondwana breakup. This formation marks the initial stages of the Santos basin deposition and the formation of its economic substrate (Chang et al., 1992; Mohriak et al., 2008). The Camboriú Formation is overlaid in the slow development of the rift system over time by the Piçarras Formation formed during the Barremian age in the early rift phases. Piçarras Formations is composed of the deposition of alluvial fans of conglomerates and polymictic sandstones in the proximal regions and sandstones, siltstones, and shales in the lacustrine portions (Moreira et al., 2007; Carlotto et al., 2017).

The main sub-salt reservoir rocks were deposited from the Neobarremian to Eoaptian and correspond to the Itapema and Barra Velha Formations. The Itapema Formation contains intercalations of high-energy calcirudites, consist of shell fragments, black shales with high organic matter in the more distal parts, and alluvial fans of conglomerate and sandstone in the proximal parts (Moreira et al., 2007). The Barra Velha Formation represents the sag/post-rift and it composes of in-situ precipitates including different morphologies of calcite shrub-like growths and

spherulites, reworked carbonates such as intraclastic grainstones, and carbonate mud with variable content of authigenic magnesian clay minerals (Wright and Barnett, 2015; Gomes et al., 2020).

Changes in lake chemistry and the diversity of deposition found in this formation were a result of the source of water input, climate and alteration in the accommodation space (Sabato Ceraldi and Green, 2017; Farias et al., 2019). The lake that allowed the deposition of the facies in the Barra Velha Formation was interpreted as a highly evaporated endorheic saline lake (Farias et al., 2019). The Ariri Formation is the last sequence deposited in the Guaratiba Group and contains evaporites that originated in a closed ocean basin (Chang et al., 1992; Moreira et al., 2007).

For pre-salt carbonate reservoirs, different interpretations have been made associated with microbial formation (Moreira et al., 2007; Saller et al., 2016; Irají et al., 2022a) or chemical and depositional controls (Wright and Barnett, 2015; Farias et al., 2019; Lima and De Ros, 2019; Gomes et al., 2020). Gomes et al., 2020 proposed a new facies categorization system for the pre-salt lacustrine carbonates, applied in this work, derived from the abundance of three main elements: mud, spherulites, and shrubs.

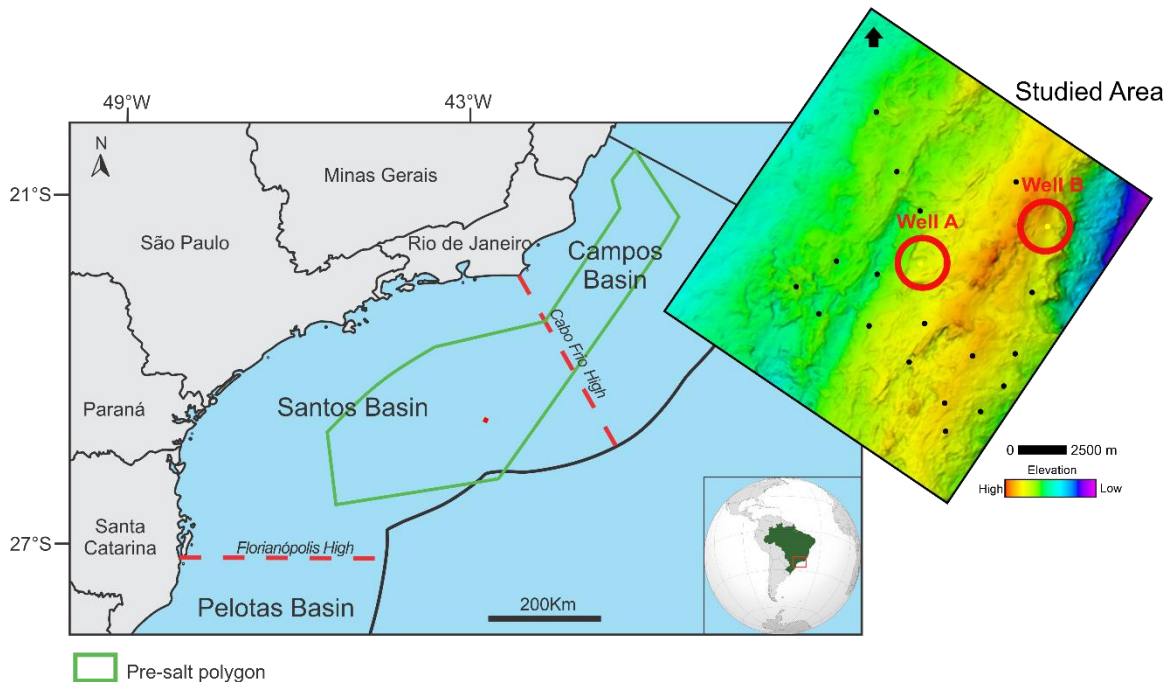


Figure 4-1. Location of the Santos Basin, South Atlantic, offshore Brazil, showing the polygon (green) that delimitates the pre-salt occurrences and the location of the wells (A and B).

## 4.2 MATERIALS AND METHODS

### 4.2.1 DATASET AND WORKFLOW

Two wells namely A and B were chosen from the Barra Velha Formation. A full collection of standard open borehole well log measurements was accessible for the target reservoir zone of these wells. Table 4-1 includes the available logs and information about their application. In addition, the intergranular porosity curve (PIGN) and mineralogy composition (clay, calcite, dolomite, and quartz volume) were established through petrophysical interpretation of wireline log and were included as part of the available dataset. Besides, the porosity profile generated from the borehole image log (BHI) by interpreting porosity and matrix according to the color scale was employed as a dataset in this study. Figure 4-2 displays the resolution of different datasets employed in this study, the values featured in the figure were sourced from (Schlumberger, 1991; Tiab and Donaldson, 2015). In addition, the available data included routine core analysis including gas permeabilities and helium porosity for 774 plug samples (208 plug samples for well A and 566 plug samples for well B), microCT images for 12 plug samples, and 239 thin sections (109 from core and 130 from sidewall core samples).

Table 4-1. Applications of available well logs.

Well log	Application
Density (RHOB)	Porosity, bulk density, fluid density, acoustic impedance, mineralogy, and fracture identification
Gamma-ray (GR)	Lithology, shale content, mineralogy, facies, and sequence stratigraphy identification
Neutron (NPHI)	Porosity, gas content, and lithology identification
Photoelectric factor (PEF)	Mineralogy and lithological identification
Nuclear Magnetic Resonance (NMR)	Porosity, irreducible water saturation, permeability, residual oil saturation, hydrocarbon typing, and oil viscosity estimation
Electric resistivity logs (Deep: RD-EP and Shallow: RS-EP)	Fluid saturations, geology, sedimentology, and geochemistry identification
Borehole Image (BHI)	Fractures, bedding planes, sedimentary structures, and reservoir property characterization

These logs were integrated with the plug data and borehole image for rock typing classification. Different conventional rock typing techniques, microCT analyses of plug, and thin section description were applied to characterize the reservoir. Machine learning was applied for the estimation of variables (porosity, permeability, and rock types). The summary of the applied methodology is illustrated in Figure 4-3, and a detailed explanation of these steps is presented in the following sections.

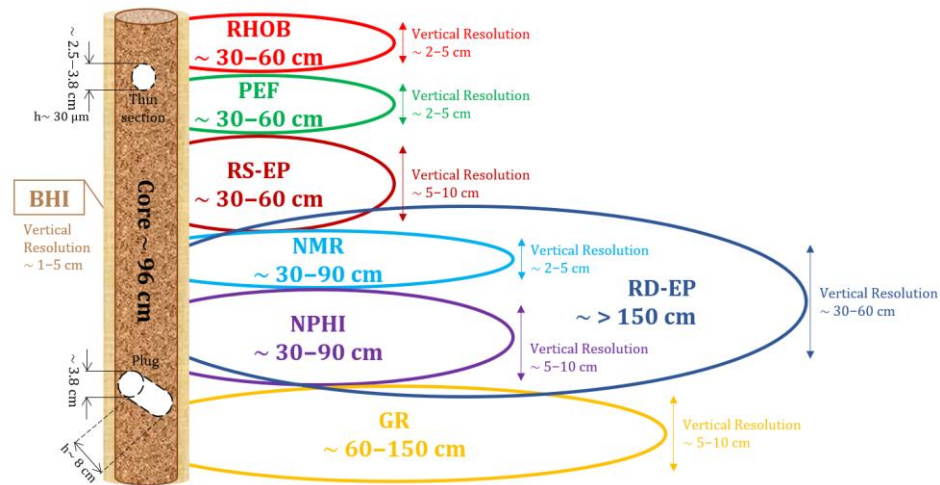


Figure 4-2. Comparison of radius of investigation and vertical resolution for well logs, core, plugs, and thin sections.

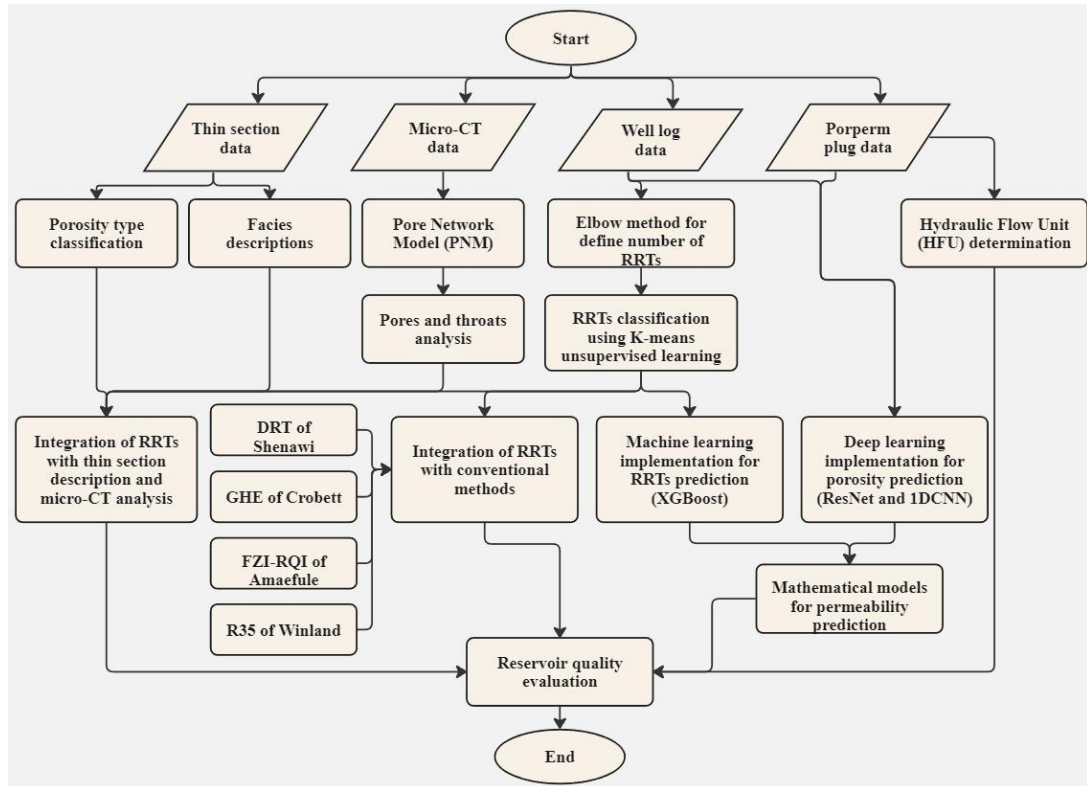


Figure 4-3. Applied workflow image for rock typing classification and reservoir quality evaluation.

#### 4.2.2 RESERVOIR ROCK TYPES (RRTS) AND HYDRAULIC FLOW UNITS (HFUS)

Reservoir rock types (RRTs) are rock formations that were deposited under similar environmental factors and have a similar composition. They have undergone the same diagenetic processes resulting in distinct petrophysical observances, such as comparable pore network characteristic, productivity, and transmissibility potential (Gunter et al., 2014). Furthermore, hydraulic flow unit

(HFU) is a word that alludes to a ceaseless stratigraphic unit that features an indicated rock type with similar stream speed (Amaefule et al., 1993; Opuwari et al., 2021).

The present plug data were subjected to reservoir rock typing utilizing several approaches, which were subsequently correlated with the HFUs produced. To support the defined rock categories, well log measurements were utilized. The hydraulic flow units were created by partitioning the examined reservoir into various flow units utilizing the SML graph.

#### **4.2.2.1 K-MEANS UNSUPERVISED LEARNING ALGORITHM**

The K-Means clustering technique was applied to partition the data into distinct groups and ensure that the information within each cluster has the same properties. The main advantage of K-means clustering is high-speed clustering of the tabular datasets, and ease of implementation. The algorithm determines the center of each group and splits the data points into the matching groups based on the input data (plug samples and corresponding log data) and the number of partitions can be selected using the elbow curve method (Duong et al., 2019), or Silhouette analysis (Rousseeuw, 1987). Based on the points' distance from the center of the groups, we assume each data point belongs to only one of the groups (Duong et al., 2019).

In the K-Means method, the number of  $k$  clusters is considered a hyperparameter that should be ascertained before clustering, to achieve precise outcomes this hyperparameter needs to be tuned. Therefore, the Elbow method was employed to determine whether  $k$  is the appropriate cluster number. This approach works by performing the clustering problem for the input data set over a range of  $k$  values. The Sum of Squared Error ( $SSE = \sum_{i=1}^N (y_i - \hat{y}_i)^2$ ) deviation of data belonging to a group versus the cluster's centroid will be calculated for each value  $k$ . Then, for each value of  $k$ , the SSE line graph is plotted. If the line chart resembles an arm, the "elbow" on the arm yields the best  $k$  value. This algorithm aims to have a small SSE, however, as  $k$  increases SSE tends to decrease to 0. As a result, the goal is to choose an optimum value of  $k$  where SSE is low (Duong et al., 2019).

#### **4.2.2.2 EFFECTIVE PORE RADIUS ( $R_{35}$ ) OF WINLAND**

Winland presented a quantitative formula that correlates porosity ( $\phi$ ) and permeability ( $k$ ) with the effective pore radius ( $R$ ) using the analysis of mercury injection curves obtained from different sandstone rocks. The foremost trustworthy connection between these variables was set up when the level of Hg saturation reaches 35% (Winland, 1972; Kolodzie, 1980). The link between these

three parameters allows foreseeing successful pore-size of each RRT and HFU unit (Gunter et al., 2014; Shalaby, 2021). For this purpose, the following equation is used.

$$\text{Log } R_{35} = 0.732 + 0.588 \text{ Log } k - 0.864 \text{ Log } \phi \quad (4-1)$$

where,  $k$  is permeability in  $mD$ ,  $\phi$  is porosity in %, and  $R_{35}$  is the pore throat radius in  $\mu m$  obtained at 35th% of Hg saturation. In this study, to obtain a continuous  $R_{35}$  dataset, the Winland formula was utilized with plug permeability and porosity.

#### 4.2.2.3 FLOW ZONE INDICATOR (FZI) AND RESERVOIR QUALITY INDEX (RQI)

Amaefule et al. proposed the  $RQI$  and  $FZI$  parameters to measure the quality of a reservoir. These variables were utilized and evaluated to classify and differentiate a reservoir into a set of  $RRTs$ , and  $HFUs$  (Amaefule et al., 1993; Bize Forest et al., 2019). These parameters can be computed as,

$$RQI = 0.0314 \sqrt{\frac{k}{\phi}} \quad (4-2)$$

$$\phi_z = \frac{\phi}{1 - \phi} \quad (4-3)$$

$$FZI = \frac{RQI}{\phi_z} = \frac{0.0314 \sqrt{\frac{k}{\phi}}}{\frac{\phi}{1 - \phi}} \quad (4-4)$$

where,  $k$  is permeability in  $mD$ ,  $\phi$  is porosity in fraction,  $\phi_z$  is the normalized porosity in fraction.  $RQI$  and  $FZI$  are expressed in  $\mu m$ .

#### 4.2.2.4 DISCRETE ROCK TYPES (DRTS)

Shenawi et al. (Shenawi et al., 2007; El Sawy et al., 2020) suggested the discrete rock type ( $DRT$ ) approach that involves dividing reservoirs into different  $RRTs$  according to the  $FZI$  parameter. In this approach, the reservoir is partitioned into different rock types using the formula below.

$$DRT = \text{Round}(2 \text{ Ln}(FZI) + 10.6) \quad (4-5)$$

where,  $DRT$  is the discrete rock type and  $FZI$  is the flow zone indicator in  $\mu m$ .

#### 4.2.2.5 GLOBAL HYDRAULIC ELEMENTS CURVES (GHE)

The Kozeny-Carman equation is an example of an empirical formula that is extensively applied to establish a connection between porosity and permeability (Kozeny, 1927; Carman, 1937). It is also sometimes used to forecast permeability based on porosity, as:

$$k = \frac{1}{cS^2} \frac{\phi^3}{(1 - \phi)^2} \quad (4-6)$$

where  $k$  represents permeability in  $mD$ ,  $\phi$  denotes porosity in fraction,  $c$  is the Kozeny constant and  $S$  is the specific surface area. To characterize a particular set of petrophysical rock types, Corbett et al. proposed the word 'petrotype.' The term 'petrotype' refers to a set of global hydraulic elements (*GHE*) characterized by a systematic arrangement of *FZI* values and prescribed graphs according to the Kozeny-Carman formula, as:

$$k = \frac{FZI^2}{0.0314^2} \frac{\phi^3}{(1 - \phi)^2} \quad (4-7)$$

In the *GHE* system, the ordered arrangement of *FZI* values is selected to cluster data and identify separate fields with common petrophysical characteristics and geologic significance. Trends can be easily determined by plotting plug data on the *GHE*'s 'basemap' and these trends can convey geologic meaning (Corbett and Potter, 2004; Hosa et al., 2020).

#### 4.2.2.6 STRATIGRAPHIC MODIFIED LORENZ (SML)

The *SML* plot is a cumulative visual representation of storage and flow capacities considering depth. The calculation of storage capacity ( $\phi h$ ) and flow capacity ( $kh$ ) is achieved by multiplying the porosity and permeability data with their corresponding bed thicknesses ( $h$ ):

$$(kh)_{cum} = k_1(h_1 - h_0) + k_2(h_2 - h_1) + \dots + k_i(h_i - h_{i-1}) / \sum k_i(h_i - h_{i-1}) \quad (4-8)$$

$$(\phi h)_{cum} = \phi_1(h_1 - h_0) + \phi_2(h_2 - h_1) + \dots + \phi_i(h_i - h_{i-1}) / \sum \phi_i(h_i - h_{i-1}) \quad (4-9)$$

It aids in determining the involvement of each *HFU* in the entire flow capacity. In this plot, each individual slope variation demonstrating a distinct *HFU* (Maglio-Johnson, 2001; Omeje et al., 2022).

### 4.2.3 THIN SECTION DESCRIPTION AND $\mu$ CT ANALYSIS

The thin section description was carried utilizing a polarizing microscope under transmitted light, emphasizing the characterization of textural features, types of pore space, and diagenetic elements. The process of recognizing and categorizing of the facies were according to (Gomes et al., 2020) and the textural features according to (Claes et al., 2017). The classification of porosity types was established using (Choquette and Pray, 1970). To differentiate calcite-dolomite, the examined thin sections underwent staining using an acid solution of alizarin red, and, for a better characterization of the pore space, they were impregnated with blue epoxy resin.

The cylindrical rock samples (plugs) were subjected to microCT imaging at the Laboratory of Porous Media and Thermophysical Properties of the Federal University of Santa Catarina (LMPT/UFSC) using a ZEISS Xradia Versa XRM-500 Scanner (RES 40  $\mu m$ ). The equipment utilizes a transmission source that generates polychromatic X-rays with a maximum power of 10 W and an energy range between 30 and 160 kV. For the  $\mu$ CT analysis, the 3D models were developed in the PerGeos software – Thermo Fisher Scientific by stacking the 2D cross-sections from plugs. The image resolution of each plug was 40.8  $\mu m$ . The images were processed, and each image was subjected to filtering and segmentation. The segmentation step determines the porous system resulting in a binary image, which represents the pore and solid material phases. This step was set by manually choosing threshold values of each interval with the “Interactive Overlay Threshold” tool. The phases (pore and solid material) were defined by their grayscale color, which was a function of the X-ray attenuation coefficient, based on their respective densities. With those steps, we can quantify and identify the total and effective porosity and the tortuosity. Pore Network Modeling (PNM) allows obtaining the relationship between the parameters of pore geometry, such as pore and throat radius.

### 4.2.4 POROSITY, PERMEABILITY, AND ROCK TYPE PREDICTION BY MACHINE LEARNING ALGORITHMS

The present study implemented the residual neural network (ResNet) approach as well as one-dimensional convolutional neural network (1D CNN) model to estimate the continuous variable of porosity and Extreme Gradient Boosting (XGBoost) Machine Learning Algorithm to predict the discrete variable of rock type in the studied sequence. The objective was to evaluate the reservoir quality and predict well performance for uncored intervals/wells. For deep learning approaches

such as ResNet and 1D CNN-based methods, the weights that produce the best results for the validation data are saved and applied to the test dataset.

The ResNet approach is a deep neural network that utilizes residual blocks to capture complex features from the data. It leverages skip connections to preserve and concatenate important features from the early layers, which are then utilized in the subsequent layers. This technique has been shown to be highly effective in deep neural network architectures by addressing the vanishing gradient problem and allowing for the successful training of much deeper networks (Khan et al., 2020). In contrast, 1D CNNs are a class of neural networks designed for analyzing data in a sequential order. The network consists of one or more layers of convolutional filters that apply a sliding window over the input data to extract features, and mainly used for 2D inputs such as images. These filters learn to detect patterns and relationships in the data and can capture local dependencies between neighboring data points. The resulting features are then fed into fully connected layers for classification or regression tasks (Harbola and Coors, 2019). In this study both ResNet and 1D-CNN-based techniques has been coded in Python and we used TensorFlow 2 framework to generate models.

The XGBoost model is frequently employed to solve supervised learning issues. A final estimate is produced by merging the forecasts from all the decision tree models that were built as part of the ensemble learning technique. The decision tree models are trained using a gradient-boosting method, which entails iteratively adding new models to the ensemble in order to remedy the errors of the earlier models. XGBoost also incorporates several advanced features, such as weight regularization, tree pruning, and a custom loss function, to further improve model accuracy and generalization (Chen and Guestrin, 2016).

In this study, all neural network models were trained using 15 input variables, which comprised of all well log data as described in the Dataset and Workflow section. The ResNet architecture used in this study was customized for the specific task of predicting porosity. The input is first passed through a dense layer with 64 nodes, followed by a batch normalization layer and the ReLU (Rectified Linear Unit) activation function. Next, three residual blocks with skip connections (each consisting of two layers) followed by another dense layer were used to learn complex features from data. The number of nodes in each residual block varied, with the initial block having 64 units and the subsequent blocks having 128 and 256 units. The ReLU activation function was used for all

layers in this study, and batch normalization was applied before the activation function in each layer to improve the training process. To prevent overfitting, the Dropout layer with a constant coefficient of 0.2 was incorporated for regularization, meaning that 20% of units were randomly excluded from each epoch. The structure of this model, including the number of layers and units, was visualized and presented in Figure 4-4.

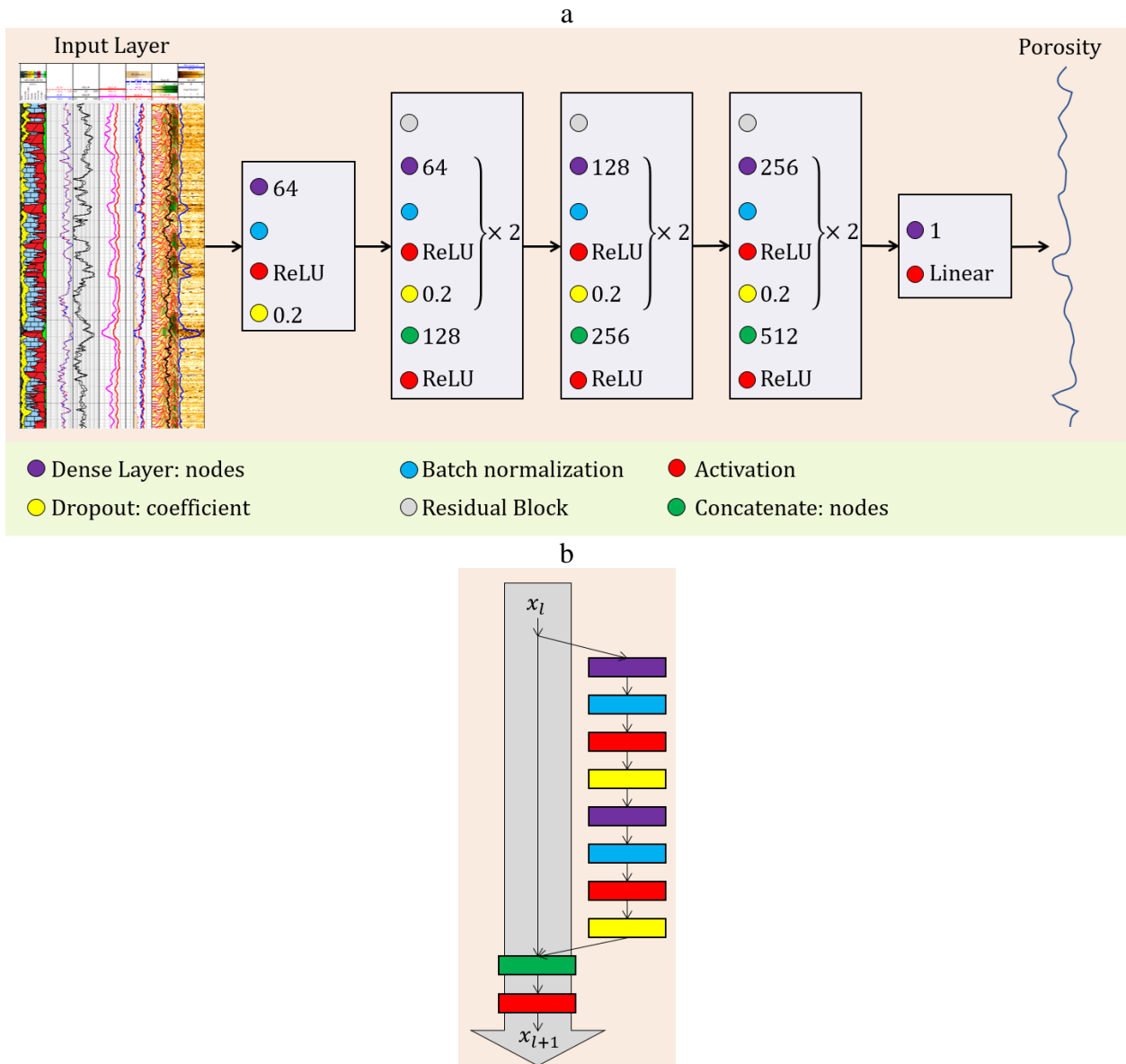


Figure 4-4. a) The architecture of the Residual neural network (ResNet) model, b) one layer of each residual block.

In our study, the network of 1D CNN-based model started with two 1-dimensional convolutional layers. A 1-dimensional max pooling layer to reduce the spatial dimensions of the feature maps was then applied. The process of applying two convolutional layers, followed by a max pooling

layer was repeated and the output was flattened into a one-dimensional vector, which is then passed through dense layers with ReLU activation function and dropout layers to reduce overfitting. Figure 4-5 illustrates and presents the structure of this model. As represented in Figure 4-5,

the architecture of the model begins with two convolutional layers, each having 64 filters and a kernel size of three. ReLU is used as the activation function, and SAME padding is used to ensure that the spatial dimensions of the output feature map are the same as those of the input data. Following the first convolutional layers, a Maxpooling layer with a pool size of 2 is added. Subsequently, there are two more convolutional layers, each with 128 filters. These layers keep the same parameters as the previous convolutional layers. After the second set of convolutional layers, there is another Maxpooling layer with a pool size of 2. The next stage incorporates two more convolutional layers, each with 256 filters and a kernel size of 3. The CNN section's output is then flattened, and two Dense blocks are added. Each Dense block contains a Dense layer with 256 nodes, followed by a Dropout layer. Also, the model has two Dropout blocks, each with 128 units, similar to the preceding blocks. Finally, the model concludes with a Dense layer consisting of 1 unit using a linear activation function. It is important to note that the dropout coefficient is treated as a hyperparameter, just as in the previous model. After thorough evaluation of various values, we determined that a dropout coefficient of 0.5 for the Dense layers with 256 units and 0.4 for the Dense layers with 128 units aided in preventing overfitting and achieving optimal error reduction.

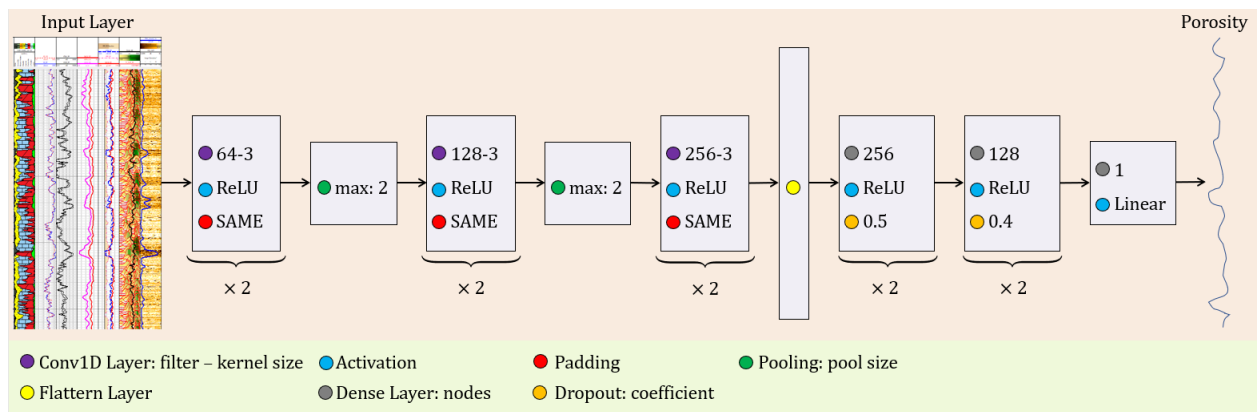


Figure 4-5. The architecture of the 1D Convolutional neural network model.

For optimization, the Adam optimizer was utilized with a learning rate of  $1e-3$ . It is worth noting that this study began with a fixed learning rate of  $1e-3$ . We later introduced a variable learning rate approach to further investigate the impact of the learning rate on the model's performance. In this scenario, we set the initial learning rate to  $1e-3$  again, but this time we let it vary as a parameter

during training. We used a dynamic adjustment mechanism for the learning rate in particular. If the validation loss function did not decrease after 50 consecutive epochs, we changed the learning rate dynamically by multiplying it by 0.5. This adaptive learning rate strategy sought to optimize the model's convergence and training process. The outcomes of these implementations revealed that the influence of the learning rate appeared to be insignificant. Both fixed and variable learning rate cases showed similar trends throughout the learning process, indicating that the impact of this hyperparameter is still limited in our particular context. These findings add to our understanding of the model's sensitivity to the learning rate and provide useful insights for future training process optimization. The loss function was the mean squared error ( $MSE = \frac{1}{N} \sum_{i=1}^N (y_i - \hat{y}_i)^2$ :  $y_i$  is the  $i^{th}$  value of the y-variable to be predicted,  $\hat{y}_i$  presents the predicted value of  $y_i$ , and  $N$  is the amount of observations). The batch size for both deep learning models was 32, and we run the model for 1,000 epochs (where in both cases the plateau behavior observed in training process). The training data constituted 80% of the total dataset, with the remaining 20% being used as the test set. The number of parameters of CNN-based model was 694,209, and for ResNet was 178,305.

Moreover, since the well-log data were in varying orders of magnitude, normalization was performed on all the data (ranging from 0 to 1). It is important to note that the architecture of the neural network (number of layers, units, activation function, regularization, different types of residual networks, etc.) and the dropout coefficient were hyperparameters that were adjusted to improve the outcomes. Dropout was used in this study with varying coefficient ranges ranging from 0.05 to 0.3 to determine the optimal value that not only produced the lowest loss function but also effectively prevented overfitting. The results clearly show that the Dropout with a coefficient of 0.2 produced the best results.

## 4.3 RESULTS

### 4.3.1 BASIC PETROPHYSICS

This section uses data from 208 plug samples for well A and 566 plug samples for well B with their corresponding well log data, microCT images for 12 plug samples, and 239 thin sections of the Barra Velha Formations. Figure 4-6-a, the plug porosity histogram for well A, reveals a fairly symmetric distribution of the values. Two frequency peaks appear in a graph, which could indicate a mixing of porosity distribution from different geological units and rock types. However, the porosity histogram for well B in Figure 4-6-b, shows less symmetric distribution. The permeability distribution of plug samples data for both wells are skewed positively, however, the log k distribution is much more symmetric than the permeability distribution (Figure 4-6-c and d).

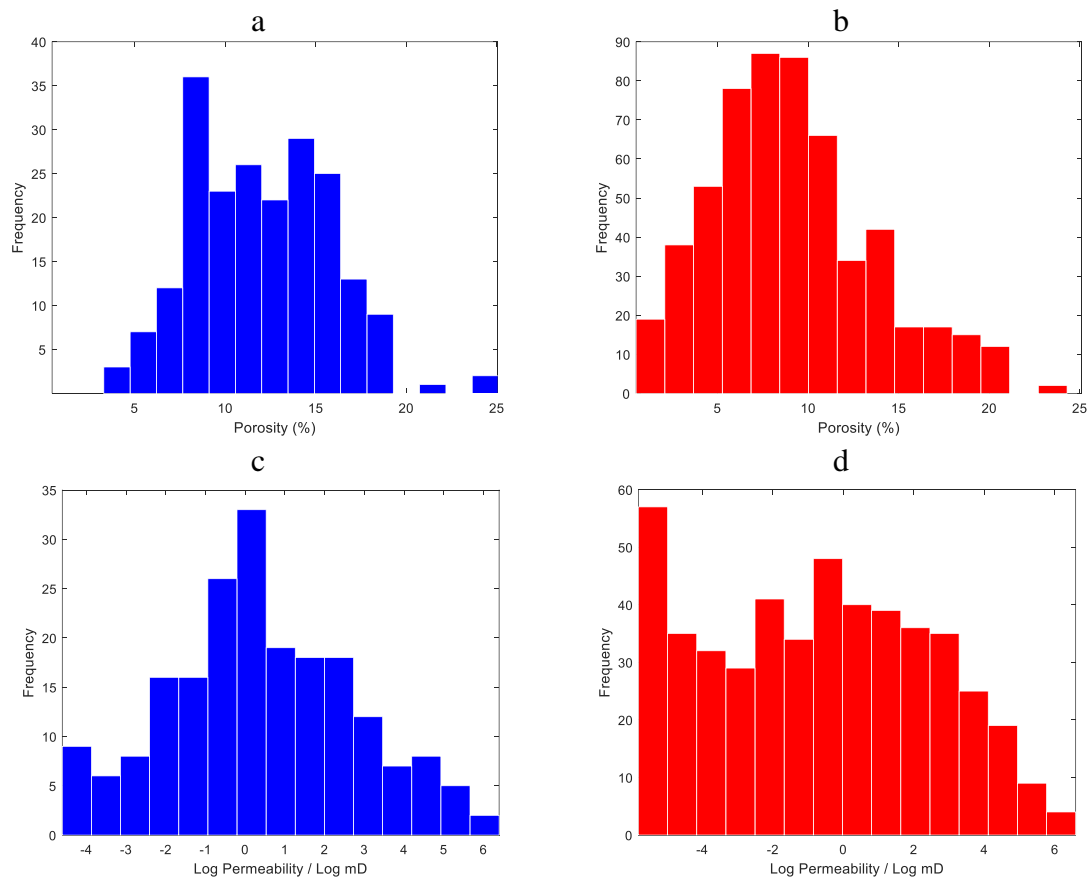


Figure 4-6. a, b) Porosity histogram for plug samples of well A and well B, c, d) permeability histogram for plug samples of well A and well B.

Table 4-2 provides the summary statistics for plug samples. For porosity data of well A, the mean and median are closer to each other in comparison with well B, indicating a symmetric distribution. In contrast, the median for the permeability data of both wells is much smaller than the mean,

suggesting a distribution with a positive skew. The coefficient of variation shows that variation in porosity is small, while for the permeability data indicates order of magnitude variations within the sample data.

Table 4-2. Summary statistics for plug samples of wells A and B.

Statistics	well A			well B		
	$\phi$ , %	k, mD	Logk	$\phi$ , %	k, mD	Logk
Mean	11.99	19.43	0.40	9.10	13.52	-1.59
Median	11.80	1.27	0.24	8.60	0.21	-1.57
Mode	8.30	0.03	-3.51	6.10	0.001	-6.91
Minimum	3.30	0.01	-4.61	0.50	0.001	-6.91
Maximum	25.10	597.00	6.39	24.30	726.00	6.59
Percentile 25	8.95	0.32	-1.16	5.90	0.01	-4.96
Percentile 50	11.80	1.27	0.24	8.60	0.21	-1.57
Percentile 75	14.80	7.60	2.03	11.60	4.13	1.42
Variance	1E-03	4236.90	5.64	2E-03	2889.10	12.96
Standard Deviation	3.76	65.09	2.38	4.46	53.75	3.60
Coefficient of Variation	0.31	3.35	6.00	0.49	3.98	-2.26
Range	21.80	596.99	11.00	23.80	726.00	13.50

### 4.3.2 FACIES DESCRIPTIONS

The core interval studied in this work from Barra Velha Formation was grouped in three main facies: (1) Crystal Shrub-dominated facies; (2) Reworked facies, and (3) Spherulitestone facies. The reworked facies were the most recurrent, comprising 80% of the analyzed thin section. This facies is composed of transported sediments with poor to moderate sorting. Crystal shrub-dominated and spherulitestone facies corresponded to more than 10% and around 8% of the total analyzed thin section, respectively. The identified depositional facies are described below.

#### 4.3.2.1 CRYSTAL SHRUB-DOMINATED FACIES

The crystal shrub-dominated facies includes shrubstones, spherulitic shrubstones, and occurrences of the shrubstones layers intercalated with thick reworked facies such as rudstones and grainstones (Figure 4-7). The crystal shrubs vary in terms of size and morphology. The size ranges from 1mm to 8mm, however, larger shrubs can reach 2 cm. The crystal shrub micromorphology varies from fan, dendritic to pustular and macromorphology from arborescent, dendriform, topustular (Claes et al., 2017; Erthal et al., 2017). The secondary component in this facies was spherulites with spherical and fractured morphology and size that varied in diameter from 0.05 to 2.2 mm.

The pore types of this facies were growth framework, interparticle, intraparticle intercrystalline, and some occurrences of vug porosity. The most common porosity was the intercrystalline and the growth framework porosity. A cementing phase, mainly dolomite, occurred in abundance among the grains, and the growth framework porosity was developed among the crystal shrubs and their

branches, and sometimes this porosity was enhanced by the dissolution process. Dolomite cementation, dissolution, and dedolomitization were the main diagenetic processes observed in this facies.

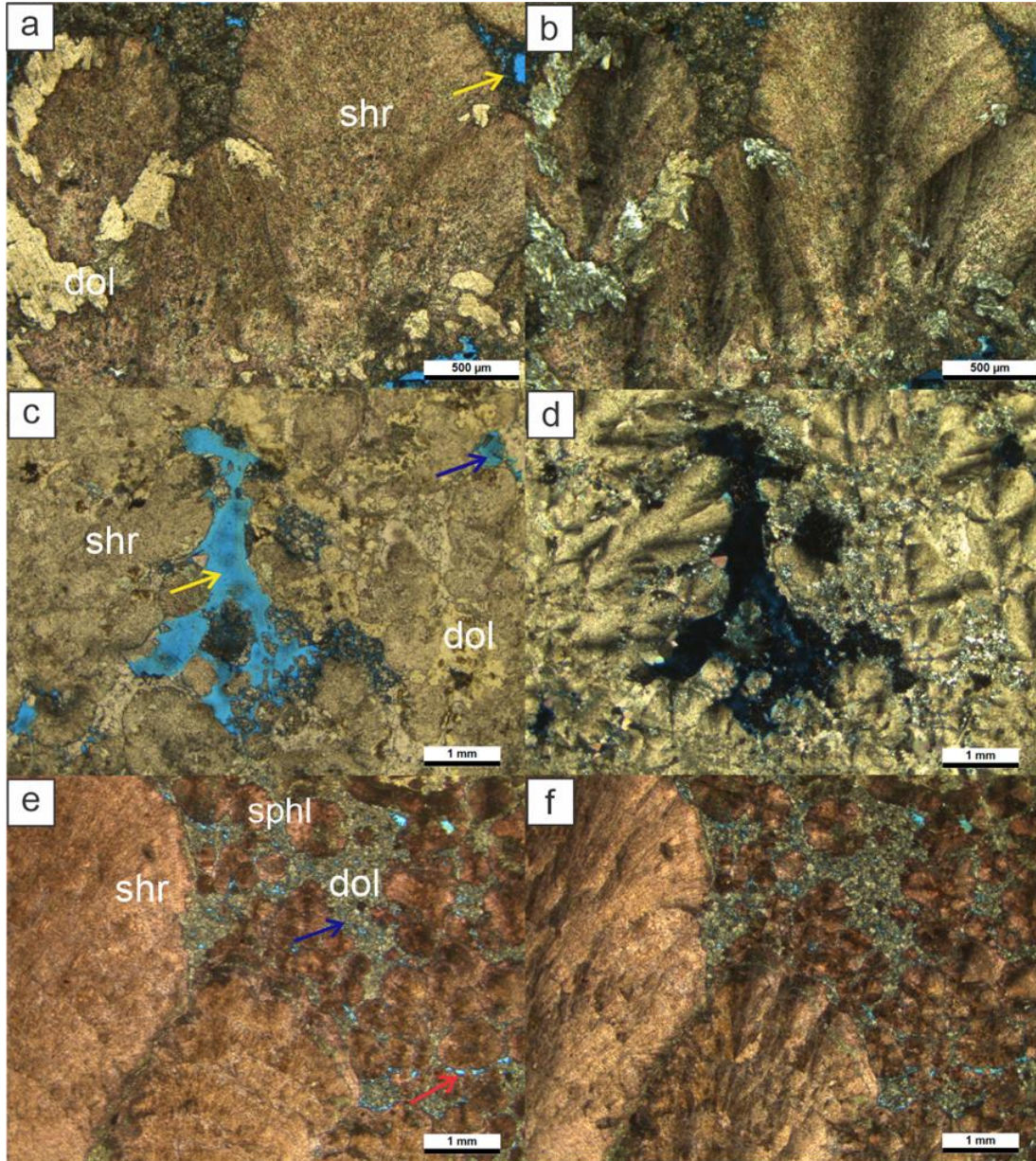


Figure 4-7. Aspects of the Crystal shrub-dominated facies: a, b) photomicrography showing crystal shrubs among dolomitic cement and pore space (blue), yellow arrow highlighting the growth framework porosity, c, d) photomicrograph showing crystal shrub surrounded by dolomite cement and partially preserved growth framework pores (yellow arrow), e, f) photomicrograph of the spherulitic shrubstone with dominated intercrystalline porosity (blue arrow) and interparticle porosity (red arrow) growth framework pore obliterated by dolomite. shr - crystal shrub; sphl - spherulite; dol - dolomite cement.

#### 4.3.2.2 REWORKED FACIES

The reworked facies includes grainstones and rudstone; the main component gives a rock name, such as intraclastic, bioclastic, and spherulitic (Figure 4-8). This facies are generally grains supported and composed of intraclastic carbonates, spherulites and shubs and fragments of both, phosphatic bioclasts, ooids, silicified particles, Mg-silicate intraclasts, volcanic fragments, and sulfides. The fabric is defined by poor to moderate sorting, tight to normal packing, and significant variations in the shape of grains to rounded to angular grains. The grain size ranges from 0.1 *mm* to 8 *mm*, however, larger grains can reach 1 *cm*. In some cases, the grains show compacted and oriented according to the lamination and fractures following the lamination.

The primary depositional texture was intensely affected by diagenetic events, such as dolomite and silica cementation, silicification, dedolomitization, dissolution, and compaction. Cementation and silicification obstructed most of the primary porosity filling the interparticle porosity. The compaction process was observed in sutured contacts between grains, crushed and fractured grains, and sometimes filled with dolomite cement. The grains affected by dissolution developed intraparticle porosity, and shub fragments are the main component altered by the dissolution. The main porosity type in this facies was intercrystalline formed between the dolomite crystal cement and interparticle, other types were intraparticle, vug, moldic, and rare fracture.

#### 4.3.2.3 SPHERULITESTONE FACIES

The samples were classified as spherulitestone facies when the most abundant component were calcite spherulites (Figure 4-9). Spherulites are generally spherical to elliptical forms of crystals radiating from a common core composed of carbonate (Chafetz et al., 2018; Gomes et al., 2020). The spherulite grains show a diameter varying from 0.15 *mm* to 1.5 *mm* and their recognition is easily done in crossed-polarized light. The main morphology of the spherulites is spherical, but they present other micromorphologies, such as composed and fractured.

In this facies the intercrystalline was the dominant porosity type; dolomite and silica were the main types of cement. The frequently pervasive dolomitization caused the replacement of the clay minerals and may destroy the spherulite's original morphology and also may obliterate primary porosity. The compaction affected the grains resulting in spherulites fragmented and showing a sutured contact.

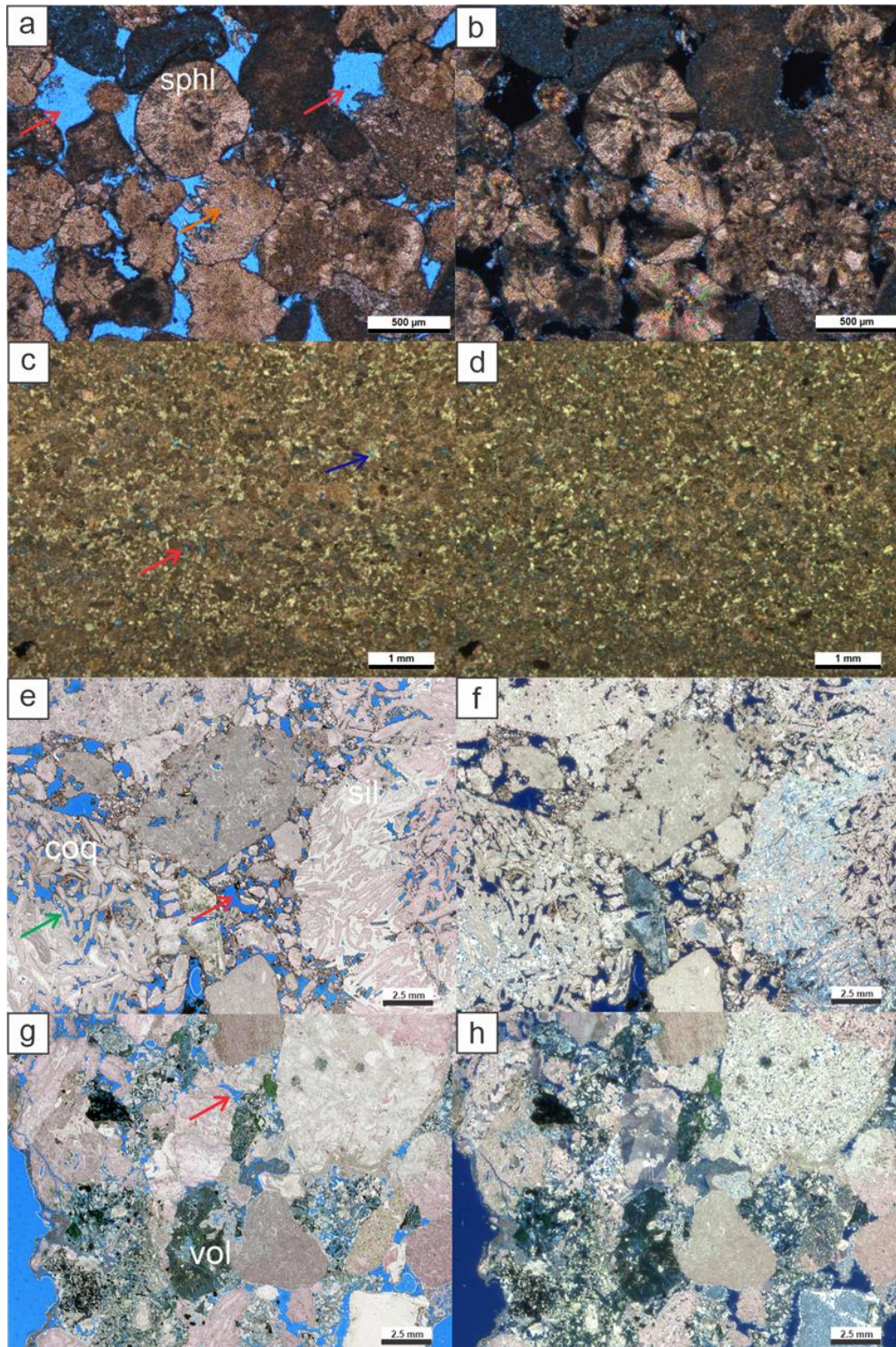


Figure 4-8. Aspects of the reworked facies: a, b) photomicrography showing a spherulitic rudstone with preserved interparticle porosity (blue area), red arrow highlighting the interparticle porosity and orange arrow showing the intraparticle porosity, c, d) photomicrograph showing an intraclastic grainstone cemented by dolomite (blue arrow highlights the intercrystalline porosity), e, f) thin section scan image of bioclastic rudstone (coq - coquinas fragments) with interparticle porosity (red arrow) and moldic porosity (green arrow), g, h) thin section scan image of volcanic rudstone with interparticle porosity (red arrow). sphl - spherulite; coq - coquinas fragments; vol - volcanic intraclast.

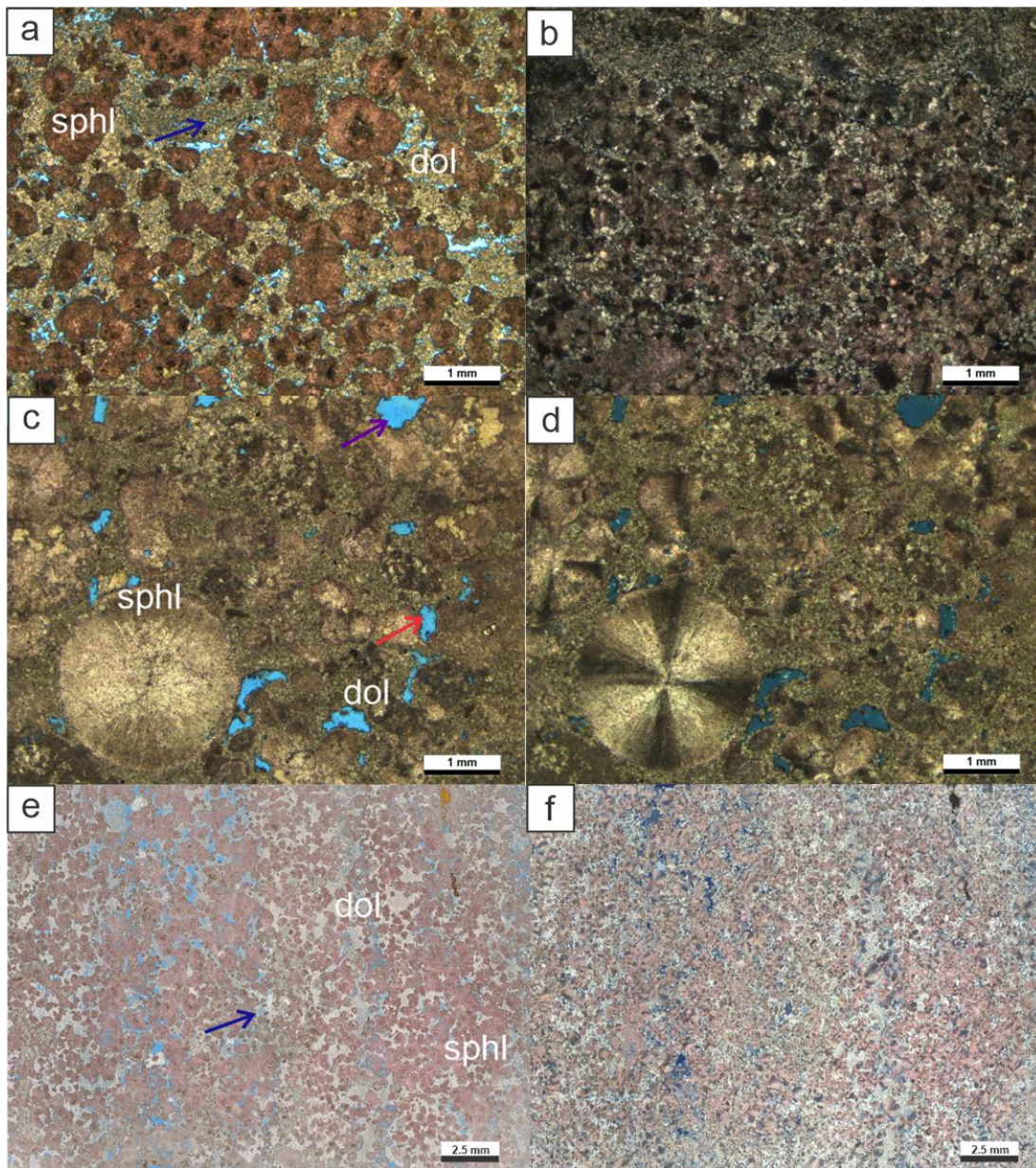


Figure 4-9. Aspects of the spherulitestone facies: a, b) photomicrography showing an spherulitestone cemented by dolomite, c, d) photomicrograph showing an spherical spherulite surrounded by dolomite cement and presence of vugular porosity (purple arrow), e, f) thin section scan image of spherulitestone with dominated intercrystalline porosity (blue arrow). sphl - spherulite; dol - dolomite cement.

### 4.3.3 RESERVOIR ROCK TYPES (RRTS)

The porosity-permeability plot of 774 multi-well plug samples data in Figure 4-10 reveals high variability and heterogeneity and makes it difficult to generate clear clustering of the samples based on conventional methods, resulting in uncertainties in defining rock types and reservoir descriptions. In this regard, the permeability and porosity data and their corresponding well log data were discriminated into RRTs according to K-means unsupervised classification algorithm for

wells A and B. The Elbow method was employed to determine the appropriate cluster number ( $k$ ). Therefore, the clustering approach for the input data set was performed over a range of  $k$  values. The Sum of Squared Error ( $SSE = \sum_{i=1}^N (y_i - \hat{y}_i)^2$ , where  $y_i$  is the  $i^{th}$  value of the y-variable to be predicted,  $\hat{y}_i$  is the predicted value) deviation of data points belonging to a cluster versus the cluster's centroid was calculated and plotted for each value  $k$ . The graph in the Figure 4-11 resembles an arm, so the elbow on the arm was chosen as an optimum value of  $k$  (number four) that describes best the distribution of 774 samples.

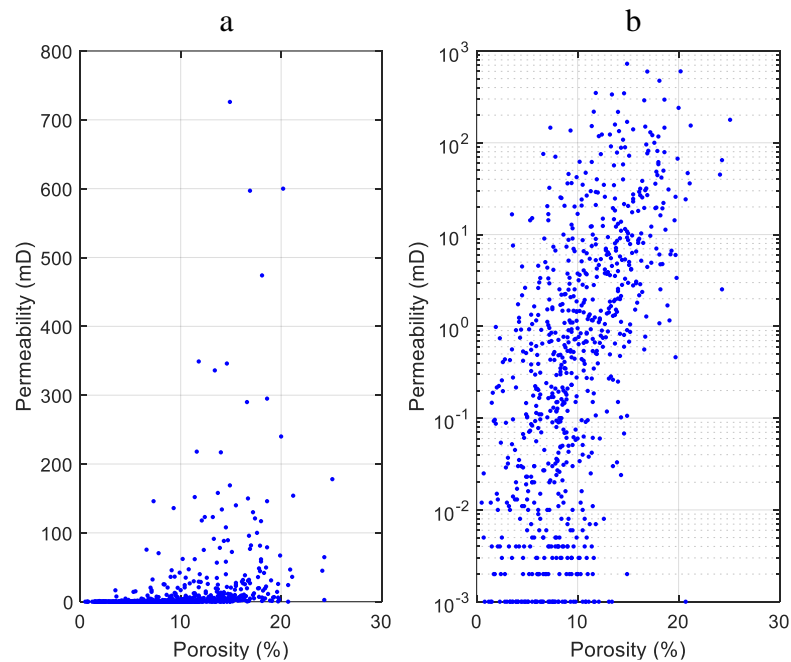


Figure 4-10. Porosity-permeability plot of the 774 data from wells A and B: a) permeability in linear scale, b) permeability in log scale.

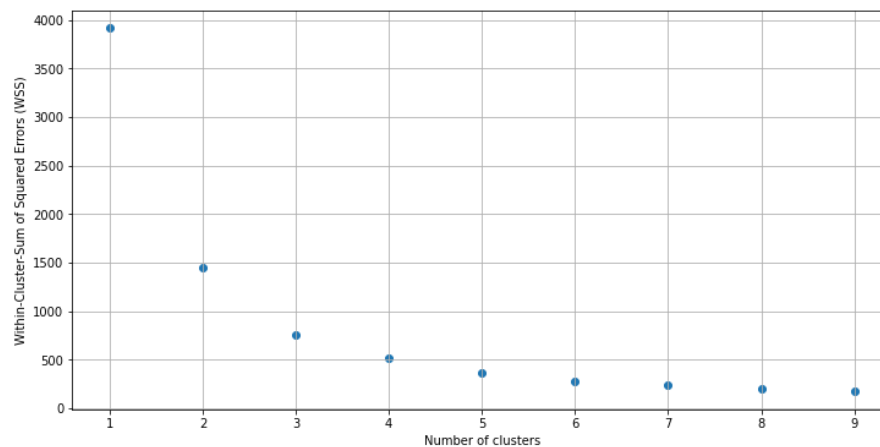


Figure 4-11. Elbow Diagram to determine the appropriate cluster number.

Using K-means algorithm, the samples were classified into these four groups with distinctive lithotypes based on their characteristics from different logs. Figure 4-12 displays the resulted porosity-permeability plot based on these four rock types according to this clustering algorithm. In this regard, statistical analysis was performed between different logs with plug permeability and porosity to find the more appropriate logs for clusterization. Neutron porosity, density log, NMR porosity, porosity profile based on image log, and mineralogy model (calcite, clay, dolomite, and quartz volume) were selected as the main parameters. The grouping was done by minimizing the sum of the distances between each object (plug porosity and permeability and the corresponding values of mentioned logs) and the group or cluster centroid. Table 4-3 presents summary statistics for plug samples data, reservoir quality parameters and well log data for all the classified reservoir rock types.

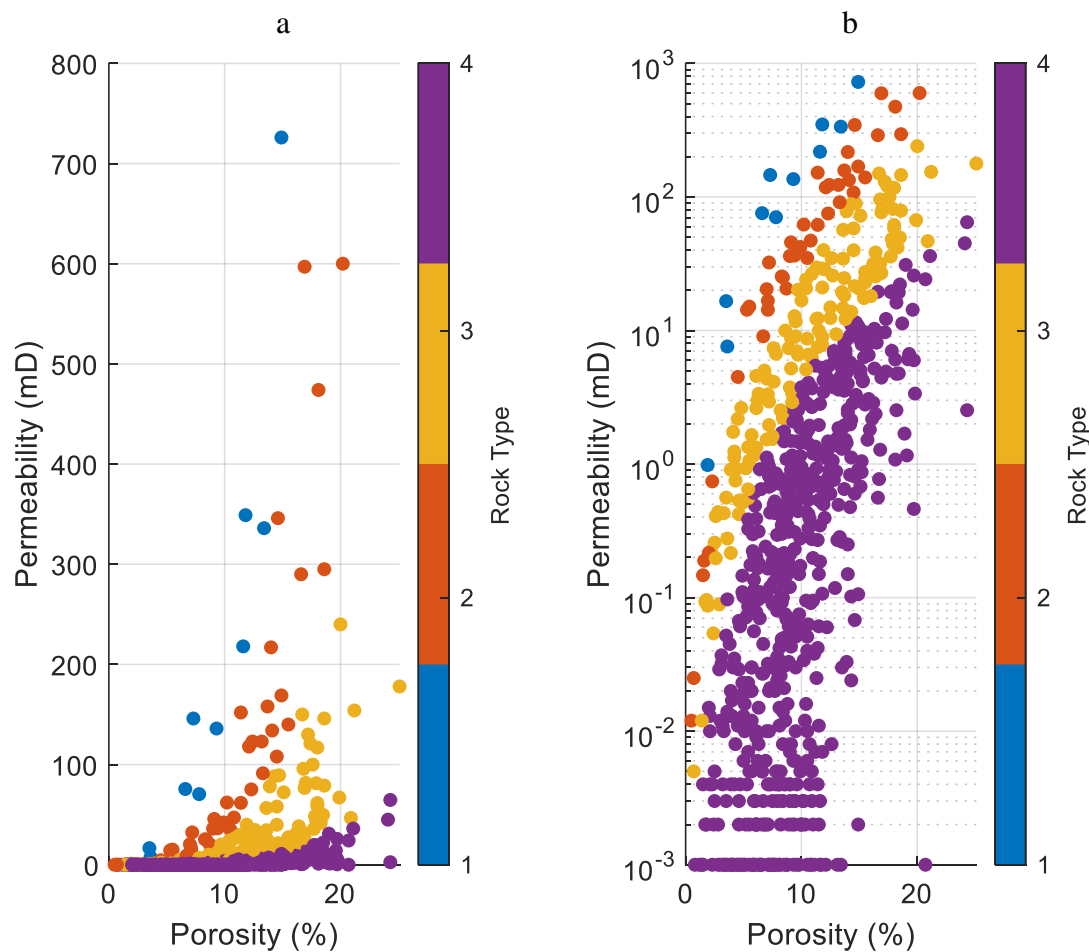


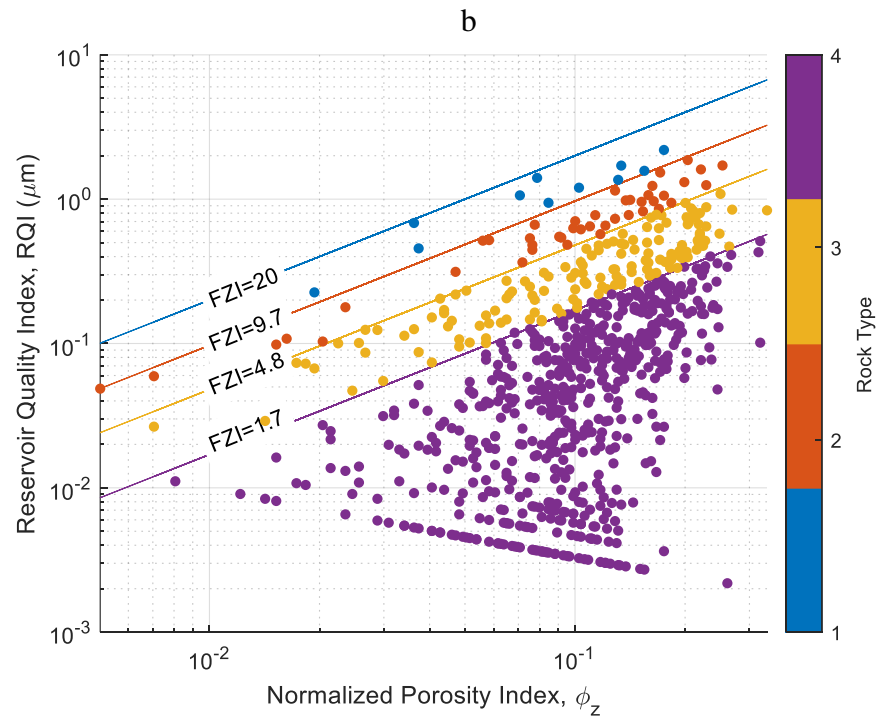
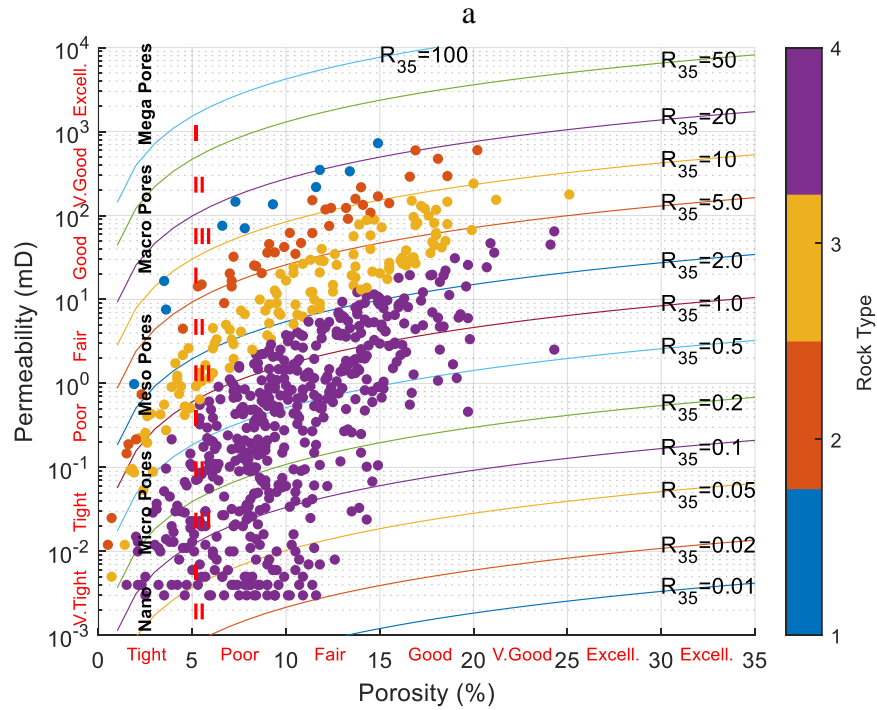
Figure 4-12. Porosity-permeability plot of the studied reservoir sequence discriminated into four RRTs according to K-means unsupervised classification algorithm: a) permeability in linear scale, b) permeability in log scale.

Table 4-3. Summary statistics for plug samples data, reservoir quality parameters and well log data.

RRTs	$k_m D$	$\phi$ , %	$\phi_z$	RQI, $\mu m$	FZI, $\mu m$	$R_{35}$ , $\mu m$	GHE	DRT	NPhi	RHOB	NMR $\phi$	NMR $k$	Image $\phi$	GR	Calcite	Clay	Dolomite	Quartz	
<b>RRT1</b>	Min	0.98	1.90	0.0194	0.2260	10.1620	3.0693	7	15	0.0552	2.5835	0.0537	0.10	0.0068	10.3010	0.0749	2.59E-05	0.0418	0.0171
	Max	726.00	14.90	0.1751	2.1918	18.8540	25.1530	8	16	0.1450	2.6659	0.1197	11.91	0.6149	30.1720	0.8247	0.0950	0.8042	0.2253
	Mean	189.30	8.34	0.0931	1.1646	13.1170	13.9480	7.55	15.73	0.0857	2.6202	0.0902	3.00	0.2210	20.4030	0.5335	0.0414	0.3148	0.1092
<b>RRT2</b>	Min	0.01	0.50	0.0050	0.0486	4.8796	0.7289	6	14	0.0367	2.4129	0.0511	0.01	0.0135	1.0797	0.0095	0.0065	0.0042	0.0002
	Max	600.00	20.20	0.2531	1.8663	9.6803	20.1080	7	15	0.2055	2.7043	0.1952	338.73	0.5811	36.7190	0.8555	0.1445	0.8175	0.2059
	Mean	111.06	10.03	0.1149	0.7541	6.6864	7.9039	6.63	14.33	0.1128	2.5673	0.1186	40.77	0.1886	17.4510	0.5760	0.0498	0.2844	0.0684
<b>RRT3</b>	Min	0.01	0.70	0.0070	0.0265	1.7429	0.2994	5	12	0.0286	2.2882	0.0362	2.8E-03	0.0068	0.1911	8E-07	3E-07	1E-05	2E-06
	Max	240.00	25.10	0.3351	1.0877	4.7846	10.1740	6	14	0.3453	2.7095	0.4054	683.13	0.6419	89.0240	0.9039	0.3328	0.8703	0.4741
	Mean	27.06	10.75	0.1245	0.3518	2.8935	3.1866	5.44	12.59	0.1243	2.5571	0.1208	52.53	0.1701	19.5250	0.5241	0.0593	0.3507	0.1088
<b>RRT4</b>	Min	0.001	0.80	0.0081	0.0022	0.0084	0.0068	1	1	0.0144	2.2148	0.0306	1.0E-07	0.0034	0.1320	9E-07	1E-07	7E-06	1E-07
	Max	64.7	24.30	0.3210	0.5124	1.7367	3.9778	5	12	0.4483	2.7153	0.3896	862.08	1	111.46	0.9129	0.5534	0.8794	0.5559
	Mean	1.71	9.68	0.1095	0.0710	0.5855	0.5229	3.04	8.57	0.1289	2.5621	0.1135	44.83	0.2005	19.7750	0.5207	0.0968	0.3119	0.1456

**Note:**  $k$  represents the permeability,  $\phi$  and  $\phi_z$  denote the helium and normalized porosity, respectively, RQI and FZI present the reservoir quality index and flow zone indicator, respectively (Amaefule et al., 1993),  $R_{35}$  is the effective pore radius of Winland (Winland, 1972), GHE is the global hydraulic element of Corbett (Corbett and Potter, 2004), DRT is the discrete rock type of Shenawi (Shenawi et al., 2007), NPhi is Neutron porosity log, RHOB is density log, NMR  $\phi$  is porosity from NMR log, NMR  $k$  is permeability from NMR log, Image  $\phi$  is porosity from image log, GR is Gamma Ray log and calcite, clay, dolomite, and quartz are the volume fraction from mineralogy model.

The resulted RRTs according to K-means unsupervised classification algorithm were integrated and supported with several techniques including the  $R_{35}$  of Winland (Figure 4-13-a), FZI-RQI of Amaefule (Figure 4-13-b), the DRT values of Shenawi, and GHE of Corbett (Figure 4-13-c).



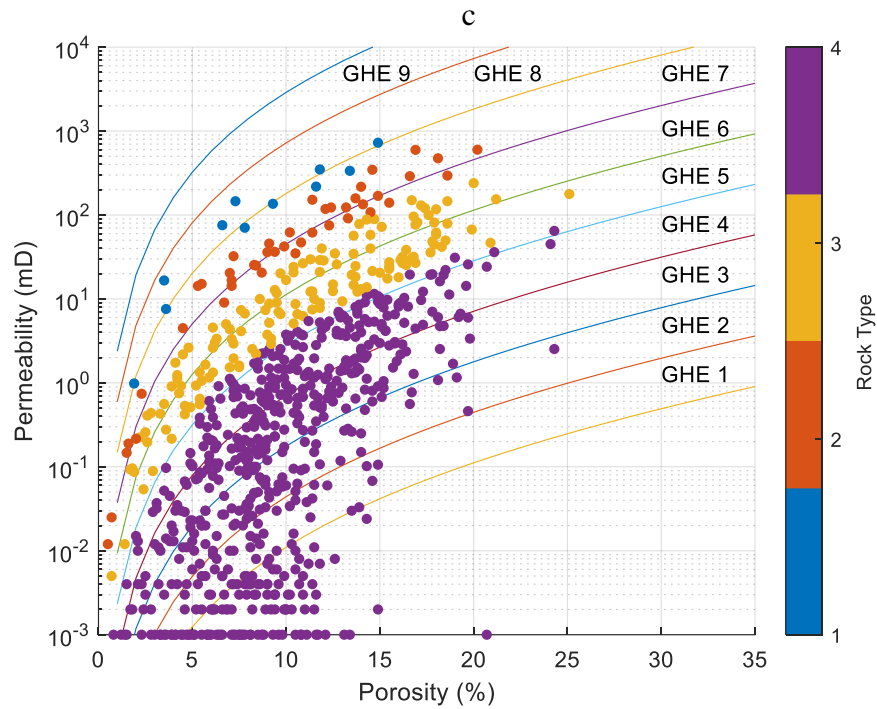


Figure 4-13. The resulted RRTs of the studied reservoir interval for the: a) Porosity-permeability graph merged with the  $R_{35}$  technique of Winland (Winland, 1972), b) RQI- $\phi_z$  plot and the segmented FZI values merged with the FZI-RQI technique of Amaefule (Amaefule et al., 1993), c) Porosity-permeability graph merged with the GHE technique of Corbett (Corbett and Potter, 2004).

Based on these plots four mathematical equations were created to predict the mean permeability (in  $mD$ ) with respect to the corresponding porosity values (in %) as follows.

$$RRT1: \quad k = 0.0495 \phi^{3.5158} \quad (4-10)$$

$$15 \leq DRT \leq 16 \quad 7 \leq GHE \leq 8 \quad 3.07 \leq R_{35} \leq 25.15$$

$$RRT2: \quad k = 0.0212 \phi^{3.411} \quad (4-11)$$

$$14 \leq DRT \leq 15 \quad 6 \leq GHE \leq 7 \quad 0.73 \leq R_{35} \leq 20.11$$

$$RRT3: \quad k = 0.01107 \phi^{3.0466} \quad (4-12)$$

$$12 \leq DRT \leq 14 \quad 5 \leq GHE \leq 6 \quad 0.299 \leq R_{35} \leq 10.17$$

$$RRT4: \quad k = 1.455e - 05 \phi^{4.621} \quad (4-13)$$

$$1 \leq DRT \leq 12 \quad 1 \leq GHE \leq 5 \quad 0.0068 \leq R_{35} \leq 3.98$$

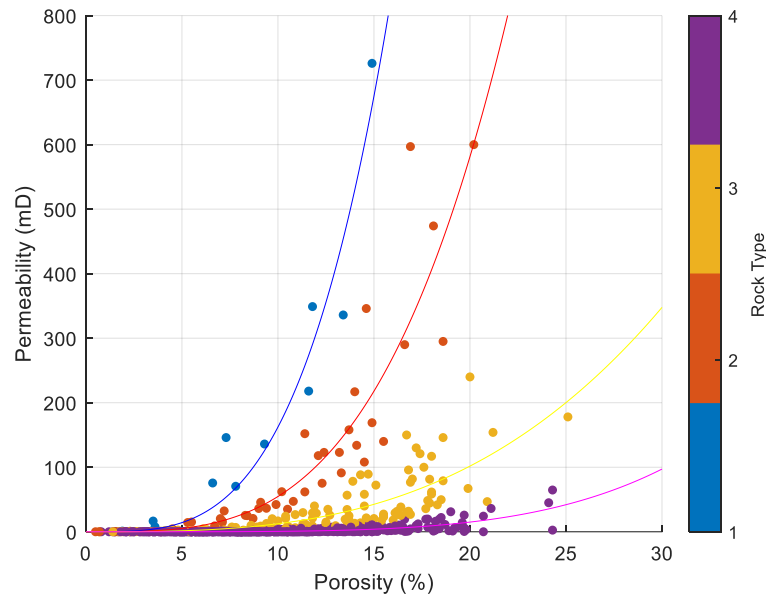


Figure 4-14. Porosity-permeability plot of the studied reservoir sequence and mathematical models of permeability estimation.

*RQI* could be a coordination sign of the capacity of reservoirs to transport fluids. Plots were generated to display the *RQI* values in relation to both permeability and porosity (Figure 4-15-a and b) for subdivided samples into different rock types to examine their key contributions to the reservoir quality. The RRTs contained various pore types (from tight to very good), resulting in the plots indicating a relatively small impact of porosity and permeability on the *RQI* parameter.

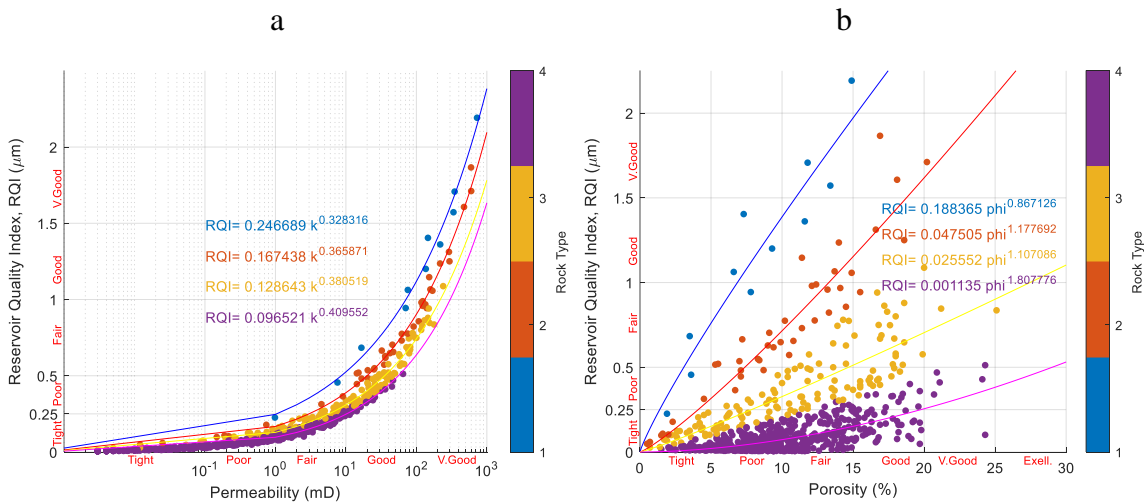


Figure 4-15. The resulted RRTs of the studied reservoir for the: a) *RQI*- permeability plot, b) *RQI*- porosity plot.

On the other hand, for reservoir quality evaluation, the *RQI*-*FZI* plot was used, where the sequence of wells is defined as tight to very good reservoir with the lowest quality attributed to RRT4, and the highest reservoir quality allocated to RRT1 (Figure 4-16).

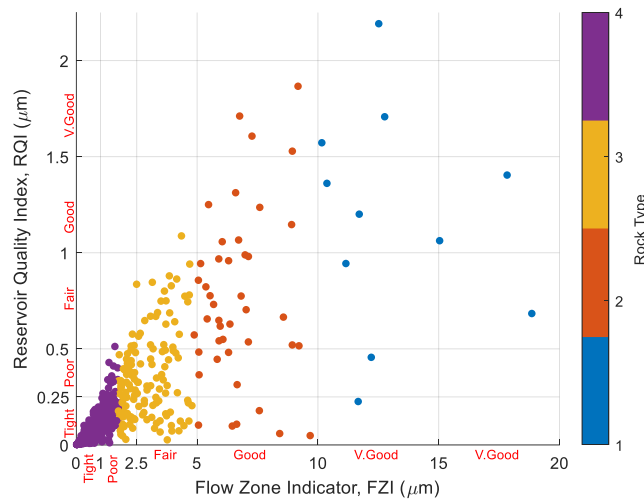


Figure 4-16. The resulted RRTs for the RQI-FZI plot of the studied reservoir.

RRT1, holds the best flow capacity with very good and good permeability (max. value 726 *mD*), interpreting the pore spaces as macro pores with higher permeability routes. The storage capacity is less than the other RRT with the porosity ranging from tight to fair (max. value 14.9%). The highest flow zone indicator is 18.85  $\mu\text{m}$  with mean of 13.11  $\mu\text{m}$  and the mean *RQI* of 1.16  $\mu\text{m}$ . The Winland curves demonstrate the maximum pore throat diameter of 25.15  $\mu\text{m}$ . The findings were presented in a manner where the various *GHE* fields were 7 and 8. The ranges of the well log data for all RRT are display in Table 4-2. Unfortunately, there was no available thin section and  $\mu\text{CT}$  images classified as RRT1.

RRT2, with maximum flow zone indicator and reservoir quality index of 9.68 and 1.86  $\mu\text{m}$ , respectively is the second-best for reservoir quality. It is with better porosity compared to RRT1 ranging from tight to good (max 20.2%), while the permeability is lower than that of RRT1 ranging from poor to very good (max 600 *mD*). The interpretation of the pore spaces suggests that they are comprised of both mesopores and macropores, while the maximum pore throat radius is reported as 20.1  $\mu\text{m}$ . The *GHE* of this kind varies between 6 and 7. In this RRT, both categories of reworked and in situ facies, such as shrubstonesand spherulitestones were found. All facies with low to moderate cementation, preserve depositional features with the predominance of interparticle. Vugular porosity and growth framework also occurred, in some cases, the growth framework porosity was enhanced by the dissolution. From the  $\mu\text{CT}$ , four plugs were classified as RRT2, two plugs of reworked facies (grainstone and rudstone), one shrubstone, and one spherulitestone. The mean pore radius, mean throat radius, and mean tortuosity were 69  $\mu\text{m}$ , 50  $\mu\text{m}$ , and 2, respectively (Figure 4-17 and Table 4-4).

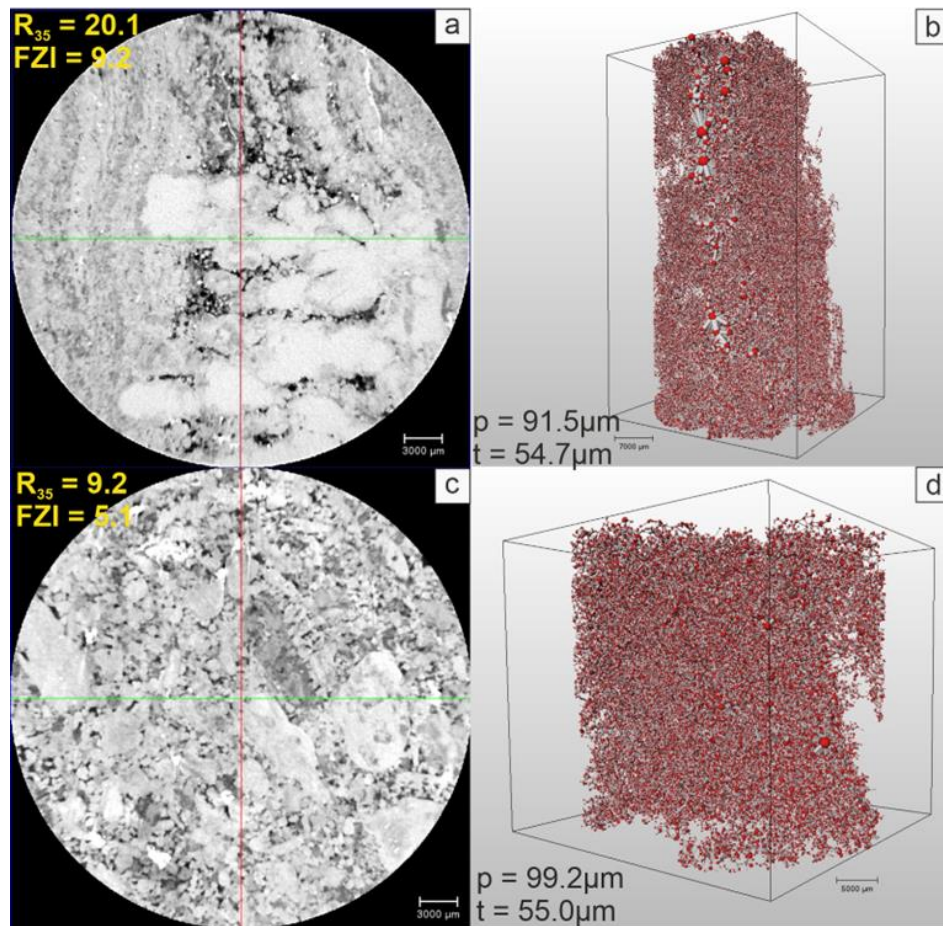


Figure 4-17. Aspects of plugs from reservoir rock type 2 showing average values of  $R_{35}$ , FZI, mean pore radius ( $p$ ) and mean throat radius ( $t$ ). a, b) CT-scan of crystal shrub-dominated facies with growth framework porosity and its distribution of pores and throats with tortuosity of 1.9, c, d) CT-scan of reworked facies with interparticle porosity and its distribution of pores and throats with tortuosity of 2.6.

For RRT3 the mean  $FZI$  and  $RQI$  show values of 2.8 and  $0.35 \mu m$ . The pore spaces classified as Micro and Meso pores with porosity from tight to excellent (average value 25.1%). the  $R_{35}$  value shows the average of  $3.18 \mu m$  and permeability values displays the wide extend from very tight to very good (average value  $27.06 mD$ ). This RRT follow GHE of 5 and 6. Reworked facies (grainstones and rudstones) and shrubstones, both with moderate to high cementation were classified as RRT3. Diagenetic processes were mainly dolomite cementation and silicification. Dissolution also acted by increasing some pores, as an example of growth framework porosity. The porosity in this RRT was predominantly intercrystalline and interparticle, with intraparticle occurrence in almost all thin sections, growth framework, vulgar, moldic, and the presence of fractures. From the PNM  $\mu CT$  analysis following results were obtained: the mean pore radius, mean throat radius, and mean tortuosity were  $67 \mu m$ ,  $49 \mu m$ , and 2.5, respectively (Figure 4-18 and Table 4-4).

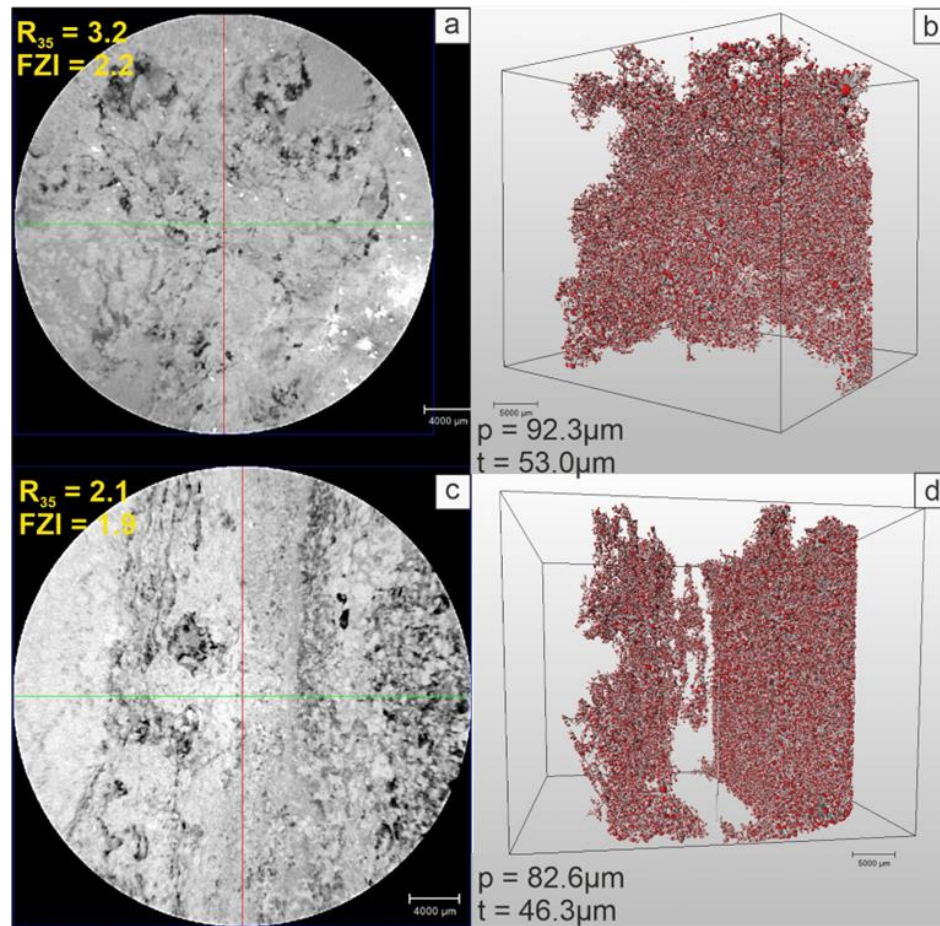


Figure 4-18. Aspects of crystal shrub-dominated facies plugs from reservoir rock type 3 showing average values of  $R_{35}$ ,  $FZI$ , mean pore radius ( $p$ ) and mean throat radius ( $t$ ). a, b) CT-scan with vug porosity and silica and dolomite cementation and its distribution of pores and throats with tortuosity of 3, c, d) CT-scan with intercrystalline porosity and its distribution of pores and throats with tortuosity of 1.9. The distribution of pores and throats was affected by the cementation process.

The RRT4 has the lowest reservoir quality with mean  $FZI$  and  $RQI$  of  $0.58$  and  $0.07 \mu m$ , respectively. From tight to very good, porosity ratings range from  $0.8$  to  $24.3\%$ . The permeability values, on the other hand, range from very tight to good, with an average of  $1.71 mD$ . The pore space shifts in the range from Nano to Meso pores. The greatest pore throat radius is measured as  $3.98 \mu m$  and the GHE distributed between 1 and 5. In this RRT, there are samples representing all facies, such as shrubstones facies, reworked facies, and spherulitestones, however, the reworked facies represented more than  $80\%$  of the thin sections. The cementation is moderate to high, which compromised the porosity dominating the intercrystalline porosity. Other porosity types are interparticle, intraparticle, vug, moldic, and rare occurrences of fracture and growth framework porosity. From the  $\mu CT$ , six plugs were classified as RRT4, five plugs of reworked facies (grainstone and rudstone), and one shrubstone. The mean pore radius, mean throat radius, and mean tortuosity were  $58 \mu m$ ,  $41 \mu m$ , and  $2.3$ , respectively (Figure 4-19 and Table 4-4).

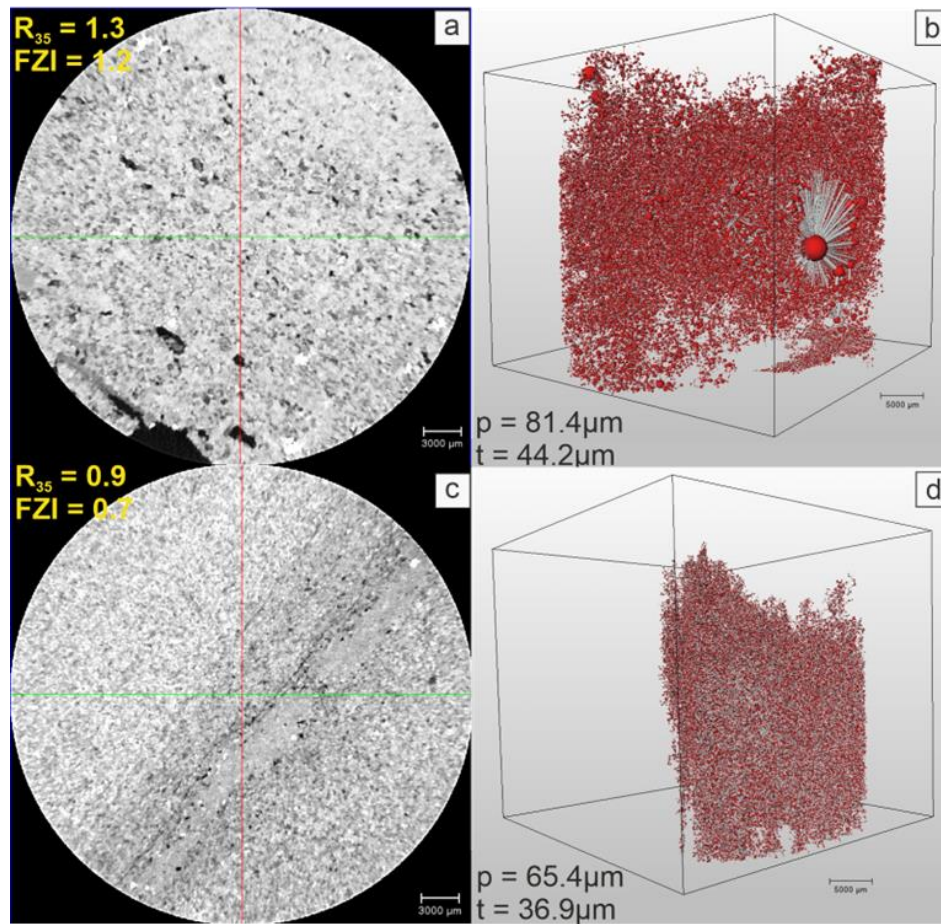


Figure 4-19. Aspects of plugs from reservoir rock type 4 showing average values of R35, FZI, mean pore radius ( $p$ ) and mean throat radius ( $t$ ). a, b) CT-scan of intraclastic grainstone moderated cemented with dominated interparticle porosity and its distribution of pores and throats with tortuosity of 2.4, c, d) CT-scan of spherulitic grainstone with intercrystalline porosity and its distribution of pores and throats with tortuosity of 2.2.

Table 4-4. Summary of the mean value of pore network characteristics of different reservoir rock types.

Total pore spaces		Total pore spaces			Connected pore spaces		
		RRT 2	RRT 3	RRT 4	RRT 2	RRT 3	RRT 4
Number of pores		304745	205534	415973	152696	102506	170114
Number of throats		354009	245819	447835	314621	217787	364457
Coordination number	Min	0	0	0	1.00	1.00	1.00
	Mean	2.32	2.33	2.17	4.09	4.16	4.26
	Max	136.50	113.50	114.50	130.25	103.50	109.83
Pore radius ( $\mu\text{m}$ )	Min	2.37	2.04	2.01	1.98	1.88	1.82
	Mean	69.37	66.79	57.71	88.47	87.42	72.05
	Max	660.52	682.13	576.48	658.62	682.38	572.18
Throat radius ( $\mu\text{m}$ )	Min	2.27	1.98	1.92	1.86	1.78	1.73
	Mean	50.07	49.09	41.29	50.41	49.67	40.56
	Max	401.43	466.91	400.95	398.41	463.32	390.02
Tortuosity		2.00	2.47	2.32	2.08	2.34	2.56
Aspect ratio		3.24	3.31	512.64	3.34	3.37	3.20

#### 4.3.4 HYDRAULIC FLOW UNITS (HFUS)

Stratigraphic modified Lorenz (SML) graph was utilized to partition the reservoir sections into several separate flow units through the inclination of the fitted line segments (Figure 4-20). In this

plot, steep slope segments with sharp angles indicate high flow capacity compared to storage capacity, resulting in a high-quality *HFU*, while gentle slope segments with low or angles approaching zero indicate very low flow capacity, resulting in very low-quality *HFU* or sealing layers such as barrier zones or baffle. The SML plots for well A and B, along with the defined *HFUs*, are displayed in Figure 4-20-a and b.

Application of *SML* graph to well A shows the existence of five *HFUs* (Figure 4-20-a). *HFU*2 and 4 are responsible for around 60% of the flow capacity, while the remaining fluid flow contribution is conveyed between the *HFU*1 and 5 and the *HFU*3 acts as a barrier (5% flow capacity). Whereas, the *SML* graph of B well shows that about 80% of the flow capacity is contributed by *HFU*1 and 3, while *HFU*4 acts as a barrier with around 3% of flow capacity (Figure 4-20-b).

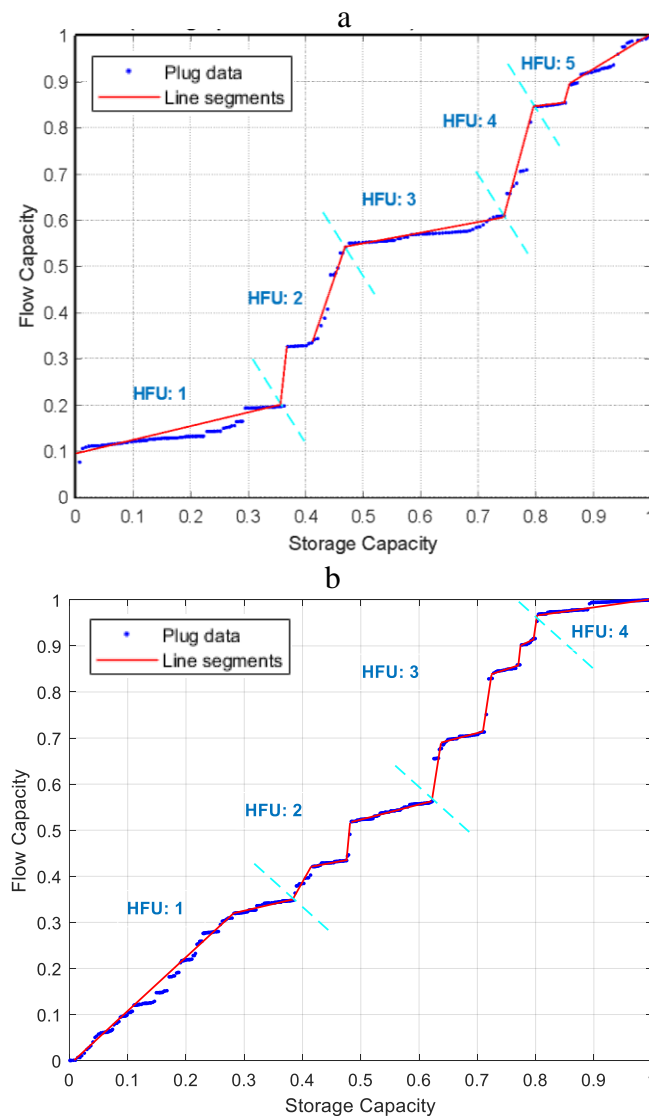


Figure 4-20. Stratigraphic modified Lorenz (SML) plot: a) well A, b) well B.

### 4.3.5 POROSITY, PERMEABILITY, AND ROCK TYPE PREDICTION BY MACHINE LEARNING ALGORITHMS

In this study, two deep learning models, ResNet and 1D CNN, were applied and trained on a well-log dataset to predict plug porosity ranging from 0.5 to 25.1 %. The training data consisted of 80% of the dataset, with the remaining 20% used as the testing and validation set. Both models were trained for 1000 epochs and the training and validation loss functions were monitored during training. The loss functions versus epoch plots for each model during training and validation are shown in Figure 4-21. Both models showed a decreasing trend in the loss function over the epochs, indicating successful learning of the data patterns (Since the batch size is not same as full dataset size, although the overall trend of loss function is reducing, there is oscillation in the loss function). The 1D CNN model reached a lower loss value than the ResNet model in both the training and validation phases, indicating better generalization ability of the 1D CNN model.

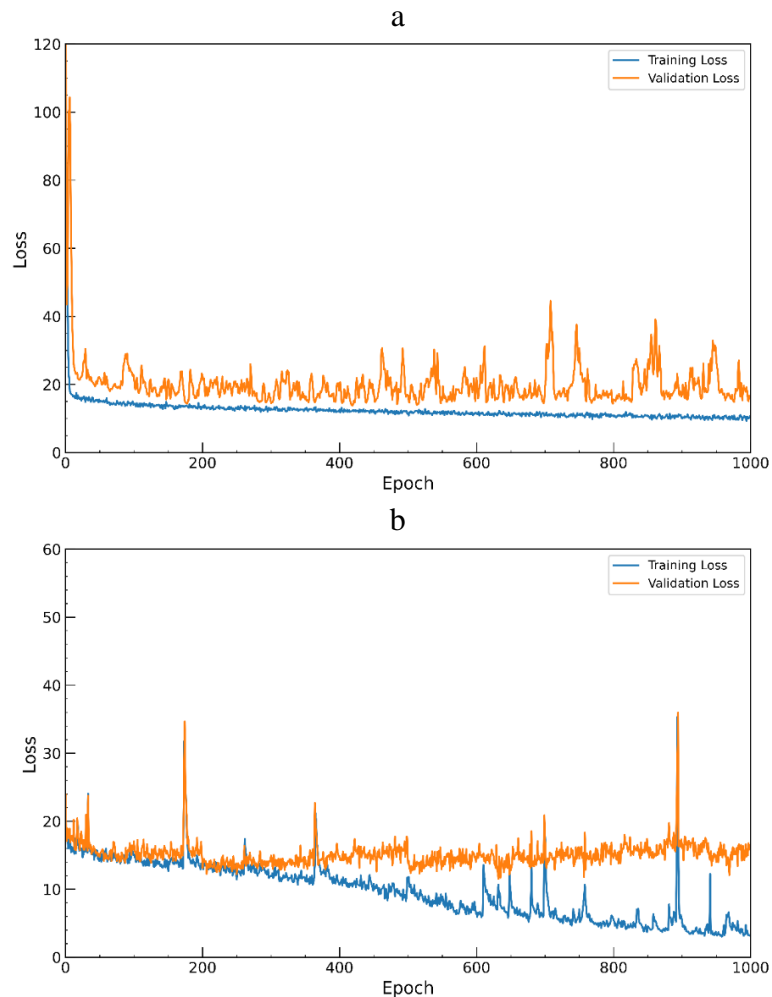


Figure 4-21. The loss function curves for porosity prediction for: a) ResNet model, b)1D CNN model.

The performance of the ResNet and 1D CNN models was evaluated using the mean squared error (MSE) metric. The MSE values for the ResNet and 1D CNN models on the test set were 13.79 and 11.85, respectively, and 12.3 and 3.19 on the train set. This indicates that the 1D CNN model outperformed the ResNet model in terms of predictive accuracy.

Figure 4-22 shows the plug porosity and predicted porosity versus depth plots for the ResNet and 1D CNN models for wells A and B. The 1D CNN model shows better alignment between the predicted and actual porosity values compared to the ResNet model and provides more accurate predictions. Figure 4-23 shows the cross plot of plug porosity versus predicted porosity for the ResNet and 1D CNN models.

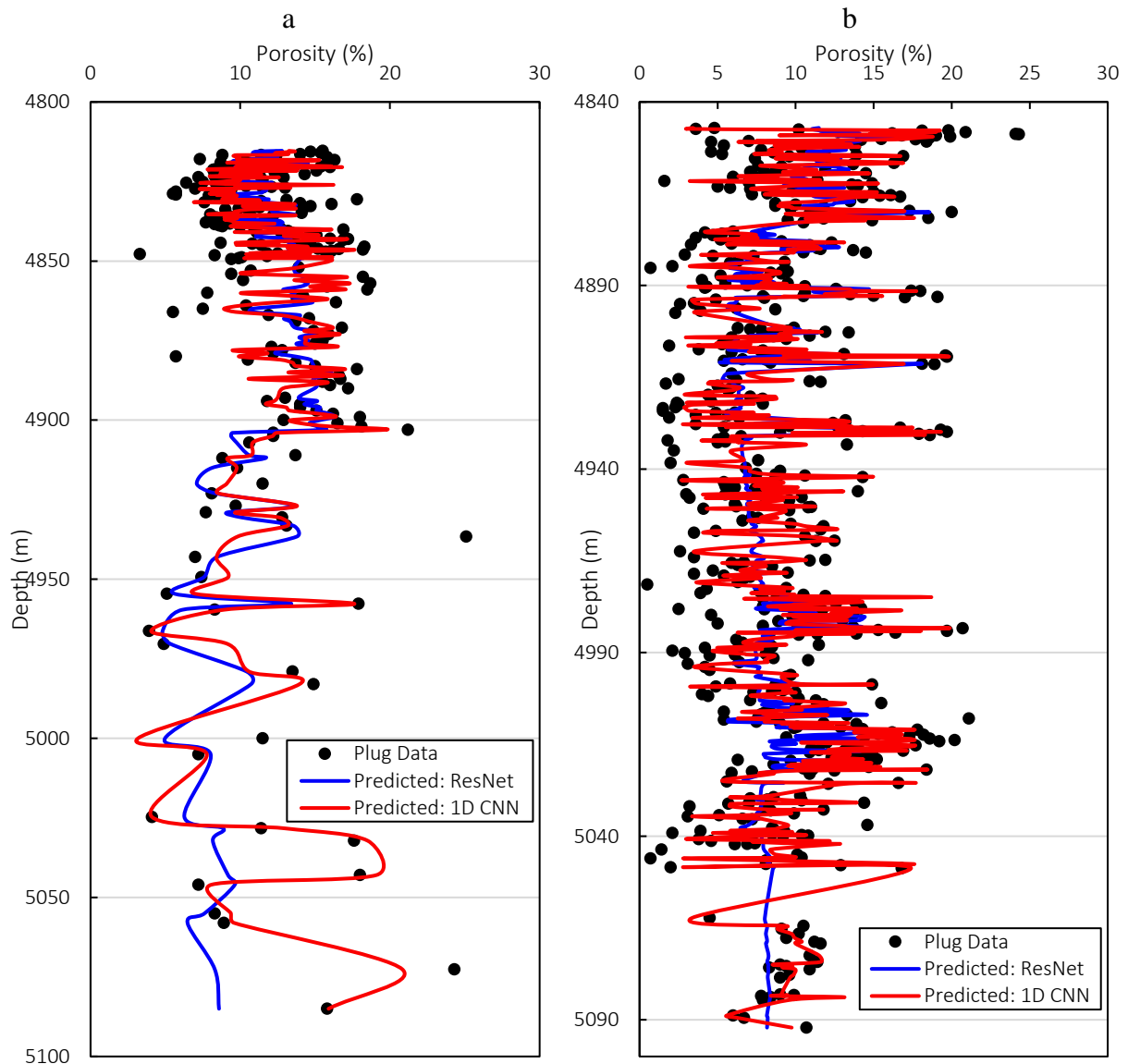


Figure 4-22. The plug porosity and predicted porosity using ResNet and 1D CNN models for: a) Well A, b) Well B.

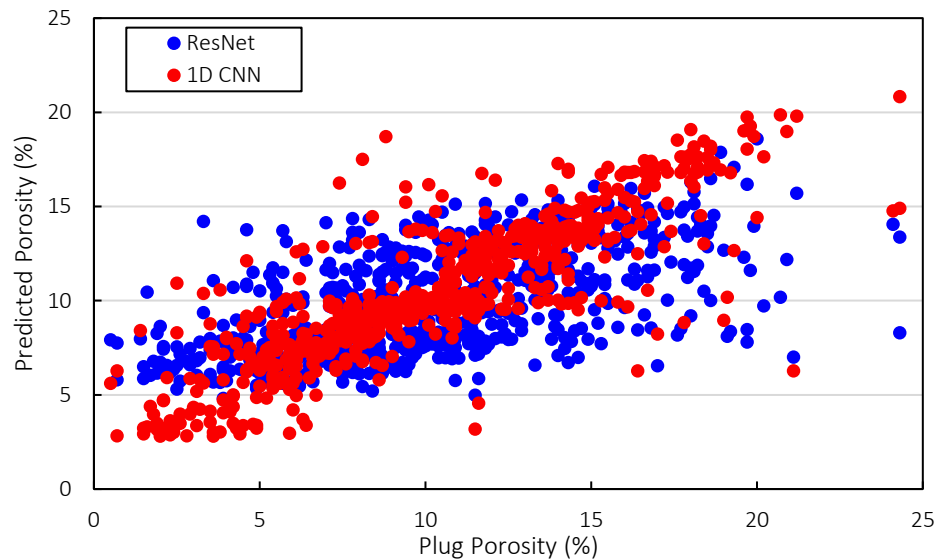


Figure 4-23 Cross plot of plug porosity versus predicted porosity for ResNet and 1D CNN models. The XGBoost algorithm was applied to predict rock type based on well log data. Again, the dataset was randomly divided into 80% training and 20% validation sets. The XGBoost model was trained, and its performance was evaluated. The XGBoost model achieved an accuracy of 93.5 % on the training set and 90.3 % on the validation set, indicating good generalization ability. The model's performance was evaluated further by plotting the calculated (using K-means unsupervised learning algorithm) and predicted (using XGBoost algorithm) rock types for two wells, as shown in Figure 4-24. Red arrows indicate the depths at which the calculated and predicted rock types differ. The XGBoost model was able to accurately predict the rock type for most of the depths, but there were few depths at which the predicted and actual rock types differed.

A cross plot was also generated to visualize the relationship between the predicted rock type (using XGBoost algorithm) and actual rock type (using K-means unsupervised learning algorithm), as shown in Figure 4-25. The plot shows the amount of data points for each combination of predicted and actual rock types, allowing us to evaluate the model's performance in more detail. The diagonal of the plot represents the instances where the predicted rock type matches the actual rock type. The majority of data points fall along the diagonal, indicating that the model is able to accurately predict the rock type. However, there are some data points that fall outside the diagonal, indicating errors in the model's predictions. Overall, the XGBoost algorithm showed promising results in predicting rock type based on well log data, achieving high accuracy on both the training and validation sets.

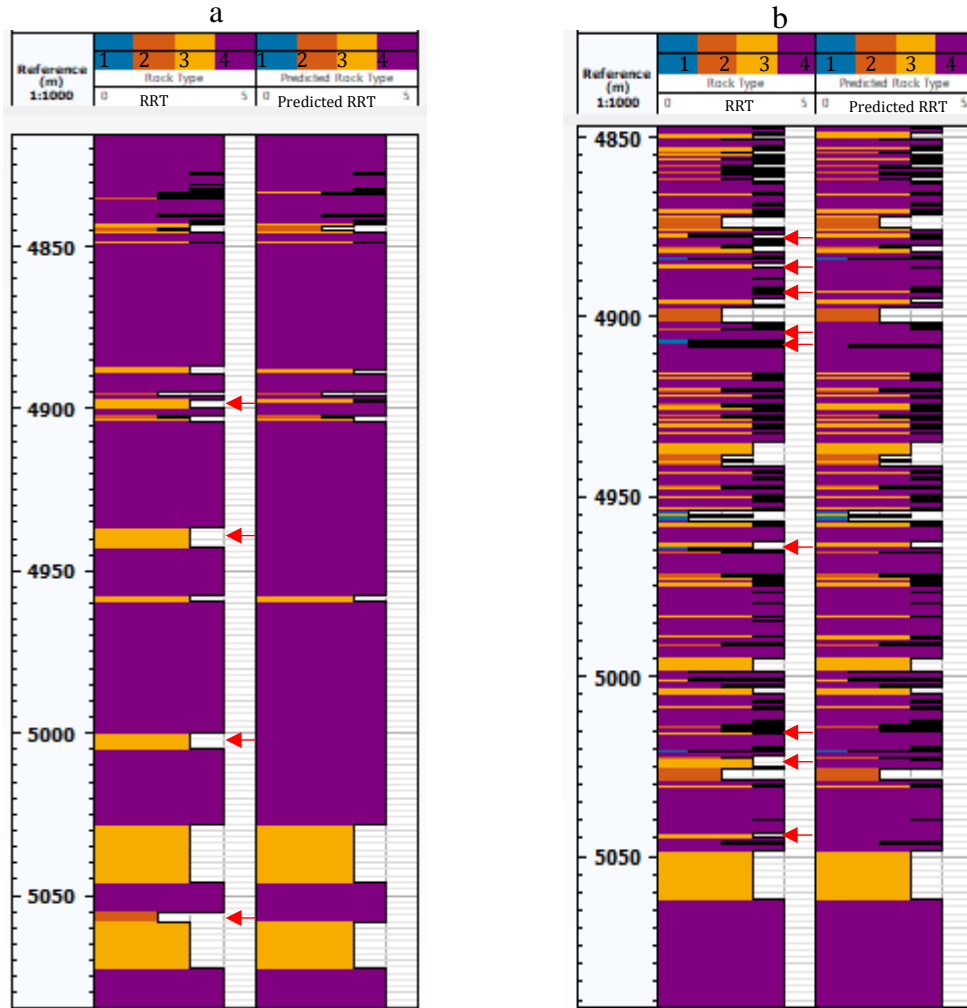


Figure 4-24. The actual and predicted rock type using XGBoost model for: a) Well A, b) Well B, with red arrows indicating the depths at which the two rock types differ.

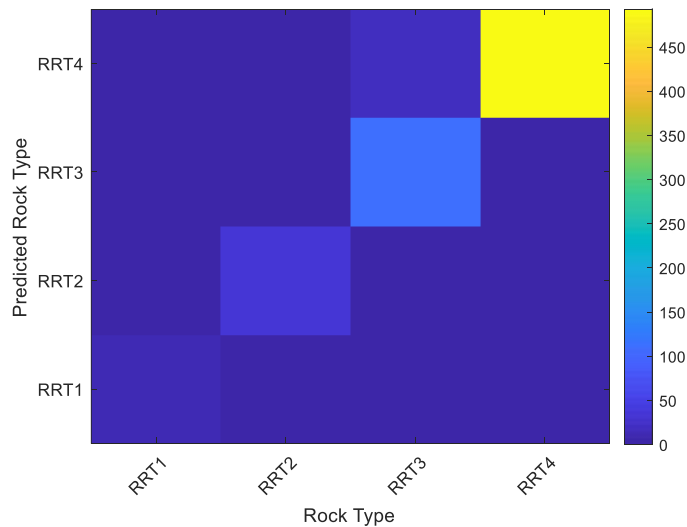


Figure 4-25. Cross plot of predicted versus actual rock types, with the percentage of data points labeled for each combination of rock types.

The porosity and rock type predictions were then used to estimate plug permeability, where we presented four mathematical models (Equations (4-10) to (4-13)) for each of the four defined rock types in the previous section. These models calculate plug permeability from predicted plug porosity for each predicted reservoir rock type. To validate our approach, these mathematical formulas for each corresponding predicted rock type were used and permeability values were calculated with predicted porosity obtained from the two different deep-learning approaches. Figure 4-26 illustrates a comparison of permeability versus depth for plug data and predicted permeability obtained from correlation with porosity values of the two different machine learning approaches for the two wells studied. The mean absolute error ( $MAE = \frac{1}{N} \sum_{i=1}^N |y_i - \hat{y}_i|$ ) values for permeability prediction from porosity values were calculated to be 8.64 for the CNN model data and 12.35 for the ResNet model data. Figure 4-27 shows the cross plot of plug permeability versus predicted permeability.

These results have significant implications for the use of deep learning models in reservoir characterization and management, which can improve our understanding of subsurface reservoir properties by enabling the evaluation of a reservoir even with incomplete datasets. Machine learning predictions based on available data can help to fill in the gaps and make accurate predictions, which can be vital in effective reservoir management. However, the differences between predicted and actual values at certain depths could be due to various factors, such as the complexity of the geological formation or measurement errors in well log or plug petrophysical data. These differences underscore the challenges associated with accurately predicting reservoir properties in heterogeneous porous media using well log data alone, highlighting the need for further research to improve our understanding of subsurface geological formations.

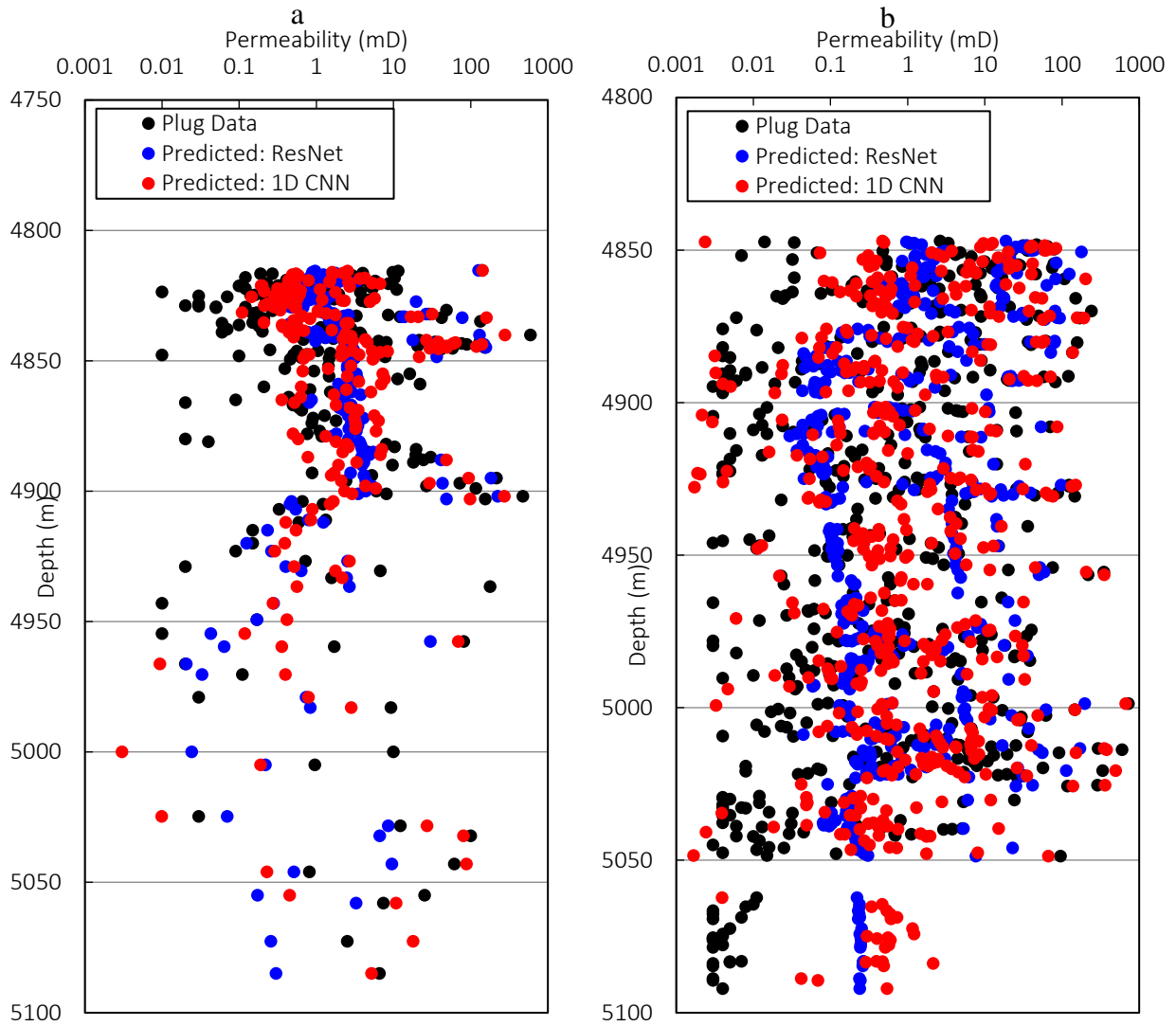


Figure 4-26. The plug permeability and predicted permeability using mathematical formulas for each reservoir rock type and correlation with predicted porosity values from ResNet and 1D CNN models for: a) Well A, b) Well B.

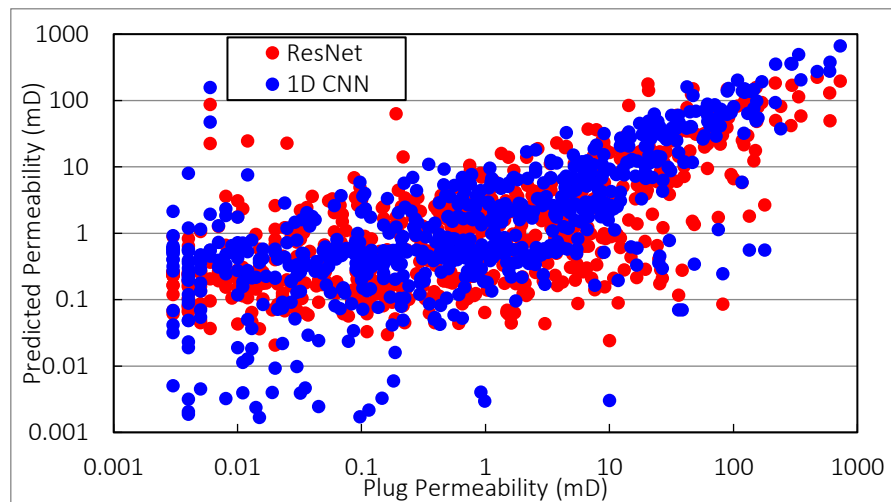


Figure 4-27. Cross plot of plug permeability versus predicted permeability using mathematical formulas for each reservoir rock type and correlation with predicted porosity values from ResNet and 1D CNN models.

#### 4.4 CONCLUSIONS

- According to K-means unsupervised classification algorithm, supported with several conventional techniques, the sequences of two wells in the Barra Velha Formation in the Santos Basin discriminated into a number of reservoir rock types (RRTs) and hydraulic flow units (HFUs) by integrating the well log data, plug data,  $\mu$ CT studies, and thin section description.
- Number 4 was selected as an optimum value of rock typing clusters, employing the elbow method by calculating the sum of squared error deviation of data points belonging to a cluster versus the cluster's centroid.
- The quality of the four defined rock types (RRT1 to RRT4) was evaluated using reservoir quality index (RQI), flow zone indicator (FZI), effective pore radius ( $R_{35}$ ), global hydraulic element (GHE), and discrete rock types (DRT). RRT1 and RRT2 were determined to be of "Very Good" and "Good" quality, respectively, while RRT3 and RRT4 had "Poor to fair" and "Tight to poor" reservoir quality.
- The studied sequence was partitioned into five and four HFUs for well A and B, respectively. For well A, HFU2 and 4 were responsible for around 60% of the flow capacity, and the HFU3 acted as a barrier. While HFU1 and 3 supplied around 80% of the flow capacity for well B, and HFU4 behaved as a barrier.
- Three groups of facies were characterized from petrological descriptions supported by thin sections from sub-salt lacustrine carbonates from Barra Velha Formation: crystal shrub-dominated facies, reworked facies and spherulitestone facies.
- The defined reservoir rock types showed a variety of facies and porosity type that compound it. The porosity in the RRT2 was interparticle, while for RRT3 and RRT4 was mainly intercrystalline. Mean pore radius, throat radius and tortuosity were: (RRT2: 91  $\mu$ m, 53  $\mu$ m, and 1.9); (RRT3: 87  $\mu$ m, 50  $\mu$ m, and 2.5), and (RRT4: 72  $\mu$ m, 41  $\mu$ m, and 2.3).
- Deep learning models of ResNet and 1D CNN, were successfully trained on well-log datasets to predict plug porosity with good accuracy.
- The 1D CNN model outperformed the ResNet model in terms of predictive accuracy, demonstrating better generalization ability.

- The XGBoost algorithm was also applied to predict rock type based on well log data, achieving high accuracy on both the training and validation sets.
- The porosity, permeability, and rock type prediction results demonstrate the potential of machine learning in reservoir characterization and management, providing valuable insights for effective reservoir management and production optimization.

## **4.5 ACKNOWLEDGMENTS**

We gratefully acknowledge the support of EPIC – Energy Production Innovation Center, hosted by the University of Campinas (UNICAMP) and sponsored by FAPESP – São Paulo Research Foundation (2017/15736-3 process). We acknowledge the support and funding from Equinor Brazil and the support of ANP (Brazil’s National Oil, Natural Gas and Biofuels Agency) through the R&D levy regulation. Acknowledgements are extended to the Center of Energy and Petroleum Studies (CEPETRO) and School of Mechanical Engineering (FEM).

## 4.6 REFERENCES

- Ahmadi, S., Motie, M., Soltanmohammadi, R., 2020. Proposing a modified mechanism for determination of hydrocarbons dynamic viscosity, using artificial neural network. *Petroleum Science and Technology* 38, 699-705.
- Amaefule, J.O., Altunbay, M., Tiab, D., Kersey, D.G., Keelan, D.K., 1993. Enhanced reservoir description: using core and log data to identify hydraulic (flow) units and predict permeability in uncored intervals/wells, SPE annual technical conference and exhibition. OnePetro.
- Beasley, C.J., Fiduk, J.C., Bize, E., Boyd, A., Frydman, M., Zerilli, A., Dribus, J.R., Moreira, J.L., Pinto, A.C., 2010. Brazil's presalt play. *Oilfield Review* 22, 28-37.
- Belila, A.M.P., Basso, M., Chinelatto, G.F., Kuroda, M.C., Vidal, A.C., 2020. Pore typing using nuclear magnetic resonance, an example with samples from cretaceous pre-salt lacustrine carbonates in the Santos Basin, Brazil. *Journal of Petroleum Science and Engineering* 190, 107079.
- Bhatt, A., Helle, H.B., 2002. Committee neural networks for porosity and permeability prediction from well logs. *Geophysical Prospecting* 50, 645-660.
- Bize Forest, N., Abbots, F., Baines, V., Boyd, A., 2019. Identifying Reservoir Rock Types Using a Modified FZI Technique in the Brazilian Pre-Salt, Offshore Technology Conference Brasil. OnePetro.
- Bruhn, C.H., Pinto, A.C., Johann, P.R., Branco, C., Salomão, M.C., Freire, E.B., 2017. Campos and Santos basins: 40 Years of reservoir characterization and management of shallow-to ultra-deep water, post-and pre-salt reservoirs-Historical overview and future challenges, OTC Brasil. OnePetro.
- Carlotto, M.A., da Silva, R.C.B., Yamato, A.A., Trindade, W.L., Moreira, J.L.P., Fernandes, R.A.R., Ribeiro, O.J.S., Gouveia Jr, W.P., Carminati, J.P., Qicai, D., 2017. Libra: A newborn giant in the Brazilian Presalt Province.
- Carman, P.C., 1937. Fluid flow through granular beds. *Trans. Inst. Chem. Eng.* 15, 150-166.
- Chafetz, H., Barth, J., Cook, M., Guo, X., Zhou, J., 2018. Origins of carbonate spherulites: implications for Brazilian Aptian pre-salt reservoir. *Sedimentary Geology* 365, 21-33.
- Chang, H.K., Kowsmann, R.O., Figueiredo, A.M.F., Bender, A., 1992. Tectonics and stratigraphy of the East Brazil Rift system: an overview. *Tectonophysics* 213, 97-138.
- Chen, T., Guestrin, C., 2016. Xgboost: A scalable tree boosting system, *Proceedings of the 22nd acm sigkdd international conference on knowledge discovery and data mining*, pp. 785-794.
- Choquette, P.W., Pray, L.C., 1970. Geologic nomenclature and classification of porosity in sedimentary carbonates. *AAPG bulletin* 54, 207-250.
- Claes, H., Erthal, M.M., Soete, J., Özkul, M., Swennen, R., 2017. Shrub and pore type classification: Petrography of travertine shrubs from the Ballık-Belevi area (Denizli, SW Turkey). *Quaternary International* 437, 147-163.
- Corbett, P.W.M., Potter, D.K., 2004. Petrotyping: A basemap and atlas for navigating through permeability and porosity data for reservoir comparison and permeability prediction, Paper SCA2004-30 presented at the International Symposium of the Society of Core Analysts.
- do Nascimento, J.B.d.S., Soares, J.A., Medeiros, L.C., Raposo, G., Dias, C.H., 2015. Petrofísica Computacional aplicada à caracterização dos tipos de porosidade em rochas carbonáticas, 14th International Congress of the Brazilian Geophysical Society & EXPOGEF, Rio de Janeiro, Brazil, 3-6 August 2015. Brazilian Geophysical Society, pp. 656-659.
- Duong, M.Q., Le Hong Lam, B.T.M., Tu, G.Q.H., Hieu, N.H., 2019. Combination of K-Mean clustering and elbow technique in mitigating losses of distribution network. *GMSARN International* 13, 153-158.

- El Sawy, M.Z., Abuhagaza, A.A., Nabawy, B.S., Lashin, A., 2020. Rock typing and hydraulic flow units as a successful tool for reservoir characterization of Bentiu-Abu Gabra sequence, Muglad basin, southwest Sudan. *Journal of African Earth Sciences* 171, 103961.
- Erthal, M.M., Capezzuoli, E., Mancini, A., Claes, H., Soete, J., Swennen, R., 2017. Shrub morphotypes as indicator for the water flow energy-Tivoli travertine case (Central Italy). *Sedimentary Geology* 347, 79-99.
- Farias, F., Szatmari, P., Bahniuk, A., Franca, A.B., 2019. Evaporitic carbonates in the pre-salt of Santos Basin—Genesis and tectonic implications. *Marine and Petroleum Geology* 105, 251-272.
- Gholami, A., Amirpour, M., Ansari, H.R., Seyedali, S.M., Semnani, A., Golsanami, N., Heidaryan, E., Ostadhassan, M., 2022. Porosity prediction from pre-stack seismic data via committee machine with optimized parameters. *Journal of Petroleum Science and Engineering* 210, 110067.
- Gomes, J., Bunevich, R., Tedeschi, L., Tucker, M., Whitaker, F., 2020. Facies classification and patterns of lacustrine carbonate deposition of the Barra Velha Formation, Santos Basin, Brazilian Pre-salt. *Marine and Petroleum Geology* 113, 104176.
- Gunter, G., Spain, D., Viro, E., Thomas, J., Potter, G., Williams, J., 2014. Winland pore throat prediction method—a proper retrospect: new examples from carbonates and complex systems, SPWLA 55th Annual Logging Symposium. *OnePetro*.
- Hadavimoghaddam, F., Ostadhassan, M., Heidaryan, E., Sadri, M.A., Chapanova, I., Popov, E., Cheremisin, A., Rafieepour, S., 2021. Prediction of dead oil viscosity: Machine learning vs. classical correlations. *Energies* 14, 930.
- Harbola, S., Coors, V., 2019. One dimensional convolutional neural network architectures for wind prediction. *Energy Conversion and Management* 195, 70-75.
- Heilbron, M., Mohriak, W.U., Valeriano, C.M., Milani, E.J., Almeida, J., Tupinambá, M., 2000. From collision to extension: the roots of the southeastern continental margin of Brazil. *Geophysical Monograph-American Geophysical Union* 115, 1-32.
- Hosa, A., Wood, R., Corbett, P., de Souza, R.S., Roemers, E., 2020. Modelling the impact of depositional and diagenetic processes on reservoir properties of the crystal-shrub limestones in the ‘Pre-Salt’ Barra Velha Formation, Santos Basin, Brazil. *Marine and Petroleum Geology* 112, 104100.
- IBM, 2020. Supervised Learning. IBM Cloud Education, pp. <https://www.ibm.com/cloud/learn/supervised-learning>.
- Iraji, S., Ayatollahi, S., 2019. Experimental investigation on asphaltene biodegradability using microorganism: cell surface properties’ approach. *Journal of Petroleum Exploration and Production Technology* 9, 1413-1422.
- Iraji, S., Soltanmohammadi, R., De Almeida, T.R., Munoz, E.R., Basso, M., Vidal, A.C., 2022a. Laboratory and numerical examination of oil recovery in Brazilian Pre-salt analogues based on CT images, Third EAGE Conference on Pre Salt Reservoirs.
- Iraji, S., Soltanmohammadi, R., Munoz, E.R., Basso, M., Vidal, A.C., 2023. Core scale investigation of fluid flow in the heterogeneous porous media based on X-ray computed tomography images: Upscaling and history matching approaches. *Geoenergy Science and Engineering*, 211716.
- Iraji, S., Soltanmohammadi, R., Munoz, E.R., Winter, A., de Almeida, R.V., Vidal, A.C., 2022b. Experimental Investigation of Waterflooding Performance by Increasing Copper Ions in Brazilian Pre-Salt Rock, 83rd EAGE Annual Conference & Exhibition. *European Association of Geoscientists & Engineers*, pp. 1-5.

- Iraji, S., Soltanmohammadi, R., De Almeida, T., Rodrigues, Munoz, E.R., Vidal, A.C., 2022c. Experimental investigation of single-phase flow pattern in highly heterogeneous carbonates rocks, Rio Oil & Gas 2022. IBP, Rio de Janeiro | Brasil.
- Khan, A., Sohail, A., Zahoor, U., Qureshi, A.S., 2020. A survey of the recent architectures of deep convolutional neural networks. *Artificial intelligence review* 53, 5455-5516.
- Kolodzie, S., 1980. Analysis of pore throat size and use of the Waxman-Smiths equation to determine OOIP in Spindle Field, Colorado, SPE annual technical conference and exhibition. OnePetro.
- Kozeny, J., 1927. *Über kapillare leitung der wasser in boden*. Royal Academy of Science, Vienna, Proc. Class I 136, 271-306.
- Lim, J.-S., Kim, J., 2004. Reservoir porosity and permeability estimation from well logs using fuzzy logic and neural networks, SPE Asia Pacific Oil and Gas Conference and Exhibition. OnePetro.
- Lima, B.E.M., De Ros, L.F., 2019. Deposition, diagenetic and hydrothermal processes in the Aptian Pre-Salt lacustrine carbonate reservoirs of the northern Campos Basin, offshore Brazil. *Sedimentary Geology* 383, 55-81.
- Lima, M., Pontedeiro, E., Ramirez, M., Boyd, A., Van Genuchten, M.T., Borghi, L., Couto, P., Raouf, A., 2020. Petrophysical correlations for the permeability of coquinas (carbonate rocks). *Transport in Porous Media* 135, 287-308.
- Maglio-Johnson, T., 2001. Flow unit definition using petrophysics in a deep water turbidite deposit, Lewis Shale, Carbon County, Wyoming. Colorado School of Mines.
- Maiti, S., Krishna Tiwari, R., Kumpel, H.-J., 2007. Neural network modelling and classification of lithofacies using well log data: a case study from KTB borehole site. *Geophysical Journal International* 169, 733-746.
- Mohriak, W., Nemčok, M., Enciso, G., 2008. South Atlantic divergent margin evolution: rift-border uplift and salt tectonics in the basins of SE Brazil. Geological Society, London, Special Publications 294, 365-398.
- Moreira, J.L.P., Madeira, C.V., Gil, J.A., Machado, M.A.P., 2007. bacia de Santos. *Boletim de Geociencias da PETROBRAS* 15, 531-549.
- Motie, M., Bemani, A., Soltanmohammadi, R., 2018. On The Estimation Of Phase Behavior Of CO<sub>2</sub>-Based Binary Systems Using ANFIS Optimized By GA Algorithm, Fifth CO<sub>2</sub> Geological Storage Workshop. European Association of Geoscientists & Engineers, pp. 1-5.
- Okon, A.N., Adewole, S.E., Uguma, E.M., 2021. Artificial neural network model for reservoir petrophysical properties: porosity, permeability and water saturation prediction. *Modeling Earth Systems and Environment* 7, 2373-2390.
- Omeje, E.T., Obiora, D.N., Okeke, F.N., Ugbor, D.O., Ibuot, J.C., Akpan, A.S., 2022. Aquifer flow unit analysis using stratigraphic modified Lorenz plot: a case study of Edem, eastern Nigeria. *Journal of Engineering and Applied Science* 69, 1-13.
- Qi, L., Carr, T.R., 2006. Neural network prediction of carbonate lithofacies from well logs, Big Bow and Sand Arroyo Creek fields, Southwest Kansas. *Computers & Geosciences* 32, 947-964.
- Rebello, T., Batezelli, A., Mattos, N., Leite, E., 2022. Flow units in complex carbonate reservoirs: A study case of the Brazilian pre-salt. *Marine and Petroleum Geology* 140, 105639.
- Rezende, M., Pope, M., 2015. Importance of depositional texture in pore characterization of subsalt microbialite carbonates, offshore Brazil. Geological Society, London, Special Publications 418, 193-207.
- Rousseeuw, P.J., 1987. Silhouettes: a graphical aid to the interpretation and validation of cluster analysis. *Journal of computational and applied mathematics* 20, 53-65.

- Rubo, R.A., de Carvalho Carneiro, C., Michelon, M.F., dos Santos Gioria, R., 2019. Digital petrography: Mineralogy and porosity identification using machine learning algorithms in petrographic thin section images. *Journal of Petroleum Science and Engineering* 183, 106382.
- Sabato Ceraldi, T., Green, D., 2017. Evolution of the South Atlantic lacustrine deposits in response to Early Cretaceous rifting, subsidence and lake hydrology. Geological Society, London, Special Publications 438, 77-98.
- Saller, A., Rushton, S., Buambua, L., Inman, K., McNeil, R., Dickson, J.T., 2016. Presalt stratigraphy and depositional systems in the Kwanza Basin, offshore Angola. *Aapg Bulletin* 100, 1135-1164.
- Schlumberger, L., 1991. Log interpretation principles/applications. Schlumberger Educational Services.
- Shalaby, M.R., 2021. Petrophysical characteristics and hydraulic flow units of reservoir rocks: Case study from the Khatatba Formation, Qasr field, North Western Desert, Egypt. *Journal of Petroleum Science and Engineering* 198, 108143.
- Shehata, A.A., Osman, O.A., Nabawy, B.S., 2021. Neural network application to petrophysical and lithofacies analysis based on multi-scale data: An integrated study using conventional well log, core and borehole image data. *Journal of Natural Gas Science and Engineering* 93, 104015.
- Shenawi, S.H., White, J.P., Elrafie, E.A., El-Kilany, K.A., 2007. Permeability and water saturation distribution by lithologic facies and hydraulic units: a reservoir simulation case study, SPE middle east oil and gas show and conference. OnePetro.
- Soltanmohammadi, R., Iraj, S., De Almeida, T.R., Munoz, E.R., Fioravanti, A.R., Vidal, A.C., 2021. Insights into Multi-Phase Flow Pattern Characteristics and Petrophysical Properties in Heterogeneous Porous Media, Second EAGE Conference on Pre-Salt Reservoir. European Association of Geoscientists & Engineers, pp. 1-5.
- Soltanmohammadi, R., Iraj, S., De Almeida, T.R., Munoz, E.R., Vidal, A.C., 2022. Upscaling Challenges of Heterogeneous Carbonate Rocks: A Case Study of Brazilian Pre-Salt Analogous, Third EAGE Conference on Pre Salt Reservoirs.
- Tiab, D., Donaldson, E.C., 2015. Petrophysics: theory and practice of measuring reservoir rock and fluid transport properties. Gulf professional publishing.
- Verma, A.K., Cheadle, B.A., Routray, A., Mohanty, W.K., Mansinha, L., 2012. Porosity and permeability estimation using neural network approach from well log data, SPE Annual Technical Conference and Exhibition, pp. 1-6.
- Winland, H., 1972. Oil accumulation in response to pore size changes, Weyburn field, Saskatchewan. Amoco Production Research Report No. F72-G25.
- Wong, P., Jian, F., Taggart, I., 1995. A critical comparison of neural networks and discriminant analysis in lithofacies, porosity and permeability predictions. *Journal of Petroleum Geology* 18, 191-206.
- Wright, V.P., Barnett, A.J., 2015. An abiotic model for the development of textures in some South Atlantic early Cretaceous lacustrine carbonates. Geological Society, London, Special Publications 418, 209-219.
- Xu, C., Misra, S., Srinivasan, P., Ma, S., 2019. When petrophysics meets big data: What can machine do?, SPE Middle East Oil and Gas Show and Conference. OnePetro.
- Zhao, L., Zou, C., Chen, Y., Shen, W., Wang, Y., Chen, H., Geng, J., 2021. Fluid and lithofacies prediction based on integration of well-log data and seismic inversion: A machine-learning approach. *Geophysics* 86, M151-M165.

## 5 CONCLUSIONS

- The part of study presents a comprehensive analysis of heterogeneous stromatolite carbonate outcrop samples from Lagoa Salgada in Rio de Janeiro State, Brazil, aimed at evaluating their petrophysical features, pore geometry, network characteristics, and fluid flow behavior through porous media. The research was motivated by the potential of these outcrop samples to serve as flow analogs for typical Brazilian Pre-salt reservoir rocks. The findings have implications for oil and gas recovery, carbon capture and storage, and groundwater management.
- Due to the high heterogeneity, differentiation, and significant pore size distribution variability, two fine-grained and vugular facies were defined for both experimental and simulation investigation to examine effect of pore geometry on oil recovery, saturation profile, and relative permeability estimations.
- Pore network modelling was employed for the microCT images of samples to determine the structure and geometry of the porous system and measure the connection between features of porous network.
- The median coordination number in samples from both facies was 3, and the columnar sample had a less dense pore network of larger pores, wider and longer throats, but weaker throat-pore connections.
- Pore radius and coordination number had a positive relation in the fine-grained sample, while larger pores were less connected in the columnar sample, and both facies showed less variation in throat radius than throat length.
- The single-phase core flooding with two distinct flow rates (0.1 and 0.5  $mL/min$ ) in combination with medical-CT scanning showed that the heterogeneity and disconnected/dead-end pores greatly affect the flow patterns, and there was a more homogenous distribution of flow lines and better fluid dispersion along the samples with better pore network connectivity (fine-grained sample). Moreover, there were connected pores in the columnar plug sample that no streamline passes through and the fluid remains stagnant inside them.
- Two-phase flow patterns revealed a preferential and heterogeneous displacement of fluids, with some pore spaces without specific flow lines and other areas with a sizable number of

flow lines, indicating that the displacing fluid was more effectively imbibed into those parts of the porous network.

- The distribution of oil saturation using medical CT data indicated heterogeneous profiles over the longitudinal section of the plugs that vary during oil and water injection. Furthermore, the analysis of images of both oil drainage and water imbibition processes revealed early breakthroughs.
- Since different pathways were chosen throughout time, there was a change in the saturation profiles' form for drainage and imbibition flow transfer.
- The heterogeneity of the sample significantly affects the flow patterns and saturation, and the relation between the saturation profiles, the porosity profiles, and the number of fluid flow patterns for the samples was evident.
- The average of these oil saturation profiles at the end of the oil and water injection operation representing initial and residual oil saturation, respectively, agreed rather well with the results from the production data of the core flooding studies.
- Core flooding experiment results showed the recovery factor in the range of 28 to 34 percent for our three plug samples during formation water injection based on the original oil in place.
- Only for the columnar plug sample, the enhancement in oil recovery after shifting to lower salinity water injection (SW) was observed according to the osmosis mechanism, while for the fine-grained samples, the recovery remained practically unchanged with further SW injection.
- To precisely evaluate the flow streamlines inside the vuggy porous material, two cross-sections were formed from high-resolution CT images and used as geometry for single and two-phase flow modeling. The velocity profile, flow streamlines, and pressure profile were derived and assessed using Navier-Stokes and continuity equations to simulate single-phase flow (water flooding). Although there are huge connected dead-end vugs with diameters in the centimeter range, the pressure fluctuation and velocity inside these regions are negligible, and fluid streamlines indicate that fluid within these zones remains stagnant.
- The lattice Boltzmann equation (LBE) was implemented to model multi-phase flow in each cross-section and obtain a saturation profile during water flooding. The findings show that the oil remained stuck in dead-end zones even close to the inlet. This remarkable volume

of bypassed oil resulted in high oil saturation and low oil recovery factor. The magnitude and volume of these dead-end regions have a significant impact on the time that breakthrough happens.

- An algorithm was operated to process the 2-D CT images of the samples, define a region of interest, and generate a fine-scale or high-fidelity grid model by converting each pixel of the image into one simulation block for the CMG simulator by applying rules for segmentation of rock types, porosity, and permeability estimations considering a Cartesian grid.
- Due to the high computational time for simulations of the fine-scale model, in the sequence, an algorithm was adapted to create upscaled or coarser models, where groups of blocks were merged into a coarser grid with any given dimension of an upscaled block.
- The simulation results for different upscaling factors were compared with experimental results of cumulative oil and water production from core flooding experiments and history matching was conducted to match these results and calculate relative oil and water permeability using the Brooks-Corey model.
- The identified curves improve our understanding of fluid flow in heterogeneous porous systems, providing a foundation for accurate assessments of oil recovery efficiency, sensible operational choices, reliable predictive models, and a better understanding of pre-salt reservoirs to minimize risks.
- In other part of research, the Barra Velha Formation in Brazilian pre-salt carbonate reservoirs was characterized and evaluated using well log data, conventional and micro-computed tomography ( $\mu$ CT) analyses of plug data, and thin section description to accurately understand the reservoir's characteristics.
- The unsupervised classification algorithm known as K-means was utilized to analyze the sequences of two wells in the Barra Velha Formation of the Santos Basin. This analysis was supported by various conventional techniques and aimed to distinguish different types of reservoir rock (RRTs) and hydraulic flow units (HFUs) by integrating well log data, plug data,  $\mu$ CT studies, and thin section descriptions.
- To determine the optimal number of rock typing clusters, the elbow method was employed, which involved calculating the sum of squared error deviation of data points belonging to

a cluster versus the cluster's centroid. The analysis determined that four clusters were the optimal number, referred to as RRT1 to RRT4.

- The reservoir quality index (RQI), flow zone indicator (FZI), effective pore radius ( $R_{35}$ ), global hydraulic element (GHE), and discrete rock types (DRT) were also determined for each of the RRTs. These parameters provide important information about the characteristics of the reservoir: (RRT1: very good reservoir quality, RRT2: good reservoir quality, RRT3: poor to fair reservoir quality, and RRT4: tight to poor reservoir quality).
- The study sequence was divided into five and four hydraulic flow units (HFUs) for well A and well B, respectively. The analysis found that HFU2 and HFU4 were responsible for approximately 60% of the flow capacity for well A, while HFU3 acted as a barrier. For well B, HFU1 and HFU3 supplied about 80% of the flow capacity, and HFU4 acted as a barrier.
- Three groups of facies were identified from petrological descriptions supported by thin sections of sub-salt lacustrine carbonates from the Barra Velha Formation: crystal shrub-dominated facies, reworked facies, and spherulitestone facies.
- The different reservoir rock types exhibited a variety of facies and porosity types. For example, RRT2 had interparticle porosity, while RRT3 and RRT4 mainly exhibited intercrystalline porosity. The mean pore radius, throat radius, and tortuosity for each of the RRTs were: RRT2 - 91  $\mu m$ , 53  $\mu m$ , and 1.9; RRT3 - 87  $\mu m$ , 50  $\mu m$ , and 2.5; and RRT4 - 72  $\mu m$ , 41  $\mu m$ , and 2.3.
- ResNet and 1D CNN models were trained on well-log datasets to accurately predict plug porosity, with the 1D CNN model performing better than the ResNet model in terms of generalization ability. Additionally, the XGBoost algorithm was utilized to predict rock type based on well log data, achieving high accuracy on both the training and validation sets. These findings showcase the potential of machine learning in reservoir characterization and management, offering valuable insights for optimizing production and effectively managing reservoirs.

## 6 REFERENCES

- Abutaha, S.M., Geiger, J., Gulyás, S., Fedor, F., 2022. Calculating the representative elementary volume of porosity using X-ray computed tomography: Boda Claystone Formation core sample/Hungary.
- ANP, A.N.d.P., 2021. Boletim Mensal da Produção de Petróleo e Gás Natural.
- Bruhn, C.H., Pinto, A.C., Johann, P.R., Branco, C., Salomão, M.C., Freire, E.B., 2017. Campos and Santos basins: 40 Years of reservoir characterization and management of shallow-to ultra-deep water, post-and pre-salt reservoirs-Historical overview and future challenges, OTC Brasil. OnePetro.
- Fitch, P.J., Lovell, M.A., Davies, S.J., Pritchard, T., Harvey, P.K., 2015. An integrated and quantitative approach to petrophysical heterogeneity. *Marine and Petroleum Geology* 63, 82-96.
- Hendry, J., Burgess, P., Hunt, D., Janson, X., Zampetti, V., 2021. Seismic characterization of carbonate platforms and reservoirs: an introduction and review. Geological Society, London, Special Publications 509, 1-28.
- Iraji, S., Soltanmohammadi, R., De Almeida, T.R., Munoz, E.R., Basso, M., Vidal, A.C., 2022a. Laboratory and numerical examination of oil recovery in Brazilian Pre-salt analogues based on CT images, Third EAGE Conference on Pre Salt Reservoirs.
- Iraji, S., Soltanmohammadi, R., Munoz, E.R., Basso, M., Vidal, A.C., 2023. Core scale investigation of fluid flow in the heterogeneous porous media based on X-ray computed tomography images: Upscaling and history matching approaches. *Geoenergy Science and Engineering*, 211716.
- Iraji, S., Soltanmohammadi, R., Munoz, E.R., Winter, A., de Almeida, R.V., Vidal, A.C., 2022b. Experimental Investigation of Waterflooding Performance by Increasing Copper Ions in Brazilian Pre-Salt Rock, 83rd EAGE Annual Conference & Exhibition. European Association of Geoscientists & Engineers, pp. 1-5.
- Iraji, S., Soltanmohammadi, R., De Almeida, T Rodrigues, Munoz, E.R., Vidal, A.C., 2022c. Experimental investigation of single-phase flow pattern in highly heterogeneous carbonates rocks, Rio Oil & Gas 2022. IBP, Rio de Janeiro | Brasil.
- Jackson, M.P., Hudec, M.R., 2017. Salt tectonics: Principles and practice. Cambridge University Press.
- Jackson, S.J., Lin, Q., Krevor, S., 2020. Representative elementary volumes, hysteresis, and heterogeneity in multiphase flow from the pore to continuum scale. *Water Resources Research* 56, e2019WR026396.
- Jensen, J., Lake, L.W., Corbett, P.W., Goggin, D., 2000. Statistics for petroleum engineers and geoscientists. Gulf Professional Publishing.
- Kang, P.K., Lee, J., Fu, X., Lee, S., Kitanidis, P.K., Juanes, R., 2017. Improved characterization of heterogeneous permeability in saline aquifers from transient pressure data during freshwater injection. *Water Resources Research* 53, 4444-4458.
- Lin, Q., Bijeljic, B., Pini, R., Blunt, M.J., Krevor, S., 2018. Imaging and measurement of pore-scale interfacial curvature to determine capillary pressure simultaneously with relative permeability. *Water Resources Research* 54, 7046-7060.
- Mohriak, W., Nemčok, M., Enciso, G., 2008. South Atlantic divergent margin evolution: rift-border uplift and salt tectonics in the basins of SE Brazil. Geological Society, London, Special Publications 294, 365-398.
- Petrobras, B., 2021. Fact Sheet.

- Reynolds, C.A., Blunt, M.J., Krevor, S., 2018. Multiphase flow characteristics of heterogeneous rocks from CO<sub>2</sub> storage reservoirs in the United Kingdom. *Water Resources Research* 54, 729-745.
- Sen, S., Abioui, M., Ganguli, S.S., Elsheikh, A., Debnath, A., Benssaou, M., Abdelhady, A.A., 2021. Petrophysical heterogeneity of the early Cretaceous Alamein dolomite reservoir from North Razzak oil field, Egypt integrating well logs, core measurements, and machine learning approach. *Fuel* 306, 121698.
- Soltanmohammadi, R., Iraj, S., De Almeida, T.R., Munoz, E.R., Fioravanti, A.R., Vidal, A.C., 2021. Insights into Multi-Phase Flow Pattern Characteristics and Petrophysical Properties in Heterogeneous Porous Media, Second EAGE Conference on Pre-Salt Reservoir. European Association of Geoscientists & Engineers, pp. 1-5.
- Soltanmohammadi, R., Iraj, S., De Almeida, T.R., Munoz, E.R., Vidal, A.C., 2022. Upscaling Challenges of Heterogeneous Carbonate Rocks: A Case Study of Brazilian Pre-Salt Analogous, Third EAGE Conference on Pre Salt Reservoirs.
- Vik, B., Bastesen, E., Skauge, A., 2013. Evaluation of representative elementary volume for a vuggy carbonate rock—Part: Porosity, permeability, and dispersivity. *Journal of Petroleum Science and engineering* 112, 36-47.
- Zahasky, C., Jackson, S.J., Lin, Q., Krevor, S., 2020. Pore network model predictions of Darcy-scale multiphase flow heterogeneity validated by experiments. *Water Resources Research* 56, e2019WR026708.

**7 APPENDIX I: INVESTIGATION OF PORE GEOMETRY  
INFLUENCE ON FLUID FLOW IN HETEROGENEOUS  
POROUS MEDIA: A PORE-SCALE STUDY**

**Author: Ramin Soltanmohammadi**

**Co-Author: Shohreh Iraji, Tales Rodrigues De Almeida, Eddy Ruidiaz Munoz, Mateus  
Basso, Alexandre Campana Vidal**

**Campinas - SP**

**2023**

## ABSTRACT

Brazilian pre-salt reservoirs are well-known for their intricate pore networks and vuggy nature, making it challenging to model and simulate fluid flow within these carbonate reservoirs. Despite their excellent petrophysical properties such as high porosity and permeability, the recovery factor in these reservoirs is typically very low, in some cases below 10%. Previous studies have shown that injecting  $CO_2$ , in the form of WAG (water alternating gas), can significantly increase the recovery factor in pre-salt reservoirs, with improvements of up to 20%. However, the mechanisms by which  $CO_2$  injection improves the recovery factor while water flooding exhibits poor recovery are unclear. In this study, we investigated the fluid flow behavior in similar heterogeneous porous material by utilizing a plug sample collected from a vugular segment of a Brazilian stromatolite outcrop, known to be flow analogous to some pre-salt reservoirs. Single-phase and multi-phase core flooding experiments were conducted in combination with medical-CT scanning to generate flow streamlines and assess water flooding efficiency. MicroCT scanning of the core sample was then performed, and two cross-sections from horizontal and vertical plates were constructed and used as geometry in a numerical simulator to examine the impact of pore geometry on fluid flow. The pore-scale modeling and experimental data analyses revealed that due to the presence of dead-end pores and vugs, a significant proportion of the fluid remains stagnant in these regions, leading to channeling-like behavior of the injected fluid in the sample, fast breakthrough, and low areal swept efficiency. The numerical simulation results also demonstrated that regardless of the size of the dead-end regions, the pressure variation within the dead-end vugs and pores is negligible. Despite the stromatolite's proper petrophysical properties (relatively high porosity and permeability and the existence of linked huge vugs), the recovery factor during water flooding remained low due to early breakthrough. The results of this study match the field data obtained from pre-salt reservoirs, providing an explanation for the low recovery factor recorded in pre-salt reservoirs during water flooding.

Keywords: Pore-scale Modeling, Pore Geometry, Flow Streamlines, Computational Modeling, Digital Rock Analysis

## 7.1 INTRODUCTION

The discovery of pre-salt reservoirs in 2006 greatly impacted the Brazilian petroleum industry. According to the Brazilian Oil and Natural Gas Agency (ANP), pre-salt reservoirs will account for more than 70% of the total produced oil (approximately 2.5 million barrels per day) in 2021 in Brazil (Alves and Polette, 2021). Producing petroleum from pre-salt reservoirs entails many challenges, including contamination by  $CO_2$  and  $H_2S$  in the gas phase, ultra-deepwater scenarios, thick salt layer drilling complexities, and, most importantly, the heterogeneous nature of lacustrine carbonate pre-salt formations (da Costa Fraga et al., 2015). Given this, having a thorough understanding of fluid flow within heterogeneous porous media is essential for ensuring dependable production. Since the discovery of pre-salt reservoirs, various enhanced oil recovery (EOR) and improved oil recovery (IOR) methods have been examined to improve oil recovery factor and production. Traditionally, due to the presence of seawater and high levels of dissolved  $CO_2$  in reservoir fluid, along with gas storage limitations in offshore fields and the detrimental effects of  $CO_2$  emissions on climate, water-alternating-gas (WAG) injection, which involves the combination of desulfated seawater and gas, has been widely regarded as an effective enhanced oil recovery (EOR) method implemented in Brazilian pre-salt reservoirs (Ligero and Schiozer, 2014; Waterworth and Bradshaw, 2018). In fact, WAG injection is presently the most commonly employed EOR method in Brazilian pre-salt reservoirs. However, there has been a recent surge in research into other techniques, such as polymer and surfactant injection (chemical EOR) and low salinity water injection, for application in pre-salt reservoirs (Soltanmohammadi et al., 2021). Water injection in Brazilian pre-salt reservoirs had revealed an early breakthrough in production wells, poor injectivity, low oil recovery factor, as well as high residual oil saturation. However, in the Lula field, within the pre-salt cluster of the Santos Basin which contains light oil, water alternative gas injection (primarily  $CO_2$  as the gas phase) provides a substantially higher oil recovery factor, owing to oil swelling and viscosity reduction (Feng et al., 2004; de Araujo Cavalcante Filho et al., 2020). Indeed, during the WAG process, the swelling and coalescence of isolated oil ganglia appear to have a considerable impact on the oil recovery factor (Sohrabi et al., 2009). Nevertheless, early breakthroughs in production wells were still detected (Branco, 2012; Drexler et al., 2022).

The diversity of pore types in Brazilian pre-salt reservoirs is categorized by interparticle, vugular, fracture, karts, and dissolution horizons or “super-k” layers (da Rocha et al., 2019; De Lima et al.,

2019; Ferreira et al., 2021). As a result, pre-salt reservoir modeling and simulation have typically been carried out with a significant degree of uncertainty (Correia et al., 2015; Bruhn et al., 2017; Alvarez et al., 2021). In this study, we collected a sample of stromatolite outcrop, which has the potential to be an flow analogue for pre-salt reservoirs (Muniz and Bosence, 2015), to better understand the petrophysical properties of pre-salt reservoirs and gain insight into fluid propagation within this type of porous media. Earlier investigations classified stromatolite core samples into two distinct subgroups, namely vugular and fine-grained, based on their average pore size. Vugular core samples have remarkably larger and connected pores that are typically centimeters in size, while fine-grained samples have smaller pore sizes (Frolov et al., 2011; Callefo et al., 2018). The main goal of this study is to investigate fluid movement within the vuggy porous medium and understand the flow streamline within this complex and heterogeneous porous system. To achieve this, we obtained a plug sample from the vugular section of the stromatolite outcrop and analyzed its pore geometry using micro computed tomography (microCT) and core flooding in conjunction with medical-CT scanning to determine its petrophysical properties. Previous research on similar stromatolite outcrops has found high permeability (800 to 1200 *mD*) and high porosity (30 to 60%), as well as a low oil recovery factor (less than 30%) even after a reasonably long period of water flooding in a core saturated with ultra-light oil (Soltanmohammadi et al., 2022). However, the reason why the oil recovery factor is poor in core samples with high porosity and permeability and largely connected vugs remains unclear. This phenomenon has also been observed in pre-salt reservoirs, where the porosity and connectivity of the pores are remarkable, but the recovery factor is low, even in some cases below 10% (Branco, 2012; Godoi and dos Santos Matai, 2021). Therefore, it is crucial to have a comprehensive pore-scale study to understand the flow pattern in these types of heterogeneous rocks. In this study, in addition to the experimental section, we used 2D microCT images as geometry in our numerical simulations to obtain flow streamlines, saturation, and velocity profiles in the core sample. These simulations helped to explain why we recorded low oil recovery factors and early breakthrough during core flooding in stromatolite samples, as well as in pre-salt reservoirs. In general, the main objective of this study was to investigate the impact of pore geometry on fluid flow in porous media by combining numerical simulation and experimental results. Specifically, we aimed to examine how the presence of dead-

end pores and vugs, in addition to their size, can affect flow patterns, recovery factors, and breakthrough times.

The structure of this paper is as follows: Section 2 provides a description of the geological setting and the location from where the core samples were collected. Section 3 details the materials and methods used in this study, including a comprehensive discussion of the experimental configuration and numerical simulation. In Section 4, we analyze and examine the results obtained from both the experiments and numerical simulation. Finally, Section 5 presents a summary of the main findings and conclusions of this work.

### 7.1.1 GEOLOGICAL SETTING

This study made use of outcrops from Lagoa Salgada in Rio de Janeiro, Brazil, where microbial carbonate rocks were identified as similar to one of the most commonly occurring pre-salt reservoir rocks in Brazil (Wright and Tosca, 2016). The geological layout of the study area is depicted in Figure 7-1, which shows the coastal zone of Rio de Janeiro State and a map of the study area. The latitude and longitude of the study location are also shown in Figure 7-1. Specifically, the latitude and longitude of the core sample investigated in this study were  $041^{\circ} 07' 58'' W$  and  $21^{\circ} 54' 10'' S$ , respectively.

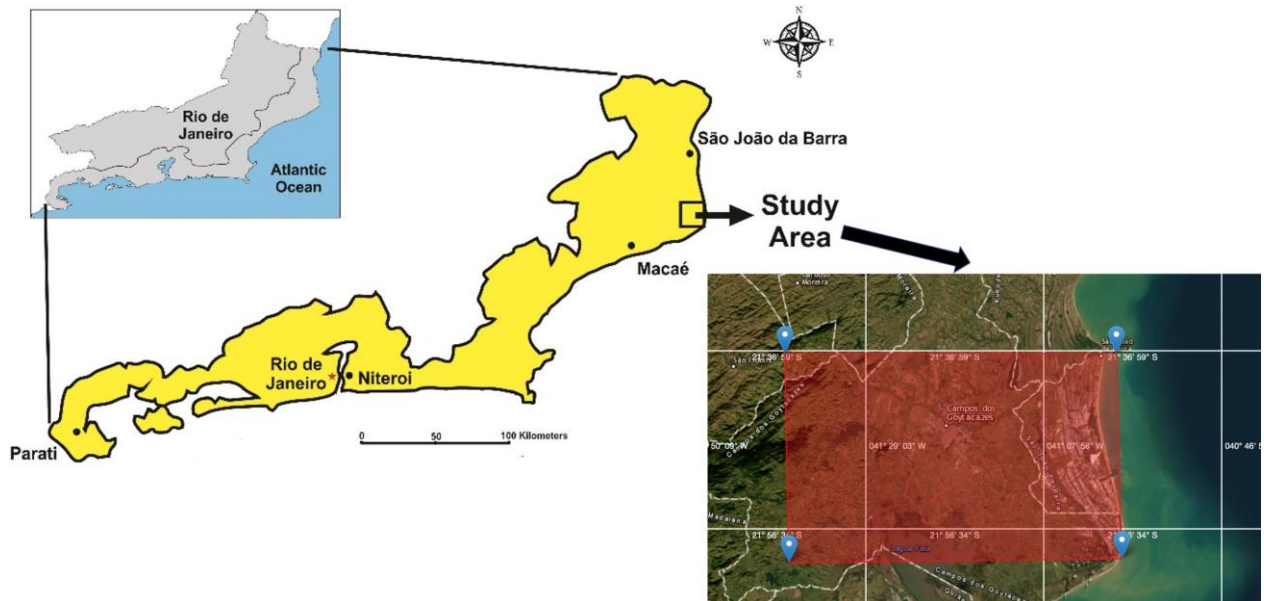


Figure 7-1. Rio de Janeiro State, highlighting the coastal zone and the location of the study area. The latitude and longitude of the core sample discussed in this paper were  $041^{\circ} 07' 58'' W$  and  $21^{\circ} 54' 10'' S$ .

## 7.2 MATERIALS AND METHODOLOGY

### 7.2.1 MATERIALS

Figure 7-2 (a) compares the sample from a Brazilian stromatolite outcrop with a sample from a pre-salt reservoir. These two sorts of rocks are remarkably similar. The medical CT scanner was used to identify regions of interest and collect representative rock phases of the outcrop samples; the rock samples were then classified into two facies based on pore size and geometry: fine-grained and columnar/vugular. The medical CT scanner used in this study was a Siemens SOMATOM Spirit scanner with a resolution of  $15.5 \text{ IP/cm}$ . Fine-grained facies have far smaller pores than columnar facies, which contain huge, linked vugs with pore diameters in the centimeter range. Figure 7-2 (a) highlights the columnar/vuggy facies. To gain a firm understanding of fluid flow in columnar facies, one core sample with a length of  $8.9 \text{ cm}$  and a diameter of  $3.68 \text{ cm}$  was drilled and selected from the indicated columnar facies, Figure 7-2 (b). The pore geometry within the core sample was obtained using a microCT scanner after the core sample had been cleaned. We utilized a ZEISS XRadia Versa XRM-500 scanner with  $40 \mu\text{m}$  voxel size for this task. The stromatolite columnar core sample was fragile and extremely heterogeneous, making core flooding studies problematic. The encapsulation process for this core sample was launched by heating a thermoplastic material to core surfaces to guarantee that the core's marginal limits remained consistent during experimental section and core flooding. To preserve the rock's integrity during the experiment, epoxy resin was poured to the thermoplastic's surface. Figure 7-2 (c) depicts the resulting encapsulated core.

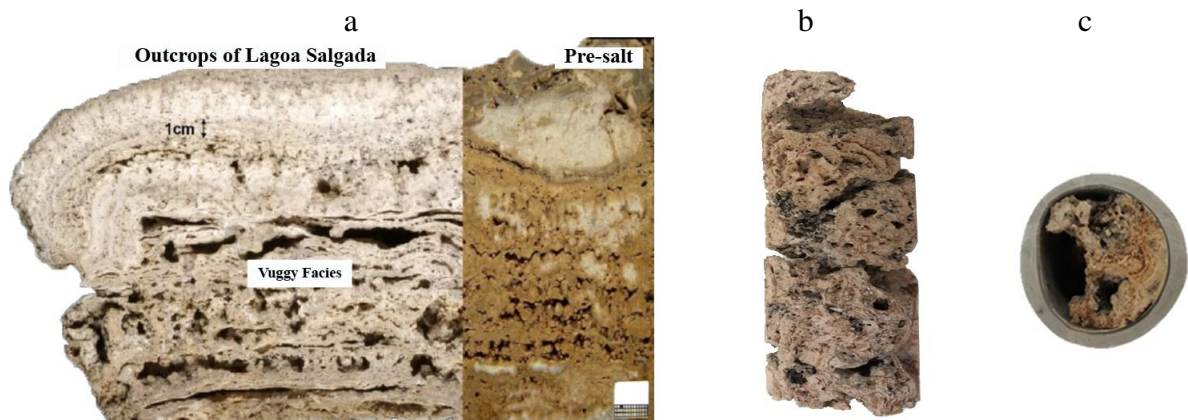


Figure 7-2. a): comparison of microbialite outcrops of Lagoa Salgada (with highlighted columnar facies) and Pre-salt rock, b) columnar plug sample, c) encapsulated plug sample.

Three different aqueous phases, namely distilled water (DW), seawater (SW), and formation water (FW), were utilized in the core flooding process. Table 7-1 provides the composition of SW and FW.

Table 7-1. Composition of SW and FW.

Salt	Sea water (SW) Composition (g/L)	Formation water (FW) Composition (g/L)
<i>NaCl</i>	23.47	163.62
<i>Na<sub>2</sub>SO<sub>4</sub></i>	0.1	0.088
<i>NaHCO<sub>3</sub></i>	0.192	0.487
<i>KCl</i>	0.724	6.911
<i>MgCl<sub>2</sub>.6H<sub>2</sub>O</i>	10.55	3.068
<i>CaCl<sub>2</sub>.2H<sub>2</sub>O</i>	1.466	19.1
<i>SrCl<sub>2</sub>.6H<sub>2</sub>O</i>	0.039	0.028
<i>BaCl<sub>2</sub>.2H<sub>2</sub>O</i>	=	0.033

The light-dead-oil used in the experimental section was sourced from a pre-salt reservoir in Brazil. The oil was centrifuged and filtered through a 5  $\mu\text{m}$  Millipore filter prior to use. The density, molar mass, and viscosity of the oil sample at 20 °C and standard pressure are 0.8751  $\text{g}/\text{cm}^3$ , 120  $\text{g}/\text{mol}$ , and 5 centipoises (*cP*), respectively.

## 7.2.2 EXPERIMENT PROCEDURE

Figure 7-3 presents the schematic diagram of the core flooding apparatus, which enables the experimentation of high pressure-temperature conditions indicative of Brazilian pre-salt reservoirs (Iraji et al., 2022). The device is made up of the following components: A high-pressure injection pump, a heating jacket capable of raising the temperature to 106 °C, fluid accumulator vessels, a coreholder, pressure transducers, a backpressure regulator capable of maintaining a pressure of 1000 *psi*, valves and lines, the medical CT scanner, and a biphasic separator. Furthermore, for pressure, temperature, flow rates, and production data, a computer-controlled system with a highly precise data acquisition was used.

One purpose of this study was to assess the flow streamlines within vuggy porous media. To precisely characterize flow patterns in single and multi-phase flows utilizing core flooding coupled with medical CT scanning, the encapsulated core sample was first assembled in a core holder with high confining pressure and temperature, 106 °C and 2200 *psi*. After achieving these conditions, the air inside the core was evacuated using a vacuum pump. Nitrogen was then pumped into the

sample until the pore pressure reached 735 *psi*. The first CT scan (dry CT) was taken after the nitrogen had been sufficiently stabilized. Then, the nitrogen was then removed from the sample using a vacuum pump, and formation water (FW) was pumped into the core at the same temperature of 106 °C, until pressure stabilization and the core was fully saturated with FW. In this step the second CT scan (wet CT) was conducted. The porosity distribution profile obtained in this step after analysing CT images. The dry and wet CT data would provide the initial porosity profile by the segmentation of the attenuation coefficient from the acquired images, as it shown in Equation (3-1) (Park et al., 2017).

$$\phi = \frac{CTR_w - CTR_g}{CT_w - CT_g} \quad (7-1)$$

Where,  $CTR_w$  is the CT value of the sample completely saturated with formation water,  $CTR_g$  is the CT value of the sample completely saturated with nitrogen,  $CT_w$  and  $CT_g$  are the average CT value of FW and nitrogen at test conditions, and  $\phi$  is the calculated porosity. Then, at a constant rate of 0.1 ml/min, 2 PV of distilled water (DW) was injected into the FW-saturated core as the tracer. It is imperative to note that the differential CT attenuation coefficient exhibited by distilled water (DW) in comparison to formation water (FW) renders DW a suitable tracer for employment in this study. The attenuation coefficients for FW and DW, as determined in the current investigation, are 433.03 and 389.17, respectively. CT scans were taken while the injection was being administered. Following that, CT scanning was done while a 2.0 PV of FW was injected at a constant rate of 0.5 ml/min. The rate was subsequently dropped to 0.1 ml/min, and the injection was continued until the DW tracer was eliminated completely. The major goal of this section was to find flow streamlines in single-phase flow within the vuggy porous medium while accounting for the effect of different rates.

Following the injection of various pore volumes of FW and the removal of DW, light oil was injected at a rate of 0.1 ml/min to examine the effect of an immiscible injection and to generate the saturation profile. During this step, 2 PV of oil was injected, and CT scan data were analyzed to determine the saturation profile for the drainage process and two-phase flow patterns. After reaching initial water saturation, 2 PV of FW with the rate of 0.1 ml/min were injected to displace the crude oil, creating an imbibition saturation map and flow patterns. PerGeos software was used

to analyze the CT images and generate the flow pattern model in each flooding process step. Experiments were finalized by injection of SW into the core until reaching residual oil saturation. Furthermore, the amount of oil and water production was recorded during the flooding steps to determine the recovery factor.

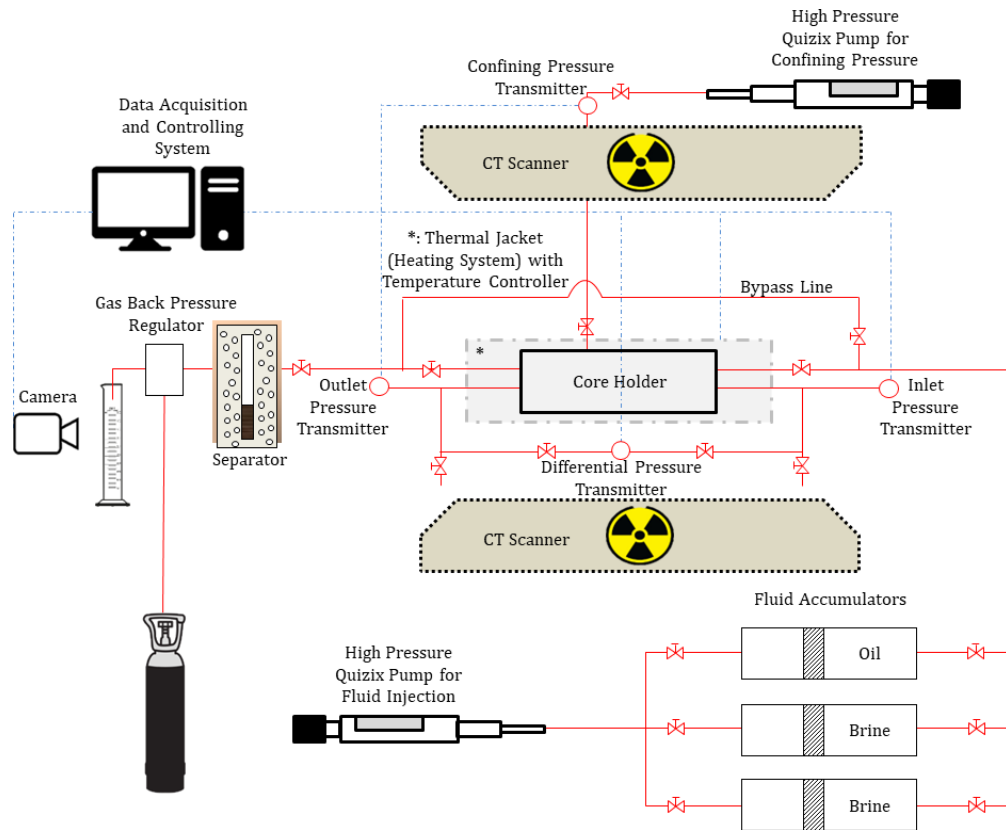


Figure 7-3. Schematic diagram of the core flooding apparatus, illustrating the experimental setup used in this study.

### 7.2.3 UNDERLYING PHYSICS

Reynolds number is one of the main parameters that affect fluid flow in porous media, particularly in vuggy porous medium. Therefore, first of all, we calculate the Reynolds number. Reynolds number is a criterion, assists to detect a flow regime; it represents the relation between inertial and viscose forces. Equation (7-2) displays Reynolds number equation, where  $\rho$  is fluid density in  $kg/m^3$ ,  $v$  is Darcy velocity divided by porosity ( $v = u/\phi$ ) in  $m/s$ ,  $d_{50}$  is median grain size of the porous media as a proxy for characteristic pore length in  $m$ , and finally  $\mu$  is fluid viscosity in  $kg/m.s$  (Bear; van Lopik et al., 2017).

$$Re = \frac{\rho v d_{50}}{\mu} = \frac{\text{inertial force}}{\text{viscose force}} \quad (7-2)$$

In general, the flow regime is divided into two distinct sections based on Reynolds number. Laminar flow exists when the Reynolds number is less than 2000. Turbulent flow, on the other hand, is defined as a flow regime with a Reynolds number greater than 2000 (Blick, 1966). The laminar flow itself, divided into the Darcy flow region, which Darcy's law is valid, and the Forchheimer flow regime (Liu et al., 1994). Darcy's law applies when viscose force dominates the inertia term and does not take the flow diffusion effect into account. Empirical Forchheimer law is a Darcy's law extension that takes into account the inertia term and is used when the Reynolds number exceeds 10; in this case, the viscous force can no longer dominate the inertia force (Nguyen and Balakotaiah, 1994; Buchori et al., 2017).

After determining the flow regime and calculating the Reynolds number, to gain a better understanding of the pore scale fluid pattern within the columnar core sample, we created a 3D model of the core using the microCT scanning outcomes, as shown in Figure 7-4. Figure 7-4 depicts the complex geometry of the core, which includes linked massive vugs and pores. To create geometry in the simulator, we generate two two-dimensional (2D) microCT images from the center of the core by intersecting it with one horizontal and one vertical plate, the yellow and blue cross-sections in Figure 7-4 respectively.

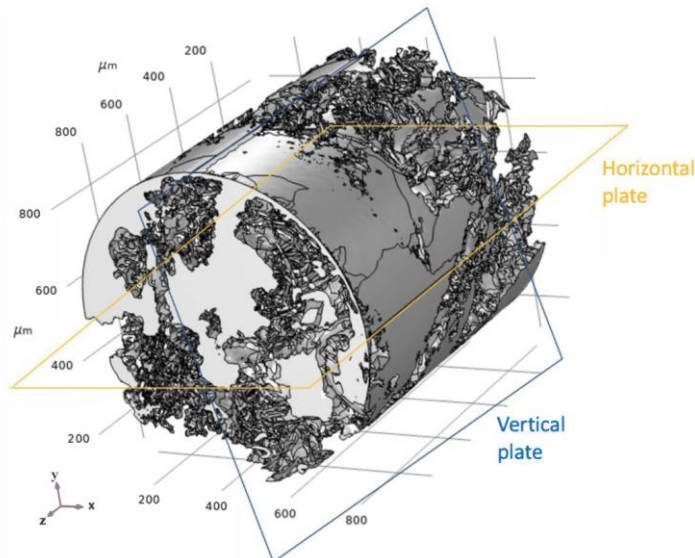
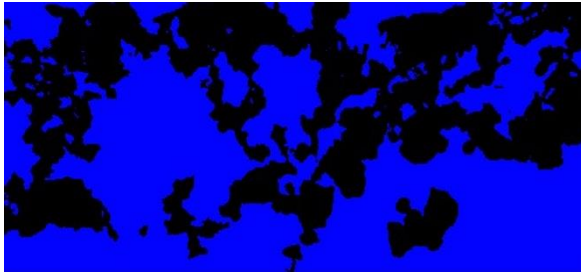
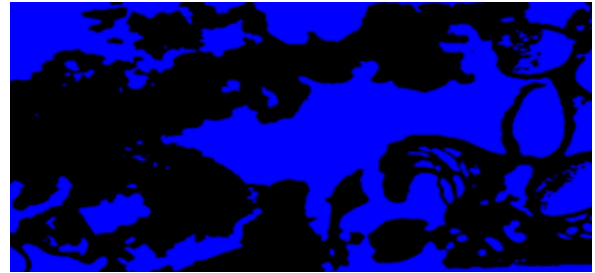


Figure 7-4. Using horizontal and vertical plates, perpendicular plates, two cross-sections are obtained and used as geometry in COMSOL Multiphysics (simulator).

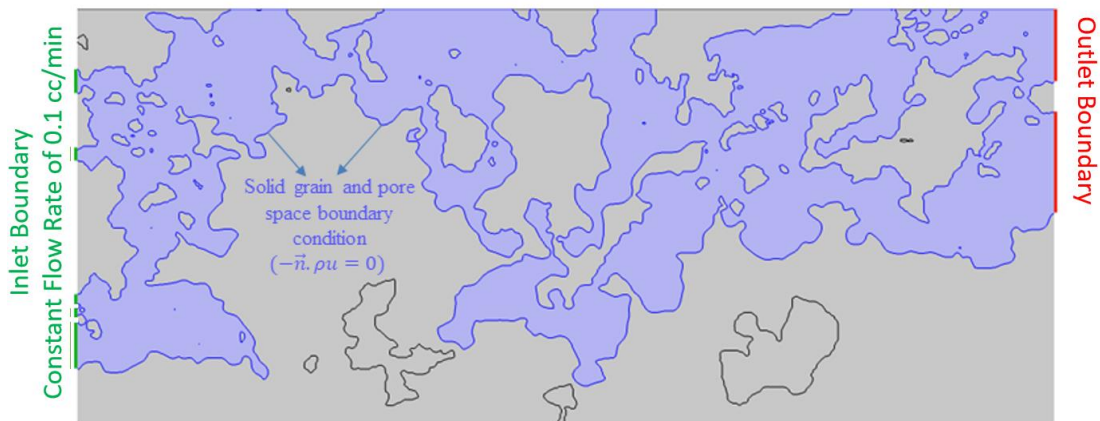
Figure 7-5 (a and b) illustrates the two-dimensional (2D) microCT images obtained by intersecting the core with horizontal and vertical plates, respectively. The pore space is displayed in black, while the solid grains are shown in blue. In Figure 7-5 (c and d), the simulator's region of interest is depicted in light blue. The inlet and outlet are highlighted in dark green and dark red, respectively. Additionally, the intersection between the solid-grain and pore space is marked, and the zero-flux term boundary condition is applied to it.



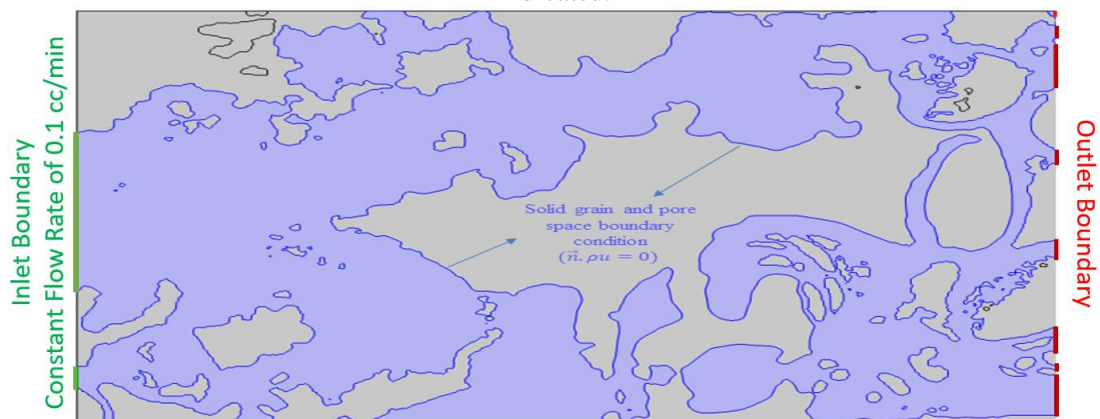
(a) A 2D cross-section was obtained using a horizontal plate; the black and blue colors represent pore space and solid grains, respectively.



(b) A vertical 2D geometry used in simulator.



(c) In the horizontal cross-section, the region of interest (connected pores), inlet, and outlet are indicated.



(d) The region of interest is shown in a vertical cross-section.

Figure 7-5. Using a 3D model, 2D microCT images were acquired and employed in numerical simulator.

Utilizing the 2D images, single-phase water-flooding has been modeled to procure velocity field; moreover, flow streamlines are drawn to clarify the flow pattern inside the vugular sample. Zero flux term ( $u = 0$ ) boundary condition is applied around the solid grains (Harlow and Amsden, 1971). Chemical reaction between water and rock is considered negligible. In this simulation, we assumed that fluid was injected through the left-hand side of Figure 7-5 (inlet with constant flow rate) and expelled through the right-hand side. Navier–Stokes equations for conservation of momentum, Equation (7-3), and the continuity equation, Equation (7-4), for conservation of mass applied to model single-phase fluid flow (Doering and Gibbon, 1995). The gravity force in the momentum equation does not involve and is supposed to be negligible,  $(\rho - \rho_{ref})g = 0$  (Gal-Chen and Somerville, 1975).

$$\rho \left( \frac{\partial u}{\partial t} + u \cdot \nabla u \right) = -\nabla p + \nabla \cdot (\mu(\nabla u + (\nabla u)^T)) - \frac{2}{3}(\mu(\nabla \cdot u)I) + F \quad (7-3)$$

$$\frac{\partial \rho}{\partial t} + \nabla \cdot (\rho u) = 0 \quad (7-4)$$

In Equation (7-3), term  $\rho \left( \frac{\partial u}{\partial t} + u \cdot \nabla u \right)$  corresponds to inertial forces, term  $-\nabla p$  is representing the pressure forces,  $\nabla \cdot (\mu(\nabla u + (\nabla u)^T)) - \frac{2}{3}(\mu(\nabla \cdot u)I)$  represents viscous forces, and  $F$  corresponds to external forces applied to fluid. Furthermore,  $u$  is fluid velocity,  $p$  is fluid pressure,  $\rho$  is fluid density, and  $\mu$  is fluid dynamic viscosity, all in *SI* units (Momani and Odibat, 2006).

We assumed that water was incompressible ( $C_w = 0$ ), and in the beginning, the core was fully saturated by water; then, we injected water with constant velocity ( $u_{inj} = 1.4 \times 10^{-4} m/s$ ) through the inlet. We considered suppressing backflow pressure is 50 *bar* ( $p_0 = 50 \text{ bar}$ ), initial pressure and temperature was 150 *bar* and 379.15 *K* ( $p_i = 150 \text{ bar}, T_i = 379.15 \text{ K}$ ), based on experiments. Temperature remains constant in the entire core flooding process. The rock compressibility is negligible, and the porosity remains constant during flooding ( $C_r = 0, \frac{\partial \phi}{\partial t} = 0$ ).

To simulate two-phase flow at the pore-scale, the lattice Boltzmann equation (LBE) was employed. In the simulation we assumed that the initial temperature and pressure is like single phase model, and we inject water with constant flow rate of 0.1 ml/min, through inlet. The two-phase flow simulation assumes a zero-backflow pressure and neglects its effect. The relative permeability

calculation was carried out using a Corey-type function, as represented by Equation (7-5) (Firoozabadi and Aziz, 1986).

$$k_{rw} = k_{rw}^e S_{wN}^{nw} \quad k_{ro} = k_{ro}^e (1 - S_{wN}^{no})$$

$$S_{wN} = \frac{S_w - S_{wc}}{1 - S_{orw} - S_{wc}} \quad (7-5)$$

Capillary pressure was considered negligible. Relative permeability and simulation parameters exhibit in Table 7-2.

Table 7-2. Relative permeability and simulation parameters.

Parameter	Value
$k_{rw}^e$	0.95
$k_{ro}^e$	0.9
$S_{wc}$	0.3
$S_{orw}$	0.05
$D_c$ (Capillary diffusion)	0
$q_{inj}$	0.1 ml/min
T	379.15 K
$C_r, C_w, C_{ro}$	0
$k$	1179 mD

## 7.3 RESULTS AND DISCUSSION

In this section, we provide a comprehensive analysis of both the experimental and numerical simulation sections' outcomes. We analyze the outcomes of CT scanning during core flooding in order to determine the oil saturation and recovery factor profile. In addition, we undertake a comprehensive investigation of the flow streamline in single phase and generate a saturation profile using numerical simulation during core flooding.

### 7.3.1 EXPERIMENTAL RESULTS

The porosity of the core sample was determined to be 52.5% through measurements using the CoreLab Company porosimeter. Figure 7-6 shows the porosity profile of the columnar core sample, which was obtained through medical-CT imaging. The porosity distribution in the vuggy core sample ranges from 44% to 61% along the length of the core. A Core flooding apparatus was employed to inject water into the core holder using a pump, and the pressure drop across the plug was measured. To obtain the difference between the inlet and outlet pressures of the core, a differential pressure transducer was installed in the setup. Using these measurements, the permeability of the core sample was calculated and determined to be 1179.02 millidarcy ( $mD$ ).

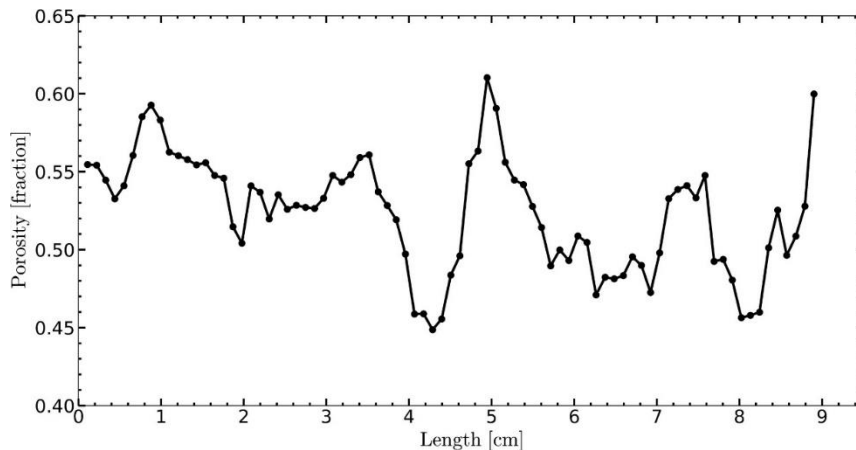


Figure 7-6. Visualization of the porosity distribution along the length of the core sample using medical-CT scanning.

#### 7.3.1.1 TRACER INJECTION (SINGLE PHASE FLOW)

Upon conducting an analysis of medical-CT images acquired during single-phase FW injection, we have generated Figure 7-7 using PerGeos software. The figure depicts gray segmentation sections that represent disconnected pores, while the blue color corresponds to connected pore areas. Additionally, red lines have been employed to depict the flow streamlines within the porous

media. Our in-depth analysis of the medical-CT scan data has revealed that a significant proportion of connected pores have remained unutilized, with no flow passing through them. Notably, the flow streamlines do not traverse a substantial area of interconnected pores, as evidenced by the lateral view of the core in Figure 7-7 (a). A remarkable region located in the bottom right side of the core, consisting of large linked vugs, has remained completely unaffected by the flow, with no existing flow streamline that has passed through this area. These findings suggest a need for further investigation into the factors affecting the flow of fluids within porous media. By expanding our knowledge in this area, we can improve our understanding of fluid flow behavior and optimize fluid transport processes in porous media applications. To investigate the flow streamline in a heterogeneous-vuggy porous system, a 2D cross-section was generated from microCT images in the simulation section. This approach was adopted because it allows for a more comprehensive examination of the complex flow dynamics within the porous medium.

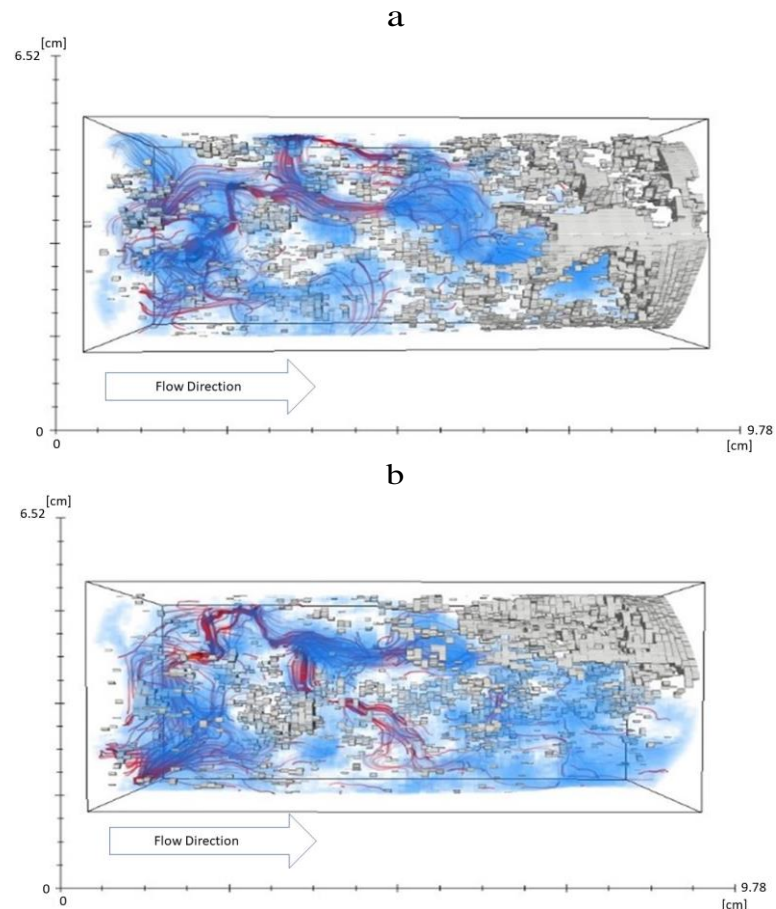


Figure 7-7. The 3D model of the core and pores with flow streamlines during single-phase FW injection. The figures on the top and bottom show the core from the lateral and top views, respectively.

To precisely investigate the flow path inside porous media and understand why a substantial portion of the connected pores remain untouched, we visualized the 3D flow streamlines on a 2D cross-section of the core, obtained from the medical-CT scanner, in subsequent studies.

The flow pattern investigation continued with the single-phase injection of the tracer. 2 PV of DW were initially injected into the core at a constant rate of  $0.1 \text{ cm}^3/\text{min}$ . Concurrently, medical-CT scanning was performed to get the concentration profile for generating the flow pattern. Following that, a 2 PV of FW was injected at a continuous rate of  $0.5 \text{ cm}^3/\text{min}$  while CT scanning was performed, and the injection was continued until the DW tracer was fully depleted.

Figure 7-8 (a) illustrates the flow streamlines of DW (yellow lines) during the displacement of FW by DW. The blue areas of the images in Figure 7-8 represent connected pores in a longitudinal cross-section of the core sample, obtained using medical-CT scanning. Next, the FW was injected with the flow rate of  $0.5 \text{ cm}^3/\text{min}$  to gain more insights of effect of flow rate on the flow patterns in the vuggy core sample. Figure 7-8 (b) depicts the flow streamlines of FW (red lines) during DW displacement by FW. The greater number of streamlines in Figure 7-8 (b) compared with the previous step, Figure 7-8 (a), clearly shows a higher fluid velocity, which corresponds to a higher injection flow rate. However, the key result after examining the data in Figure 7-8 was the significant fraction of pores and vugs that remained unaffected during core flooding. In fact, while the FW is being injected, we observe a channeling-like behavior of FW, and a strikingly large, connected area stays unswept. The CT scan results revealed that these untouched areas are mostly associated with dead-end zones.

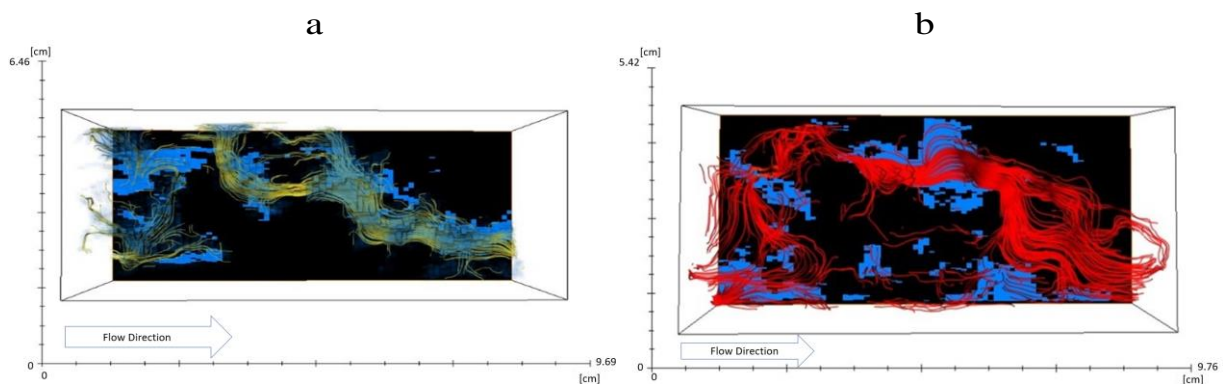


Figure 7-8. Flow streamlines in 2D cross-sections that derived from medical-CT scanning during single phase flow. The figure on the left shows DW displacing FW (flow rate =  $0.1 \text{ cm}^3/\text{min}$ ), whereas the one on the right shows FW displacing DW (flow rate =  $0.5 \text{ cm}^3/\text{min}$ ).

### 7.3.1.2 TWO PHASE FLOW

It is worth noting that a prior investigation of a similar core, utilizing contact angle tests and the analysis of medical CT images, revealed that the core exhibits an oil-wet nature. Indeed, the analysis of medical CT images from earlier studies exhibited oil covering the rock surface, while water bubbles were observed in the middle. The oil was then injected into the columnar core sample at the rate of  $0.1 \text{ cm}^3/\text{min}$  to gain a better understanding of the immiscible two-phase flow. After processing the medical-CT image data, flow streamlines are generated. Figure 7-9 (a) depicts the flow patterns of the oil (yellow lines) during the displacement of the FW by oil (oil drainage). Analyzing the flow streamlines in Figure 7-9 (a) reveals that the oil is unable to penetrate some pores and vugs, such as the large dead-end vug in the middle of the core shown in the Figure 7-9 (a), which remains nearly full of FW. We observed that produced water was approximately  $32 \text{ cm}^3$ , which by considering the effective pore volume of  $49.7 \text{ cm}^3$ , represents that the water saturation after oil drainage process was 35.6% and the oil saturation was 64.4%. This information was obtained by recording production data such as produced water and oil during oil flooding. Moreover, the intensity of the number of streamlines in Figure 7-9 (a) shows high oil velocity within specific regions, while the velocity of the fluid is markedly low in a notable volume, more explicitly inside the dead-end pores and vugs. Medical-CT scanning was used to track changes in the oil saturation distribution within the core sample throughout the two-phase flow process along the longitudinal of the sample (Figure 7-10). Figure 7-10 (a) shows the oil saturation profiles for two steps: after 0.2 PVI of oil and after 2 PVI (end of the oil drainage process). Both the produced oil during core flooding and the medical-CT results exhibited oil breakthrough shortly after the injection begins. In fact, after 0.2 PVI, Figure 7-10 (a) reveals that the oil saturation at the outlet is greater than 10%, implying an early breakthrough. The lowest oil saturation, obtained from CT data, after the oil flooding operation was 52% and was found in the middle of the core (Figure 7-10 (a)), where there are fewer flow lines and more the dead zones exist (Figure 7-9 (a)).

Following the injection of oil, FW was injected at a flow rate of  $0.1 \text{ cm}^3/\text{min}$ , followed by medical-CT scanning to investigate the oil recovery and to drive flow streamlines in a two-phase immiscible process. Figure 7-9 (b) depicts the flow pattern of the displaced fluid, oil (yellow line), during the displacement of oil by FW (FW imbibition process). Preferential displacement was observed in the oil flow pattern, notably in some areas fluid was swept and bypassed in others. The

intensity and quantity of flow streamlines in Figure 7-8 and Figure 7-9 show that fluid velocity is higher near the outlet, but because there are dead-end zones in this region (Figure 7-7), the fluid remains stagnant in many pores and vugs near the outlet during core flooding. According to an assessment of CT scan data, the average residual oil saturation after FW injection was 42.2%. To track changes in the distribution of oil saturation within the core during the FW injection (water imbibition) process, the core sample was regularly CT-scanned. Figure 7-10 (b) shows the findings of the medical-CT data, where the oil saturation profiles correspond to two stages: 0 PVI of FW injection (immediately after 2.0 PVI of oil), and the results after 2.0 PVI of FW. We also observed the breakthrough during the preliminary stage of the FW injection. In fact, it appears that the existence of a remarkable volume of dead-end zones, as well as suitable petrophysical features of the core sample (relatively high porosity and permeability, as well as the presence of linked vugs), prompted the breakthrough. Similar behavior, early breakthrough, has been observed in pre-salt reservoirs as well, during both water flooding and WAG process.

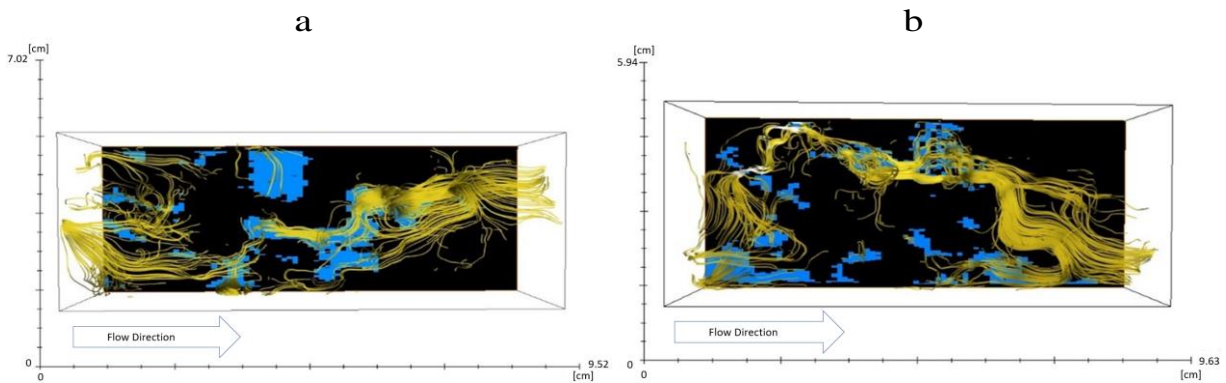
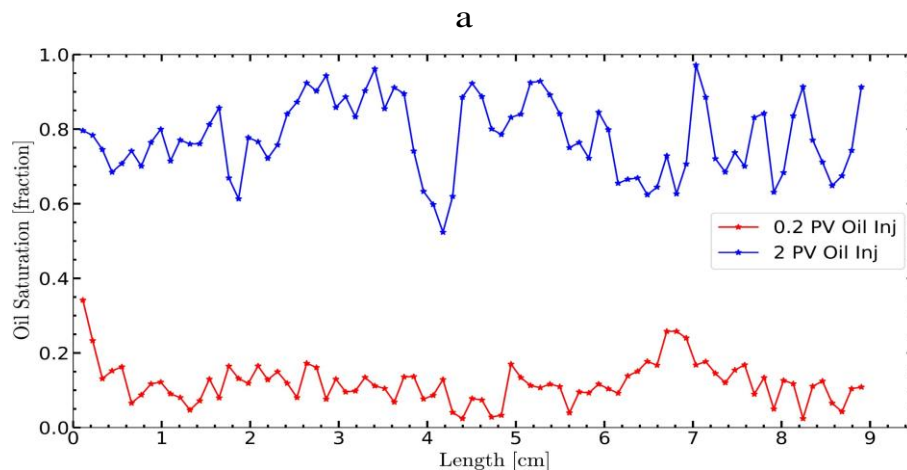


Figure 7-9. a): the flow of oil streamlines (yellow lines), during the process of oil drainage, pushing FW by oil; b): the water flow lines (yellow lines) during the displacement of oil and injection of FW.



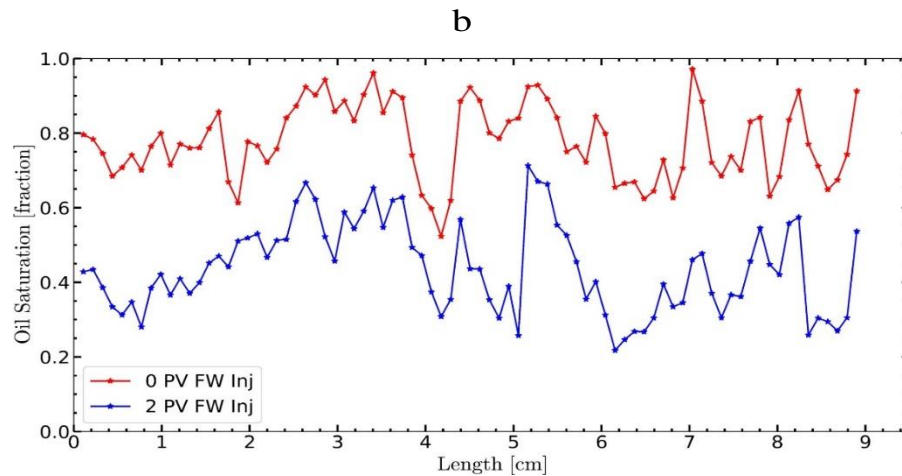


Figure 7-10. a): oil saturation profile after 0.2 and 2.0 PV of oil injection; b): oil saturation during FW injection, obtained from CT images examination.

After injecting 2 PV of formation water (FW), we subsequently injected seawater (SW) and measured the produced liquid to determine the recovery factor. The resulting recovery factor during both FW and SW injections is presented in Figure 7-11. Our findings indicate that oil production began shortly after FW injection, and after less than 1 PVI, a breakthrough occurred, resulting in no further oil production during FW injection. Following FW injection, the residual oil saturation was found to be 42.2%, which was reduced to 39.2% after SW injection. Notably, SW has a lower salinity than FW, as illustrated in Table 7-1. Interestingly, our results show that the oil recovery factor increased by 4.7% following SW injection, likely due to the osmosis mechanism. Specifically, the oil was mobilized due to osmotic water transfer to dead-end pores.

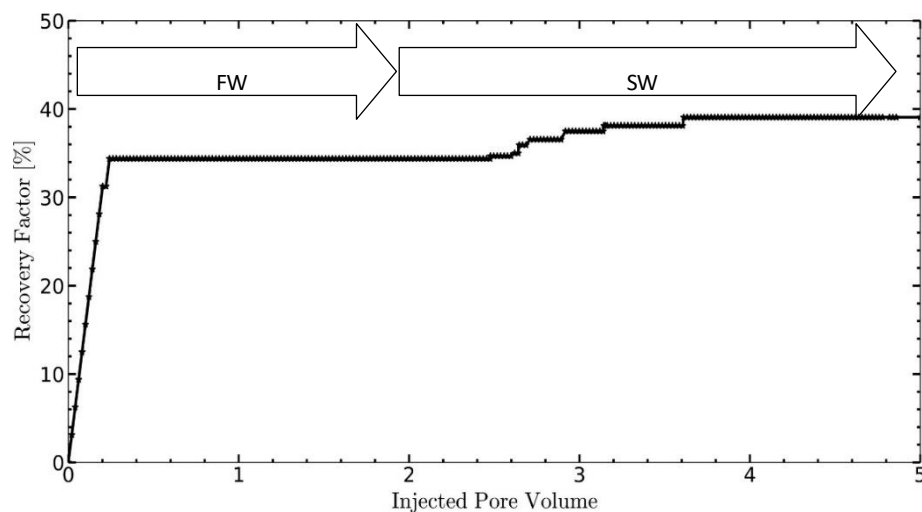


Figure 7-11. Oil recovery factor determined by measuring produced liquid during FW and SW injection experiments.

This study's recovery factor results are consistent with data from Brazilian pre-salt reservoirs. In both instances, a rapid breakthrough occurred despite the presence of porous media with suitable petrophysical properties, and the recovery factor remained low. Despite the fact that medical CT images revealed that certain areas remained undisturbed, and that fluid does not pass through certain large pores, the low resolution of these images makes it difficult to determine the precise causes of this phenomenon. Using microCT images, which have a much higher resolution than medical CT, additional numerical models were developed to acquire further insight. These models were created to investigate this matter in greater depth.

### 7.3.2 NUMERICAL MODELING

This section presents an analysis of two cross-sections obtained from microCT imaging. Using these cross-sections, we generate flow streamlines, velocity profiles, and pressure profiles for single-phase flow using the Navier-Stokes equation. Additionally, we obtained a saturation profile for a two-phase flow model. Finally, we conduct an analysis of the calculated results to better understand the behavior of fluids in stromatolite samples.

#### 7.3.2.1 SINGLE PHASE FLOW

To understand the flow regime in our core sample, using Equation (7-2), we obtained the Reynolds number alongside the core length. Figure 7-12 displays the Reynolds number during water flooding in two different flow rates ( $q_1 = 0.1 \text{ cm}^3/\text{min}$ ,  $q_2 = 0.5 \text{ cm}^3/\text{min}$ ). The findings demonstrated that even at a higher experimental flow rate of 0.5 cc/min, the Reynolds number is still less than 10, despite the fact that our stromatolite core sample had connected vugs with diameters in the centimeter range.

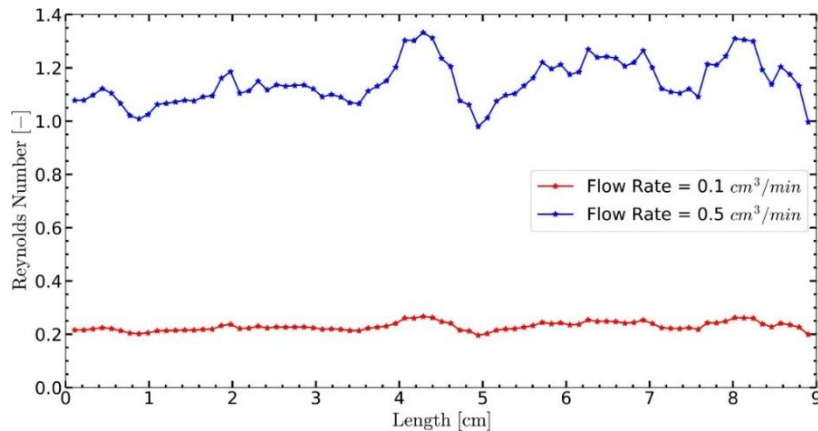
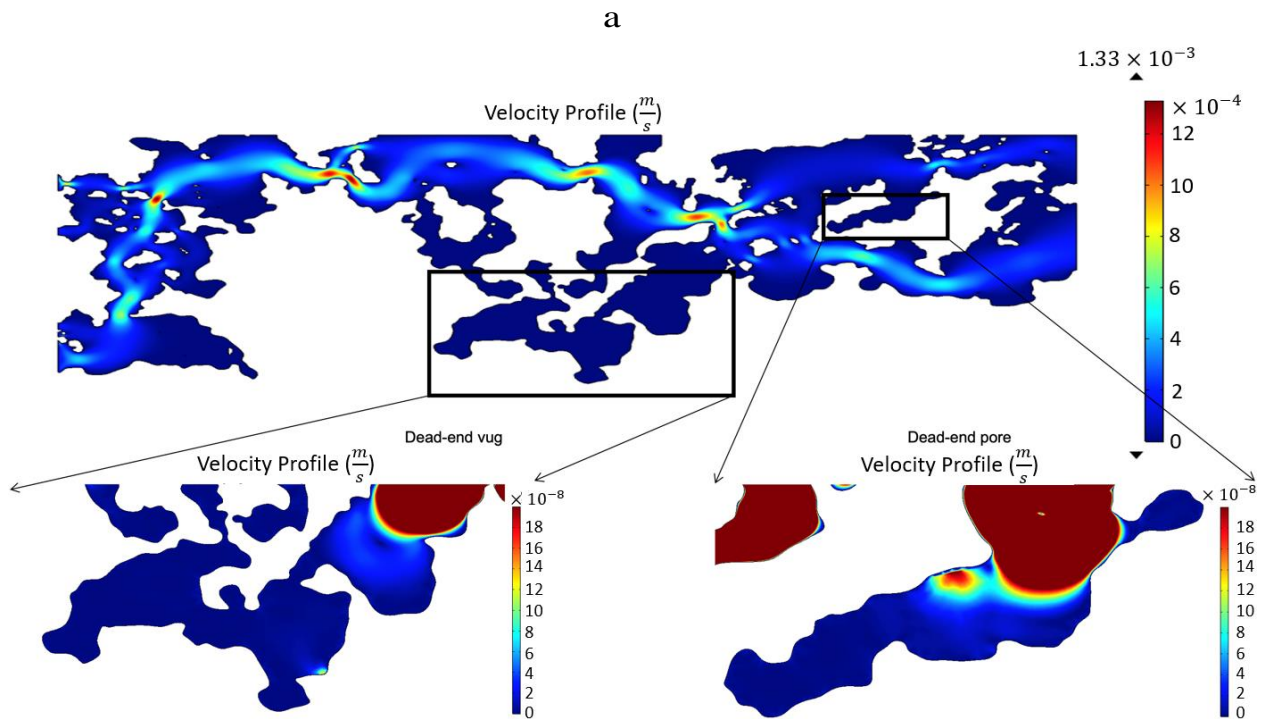


Figure 7-12. The Reynolds number alongside the core length.

To gain a better insight of fluid pattern inside vuggy porous media, two 2D cross-sections, one horizontal and one vertical (Figure 7-4), were generated using microCT data and used as geometry in the simulator. Figure 7-5 depicts the cross-sections. First, single-phase water flooding was modeled using Navier-Stokes and continuity equations (Equations (7-3) and (7-4)). The numerical simulation was carried out using COMSOL Multi-physics, a finite-element-based software.

Figure 7-13(a and b) demonstrate the velocity profiles of horizontal and vertical cross-sections, respectively. The fluid velocity increases dramatically when the fluid passes through throats, as illustrated. In fact, we injected water through the inlet at a constant velocity of  $1.4 \times 10^{-4} \text{ m/s}$  in both cases. However, because the diameter of throats in Figure 7-13(b) is smaller, the maximum velocity can reach up to  $3.67 \times 10^{-3} \text{ m/s}$ , whereas the maximum velocity in Figure 7-13(a) is  $1.33 \times 10^{-3} \text{ m/s}$ . Moreover, we noticed negligible fluid velocity inside dead-end zones in both cross-sections. To better illustrate the velocity in each cross-section, we picked a dead-end vug and a dead-end pore and zoomed in. As shown in Figure 7-13, the fluid velocity inside dead-end zones is nearly zero (red color displays the velocity of  $2 \times 10^{-7} \text{ m/s}$ ), and fluid remains stagnant within these regions despite the large volume that they may have.



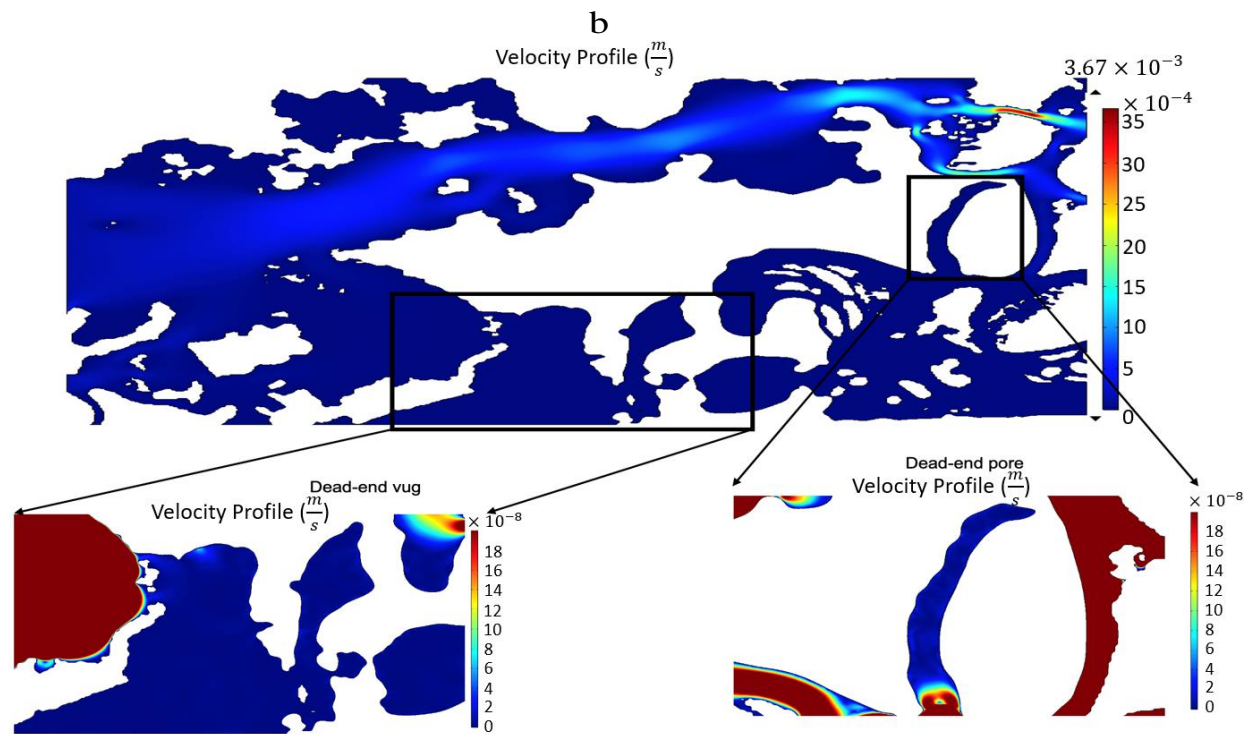


Figure 7-13. a): velocity profile inside horizontal cross-section, we zoomed inside a dead-end vug and a dead-end pore as well to evaluate velocity in dead-end regions; b): velocity profile in vertical cross-section that obtained from microCT data. The color bars beside each figure represent the velocity value, dark-red represents high and dark-blue low water velocity.

Figure 7-14 shows streamlines, which are used to visualize vector quantities by depicting curves tangent to a vector field. The density of streamlines varies with the magnitude velocity vector field in Figure 7-14; arrows on streamlines represent flow direction, and the color displays water velocity. The flow patterns confirm the experimental findings, that some dead-end vugs with significant volume remain untouched during flooding. Numerical simulation revealed that dead-end zones correspond to unswept regions. Indeed, streamlines provided us with a solid intuition about fluid propagation in single-phase flow in vuggy porous media; streamlines rendered the effect of dead-end zones on modifying flow path; this phenomenon, which was previously dismissed in most Brazilian pre-salt reservoir modeling, can now be implemented in future simulations to provide more reliable models.

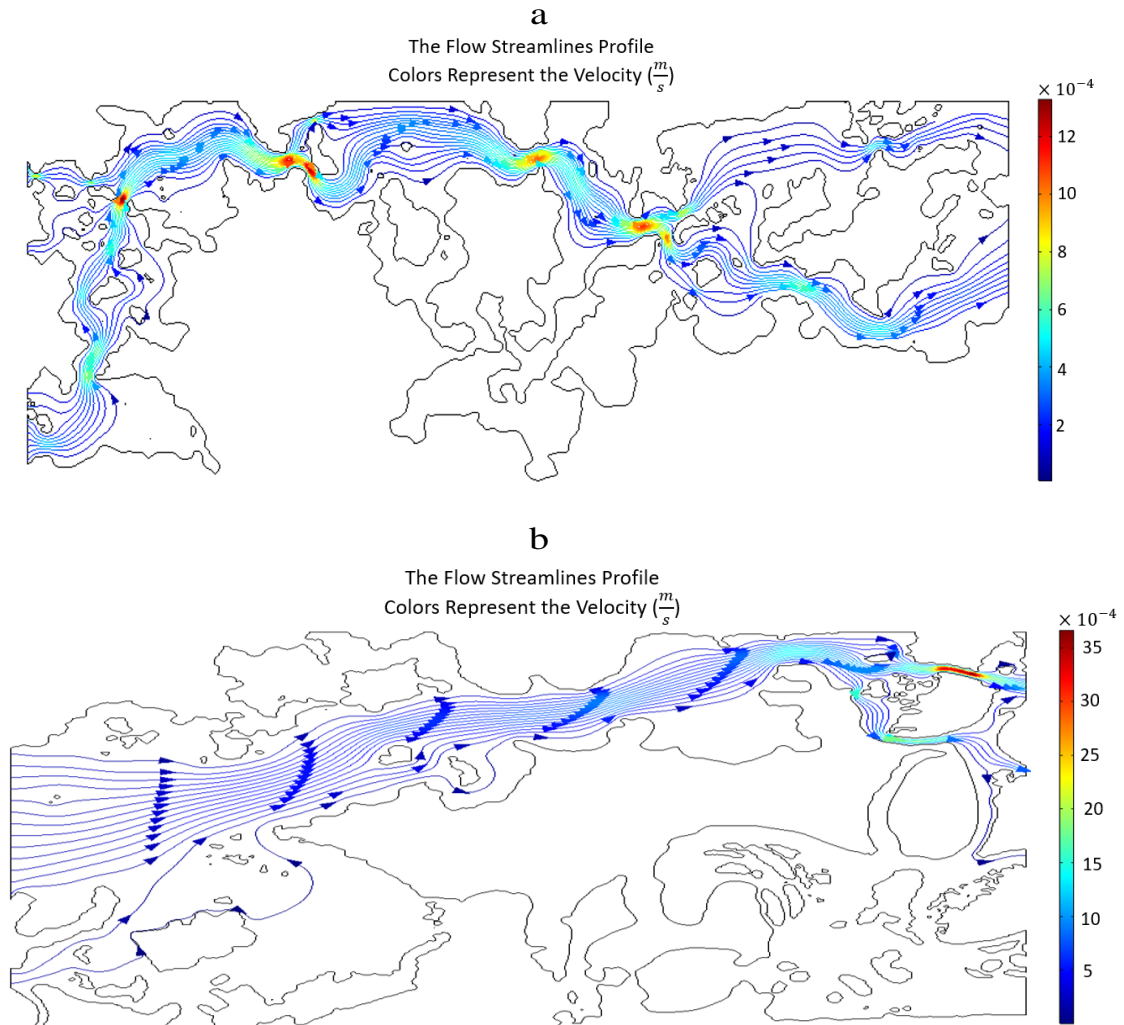


Figure7-14. a): streamlines inside the horizontal cross-section; b): streamlines inside the vertical cross-section. The color of streamlines and the arrows designate velocity and flow direction, respectively.

In order to track the pressure exchange within the dead-end zones, we next obtained the relative pressure variation within the horizontal cross-section. Figure 7-15 illustrates how the related pressure gradually decreases from  $490 Pa$  at the input to  $0 Pa$  at the outlet. The pressure change inside the dead-end zones, on the other hand, is small and nearly zero, as predicted by the velocity profile.

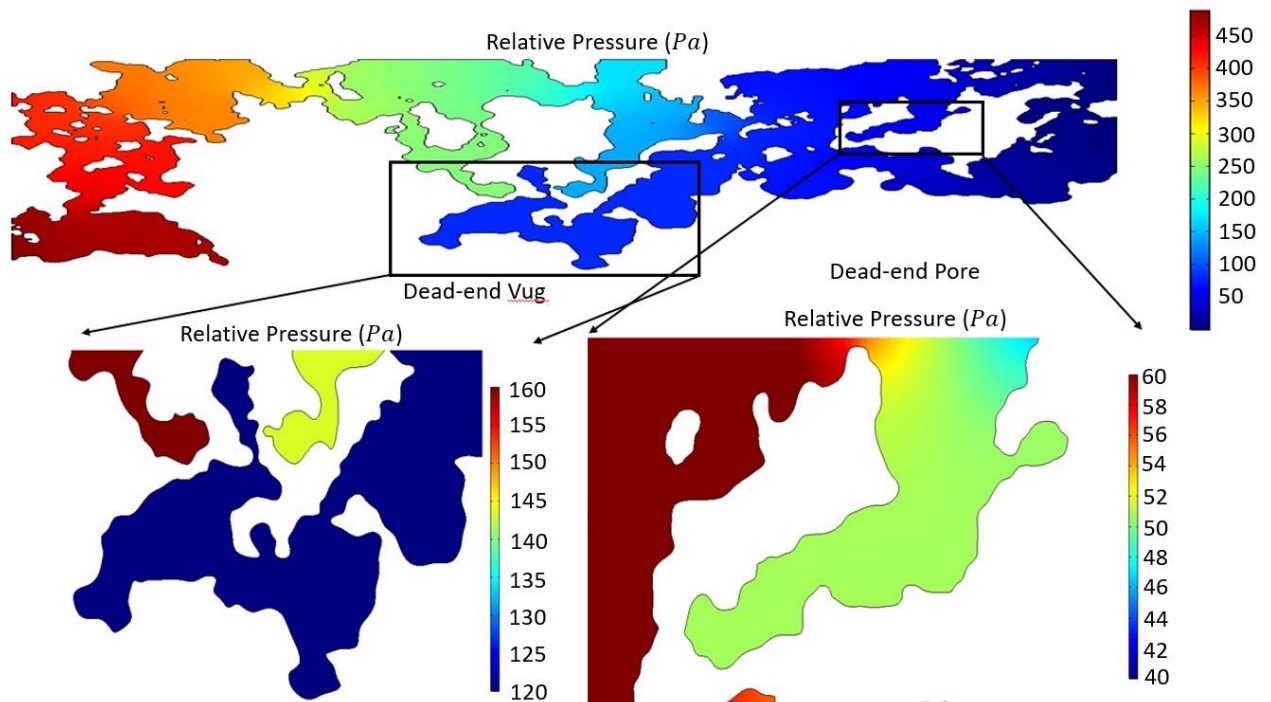


Figure 7-15. Variation in relative pressure within the horizontal cross-section. The relative pressure also appears in magnified dead-end zones. The color bar represents the pressure value.

### 7.3.2.2 MULTIPHASE FLOW

To evaluate the saturation profile during water flooding and investigate the effect of dead-end zones, the simulator was equipped with the pertinent relative permeability data, numerical simulation parameters, and assumptions as presented in Table 7-2. The implementation of these parameters and assumptions was aimed at accurately capturing the behavior of the fluid flow in the porous media system. Specifically, the relative permeability data was utilized to model the fluid phase behavior, while the numerical simulation parameters were employed to govern the computational processes of the simulator. By considering these factors, the study aimed to provide a robust analysis of the fluid flow dynamics and the effect of dead-end zones in the porous media system. Figure 7-16 and Figure 7-17 illustrate, respectively, the saturation profiles for the horizontal and vertical cross-sections for each time step of 0.2 PVI, from 0.2 to 1.2 PVI. In this simulation, water is injected at a constant rate of  $0.1 \text{ cm}^3/\text{min}$ , and early breakthrough is detected in both cross-sections; furthermore, the saturation profile does not vary appreciably after breakthrough. The findings show that oil in dead-end areas cannot be displaced by water. Even inside large vugs close to inlet, there was still a significant amount of bypassed oil present after core flooding. When Figure 7-16 and Figure 7-17 are examined, it is clear that the horizontal cross-

section has more dead-end zones than the vertical does, which causes to have a lower areal swept efficiency and faster breakthrough, in 2D simulation.

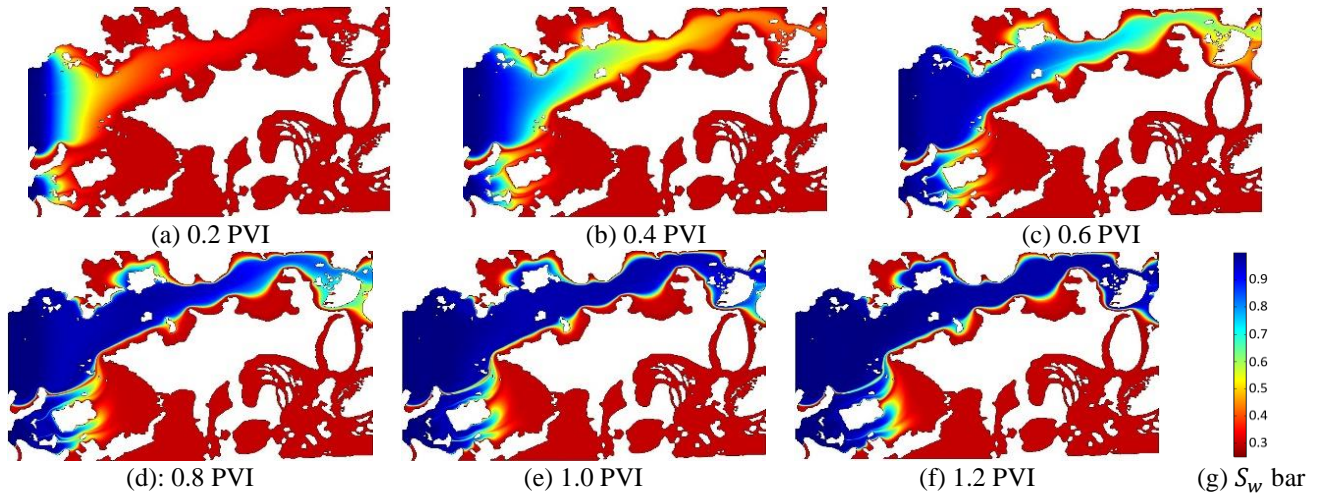


Figure 7-16. Saturation profile during water flooding (horizontal cross-section). The color bar depicts the water saturation profile, where blue represents higher water saturation and red represents greater oil saturation.

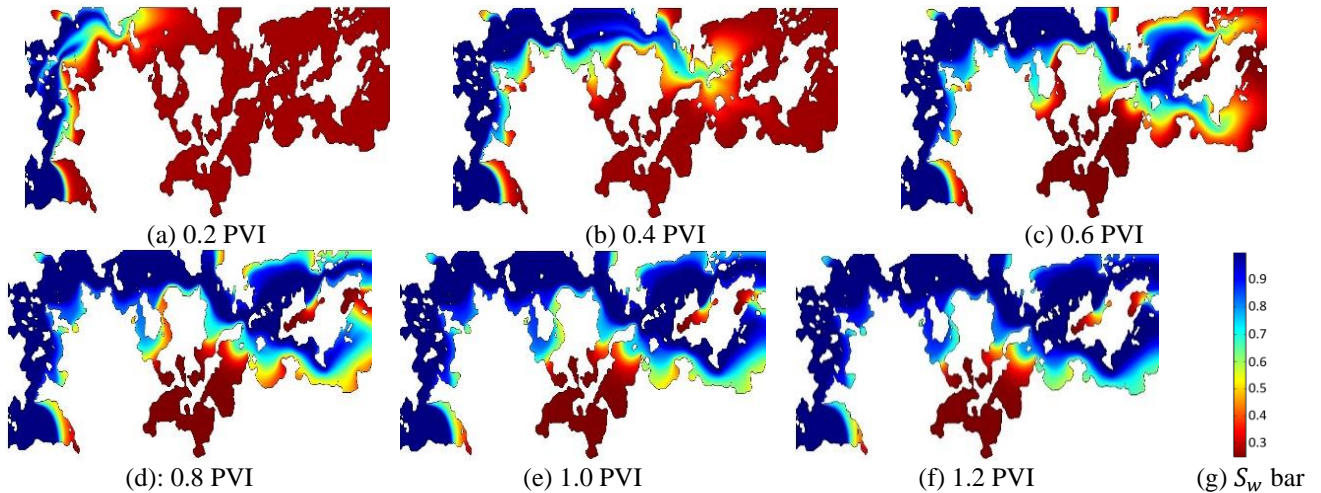


Figure 7-17. Saturation profile of vertical cross-section in each 0.2 PVI, during water flooding with constant flow rate of  $0.1 \text{ cm}^3/\text{min}$ .

Figure 7-18 (a) depicts the average water saturation in each cross-section, whereas Figure 7-18 (b) displays the water saturation in produced fluid (in the outlet). In both cases, we record merely the oil production at first, and then the water monitored in the outlet after the breakthrough. Prior to the breakthrough, we observed linear behavior in the average water saturation in each cross-section. However, following the breakthrough, the tangent of the water saturation line gradually declined, even though in both cases a notable amount of oil was still present in dead-end regions.

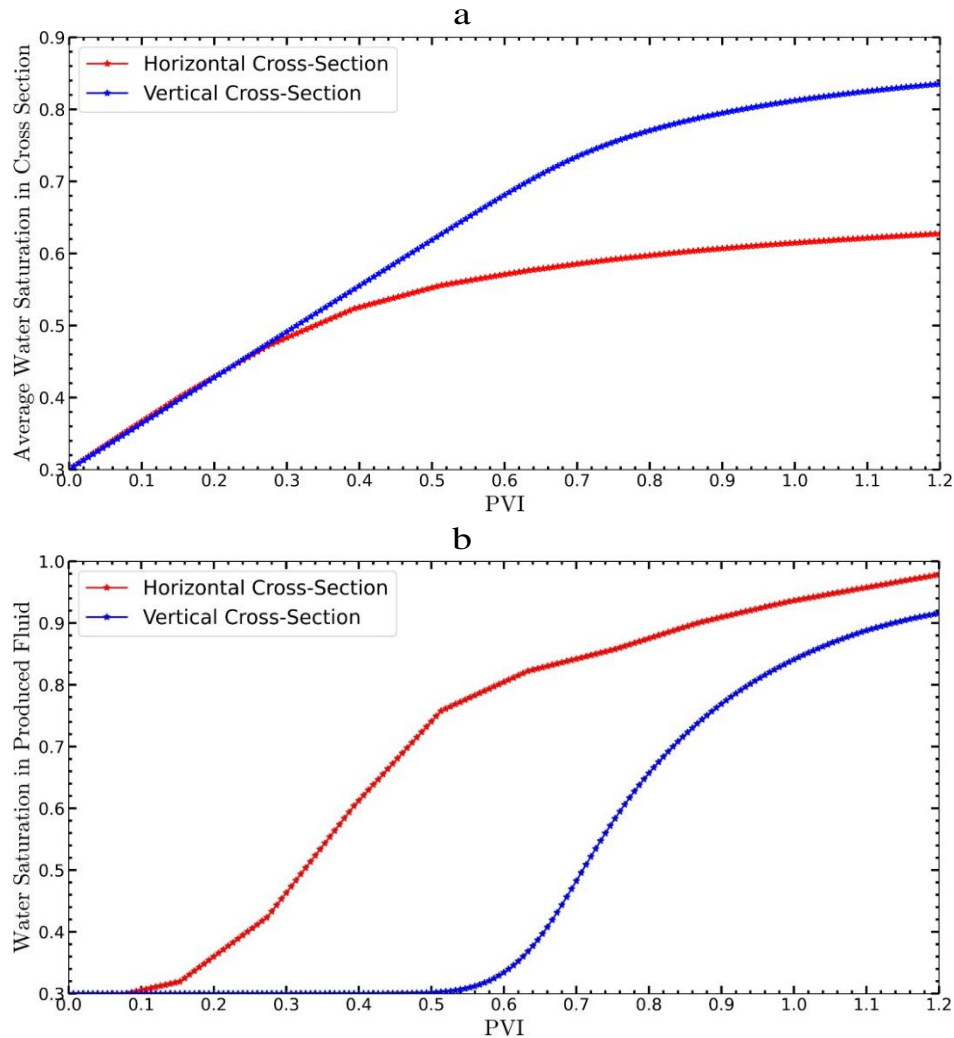


Figure 7-18. a): average water saturation during water flooding in each cross-section; b): water saturation in produced liquid (water saturation in outlet).

The findings show that, regardless of the size of the dead-end zones, the oil was still bypassed in these regions, resulting in low areal swept efficiency. Simulation outcomes on both microCT images clearly show poor recovery factor following flooding with water, which is congruent with laboratory and field results. Indeed, one of the observations gained from this simulation is that, in order to boost the recovery factor, we need to push oil out of dead-end zones by different EOR techniques such as  $CO_2$  injection, which causes oil swelling (Rezk and Foroozesh, 2018). Similar outcomes have also been reported for the light oil-containing Lula field in Brazilian pre-salt reservoirs, where water flooding caused a poor oil recovery factor but water alternative gas ( $CO_2$  as gas phase) was associated with a remarkably higher recovery factor (McGuire et al., 2005).

This paper presents a study investigating the influence of pore geometry on fluid flow pattern, saturation profile, pressure profile, recovery factor, and fluid velocity during fluid injection in porous media. Our findings demonstrate that, in addition to petrophysical properties and fluid-rock characterization, pore geometry significantly impacts fluid flow pattern in porous media. We compared our results to previous field data for  $CO_2$  injection and water flooding in Brazilian pre-salt reservoirs, revealing a match with the previously reported low recovery factor (in some cases around 10%). Although our study provides comprehensive insight into the impact of porous structure on fluid flow, future research should consider 3D simulation of  $CO_2$  injection, while also taking into account the chemical reactions between  $CO_2$ , brine, oil, and rock. It is worth noting that while this study was conducted using plug samples collected from stromatolites in Brazil, the same methodology can be applied to simulate fluid flow in other types of porous media.

## 7.4 CONCLUSIONS

This study's primary goal was to assess the petrophysical characteristics and flow pattern within a vuggy core plug obtained from a Brazilian stromatolite outcrop, located in Lagoa Salgada in Rio de Janeiro, which is known to be flow analogous to Brazilian pre-salt reservoirs. The study has yielded the following results:

- The experimental findings indicate that the core samples collected from Lagoa Salgada field possess desirable petrophysical properties, including an average permeability of 1179.02 millidarcy and a porosity of 52.5%.
- The single-phase core flooding with two distinct flow rates (0.1 and 0.5  $cm^3/min$ ) in combination with medical-CT scanning indicated that there are connected pores in the core sample that no streamline passes through and the fluid remains stagnant inside them. The same phenomenon was seen during the process of oil drainage and water imbibition.
- The results indicate a low oil recovery factor due to the specific fluid flow pattern observed after the injection of formation water and seawater in a core that was saturated with light oil for a reasonably long time. Furthermore, the analysis of medical-CT images of both oil drainage and water imbibition processes revealed early breakthrough.
- To precisely evaluate the flow streamlines inside the vuggy porous material, microCT scanning with high resolution (40  $\mu m/voxel$ ) was conducted, and two cross-sections were formed and used as geometry for single and two-phase flow modeling. The velocity profile, flow streamlines, and pressure profile were derived and assessed using Navier-Stokes and continuity equations to simulate single-phase flow (water flooding). Although there are huge connected dead-end vugs with diameters in the centimeter range, the pressure fluctuation and velocity inside these regions are negligible, and fluid streamlines indicate that fluid within these zones remains stagnant.
- The lattice Boltzmann equation (LBE) was implemented to model multi-phase flow in each cross-section and obtain a saturation profile during water flooding. The findings show

that the oil remained stuck in dead-end zones even close to the inlet. This remarkable volume of bypassed oil resulted in high oil saturation and low oil recovery factor. The magnitude and volume of these dead-end regions have a significant impact on the time that breakthrough happens.

In summary, this study aimed to elucidate the factors underlying the low oil recovery factor observed in Brazilian pre-salt reservoirs, despite possessing favorable oil-producing properties and being characterized by the presence of large, interconnected vugs and pores. Furthermore, this paper investigates the impact of pore geometry on fluid patterns using a combination of experimental and computational modeling techniques. The field data, in previous studies, observed that the injection of  $CO_2$  results in a significant increase in the recovery factor, and this study aimed to provide insight into the underlying mechanisms, and in particular impact of porous geometry, responsible for this observation.

## **7.5 ACKNOWLEDGMENTS**

We gratefully acknowledge the support of EPIC-Energy Production Innovation Center, hosted by the University of Campinas (UNICAMP) and sponsored by FAPESP - Sao Paulo Research Foundation (2017/15736-3 process). We acknowledge the support and funding from Equinor Brazil and support of ANP (Brazil's National Oil, Natural Gas and Biofuels Agency) through the R&D levy regulation. Acknowledgments are extended to the Center for Energy and Petroleum Studies (CEPETRO) and School of Mechanical Engineering (FEM).

## 7.6 REFERENCES

- Alvarez, L.L., Guimarães, L.J.d.N., Gomes, I.F., Beserra, L., Pereira, L.C., de Miranda, T.S., Maciel, B., Barbosa, J.A., 2021. Impact of fracture topology on the fluid flow behavior of naturally fractured reservoirs. *Energies* 14, 5488.
- Alves, J.A., Polette, M., 2021. Political, economic, and institutional aspects of oil and gas exploration and production in Brazil. *América Latina en la historia económica* 28.
- Bear, J., *Dynamics of fluids in porous media* (Courier Corporation, 1988). Google-Books-ID: lurrmlFGhTEC.
- Blick, E.F., 1966. Capillary-orifice model for high-speed flow through porous media. *Industrial & Engineering Chemistry Process Design and Development* 5, 90-94.
- Branco, C.C., 2012. Challenges in implementing an EOR project in the pre-salt province in deep offshore Brasil, SPE EOR Conference at Oil and Gas West Asia. OnePetro.
- Bruhn, C.H., Pinto, A.C., Johann, P.R., Branco, C., Salomão, M.C., Freire, E.B., 2017. Campos and Santos basins: 40 Years of reservoir characterization and management of shallow-to ultra-deep water, post-and pre-salt reservoirs-Historical overview and future challenges, OTC Brasil. OnePetro.
- Buchori, L., Supardan, M., Bindar, Y., Sasongko, D., Makertihartha, I., 2017. The Effect of Reynolds Number at Fluid Flow in Porous Media. *Reaktor* 6, 48-55.
- Callefo, F., Arduin, D., Ricardi-Branco, F., Galante, D., Rodrigues, F., Branco, F., 2018. The giant stromatolite field at Santa Rosa de Viterbo, Brazil (Paraná Basin)—A new paleoenvironmental overview and the consequences of the Irati Sea closure in the Permian. *Journal of South American Earth Sciences* 84, 299-314.
- Correia, M., Hohendorff, J., Gaspar, A., Schiozer, D., 2015. UNISIM-II-D: Benchmark case proposal based on a carbonate reservoir, SPE Latin American and Caribbean Petroleum Engineering Conference. OnePetro.
- da Costa Fraga, C.T., Capeleiro Pinto, A.C., Branco, C.C.M., da Silva Paulo, C.A., 2015. Brazilian pre-salt: An impressive journey from plans and challenges to concrete results, Offshore Technology Conference. OnePetro.
- da Rocha, H.O., da Costa, J.L.S., Carrasquilla, A.A.G., Carrasco, A.M.V., 2019. Petrophysical characterization using well log resistivity and rock grain specific surface area in a fractured carbonate pre-salt reservoir in the Santos Basin, Brazil. *Journal of Petroleum Science and Engineering* 183, 106372.
- de Araujo Cavalcante Filho, J.S., Santos Silva, V.L., de Sant'Anna Pizarro, J.O., 2020. Assessment of miscible WAG injection performance in a giant carbonate reservoir using analytical and numerical approaches, SPE Improved Oil Recovery Conference. OnePetro.
- De Lima, A., Fournó, A., Noetinger, B., Schiozer, D.J., 2019. Characterization and modeling of the fault network of a Brazilian pre-salt reservoir and upscaling results, SPE Annual Technical Conference and Exhibition. OnePetro.
- Doering, C.R., Gibbon, J.D., 1995. *Applied analysis of the Navier-Stokes equations*. Cambridge university press.
- Drexler, S., Bastos Alves, R., Silos, V., Ferreira De Siqueira, M., Toelke, J., 2022. New Method to Simulate Digital Petrophysical Properties in Heterogeneous Carbonates Using Multiscale Micro Computed Tomography Imaging and Customized Laboratory Experiments, International Petroleum Technology Conference. OnePetro.

- Feng, Q.-x., Di, L.-c., Tang, G.-q., Chen, Z.-y., Wang, X.-l., Zou, J.-x., 2004. A visual micro-model study: The mechanism of water alternative gas displacement in porous media, SPE/DOE Symposium on Improved Oil Recovery. OnePetro.
- Ferreira, D.J.A., Dias, R.M., Lupinacci, W.M., 2021. Seismic pattern classification integrated with permeability-porosity evaluation for reservoir characterization of presalt carbonates in the Buzios Field, Brazil. *Journal of Petroleum Science and Engineering* 201, 108441.
- Firoozabadi, A., Aziz, K., 1986. Relative permeability from centrifuge data, SPE California Regional Meeting. OnePetro.
- Frolov, S.V., Akhmanov, G.G., Kozlova, E.V., Krylov, O.V., Sitar, K.A., Galushkin, Y.I., 2011. Riphean basins of the central and western Siberian Platform. *Marine and Petroleum Geology* 28, 906-920.
- Gal-Chen, T., Somerville, R.C., 1975. On the use of a coordinate transformation for the solution of the Navier-Stokes equations. *Journal of Computational Physics* 17, 209-228.
- Godoi, J.M.A., dos Santos Matai, P.H.L., 2021. Enhanced oil recovery with carbon dioxide geosequestration: first steps at Pre-salt in Brazil. *Journal of Petroleum Exploration and Production* 11, 1429-1441.
- Harlow, F.H., Amsden, A.A., 1971. A numerical fluid dynamics calculation method for all flow speeds. *Journal of Computational Physics* 8, 197-213.
- Iraji, S., Soltanmohammadi, R., De Almeida, T., Rodrigues, Munoz, E.R., Vidal, A.C., 2022. Experimental investigation of single-phase flow pattern in highly heterogeneous carbonates rocks, Rio Oil & Gas 2022. IBP, Rio de Janeiro | Brasil.
- Ligero, E.L., Schiozer, D.J., 2014. Miscible WAG-CO<sub>2</sub> light oil recovery from low temperature and high pressure heterogeneous reservoir, SPE Latin America and Caribbean Petroleum Engineering Conference. OnePetro.
- Liu, S., Afacan, A., Masliyah, J., 1994. Steady incompressible laminar flow in porous media. *Chemical engineering science* 49, 3565-3586.
- McGuire, P., Redman, R., Jhaveri, B., Yancey, K., Ning, S., 2005. Viscosity reduction WAG: an effective EOR process for North Slope viscous oils, SPE Western Regional Meeting. OnePetro.
- Momani, S., Odibat, Z., 2006. Analytical solution of a time-fractional Navier–Stokes equation by Adomian decomposition method. *Applied Mathematics and Computation* 177, 488-494.
- Muniz, M., Bosence, D., 2015. Pre-salt microbialites from the Campos Basin (offshore Brazil): image log facies, facies model and cyclicity in lacustrine carbonates. *Geological Society, London, Special Publications* 418, 221-242.
- Nguyen, D., Balakotaiah, V., 1994. Flow maldistributions and hot spots in down-flow packed bed reactors. *Chemical engineering science* 49, 5489-5505.
- Park, H., Jiang, L., Kiyama, T., Zhang, Y., Ueda, R., Nakano, M., Xue, Z., 2017. Influence of sedimentation heterogeneity on CO<sub>2</sub> flooding. *Energy Procedia* 114, 2933-2941.
- Rezk, M.G., Foroozesh, J., 2018. Determination of mass transfer parameters and swelling factor of CO<sub>2</sub>-oil systems at high pressures. *International Journal of Heat and Mass Transfer* 126, 380-390.
- Sohrabi, M., Riazi, M., Jamiolahmady, M., Ireland, S., Brown, C., 2009. Mechanisms of oil recovery by carbonated water injection, SCA annual meeting, pp. 1-12.
- Soltanmohammadi, R., Iraji, S., De Almeida, T.R., Munoz, E.R., Fioravanti, A.R., Vidal, A.C., 2021. Insights into Multi-Phase Flow Pattern Characteristics and Petrophysical Properties in Heterogeneous Porous Media, Second EAGE Conference on Pre-Salt Reservoir. European Association of Geoscientists & Engineers, pp. 1-5.

Soltanmohammadi, R., Iraj, S., De Almeida, T.R., Munoz, E.R., Vidal, A.C., 2022. Upscaling Challenges of Heterogeneous Carbonate Rocks: A Case Study of Brazilian Pre-Salt Analogous, Third EAGE Conference on Pre Salt Reservoirs.

van Lopik, J.H., Snoeijers, R., van Dooren, T.C., Raouf, A., Schotting, R.J., 2017. The effect of grain size distribution on nonlinear flow behavior in sandy porous media. *Transport in Porous Media* 120, 37-66.

Waterworth, A., Bradshaw, M.J., 2018. Unconventional trade-offs? National oil companies, foreign investment and oil and gas development in Argentina and Brazil. *Energy policy* 122, 7-16.

Wright, P., Tosca, N., 2016. A geochemical model for the formation of the pre-salt reservoirs, Santos Basin, Brazil: implications for understanding reservoir distribution. *AAPG Search and Discovery*, article 51304.

**8 APPENDIX II: LABORATORY AND NUMERICAL  
EXAMINATION OF OIL RECOVERY IN BRAZILIAN PRE-SALT  
ANALOGUES BASED ON CT IMAGES**

**Author: Shohreh Iraji**

**Co-Author: Ramin Soltanmohammadi, Tales Rodrigues De Almeida, Eddy Ruidiaz Munoz,  
Mateus Basso, Alexandre Campana Vidal**

**Campinas - SP**

**2023**

D2- 2

## Laboratory and Numerical Examination of Oil Recovery in Brazilian Pre-salt Analogues Based on CT images

S. Irají<sup>1</sup>, R. Soltanmohammadi<sup>1</sup>, T. Rodrigues De Almeida<sup>1</sup>, E. Ruidiaz Munoz<sup>1</sup>, M. Basso<sup>1</sup>, A. Campana Vidal<sup>1</sup>

UNICAMP<sup>1</sup>

### Summary

---

Summary it is not available

## Introduction

Brazilian pre-salt reservoirs are regarded as one of the most important recent oil field finds because of their tremendous hydrocarbon production potential (Bruhn et al., 2017). The high heterogeneity and complexity of these reservoirs including variations in pore geometry and size, further add to the uncertainties and challenges associated with managing and modeling these reservoirs (Hosa et al., 2020). To reduce risks and ambiguities, it is essential to have a thorough understanding and proper evaluation of the fluid flow transfer, petrophysical features, and oil recovery efficiency of pre-salt reservoirs. In this paper, experiments and simulations were performed for the determination and quantification of the porous media and the fluid flow in a stromatolite sample from Lagoa Salgada in Rio de Janeiro State, Brazil, which is known as analogous to some pre-salt reservoirs. The rock pore structure was divided into two facies based on pore size; vugular/columnar and fined-grained. After the acquisition of the CT data of the core, the 2-D tomography images were manipulated and processed to create a 3-D fine-scale grid to simulate the porous media and the fluid flow. To reduce computational time, upscaling techniques were applied to create the coarse simulation grids, and simulated oil recovery factor and water cut results for different upscaled models were compared with the experimental results from core flooding.

## Method and/or Theory

Rock samples from outcrops of Lagoa Salgada in Rio de Janeiro State, Brazil, were collected and employed as possible analogues of some Pre-salt reservoir rocks (Wright and Tosca, 2016) to assess the water flooding performance in this carbonate rock. One core sample (8.9 x 3.68 cm) was drilled and chosen in order to thoroughly understand fluid flow in the rock. For this sample, we divided the rock pore structure into two facies: columnar (vugular), with huge and connected pores/vugs, and fine-grained, with relatively small pores. Core flooding investigations were difficult since the stromatolite core sample was delicate and highly diverse; the encapsulation procedure was employed to solve this difficulty (Iraji et al., 2022; Soltanmohammadi et al., 2021). The history production data (oil and water production data) were recorded during core flooding experiments to compare with simulation results. The pore geometry within the core sample was retrieved using a Siemens SOMATOM Spirit medical CT scanner with a slice thickness of 10 mm, and pixel resolution of 512x512.

After the acquisition of the two-dimensional data of the core (cross-section CT images, DICOM files, representing pore structures), a Python Code was developed to manipulate and process tomograph 2-D images and create a 3-D fine-scale grid (high fidelity model) to be inputted into the simulation model for the determination and quantification of the porous media and the fluid flow. The Python Code automatically reads the images, and creates the output files for the simulation, considering a Cartesian grid. The dimensions of the core were measured from the CT Images, the Pixel size for this case, was 0.10 mm. As each image had 512x512 pixels, the size of the image was 53x53 mm. Each pixel of the image was converted into one simulation block. Each slice had one mm thickness, with a total of 87 mm, or 87 slices (the first and last slices did not consider for building the model). The fine grid simulation model was constituted of 512x512x87 blocks (22,806,528 blocks).

Some initial rules for segmentation, porosity, and permeability estimations were applied. The separation of facies was based on an adaptive threshold value of CT. The value of 1500 was selected by analyzing the images. With this, points where  $CT > CT_{thres}$  were assigned to the Rock Type 1

(fine-grained), and points where  $CT < CT_{thres}$  Rock Type 2 (vugular). Porosity was considered to keep a linear relationship with CT value. For the fine porosity facies, limits of 0.1% and 35% were considered and linearly correlated with the CT values. For the vugular facies, porosities from 85% to 98% were considered, also with a linear correlation with CT value. Permeability for fine facies was calculated using the correlation with porosity, while for the vugular facies, a value of 10 D was considered. Blocks outside the rock part of the image were set to null blocks. The resulting model contained a total of 9,476,244 active blocks. Figure 1 shows a 3D representation of the porosity of the model.

The output files include all necessary files for running the simulator containing the porosity, permeability, rock type, and null blocks. The simulator used in this work was the CMG-IMEX®, which is a commercial Black-Oil reservoir simulator.

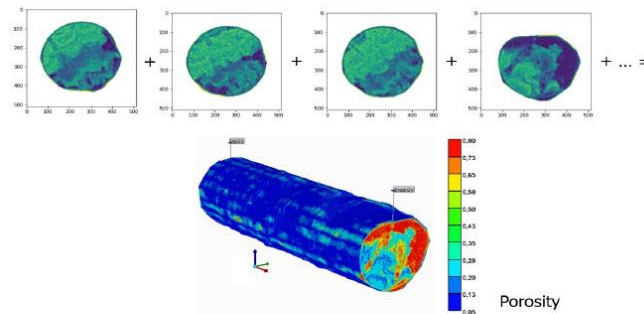


**Figure 1** 3-D representation of the simulation model

The Brooks-Corey relationships model (Equation 1) was used to describe oil and water relative permeabilities; for rock type 1, the exponents  $n_o$  and  $n_w$  were considered as 6, while for rock type 2 number 1 was selected resulting in a linear relationship between saturation and relative permeabilities. Data of residual oil saturation and connate water saturation was obtained from core flooding experiments.

$$k_{ro} = k_{ro,max} \left( \frac{S_o - S_{or}}{1 - S_{or} - S_{wc}} \right)^{n_o}, \quad k_{rw} = k_{rw,max} \left( \frac{S_w - S_{wc}}{1 - S_{or} - S_{wc}} \right)^{n_w} \quad \text{Equation 1}$$

Wells were designed to represent the core holder diffuser. Figure 2 displays detail of the wells. The producer was kept with a constant pressure of  $100 \text{ kgf/cm}^2$  (1422 psi) and the injector operated with a flow rate of  $0.1 \text{ cm}^3/\text{min}$ .

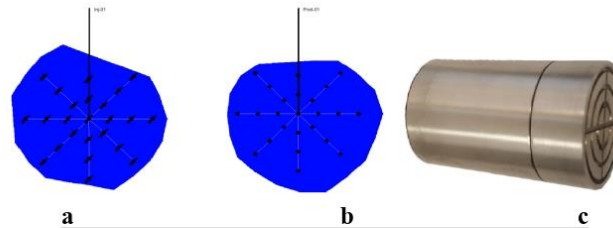


**Figure 2** Position and completions of the injector (a) and producer (b) and physical diffuser (c)

Since this model contains a very large number of grid blocks, simulations of the complete model were very time-consuming, and not practical, thus, it became evident that an upscaling technique is necessary. In this step, an algorithm was implemented in Python to create upscaled models, where groups of blocks were merged into a coarser simulation grid. The software allowed the upscaling to any given dimension of an upscaled block. The refined model was the one obtained directly from CT data. Preliminary upscaling rules were applied, to allow the creation of the algorithm.

The upscaling of porosity was performed with a simple arithmetic average. The software developed in the previous section automatically groups the blocks and averages the porosity for each block. Blocks were considered to be null when all the blocks from refined models were null. If null blocks from the refined model are present in the region of the upscaled block, porosity was set to zero in these blocks, and then the arithmetic average was performed. Regarding rock type, the value taken into consideration was the one with the most frequent value in the refined blocks. Finally, for permeability, a log average was considered, according to Equation 2.

$$k_{upscaled} = \exp\left(\frac{\sum \log(k_i)}{n}\right)$$

Equation 2

It is important to notice that Equation 1 is consistent with other equations, corroborating the conclusion that the correlation between porosity and permeability remains valid when the scale is changed. Blocks with 100% of refined blocks as rock type 1 had the permeability value calculated from the correlation between porosity and permeability, while blocks with 100% of refined blocks of rock type 2 had the permeability value of 10 D.

Upscaled models were created for four upscaling factors (n= 3, 5, 6, and 12), considering each upscaled block to be generated from  $n \times n \times 1$  refined blocks. Figure 3 compares a 2D visualization of the porosity and permeability of the model with upscaling factors of 6 and 12 for the J direction middle plane.

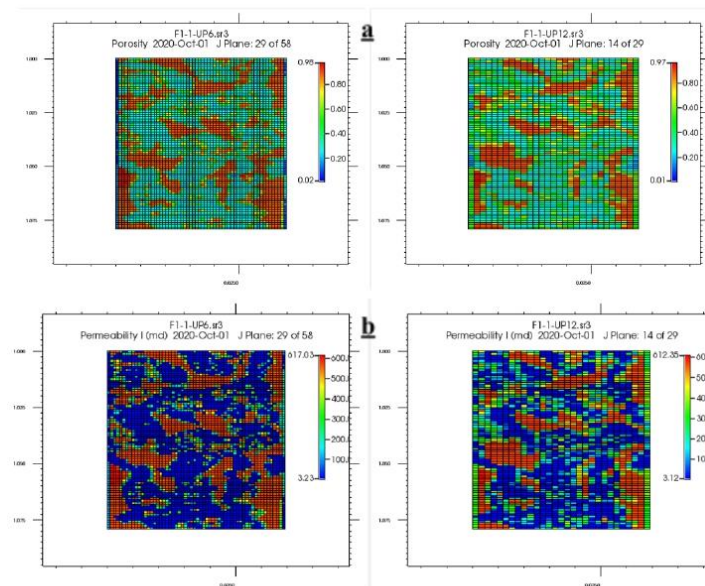


**Figure 3** Porosity (a) and permeability (b) models visualization for upscaling factors of 6 (left) and 12 (right)

Figure 4 shows the oil and water production results obtained from the experiments and simulator results for two upscaled models. The experimental recovery factor by water injection (Figure 4-a) reached values up to around 39% of the original oil in place. The initial water saturation for this sample was 0.356 (0.644 initial oil saturation) and the residual oil saturation was recorded as 0.392 after the water injection process. During water injection, the breakthrough of water occurred at around 0.2 pore volume of injected water, and the water cut increased and reached around 95% of production (Figure 4-b). Simulation results (Figure 4-c and d) demonstrated that the oil recovery factors and water cut for two coarse models with differing upscaling factors (6 and 12) are nearly identical, which reveals the effectiveness of the implemented upscaling techniques.

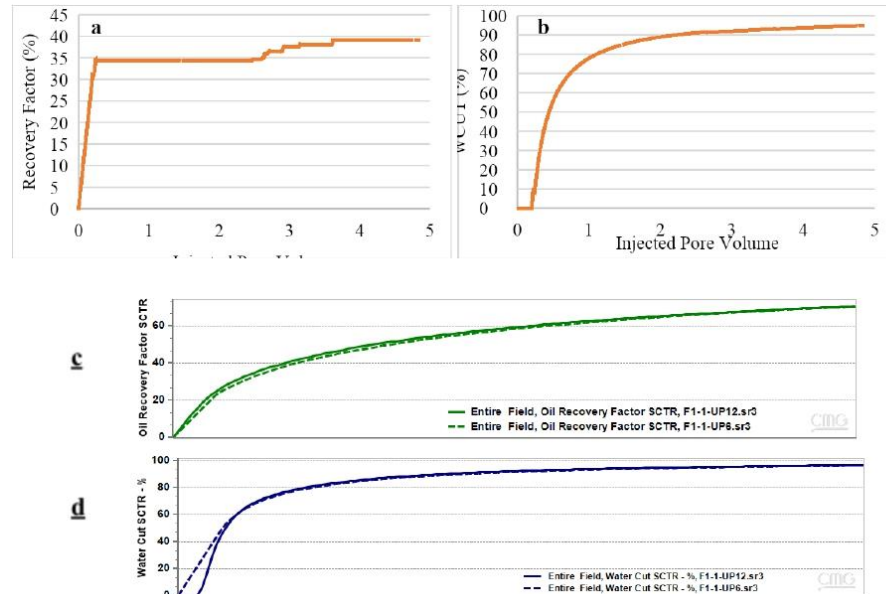


**Figure 4** a) Recovery factor results from the experiments b) water cut results from the experiments c) recovery factor results for upscaling factors of 6 and 12 d) water cut results for upscaling factors of 6 and 12 (solid line: factor of 12, dashed line: factor of 6)

### Conclusions

In this study, the petrophysical properties of stromatolite rock samples taken from Lagoa Salgada in Rio de Janeiro State, Brazil, were examined. The exceptional differentiation and high variability in pore size distribution were found in this sample, resulting in the separation of fine-grained and vugular facies.

Core flooding experiments were performed and production history data for both oil and water were recorded. The results revealed that the oil recovery efficiency during water injection achieved a value of around 39% based on original oil in place (OOIP). The sample was scanned with a CT scanner and an algorithm was developed to interpret images and produce fine-scale grid data with a large number of grid blocks to be used in the CMG simulator. Since simulations of the fine-scale (high fidelity) model required a high computational time, an algorithm was used to build upscaled models. The simulation results for different upscaling factors were comprised and compared with experimental results of oil recovery factor and water cut from core flooding experiments. The simulation results with different upscaling factors showed acceptable congruent.

### Acknowledgements

We acknowledge the support and funding from Equinor Brazil and the support of ANP (Brazil's National Oil, Natural Gas and Biofuels Agency) through the R&D levy regulation. Acknowledgments are extended to the Center for Petroleum Studies (CEPETRO) and the School of Mechanical Engineering (FEM).

### References

Bruhn, C.H., Pinto, A.C., Johann, P.R., Branco, C., Salomão, M.C., Freire, E.B., 2017. Campos and Santos basins: 40 Years of reservoir characterization and management of shallow-to ultra-deep water, post-and pre-salt reservoirs-Historical overview and future challenges, OTC Brasil. OnePetro.

# EAGE

- Hosa, A., Wood, R., Corbett, P., de Souza, R.S., Roemers, E., 2020. Modelling the impact of depositional and diagenetic processes on reservoir properties of the crystal-shrub limestones in the 'Pre-Salt' Barra Velha Formation, Santos Basin, Brazil. *Marine and Petroleum Geology* 112, 104100.
- Iraji, S., Soltanmohammadi, R., Munoz, E.R., Winter, A., de Almeida, R.V., Vidal, A.C., 2022. Experimental Investigation of Waterflooding Performance by Increasing Copper Ions in Brazilian Pre-Salt Rock, 83rd EAGE Annual Conference & Exhibition. European Association of Geoscientists & Engineers, pp. 1-5.
- Soltanmohammadi, R., Iraji, S., De Almeida, T.R., Munoz, E.R., Fioravanti, A.R., Vidal, A.C., 2021. Insights into Multi-Phase Flow Pattern Characteristics and Petrophysical Properties in Heterogeneous Porous Media, Second EAGE Conference on Pre-Salt Reservoir. European Association of Geoscientists & Engineers, pp. 1-5.
- Wright, P., Tosca, N., 2016. A geochemical model for the formation of the pre-salt reservoirs, Santos Basin, Brazil: implications for understanding reservoir distribution. *AAPG Search and Discovery*, article 51304.

**9 APPENDIX III: EXPERIMENTAL INVESTIGATION OF SINGLE-PHASE FLOW PATTERN IN HIGHLY HETEROGENEOUS CARBONATES ROCKS**

**Author: Shohreh Iraji**

**Co-Author: Ramin Soltanmohammadi, Tales Rodrigues De Almeida, Eddy Ruidiaz Munoz,  
Alexandre Campana Vidal**

**Campinas - SP**

**2023**



Rio Oil &amp; Gas Expo and Conference 2022

ISSN 2525-7579

Conference Proceedings homepage: <https://biblioteca.ibp.org.br/rioilegas>

Technical Paper

# Experimental investigation of single-phase flow pattern in highly heterogeneous carbonates rocks

Shohreh Irají <sup>1</sup>Ramin Soltanmohammadi <sup>2</sup>Tales Rodrigues de Almeida <sup>3</sup>Eddy Ruidiaz <sup>4</sup>Alexandre Campane Vidal <sup>5</sup>.

1. UNICAMP STATE UNIVERSITY OF CAMPINAS, SCHOOL OF MECHANICAL ENGINEERING (FEM), CENTER FOR PETROLEUM STUDIES (CEPETRO). CAMPINAS - SP - BRASIL, [s265289@dac.unicamp.br](mailto:s265289@dac.unicamp.br)

2. UNICAMP STATE UNIVERSITY OF CAMPINAS, SCHOOL OF MECHANICAL ENGINEERING (FEM), CENTER FOR PETROLEUM STUDIES (CEPETRO). CAMPINAS - SP - BRASIL, [r265288@dac.unicamp.br](mailto:r265288@dac.unicamp.br)

3. UNICAMP STATE UNIVERSITY OF CAMPINAS, INSTITUTE OF GEOSCIENCES (IGE), CENTER FOR PETROLEUM STUDIES (CEPETRO). CAMPINAS - SP - BRASIL, [tales.r.almeida@gmail.com](mailto:tales.r.almeida@gmail.com)

4. UNICAMP STATE UNIVERSITY OF CAMPINAS, SCHOOL OF MECHANICAL ENGINEERING (FEM), CENTER FOR PETROLEUM STUDIES (CEPETRO). CAMPINAS - SP - BRASIL, [ruidiaz@unicamp.br](mailto:ruidiaz@unicamp.br)

5. UNICAMP STATE UNIVERSITY OF CAMPINAS, INSTITUTE OF GEOSCIENCES (IGE), CENTER FOR PETROLEUM STUDIES (CEPETRO). CAMPINAS - SP - BRASIL, [vidal@unicamp.br](mailto:vidal@unicamp.br)

## Abstract

- Abstract

*The study of drainage strategies through flow patterns is one of the main challenges in the oil industry, especially in highly heterogeneous microbialite carbonate rocks. They present a high degree of heterogeneity, which translates to a variation of pore size distribution in the porous system, and a high variation in absolute permeability. These properties create difficulty and uncertainty when generating predictive models and hydrocarbon production forecasts. Therefore, the design and implementation of drainage strategies for these reservoirs is a challenging task. Since conventional methods for describing rock characteristics and physics are insufficient to elucidate the impact on flow rate through this rock material, the proper evaluation and analysis of the porous media's characteristics and fluid transport in these complex pore systems are essential for better characterizing microbial carbonate reservoirs. In this paper, experiments are performed to obtain the driven flow patterns obtained from medical CT scan images in single-phase flow and their impact on flow rate, in both vuggy and fine-grained carbonate rock core samples.*

**Keywords:** Flow patterns. Carbonates. Heterogeneous. Microbialite

**Received:** October 06, 2021 | **Accepted:** August 25, 2022 | **Available online:** September 26, 2022

**Article n°:** 024

**Cite as:** Proceedings of the Rio Oil & Gas Expo and Conference, Rio de Janeiro, RJ, Brazil, 2022.

**DOI:** <https://doi.org/10.48072/2525-7579.rog.2022.024>

© Copyright 2022. Brazilian Petroleuma and Gas Institute - IBP. This Technical Paper was prepared for presentation at the Rio Oil & Gas Expo and Conference, held in September 2022, in Rio de Janeiro. This Technical Paper was selected for presentation by the Technical Committee of the event according to the information contained in the final paper submitted by the author(s). The organizers are not supposed to translate or correct the submitted papers. The material as it is presented, does not necessarily represent Brazilian Petroleum and Gas Institute' opinion, or that of its Members or Representatives. Authors consent to the publication of this Technical Paper in the Rio Oil & Gas Expo and Conference 2022 Proceedings.

Experimental investigation of single-phase flow pattern in highly heterogeneous carbonates rocks

Authors: Shohreh Iraj, Ramin Soltanmohammadi, Tales Rodrigues De Almeida, Eddy Ruidiaz Munoz, Alexandre Campana Vidal\*

\* Center for Petroleum Studies (CEPETRO), UNICAMP State University of Campinas, Brazil, { [vidal@unicamp.br](mailto:vidal@unicamp.br) }

## 1. Introduction

The discovery of the giant pre-salt reservoirs in Santos and Campos Basins in Brazil is considered to be one of the most important oilfield discoveries in the last decade. The reservoirs are described as lacustrine carbonate rocks deposited during the rift tectonics related to the break-up of South America and Africa continents and consequently, the opening of the South Atlantic Ocean during the Cretaceous period (BRUHN; PINTO; JOHANN; BRANCO et al., 2017).

The carbonate rocks were deposited under two tectonic phases, the rift and sag after accomplishing these stages “microbialites” were deposited (LIMA; DE ROS, 2019). The high heterogeneity and complicated pore structures of these carbonate rocks are due to many factors (MATULA, 1969). In reservoir characterization, heterogeneity specifically applies to the variability that affects fluid flow, includes a variation of pore size distribution in the porous system, and high variation in absolute permeability (JENSEN; LAKE; CORBETT; GOGGIN, 2000). The classical concepts of fluid flow and drainage strategies in porous media are not valid for heterogeneous media (VIK; BASTESSEN; SKAUGE, 2013).

In general, the heterogeneous nature of carbonate reservoirs makes it difficult to generate predictive models, resulting in significant uncertainty in the hydrocarbon production forecast and reservoir description, thus accurate understanding of petrophysics and reservoir engineering is necessary for these reservoirs. In this regard, the design and implementation of drainage strategies for these carbonate reservoirs is a vital and challenging task, and usually require underpinning laboratory work to evaluate and analyse the porous media characteristics and fluid transport in these complex pore systems (VIK; BASTESSEN; SKAUGE, 2013).

In this study, laboratory experiments are performed in two facies, columnar and fine-grained carbonate rock, to acquire the driven flow patterns obtained from medical Computed Tomography (CT) scan images in single-phase flow and their impact on flow rate.

## 2. Method and result

To evaluate the flow pattern in this carbonate rock, samples from outcrops of Lagoa Salgada in Rio de Janeiro State, Brazil, were used as potential analogues of some Pre-salt reservoir rocks. Before plugging and cleaning, the samples were scanned using a CT scanner to identify regions of interest and obtain representative phases of rock. In this study, the rock samples can be divided into two main facies according to their pore size distribution: fine-grained with relatively small pores and columnar phase with large connected pores and vugs. Most of the samples were highly heterogeneous and fragile, thus the preparation of a representative core plug was a challenge. Figure 1 displays the workflow called “from block to plug”, which consists of drilling a block in a target. Both samples had to be wrapped in epoxy to obtain a representative sample. A thermoplastic material was used for the encapsulation process to ensure that the marginal limits of the core remained unchanged and its main flow characteristics preserved during flooding experiments. After this initial preparation, two composite cores were prepared for the evaluation of flow pattern and characterization.

Experimental investigation of single-phase flow pattern in highly heterogeneous carbonates rocks

Authors: Shohreh Iraj, Ramin Soltanmohammadi, Tales Rodrigues De Almeida, Eddy Ruidiaz Munoz, Alexandre Campana Vidal\*

\* Center for Petroleum Studies (CEPETRO), UNICAMP State University of Campinas, Brazil, { [vidal@unicamp.br](mailto:vidal@unicamp.br) }



**Figure 1**– Drilled core samples with Workflow of “from block to plug” from microbialite outcrops: a) Fine-grained and b) Columnar facies

To analyze flow patterns, at first, both samples were characterized by the dry and wet measures of the CT scan. In this procedure, each composite sample of fine-grained and columnar microbialites cores was assembled in a core holder with high pressure and temperature (106°C and 150 bar) condition. After reaching these conditions, a vacuum pump was used for evacuation of the air inside the composite. In this step, nitrogen was injected into the composite core until the pore pressure reached 50 bar. Once the nitrogen was properly stabilized, the first CT scan (dry CT) was performed. Then, the nitrogen was evacuated from the sample using a vacuum pump, and formation water (FW) with a salinity of 193.76 g/l (Table 1) at the same temperature of the core sample was injected into the composite core until stabilization. In this step, the second CT scan (wet CT) was taken to complete the initial characterization of the dry and brine-saturated composite core. This information would provide the initial porosity profile by the segmentation of the attenuation coefficient from the acquired images (MARKUSSEN; DYPVIK; HAMMER; LONG et al., 2019). Figure 2 demonstrates the schematic diagram of the flooding apparatus.

**Table 1**- Composition of formation water

Salt	NaCl	Na <sub>2</sub> SO <sub>4</sub>	NaHCO <sub>3</sub>	KCl	MgCl <sub>2</sub> .6H <sub>2</sub> O	CaCl <sub>2</sub> .2H <sub>2</sub> O	BaCl <sub>2</sub> .2H <sub>2</sub> O	SrCl <sub>2</sub> .6H <sub>2</sub> O
Composition (g/L)	163.62	0.09	0.49	6.91	3.07	19.10	0.03	0.03

Experimental investigation of single-phase flow pattern in highly heterogeneous carbonates rocks

Authors: Shohreh Iraj, Ramin Soltanmohammadi, Tales Rodrigues De Almeida, Eddy Ruidiaz Munoz, Alexandre Campane Vidal\*

\* Center for Petroleum Studies (CEPETRO), UNICAMP State University of Campinas, Brazil, { [vidal@unicamp.br](mailto:vidal@unicamp.br) }

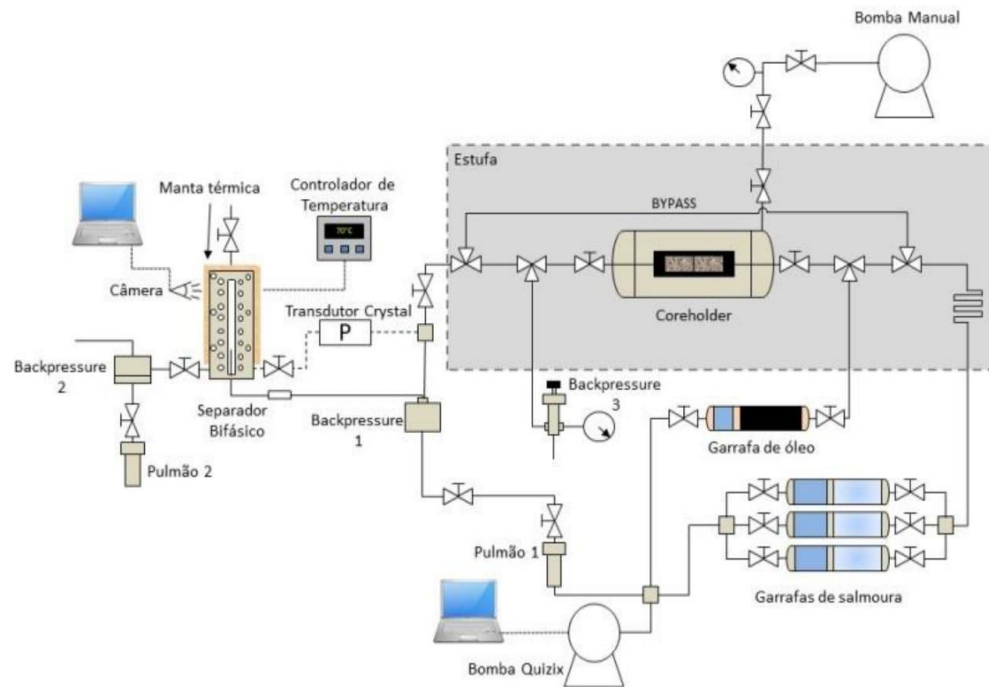


Figure 2- Schematic diagram of core flooding apparatus

The porosity of the composite sample measured with the CT imaging processed was calculated with the Equation 1. With the CT values, we were able to obtain the porosity in each slide of the composite core as the porosity profile.

$$\phi = \frac{CTR_w - CTR_g}{CT_w - CT_g} \quad (1)$$

Where,

CTR<sub>w</sub> is the CT value of the sample completely saturated with formation water

CTR<sub>g</sub> is the CT value of the sample completely saturated with nitrogen

CT<sub>w</sub> is the CT value of the average of the fluid (formation water at test condition)

CT<sub>g</sub> is the CT value of the average of the fluid (nitrogen at test condition)

Figure 3 exhibits the porosity profile of both fine-grained and columnar samples. The variation along the entire composite was due to the predominant columnar features in each core sample, which

Experimental investigation of single-phase flow pattern in highly heterogeneous carbonates rocks

Authors: Shohreh Iraj, Ramin Soltanmohammadi, Tales Rodrigues De Almeida, Eddy Ruidiaz Munoz, Alexandre Campana Vidal\*

\* Center for Petroleum Studies (CEPETRO), UNICAMP State University of Campinas, Brazil, { [vidal@unicamp.br](mailto:vidal@unicamp.br) }

is a clear characteristic of stromatolite samples. The average value of porosity yields 42.6% for the columnar sample and 36.0% for fine-grained sample.

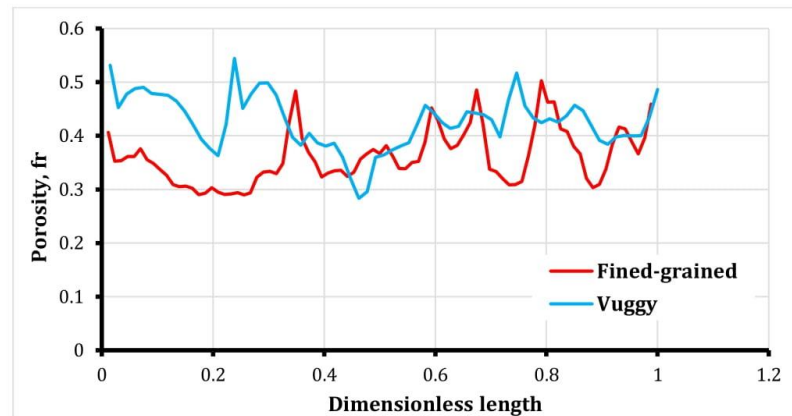


Figure 3– Porosity profile for the composite core from the fine-grained and columnar (vuggy) facies

After obtaining the initial characterization and saturating the sample with formation water, two theoretical pore volume of the first tracer (sodium iodide brine with the same concentration of formation water) at a constant rate of 0.1 ml/min was injected into the FW brine-saturated core. CT scans were taken during tracer injection. The process was followed by the injection of 2.0 porous volume of the second tracer (distilled water) at a constant rate of 0.5 ml/min coupled with CT. Therefore, it is possible to obtain the main trend as a function of rate injection. As a result of this procedure, several images need to be processed using Python scripts (LAMAS; RUIDIAZ; VIDAL, 2019) and PerGeos software to generate the stages of flow pattern (IASSONOV; GEBRENEGUS; TULLER, 2009).

The following steps were followed to generate the flow patterns: Firstly, sharpening filters were applied to the edges of the CT images to highlight the delimitation of the pore and rock edges [1, 2]. The next step involved selecting a region of interest (ROI). The ROI englobes a cropped region that contains only the image of the rock, excluding the outer part that is correlated to the air, epoxy resin, and thermal plastic. Therefore, it was possible to work with different segmentation algorithms and obtain a reliable basis to compare both segmented and non-segmented images (Figure 4A and B).

The CT scan images were digitally segmented based on the X-ray attenuation values of each voxel. In this study, the interactive overlay threshold was applied to the auto-segmented 3D greyscale image (Figure 4C). This tool allows thresholds to be selected interactively (Figure 4D).

Experimental investigation of single-phase flow pattern in highly heterogeneous carbonates rocks

Authors: Shohreh Iraj, Ramin Soltanmohammadi, Tales Rodrigues De Almeida, Eddy Ruidiaz Munoz, Alexandre Campana Vidal\*

\* Center for Petroleum Studies (CEPETRO), UNICAMP State University of Campinas, Brazil, { [vidal@unicamp.br](mailto:vidal@unicamp.br) }

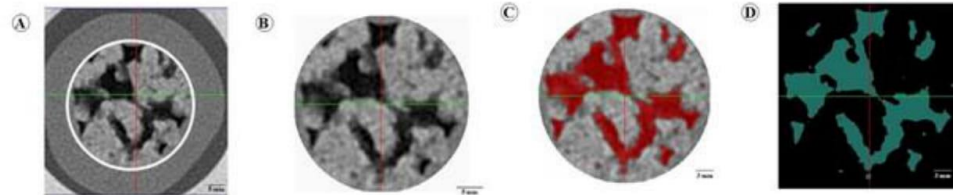


**Figure 4–** A) CT image of the analyzed core with delimitation of region of interest (ROI) in the white circle; B) The ROI; C) Segmentation process, using the interactive overlay threshold tool, considering the gray scale values of the cropped CT images; D) The binary selection image of the core

Figure 5 exhibits the flow patterns during two tracers injection (red lines for first tracer injection with the rate of 0.1 ml/min and blue lines for second tracer injection with the rate of 0.5 ml/min) in the fine-grained sample considering the rate change effect. As the figure shows, two main paths are observed, along with the composite. Also, capillary contact between each sample represents continuity in the lines which were generated by the concentration difference at each step of the tracer injection. One can also notice a point of high concentration, which can be related to the stagnation of the fluids, providing insight into bad capillary contact in the composite.

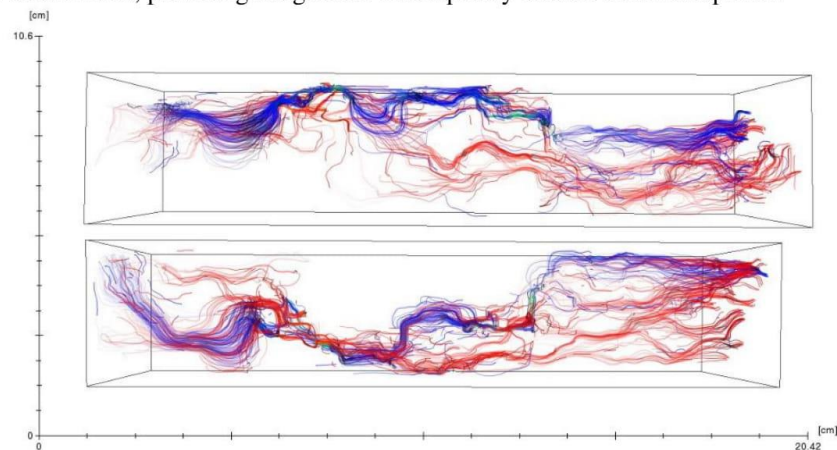


**Figure 5–** Flow patterns in the fine-grained sample during tracer injection, considering the rate change effect; Red lines: first tracer (low rate); blue lines: distilled water (high rate)

According to the flow lines in Figure 5, both blue and red lines exhibit one main flow channeling, which was created in the tracer injection, and indicates a fast breakthrough of the tracer. Figure 5 shows a good connection between each core sample and, on the face of it, columnar carbonate rocks present large pores, which creates continuity in the flow lines at the time of their formation. Figure 5 also shows the discontinuity in the flow pattern in the last pair of samples.

Figure 6 displays the same result of injecting distilled water (blue lines) five times the rate of the first tracer (red lines) in columnar sample. As we can see, there is a confirmation of one main channel in the composite, which was clearly defined with this process. Also, at this evaluation rate, it

Experimental investigation of single-phase flow pattern in highly heterogeneous carbonates rocks

Authors: Shohreh Iraj, Ramin Soltanmohammadi, Tales Rodrigues De Almeida, Eddy Ruidiaz Munoz, Alexandre Campana Vidal\*

\* Center for Petroleum Studies (CEPETRO), UNICAMP State University of Campinas, Brazil, { [vidal@unicamp.br](mailto:vidal@unicamp.br) }

is possible to observe some areas unswept by the increase in rate. When comparing the flow lines at low rate in Figure 6, there are more areas in which the low rate injection unswept the composite.

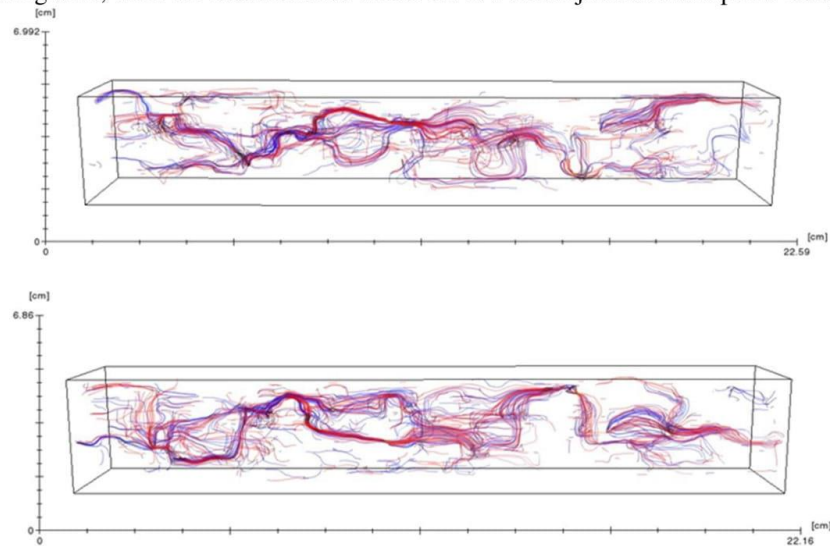


**Figure 6** – Flow patterns on columnar sample during tracer injection, considering the rate change effect, Red lines: first tracer (low rate); blue lines: distilled water (high rate)

The use of rate injection to assess the flow pattern in these rock samples shows a systematic trend regarding the driven path in composite cores, which helps us better understand the flow through porous media, dominated by heterogeneity in their porous systems. Some phenomena were identified, such as high concentration areas, which can be interpreted as stagnation pores where the tracer could not sweep. As a consequence, there is an indication of a fast breakthrough of the tracer. Despite this information, the processing continued in order to obtain information regarding the flow pattern in the miscible process and rate the evaluation. This aspect is relevant in the flow pattern through porous media in such rocks.

### 3. Final Remarks

The single-phase flow pattern experiments revealed two main behaviors and preferential flow paths, which indicates that miscible displacement in this type of rock is fully dependent on the diffusion and pore size of the system. It was also observed that flow patterns in single-phase flow are a function of the injection rate and total fluid/tracer concentration. Furthermore, these flow lines provided us with excellent insight into unswept areas, fingering, and capillary contact. Moreover, the porosity profile obtained by CT scan images indicates high variation along the composite length due to predominant heterogeneous columnar features of these rock samples. The measure of the flow pattern in columnar stromatolite rock samples presents a trend that was undistinguished and, therefore, it was impossible to obtain any interpretation of the analytical response. Additional aspects can drastically affect the further analysis of flow through this porous media.

Experimental investigation of single-phase flow pattern in highly heterogeneous carbonates rocks

Authors: Shohreh Iraj, Ramin Soltanmohammadi, Tales Rodrigues De Almeida, Eddy Ruidiaz Munoz, Alexandre Campana Vidal\*

\* Center for Petroleum Studies (CEPETRO), UNICAMP State University of Campinas, Brazil, { [vidal@unicamp.br](mailto:vidal@unicamp.br) }

#### **4. Acknowledgments**

The author would like to thank the Center for Petroleum Studies (CEPETRO-UNICAMP), for the laboratory instruments, Equinor Energy Brasil for its support and to ANP (Agência Nacional do Petróleo - proc. 20727-4).

## Referências

- Bruhn, C. H., Pinto, A. C., Johann, P. R., Branco, C., Salomão, M. C., & Freire, E. B. (2017) *Campos and Santos basins: 40 years of reservoir characterization and management of shallow-to ultra-deep water, post-and pre-salt reservoirs-historical overview and future challenges*. <https://doi.org/10.4043/28159-MS>
- lassonov, P., Gebrenegus, T., & Tuller, M. (2009). Segmentation of X-ray computed tomography images of porous materials: A crucial step for characterization and quantitative analysis of pore structures. *Water Resources Research*, 45(9), W09415. <https://doi.org/10.1029/2009WR008087>
- Jensen, J., Lake, L. W., Corbett, P. W., & Goggin, D. (2000). *Statistics for petroleum engineers and geoscientists* Gulf Professional Publishing. <http://books.google.com/books?vid=ISBN0444505520>
- Lamas, L. F., Ruidiaz, E. M., & Vidal, A. C. (2019). Automated methodology for detecting border in CT-scan images of non-circular rock samples. *Brazilian Journal of Petroleum and Gas* 13(4), 275–281. <https://doi.org/10.5419/bjpg2019-0023>
- Lima, B. E. M., & De Ros, L. F. (2019). Deposition, diagenetic and hydrothermal processes in the Aptian Pre-Salt lacustrine carbonate reservoirs of the northern Campos Basin, offshore Brazil. *Sedimentary Geology*, 383, 55–81. <https://doi.org/10.1016/j.sedgeo.2019.01.006>
- Markussen, Ø., Dypvik, H., Hammer, E., Long, H., & Hammer, Ø. (2018). 3D characterization of porosity and authigenic cementation in Triassic conglomerates/arenites in the Edvard Grieg field using 3D micro-CT imaging. *Marine and Petroleum Geology*, 99, 265–281. <https://doi.org/10.1016/j.marpetgeo.2018.10.015>
- Matula, M. (1969). *Engineering Geologic Investigations Of Rock Heterogeneity*. <https://onepetro.org/ARMAUSRMS/proceedings-abstract/ARMA69/AI-ARMA69/ARMA-69-0025/130451>
- Vik, B., Bastesen, E., & Skauge, A. (2013). Evaluation of representative elementary volume for a vuggy carbonate rock—Part: Porosity, permeability, and dispersivity. *Journal of Petroleum Science and Engineering* 112, 36–47. <https://doi.org/10.1016/j.petrol.2013.03.029>

**10 APPENDIX IV: INSIGHTS INTO MULTI-PHASE FLOW  
PATTERN CHARACTERISTICS AND PETROPHYSICAL  
PROPERTIES IN HETEROGENEOUS POROUS MEDIA**

**Author: Ramin Soltanmohammadi**

**Co-Author: Shohreh Iraj, Tales Rodrigues De Almeida, Eddy Ruidiaz Munoz, Alexandre  
Campane Vidal**

**Campinas - SP**

**2023**

D2-3

## Insights into Multi-Phase Flow Pattern Characteristics and Petrophysical Properties in Heterogeneous Porous Media

R. Soltanmohammadi<sup>1</sup>, S. Irajli<sup>1</sup>, T. Rodrigues De Almeida<sup>1</sup>, E. Ruidiaz Muñoz<sup>1</sup>, A. Ricardo Fioravanti<sup>1</sup>, A. Campana Vidal<sup>1</sup>

UNICAMP (State University of Campinas)<sup>1</sup>

### Summary

---

Flow pattern modeling of Brazilian pre-salt reservoirs is a sophisticated and complicated task due to complex texture and pore-geometry, and the high heterogeneity of reservoir rock. To overcome this problem, in this study, we examined stromatolite samples collected from Lagoa Salgada in Rio de Janeiro State that analogues to Brazilian pre-salt carbonate rock reservoirs. To scrutinize petrophysical properties, oil recovery factor, and fluid movement pattern in multiphase flow, we divided cores into vugular and fined-grain samples base on average pore size. In the first step of our experiment, we obtained the porosity of each core sample, then core flooding coupled with Computed Tomography (CT) scan to compute absolute permeability and analysis flow pattern during the imbibition and drainage process in both vugular and fined-grain composite rock samples. This segment aimed to explore absolute permeability difference and flow pattern contrast in vugular and fined-grain composites. After interpretation of flow pattern, core flooding was conducted in three different composite rock samples to investigate the final oil recovery factor in vugular, fined-grained, and combined composites.

### Introduction

The pre-salt reservoirs in Brazil are considered one of the most significant recent discoveries due to their high capacities for hydrocarbon production. At the same time, the high heterogeneity and complexity in these reservoirs increase the uncertainty and difficulties during reservoir management and modeling. It is therefore crucial to have a robust understanding of the petrophysical characteristics of pre-salt reservoirs as well as fluid flow patterns to diminish risks and ambiguities. To extend our knowledge on carbonate rock reservoirs, we collected stromatolite samples from Lagoa Salgada in Rio de Janeiro State, Brazil, which are potential analogues to some Pre-salt reservoir rocks, to scrutinize petrophysical properties such as porosity and absolute permeability. In this paper, we classified cores into vugular and fine-grained samples and conducted Computed Tomography (CT) scan images coupled with core flooding to evaluate porosity and absolute permeability in both types of cores. In addition, we examined flow patterns in multiphase flow during the drainage and imbibition processes and compared the oil recovery factor in vugular and fine-grained samples to investigate the effect of vugs in both the flow patterns and recovery factor.

### Method

In this paper, we investigated the two-phase flow patterns, plus the oil recovery factor in core samples from a complex and heterogeneous carbonate rock outcrop. To do so, the petrophysical properties of the samples were obtained by employing core flooding coupled with medical CT scanning. Outcrop rocks are widely used in laboratory experiments to gain reservoir characteristics, mainly because reservoir cores are difficult and very expensive to collect [2]. Several core samples (Figure 1) from the outcrop of Lagoa Salgada in Rio de Janeiro State, Brazil, were collected for this research to investigate the petrophysical properties of this heterogeneous carbonate rock [3].

As represented in Figure 1, the pore size distribution was different among our core samples. Hence, we divided the cores into vugular, with huge connected pores, and fine-grained, with relatively small pores. However, the creation of a representative core plug from this rock sample was a vital challenge since most of the samples were highly heterogeneous and fragile. To overcome this challenge, the encapsulation of the core samples was performed, and a thermoplastic material used for the encapsulation process to ensure that the marginal limits of the core remained unchanged and its main flow characteristics preserved during flooding experiments.

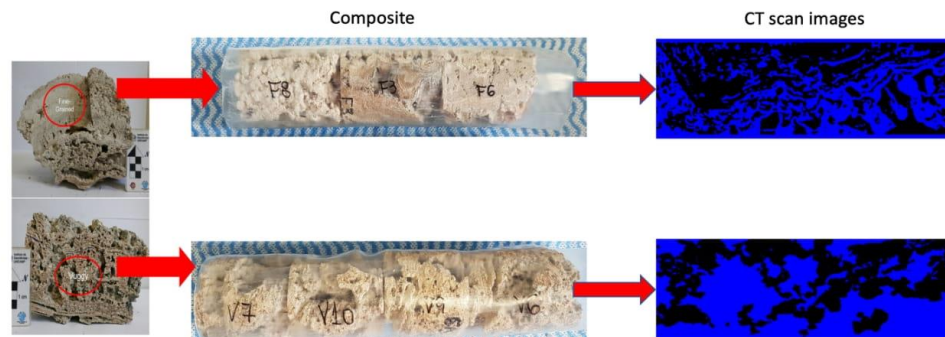


**Figure 1:** composite rock samples collected from Lagoa Salgada and the CT scan images of one vugular and one fine-grained core. Name of each core sample mentioned on each composite. (black areas in CT images represent pores)

To obtain the permeability and porosity of the cores, we followed these steps: first, we assembled the composite of each fine-grained and vuggy samples. Then, a vacuum was applied until complete removal of air and then, nitrogen flooded. At this point, we measure the absolute permeability and take the first CT scan that represents the dry CT scanning. Then, we vacuum the nitrogen to saturate the composite with formation water. The system kept monitoring until reaching the target temperature of 106°C. As a final action, we perform the CT scan to obtain the wet condition.

The values of the porosity for all samples were obtained from the CT scan image processing where, after segmentation, it was possible to count the pixels of the pore and rock system [4]. With the CT values, we obtained the porosity in each slide of the core samples as a porosity profile (Figure 2). Therefore, the porosity of the samples was calculated according to Equation 1, where  $CTR_w$  is the CT value of the sample completely saturated with formation water,  $CTR_g$  is the CT value of the sample completely saturated with nitrogen,  $CT_w$  is the average CT value of the fluid (formation water at test condition), and  $CT_g$  is the average CT value of the fluid (nitrogen at test condition):

$$\phi = \frac{CTR_w - CTR_g}{CT_w - CT_g} \quad \text{Equation 1}$$

Figure 2 depicts the porosity profile for each fine-grained and vuggy core sample in Figure 1, using processed values of dry and wet CT images. The samples exhibited a high variation in porosity but the vugular samples with huge connected vugs had a wider porosity distribution (from 0.28 to 0.56), which expresses a greater degree of heterogeneity. Although the vugular samples had huge connected vugs, the results reveal that the porosity difference between vugular and fine-grained samples is not remarkable. In other words, pore size did not influence the effective porosity.

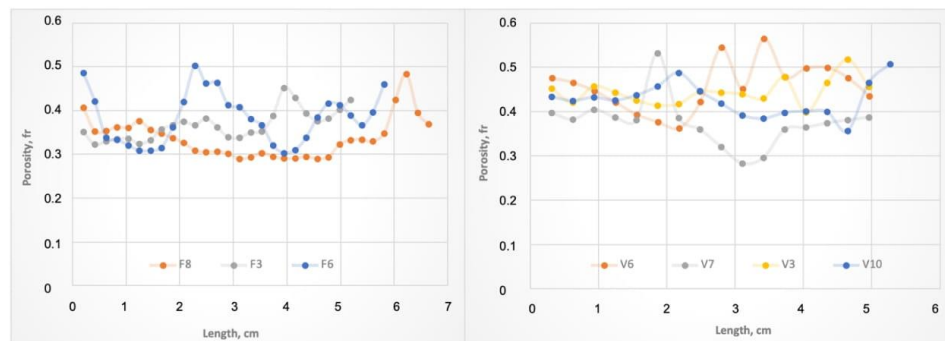


**Figure 2** – Porosity profile for core samples of the fine-grained and vuggy facies, respectively, from left to right. (F3, F6, and F8 are fine-grained samples and V3, V6, V7, and V10 are vugular samples)

To calculate the absolute permeability, formation water was injected into the core holder using a pump, and this resulted in an observed pressure drop across the plug. In the setup, a differential pressure transducer was installed to measure the differences between the inlet and outlet pressure of the core. The brine absolute permeability was estimated by applying Darcy's law [1, 5].

For vugular and fine-grained composite core samples, water was injected at flow rates of 0.5, 1 and 5 cc/min. The experimental outcome of pressure variation during the water flooding exposed that the average permeability of vugular composite is 1179.02 mD, while the average permeability in the fine-grained composite is 828.6 mD (the composites used for this experiment are the same as Figure 1).

An investigation of flow patterns during the imbibition and drainage process may help us to achieve a solid basis of flow propagation in pre-salt reservoirs.

Accordingly, in the next step, we began injecting oil (non-wetting phase) into a fully water-saturated composite and interpreting the CT scan images simultaneously to achieve flow patterns during the drainage process for both vugular and fine-grained composite samples. This process continued until the water reached irreducible saturation and the pores filled with oil. After performing the drainage process in both composites, we began injecting water (wetting phase) through composites to accomplish imbibition (we have a water-wet scenario in this study).

The results in Figure 3 represents the flow pattern acquired through experimental results after concluding the drainage and imbibition process. For both fine-grained and vugular composites, the flow

patterns obtained are shown in both top views (Figure 3(B) and 3(D)) and lateral views (Figure 3(A) and 3(C)).

The blue lines in Figure 3 represent the imbibition process while the red lines express the drainage process. A comparison between the drainage and imbibition lines demonstrated that, in vugular composite (3C and 3D), there is a better match between the red and blue lines, which describes the fluid flowing along huge connected vugs in both imbibition and drainage processes. On the other hand, in the fine-grained composite (3B and 3C), due to the capillary effect, the blue lines and red lines exhibited less match, which renders a higher capillary effect in smaller fine-grained pores.

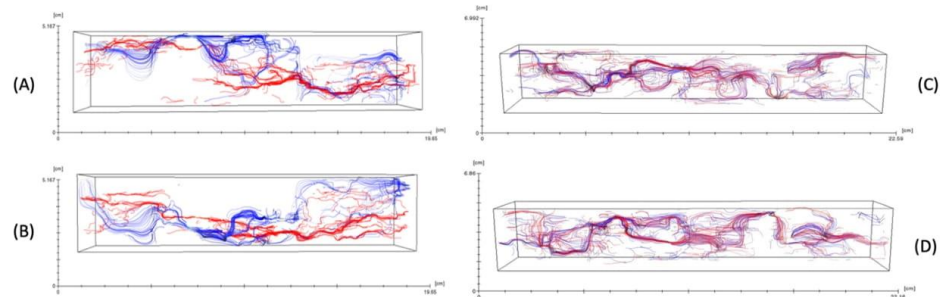


**Figure 3:** flow patterns during drainage and imbibition while the red and blue lines display drainage and imbibition, respectively. (A) lateral view of fine-grained composite, (B) top view of fine-grained composite, (C) lateral view of vugular composite, (D) top view of vugular composite.

The results of the flow patterns research led to a better understanding of the fundamental characteristics of the samples during the drainage and imbibition processes and enhanced the evaluation of pore network connectivity in both fine-grained and vuggy samples. Furthermore, the results exhibit a good match between blue and red lines in the vugular sample (3C and 3D) that emphasize the negligible capillary effect on the vugular sample.

The core flooding experiments were conducted using three composite samples: four vuggy cores (Vug Stro F4), three fine-grained cores (Fine Strom F2), and a combination of both vugular and fine-grained cores (Init Wett C\_7). To find the effect of brine composition on the main mechanisms of releasing the trapped oil, the composite samples were flooded using formation brine followed by seawater and 10X diluted seawater as second and third flooding stages (Figure 4). The results represent 21.28%, 30.65%, and 35.35% final recovery factor for vuggy (Vug Stro F4), fines-grain (Fine Strom F2), and combined (Initt Wett C\_7) samples respectively.

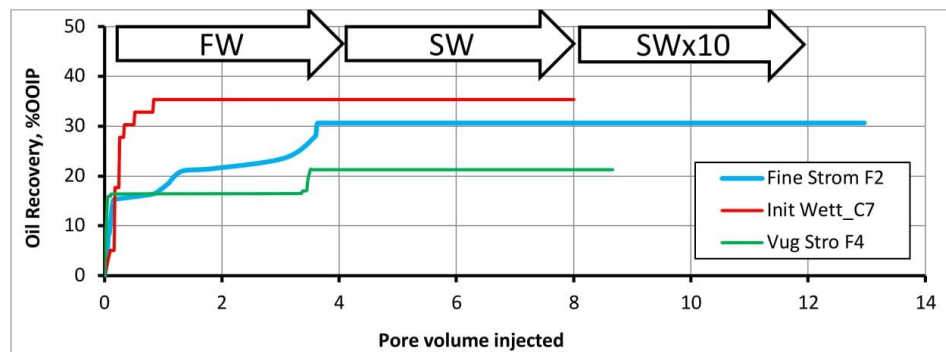


**Figure 4** Comparison of Oil Recovery between wetting sample, vuggy and fine-grained stromatolite samples

### Conclusions

In this paper, we investigated the petrophysical characteristics of Stromatolite core samples collected from Lagoa Salgada in Rio de Janeiro State, Brazil. An examination of the pore size distribution of the rock samples exhibited extraordinary distinction and high heterogeneity, which resulted in the separation of fine-grained and vugular sections. Accordingly, to further interpret the petrophysical features, cores were divided into vugular (containing huge, mostly connected pores) and fine-grained samples.

The effective porosity of composites in the flow direction axis was obtained by analyzing the medical CT scan images during core flooding. The porosity profile results across the composite length illustrated slightly higher porosity in vugular samples. Accordingly, the existence of large vugs in vugular samples did not provoke a significant difference between the porosity of the composites. On the other hand, the porosity profile showed a wider porosity distribution in vugular samples when compared to fine-grained cores.

In this study, we also implemented water flooding operations at three different flow rates to interpret the pressure exchange, and applied Darcy's law to achieve absolute permeability in vugular and fine-grained samples. The results of the permeability calculation revealed notably higher permeability in the vugular core samples when compared to the fine-grained samples. The average brine absolute permeability in the vugular samples was 1179.02 mD while, in the fine-grained samples, it was 828.6 mD.

Flow patterns during the imbibition and drainage process in both vugular and fine-grained composites were achieved after scrutinizing the CT images. For the vugular composite, the results exhibited that the fluid flows through large vugs among the vuggy core samples and the capillary effect are negligible. By contrast, fine-grained composite drainage and imbibition revealed two different flow patterns due to the capillary effect. This research exposed that capillary pressure has an undeniable impact on the fluid flow in fine-grained samples but a negligible influence in huge vuges.

From coreflooding experiments, we concluded that the second and third flooding stages had minimal effect on the oil production for all the composite samples. The results for three composite cores revealed an oil recovery efficiency of 21.28%, 30.65%, and 35.35% based on original oil in place (OOIP), respectively, which clarifies the effectiveness of soaking to exploit the wettability alteration mechanism.

### Acknowledgements

All the experiments in this paper were conducted at the Center for Petroleum Studies (CEPETRO), of UNICAMP, and the authors would like to thank the financial assistance provided by Agencia Nacional do Petroleo, Gas Natural e Biocombustiveis (ANP), and Equinor.

### References

1. Ebrahim Fathi, A. T. (2012). Correction to Klinkenberg slip theory for gas flow in nano-capillaries. *International Journal of Coal Geology*, 51-59.
2. Håvard D. Enge, S. J. (2007). From outcrop to reservoir simulation model: Workflow and procedures. *Geosphere*.
3. Kristian E. Meisling, P. R. (2001). Segmentation of an Obliquely Rifted Margin, Campos and Santos Basins, Southeastern Brazil. *AAPG Bulletin*.
4. Nguyen Lam Quoc Cuong, N. H. (2018). Porosity Estimation from High Resolution CT SCAN Images of Rock Samples by Using Housfield Unit. *Open Journal of Geology*.
5. Ping Sheng, M. Y. (1988). Dynamic Permeability in Porous Media. *PHYSICAL REVIEW LETTERS*.

**11 APPENDIX V: UPSCALING CHALLENGES OF  
HETEROGENEOUS CARBONATE ROCKS: A CASE STUDY OF  
BRAZILIAN PRE-SALT ANALOGOUS**

**Author: Ramin Soltanmohammadi**

**Co-Author: Shohreh Iraj, Tales Rodrigues De Almeida, Eddy Ruidiaz Munoz, Alexandre  
Campane Vidal**

**Campinas - SP**

**2023**

D3-3

## Upscaling Challenges of Heterogeneous Carbonate Rocks: A Case Study of Brazilian Pre-Salt Analogous

R. Soltanmohammadi<sup>1</sup>, S. Iraj<sup>1</sup>, T. Rodrigues de Almeida<sup>1</sup>, E. Ruidiaz Munoz<sup>1</sup>, A. Campana Vidal<sup>1</sup>

State University of Campinas (UNICAMP)<sup>1</sup>

### Summary

---

Summary is not available

## Introduction

Exploration of pre-salt reservoirs has caused a remarkable impact on the petroleum industry in Brazil. According to the Brazilian Oil and Natural Gas Agency (ANP), more than 70% of total produced oil (roughly 2.5 million barrels per day) in 2021 was through pre-salt reservoirs (Alves and Polette, 2021). Producing petroleum through carbonate pre-salt reservoirs poses several challenges, in particular: contamination from  $CO_2$  (8 -15%) and  $H_2S$  in the gas phase; ultra-deep-water drilling (ranging from 2000 to 2300 m); drilling through thick salt layer; and above all, heterogeneous in porous distribution (Fraga et al., 2015). The heterogeneity of Brazilian pre-salt reservoirs is marked by diversity in pore types, such as interparticle, vugular, fracture, and dissolution horizons or "super-k" layers (da Rocha et al., 2019). Consequently, the flow simulation applied to pre-salt reservoirs has usually been conducted with a high degree of uncertainty and complexity (Correia et al., 2015). Also, the existence of huge connected vugs and dissolution structures became a challenge to perform fluid flow simulation and commonly used equations such as Darcy's law cannot be implemented because of the high Reynolds number (Ungarish, 2007).

To analyze the complexities of these reservoirs, analogous rocks were used, in this case, the stromatolite samples from Lagoa Salgada - RJ. These carbonate stromatolite rocks show high permeability, between 800 to 1200 millidarcy (mD), and porosity from 30% to 60%. On the other hand, a low oil recovery factor below 35% (using light oil) was obtained, even after a reasonably long injection period of brine (more than 10 pore volume injected) (Soltanmohammadi et al., 2021). Therefore, to obtain more reliable results on fluid behavior in stromatolite core samples, we simulated the fluid propagation on a new set of stromatolite samples during core flooding using high-resolution computed tomography (hCT) images from vugular facies. This study aims to provide a more trustworthy understanding of fluid movement in single and multi-phase flow using images acquired from hCT scanning of a vugular stromatolite facies to exhibit the main reason for the low oil recovery factor. Results of the single-phase flow and 2D simulation are then transferred to the multi-phase and 3D model to provide a solid foundation for the proper upscaling degree to reduce computational time during numerical simulation as well as creating an accurate model of vuggy porous media.

## Method and Theory

### ●Single-Phase Flow Simulation

As the first step, the rock samples were cleaned and scanned using a medical-CT scanner to distinguish regions of interest and obtain representative phases of rock. Two facies were defined based on their pore size and geometry: fine-grained and columnar/vugular. The columnar sample has connected vugs, with pore diameter in the order of centimeters, while fine-grained samples have considerably smaller pores. In this study, we examine fluid flow characteristics in a columnar sample. The sequence that comprises drilling a block in a target area of the sample and the encapsulation displays in Figure 1. Thermoplastic material was used for the encapsulation process to ensure that the marginal limits of the core remained unchanged.



**Figure 1** Samples drilled from columnar/vuggy facies of microbialite outcrops, and prepared for experimental section.

A core sample from columnar facies (with 8.9cm length and 3.68cm diameter) was investigated. The porosity of the core (52.5%) was obtained using a gas porosimeter. Liquid permeability of the core sample, after obtaining pressure drop during core flooding, was 1179.02 millidarcy (mD). The

# EAGE

porosity profile for the columnar core sample using hCT images is shown in Figure 2(a). Using hCT images of the core a 3D model was obtained, and two 2D hCT images from horizontal and vertical cross-section plates were generated. The vugular 3D core sample and two plates are shown in Figure 2(b). The 2D hCT image displayed in Figure 3(a), represents the pores and solid grains. The connected pore zone is shown in Figure 3(b)

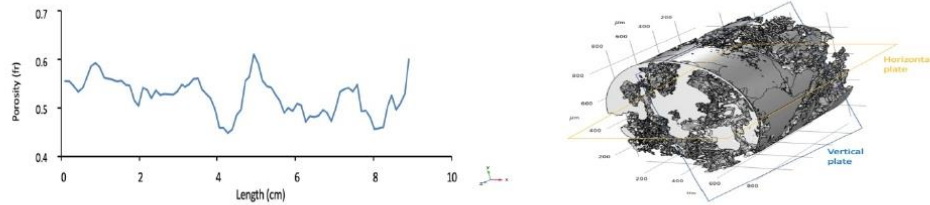


**Figure 2** (a): The porosity alongside the core length (obtained from medical-CT scanning during core flooding). (b): 3D model and two 2D cross-sections, the horizontal and vertical sections are marked in yellow and blue, respectively. A horizontal plate was used as geometry in the simulation.

Using the 2D image, single-phase water-flooding was modeled to procure a velocity field. Moreover, flow streamlines were drawn to clarify the flow pattern within the vugular sample. Zero flux term ( $u = 0$ ) boundary condition is applied around grains. The chemical reaction between water and rock was considered negligible. In this simulation, we assumed that fluid was injected through the left of Figure 3(b) (inlet with constant velocity) and expelled through the right.

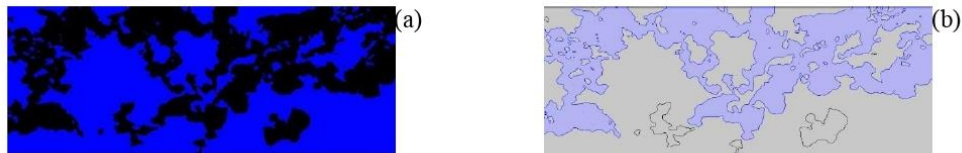


**Figure 3** (a): 2D cross-section, collected from hCT scanning, acquired through horizontal plate; black and blue colors display pores and solid-grains respectively. (b): Blue color exposes connected pores in a horizontal cross-section. The length and height of the image is 8.9 and 3.68 cm, respectively.

Navier–Stokes equations for conservation of momentum (Equation 1) and the continuity equation (Equation 2) for conservation of mass were applied to model single-phase fluid flow (Momani and Odibat, 2006). The gravitational force in the momentum equation does not include in Equation 1 and is considered negligible.

$$\rho \frac{\partial u}{\partial t} + u \cdot \nabla u = -\nabla p + \nabla \cdot (\mu (\nabla u + (\nabla u)^T) - 2\mu (\nabla \cdot u) I) + F \tag{Equation 1}$$

$\frac{\partial}{\partial t}$ 
Pressure force
 $\frac{\partial}{\partial t}$ 
Viscous force
External force

$$\frac{\partial \rho}{\partial t} + \nabla \cdot (\rho u) = 0 \tag{Equation 2}$$

In Equation 1,  $u$  is the fluid velocity,  $p$  is the fluid pressure,  $\rho$  is the fluid density, and  $\mu$  is the fluid’s dynamic viscosity. We assumed that water was incompressible ( $C_{\#} = 0$ ), and in the beginning, the core

# EAGE

was fully saturated with water; we then injected water with constant velocity ( $u_{in} = 1.4 \times 10^{-6}$  m/s) through the inlet. We considered suppressing backflow pressure was 50 bar ( $p_2 = 50$  bar), initial pressure and temperature was 150 bar and 379.15 K ( $p_5 = 150$  bar,  $T_5 = 379.15$  K).

The velocity field in the horizontal plate is displayed in Figure 4. Fluid velocity dramatically increases in pore throats, the color bars represent the velocity value (red corresponds to higher and blue to lower values). The fluid velocity field illustrates that fluid propagates faster when moving through connected vugs, while in dead-end pores and vugs, water remains almost stagnant. Although velocity approached more than  $1.1 \times 10^{-6}$  m/s in pore throats, in dead-end pores and vugs, it is less than  $2 \times 10^{-7}$  m/s, disregarding the size of vugs. In fact, fluid tended to propagate only through connected vugs. Even in huge dead-end vugs, with the radius in order of centimeters, water remains stagnant. As a consequence, we observed channeling-like behavior in the vugular sample, which can lead to significant untouched regions

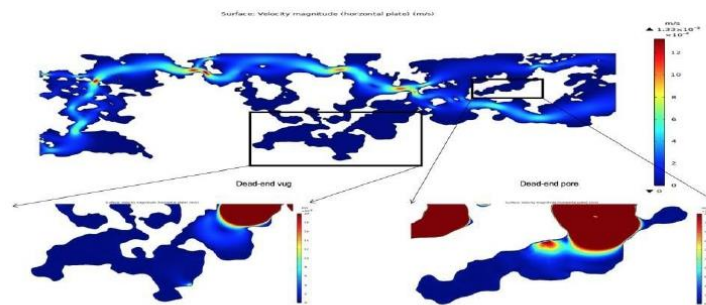


**Figure 4** The simulated velocity field represents that the maximum velocity in this cross-section is  $1.33 \times 10^{-6}$  m/s when the fluid passes through the pore throat. On the other hand, in both dead-end pores and vugs, the water velocity is less than  $2 \times 10^{-7}$  m/s.

The streamlines are used to visualize vector quantities by showing curves tangent to a vector field (Figure 5). The density of streamlines varies depending on the magnitude of the velocity vector field, the arrows on streamlines represent flow direction, and the color exhibits water velocity (Figure 5). The streamlines can legitimize the flow pattern obtained from previous experiments on stromatolites (Soltanmohammadi et al., 2021). Admittedly, numerical simulation unveiled that those regions in flow patterns that remain untouched correspond to dead-end zones. Indeed, streamlines provided us robust understanding on fluid propagation in single-phase flow in the stromatolite vugular sample. Streamlines rendered the effect of dead-end zones on modifying flow path, and this phenomenon can be implemented in the next simulations to proffer more reliable models.

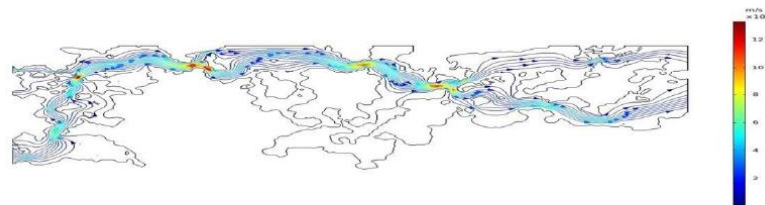


**Figure 5** Streamlines in the horizontal plate. As given in figure 4, the water in dead-end zones remained stagnant. The color bar represents the velocity profile in pore-scale model.

### •Multiphase Flow Simulation and Upscaling

Even in the core scale, it is computationally expensive to simulate a 3D model using hCT images while employing the Navier-Stokes equation. Therefore, it is crucial to simplify the model using upscaling methods. In addition, in stromatolite samples, dead-end zones appear to have a tremendous effect on residual oil. Therefore, to investigate the influence of different upscale factors, the three-dimensional simulation was conducted, under the same conditions as the 2D model with four different upscaling factors using the upscaling method from Hangyu Li (Li and Durlofsky, 2016). The purpose of this simulation was to evaluate the impact of various upscaling factors on final residual oil saturation after a long brine injection. Upscaling was performed for the model with four factors (U-3, U-5, U-6, and U-12), and for each factor U-n, the process was performed by grouping sets of  $n \times n \times 1$  blocks, resulting in an upscaled model with  $1 \times 1 \times 1$  blocks. The initial oil saturation in these four upscaling factors seems quite similar (Figure 6(c)). Nevertheless, after a long injection duration (Figure 6(b)), the residual oil profile illustrates that upscaling factors 6 and 12 are not able to detect dead-end zones while residual oil saturation was obtained using upscale factors 3 (U-3) and 5 (U-5) seem quite similar, though U-5 is almost eight times faster than U-3. Given the impact of dead-end zones in bypassed oil in vugular porous media, having a reliable and reasonably fast model that can predict the reservoir behavior required a precise examination of upscaling factors in the way that the model contains both the effect of dead-end vugs and pores and reasonable computational time

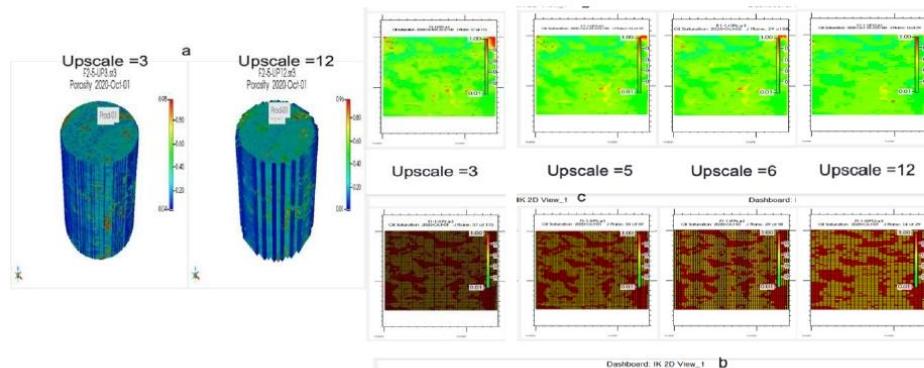


**Figure 6** (a): comparison of porosity profile in a core model with two different upscaling factors (U-3 and U-12). (b): residual oil saturation in four different upscaling factors (red represents the oil). (c): initial oil saturation in different upscaling factors.

### Conclusions

The porosity and permeability of the stromatolite core sample in this study were 0.52 and 1179.02 mD, respectively. A previous study on the same rock type displayed a relatively low oil recovery factor, coupled with high porosity and permeability. Firstly, using the Navier-Stokes equation and hCT image of the core, the 2D of single-phase flow was generated to analyze fluid flow streamlines. The results show that because of dead-end pores and vugs, a remarkable amount of fluid remains stagnant in these regions, regardless of pore/vug size. We also observed channeling-like behavior in the vugular sample causing a fast breakthrough. By creating four models with different upscaling factors, we observed that the U-5 model is the optimum upscaling factor number that detects the dead-end zone effect and has a reasonably low computational cost. These results can use in further simulation studies to have a high accuracy model with reduced computational time. Although stromatolite core samples have suitable petrophysical characteristics (high porosity/permeability, connected vugs/fractures), interpreting the hCT and flow patterns images showed a remarkable amount of bypassed fluid after a long period of brine injection in dead-end zones, which is well in line with previous experimental results.

### Acknowledgements

We gratefully acknowledge the support of EPIC – Energy Production Innovation Center, hosted by the University of Campinas (UNICAMP) and sponsored by FAPESP – São Paulo Research Foundation (2017/15736-3 process). We acknowledge the support and funding from Equinor Brazil and the support of ANP (Brazil’s National Oil, Natural Gas and Biofuels Agency) through the R&D levy regulation.

### References

- Alves, J.A., Polette, M., 2021. Political, economic, and institutional aspects of oil and gas exploration and production in Brazil. *América Latina en la historia económica* 28.
- Correia, M., Hohendorff, J., Gaspar, A., Schiozer, D., 2015. UNISIM-II-D: Benchmark case proposal based on a carbonate reservoir, SPE Latin American and Caribbean Petroleum Engineering Conference. OnePetro.
- Fraga, C.T. C., Pinto, A.C.C., Branco, C.C.M., da Silva Paulo, C.A., 2015. Brazilian pre-salt: An impressive journey from plans and challenges to concrete results, Offshore Technology Conference. OnePetro.
- da Rocha, H.O., da Costa, J.L.S., Carrasquilla, A.A.G., Carrasco, A.M.V., 2019. Petrophysical characterization using well log resistivity and rock grain specific surface area in a fractured carbonate pre- salt reservoir in the Santos Basin, Brazil. *Journal of Petroleum Science and Engineering* 183, 106372.
- Li, H., Durlofsky, L.J., 2016. Upscaling for compositional reservoir simulation. *SPE journal* 21, 0873-0887.
- Momani, S., Odibat, Z., 2006. Analytical solution of a time-fractional Navier–Stokes equation by Adomian decomposition method. *Applied Mathematics and Computation* 177, 488-494.
- Soltanmohammadi, R., Iraj, S., De Almeida, T.R., Munoz, E.R., Fioravanti, A.R., Vidal, A.C., 2021. Insights into Multi-Phase Flow Pattern Characteristics and Petrophysical Properties in Heterogeneous Porous Media, Second EAGE Conference on Pre-Salt Reservoir. European Association of Geoscientists & Engineers, pp. 1-5.
- Ungarish, M., 2007. A shallow-water model for high-reynolds-number gravity currents for a wide range of density differences and fractional depths. *Journal of Fluid Mechanics* 579, 373-382.

**12 APPENDIX VI: EXPERIMENTAL INVESTIGATION OF  
WATERFLOODING PERFORMANCE BY INCREASING COPPER  
IONS IN BRAZILIAN PRE-SALT ROCK**

**Author: Shohreh Iraji**

**Co-Author: Ramin Soltanmohammadi, Eddy Ruidiaz Munoz, Alessandra Winter, Rafael  
Valladares de Almeida, Alexandre Campana Vidal**

**Campinas - SP**

**2023**



## EXPERIMENTAL INVESTIGATION OF WATERFLOODING PERFORMANCE BY INCREASING COPPER IONS IN BRAZILIAN PRE-SALT ROCK

S. Irajil<sup>1</sup>, R. Soltanmohammadi<sup>1</sup>, E. Ruidiaz Munoz<sup>1</sup>, A. Winter<sup>1</sup>, R. Valladares de Almeida<sup>2</sup>, A. Campana Vidal<sup>1</sup>

<sup>1</sup> Unicamp; <sup>2</sup> Repsol Sinopec Brasil

### Summary

---

Low salinity water injection technique employs modified injection brine chemistry to reach the favorable conditions for crude oil/brine/rock interactions which allows the oil to be moved easily in the porous media and obtain higher oil recovery. This work is aimed to investigate the efficiency of low salinity water injection with laboratory experimental approach. A case study includes three different core samples from different wells of Brazilian Pre-Salt carbonate reservoir to examine oil recovery factor variation during sea water injection followed by sea water with the addition of copper ion. The recovery factor by seawater reached values up to around 25% of the OOIP. Additional oil recovery was observed during the injection of seawater with the addition of copper chloride. During this process, the recovery increased around 6 to 29% of the OOIP for different core samples which shows the application potential of low salinity water injection process and effectiveness of mechanism of desorption of the acidic oil from the rock surface by forming acid-copper complexes.



## Experimental Investigation of Waterflooding Performance by Increasing Copper Ions in Brazilian Pre-salt Rock

### Introduction

Water flooding is a proven technique worldwide to improve oil recovery. Low salinity water injection method has been demonstrated to be more effective in improving oil recovery compared to water injection[1]. This method acts in such a way that the equilibrium of the initial crude oil/brine/rock could be modified to the favorable conditions which allow the oil to be moved easily in the porous media [2]. The popularity of this EOR method comes from unique advantages of this technique, which include: efficiency of producing light to medium gravity crude oils, simplicity of injection into hydrocarbon formations, water sources availability, environmentally friendly, lack of expensive chemical additives, low damage risks and low capital and operating costs, especially for the fields, were presently flooded by water[3].

Different mechanisms have been proposed for incremental oil production during this process[4]. Detachment of fine mixed wet particles (fine migration) may lead to a more water-wet condition and a rise in microscopic sweep efficiency[5]. DLVO theory is implemented for the detachment of fine particles. According to this theory, fine detachment takes place whenever the injected brine salinity is lower than or equal to the critical flocculation concentration. Additionally, increased pH and Osmosis are possible mechanisms for enhanced oil recovery [6]. pH will affect IFT and emulsification. The chance for water-in-oil (w/o) emulsification increases during water injection into the reservoirs, where the droplet size distribution of emulsion depends on the salinity and composition of the injected brine[7]. A recent study reveals that adding Cu(II) ions into the injected seawater, result a significant incremental oil production in carbonate reservoirs. EOR mechanism in this process involve, desorbtion of the acidic oil from the rock surface by forming acid-copper complexes that are dragged by the injected fluids[8].

This work is aimed to investigate the efficiency of water injection with laboratory experimental approach. A case study includes three different core samples from different wells of the Brazilian Pre-Salt reservoir to examine oil recovery factor variation during sea water injection followed by sea water with the addition of copper ions.

### Method and/or Theory

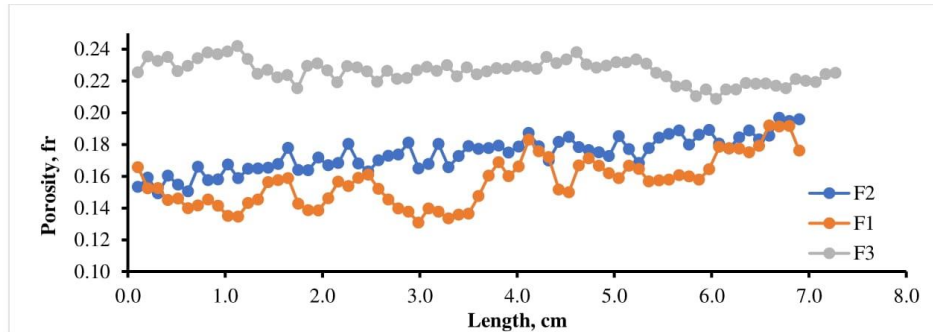
In order to investigate the effect of injection brine chemistry on oil recovery, core flooding experiments were performed on three plug samples from different wells of the Brazilian Pre-Salt reservoir. Core specifications are shown in Table 1.

**Table 1:** Core properties

Sample ID	Length, (cm)	Pore Volume, (cc)	Porosity, (%)	Permeability, (md)
F1	6.9	11.0	14.2	126.0
F2	6.9	13.6	17.2	320.0
F3	7.3	17.8	21.1	173.0

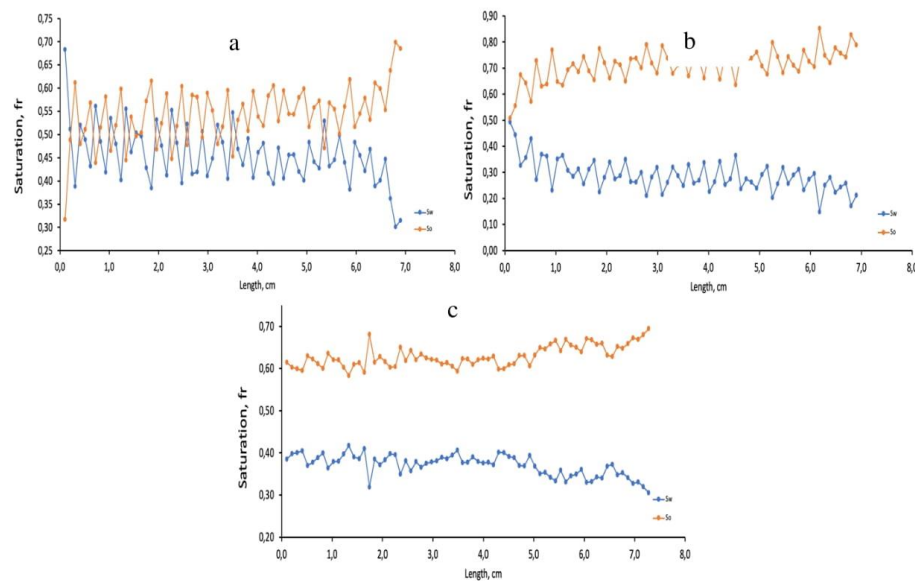
To analyze the samples, at first, all samples were characterized by the dry and wet measures of the CT scan. In this procedure, nitrogen was used to perform the measurement of dry CT scan and formation water (FW) with a salinity of 245.2 g/l, to perform the measurement of wet CT scan, both at the experimental condition of 69°C and 8230 psi. This information would provide the initial porosity profile by the segmentation of the attenuation coefficient from the acquired images [9].

Figure 1 exhibits the porosity profile of our three core samples. The variation along the entire length for each core sample is due to the predominant heterogenetic nature of carbonate reservoir, that basic petrophysical properties vary significantly horizontally and vertically in different scales.



**Figure 1:** Porosity profile for the three samples

A brief description of the used procedure for core flooding experiments to investigate waterflooding performance is as follows. In the first step, the selected plugs were cleaned with a Soxhlet extractor and then dried in the oven. In the next step, the cores were placed in the core holder and flooded with several pore volumes of FW with 0.1 ml/min to saturate the cores. The injection of brine was continued until the injection pressure stabilized. In the next stage, the saturated cores with brine were then flooded by crude oil from the Brazilian Pre-Salt reservoir with the same injection rate of FW until no more brine was produced. The oil and water saturation along the core length for all core samples obtained by CT values are displayed in Figure 2. At this point, it is possible to calculate the connate water saturation (0.410, 0.339, and 0.381 for F1, F2, and F3, respectively).



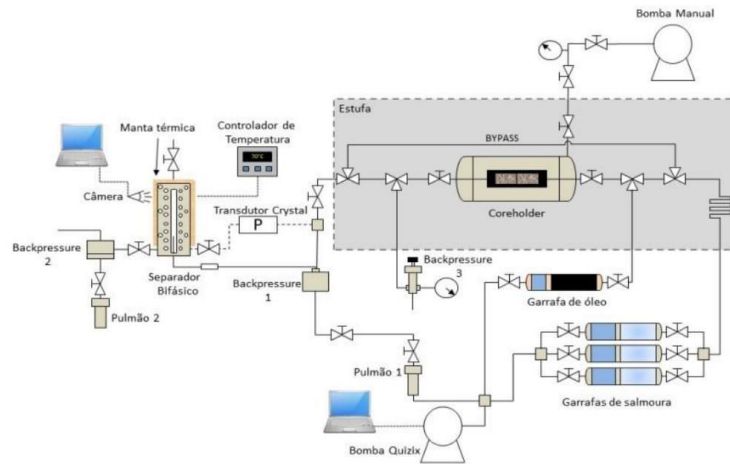
**Figure 2:** Oil and water saturation profile along the core length after oil flooding stage a) F1 b) F2 c) F3 core samples

In the next stage, all the plugs were placed in crude oil and aged for 14 days at 90°C to restore the wetting properties of the reservoir. After completion of this stage and recording the production data, the water flooding process was start to mimic the secondary oil recovery process. In this step, the sea water (SW: refer to Table 2) was started to inject and followed by recording the production data

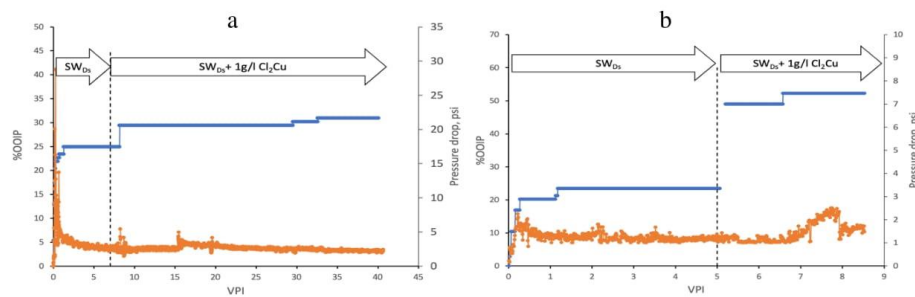
including pressure drop, produced water, and oil volumes to calculate the oil recovery factor. In the next stage, the injection of low salinity water (SW+M: refer to Table 2) was injected to find the efficiency of the smart water injection. In this study  $SO_4^{2-}$  and  $Cu^{2+}$  are assumed to be potential determining ions. Figure 3 demonstrates the schematic diagram of the flooding apparatus. Figure 4 indicates oil recovery factor results. The results represent 24.91%, 23.44%, and 20.0% recovery factor after SW injection which increased to 30.94%, 52.22%, and 30.0% recovery factor after low salinity water injection for F1, F2, and F3, respectively.

**Table2:** Composition of sea water and low salinity water

Salt	NaCl	CaCl <sub>2</sub> x2H <sub>2</sub> O	MgCl <sub>2</sub> x6H <sub>2</sub> O	KCl	SrCl <sub>2</sub> x6H <sub>2</sub> O	Na <sub>2</sub> SO <sub>4</sub>	NaHCO <sub>3</sub>	CuCl <sub>2</sub>	TDS (ppm)
SW (g/L)	23.472	1.467	10.551	0.725	0.039	3.917	0.193	0.000	34380
SW+M (g/L)	23.472	1.467	10.551	0.725	0.039	0.100	0.193	1.00	35380



**Figure 3:** Schematic diagram of core flooding apparatus



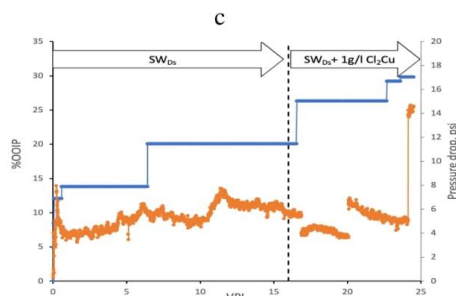


**Figure 4:** Comparison of Oil Recovery (blue) and pressure drop (orange) during SW followed by low salinity water injection for a) F1 b) F2 c) F3 core samples

### Conclusions

The effect of brine composition on oil recovery of Brazilian Pre-Salt carbonate reservoir during low salinity water injection was analyzed in this study. The recovery factor by seawater reached values up to around 25% of the OOIP, these recovery patterns are representative of preferential oil-wetting properties of these samples.

Additional oil recovery was observed during the injection of seawater with the addition of copper chloride. During this process, the recovery increased around 6 to 29% of the OOIP for different core samples which shows the application potential of the low salinity water injection process and effectiveness of mechanism of desorption of the acidic oil from the rock surface by forming acid-copper complexes.

The effective porosity of three core samples in the flow direction axis was obtained by analysing the medical CT scan images during wet and dry core flooding. The porosity profile results across the length illustrated the heterogenetic nature of carbonate reservoir.

### Acknowledgements

All the experiments in this paper were conducted at the Center for Petroleum Studies (CEPETRO) of UNICAMP, and the authors would like to thank the financial assistance provided by Agencia Nacional do Petroleo (ANP), and Repsol Sinopec Brasil.

### References

- Pooryousefy, E., et al., *Drivers of low salinity effect in sandstone reservoirs*. Journal of Molecular Liquids, 2018. **250**: p. 396-403.
- Sheng, J., *Critical review of low-salinity waterflooding*. Journal of Petroleum Science and Engineering, 2014. **120**: p. 216-224.
- Jadhunandan, P. and N.R. Morrow, *Effect of wettability on waterflood recovery for crude-oil/brine/rock systems*. SPE reservoir engineering, 1995. **10**(01): p. 40-46.
- Chai, R., et al., *Dynamic behaviors and mechanisms of fluid-fluid interaction in low salinity waterflooding of carbonate reservoirs*. Journal of Petroleum Science and Engineering, 2022. **208**: p. 109256.
- Berg, S., et al., *Direct experimental evidence of wettability modification by low salinity*. Petrophysics, 2010. **51**(05).
- Lager, A., et al., *Low salinity oil recovery-an experimental investigation I*. Petrophysics, 2008. **49**(01).
- Maaref, S. and S. Ayatollahi, *The effect of brine salinity on water-in-oil emulsion stability through droplet size distribution analysis: a case study*. Journal of Dispersion Science and Technology, 2018. **39**(5): p. 721-733.
- Bernardinelli, O.D., et al., *Mechanism for enhanced oil recovery from carbonate reservoirs by adding copper ions to seawater*. Fuel, 2021. **305**: p. 121605.
- Markussen, Ø., et al., *3D characterization of porosity and authigenic cementation in Triassic conglomerates/arenites in the Edvard Grieg field using 3D micro-CT imaging*. Marine and Petroleum Geology, 2019. **99**: p. 265-281.